RULES FOR UNDERSTANDING RARE-EARTH MAGNETIC COMPOUNDS

A Dissertation

by

LINDSAY ELIZABETH ROY

Submitted to the Office of Graduate Studies of
Texas A&M University
in partial fulfillment of the requirements for the degree of

DOCTOR OF PHILOSOPHY

August 2006

Major Subject: Chemistry

RULES FOR UNDERSTANDING RARE-EARTH MAGNETIC COMPOUNDS

A Dissertation

by

LINDSAY ELIZABETH ROY

Submitted to the Office of Graduate Studies of
Texas A&M University
in partial fulfillment of the requirements for the degree of

DOCTOR OF PHILOSOPHY

Approved by:

Chair of Committee,	Timothy Hughbanks
Committee Members,	D. Wayne Goodman
	Michael B. Hall
	Donald G. Naugle
Head of Department,	Emile A. Schweikert

August 2006

Major Subject: Chemistry

ABSTRACT

Rules for Understanding Rare-Earth Magnetic Compounds. (August 2006)

Lindsay Elizabeth Roy, B.S., University of North Texas

Chair of Advisory Committee: Dr. Timothy Hughbanks

Results of spin density functional theory (SDFT) calculations were used to construct and check features of a generally applicable semi-quantitative approach to understanding magnetic coupling in gadolinium-containing molecules, clusters, and solids. Using fragments based on structures of metal-rich lanthanide compounds, we have investigated molecular and low-dimensional extended structures, and have shown that open-*d*-shell clusters facilitate strong ferromagnetic coupling whereas closed-*d*-shell systems prefer antiferromagnetic coupling. The qualitative features can be interpreted using a perturbative molecular orbital (PMO) model that focuses the influence of the $4f^7$-*d* exchange interaction on the *d*-based molecular orbitals. The *f*-*d* exchange interaction, mediated by spin polarization of both filled and partially-filled metal-metal bonding orbitals, is described for the model system $Gd_3I_6(OPH_3)_{12}^{n+}$ using basic perturbation methods. This approach is successful for predicting the magnetic ground state for Gd_2Cl_3, a semiconducting system for which calculations predict antiferromagnetic ordering of the $4f^7$ moments in a pattern consistent with published neutron diffraction data. An attempt to account for the calculated magnetic energies of spin patterns using an Ising model was unsuccessful, indicating that the Ising model is inappropriate. Instead, the *d*-electron mediated *f*-*f* exchange interaction was interpreted using our basic perturbation theory approach. Computed density of states and spin polarization information was used to support the perturbation-theoretic analysis. This method has also been successful

evaluating the ground state for $Gd[Gd_6FeI_{12}]$. Using the model $[Gd_6CoI_{12}](OPH_3)_6$, which has three unpaired electrons in the HOMO, the 4*f* moments prefer spin alignment with the unpaired electrons in the system and the ferromagnetic $4f^7$ spin arrangement is the ground state. We have extended our analysis of R_6X_{12} clusters to include nonmetal interstitial atoms, the bioctahedral cluster compounds $Gd_{10}Cl_{17}C_4$ and $Gd_{10}I_{16}C_4$, and $Gd_5(O)(OPr^i)_5$. Finally, we have shown that we can successfully predict the ground state magnetic structures of several metallic and semiconducting Gd-containing compounds, Gd_2Cl_3, GdB_2C_2, α-Gd_2S_3, Gd_5Si_4, and Gd_5Ge_4, using semi-empirical calculations which closely simulates the exchange effects exerted by the 4*f* electrons. In a more speculative vein, ideas concerning the incorporation of anisotropic rare-earth metal atoms to the cluster framework are touched upon.

ACKNOWLEDGEMENTS

I am very grateful to my advisor, Dr. Timothy Hughbanks, who accepted me as a "not easy to handle" student and provided me with scientific guidance, patience, and encouragement throughout our four years together. It is not often one finds an advisor who is not only a great teacher and scientist, but also a good friend. I am truly indebted to him. Also, this research could not have been possible without technical advice from Dr. Lisa Pérez and Dr. Charles Edwin Webster. I would also like to thank all of the members of the Hughbanks' research group for their support and discussions; Scott Dempsey, Brady Dykema, Carmela Magliocchi, Fanqin (Jane) Meng, Jingyi Shen. In particular, I would like to thank Luke Sweet who provided the experimental results for the Gd-containing 6-12 clusters. This work was supported by the Texas Advanced Research Program and the Robert A. Welch Foundation. I also wish to thank the Supercomputing Facility at Texas A&M University and the Laboratory for Molecular Simulation for computing time and other support.

NOMENCLATURE

AO	Atomic orbital
ASA	Atomic sphere Approximation
B3LYP	Becke 3 parameter + LYP functional
BLYP	Becke-Lee-Yang-Parr functional
BPW91	Becke + Perdew-Wang 91 functional
BS	Broken symmetry
CAESAR	Crystal and Electronic Structure AnalyseR
CBE	Cluster bonding electron
CF	Crystal field
DFT	Density functional theory
DOS	Density of states
ECP	Effective core potential
E_F	Fermi Level
EHTB	Extended Hückel-Tight Binding
GGA	Generalized gradient approximation
HDVV	Heisenberg-Dirac-Van Vleck spin Hamiltonian
HK	Hohenberg-Kohn
HOMO	Highest-occupied molecular orbital
HS	High spin
HTH	Hay, Thibeault, Hoffmann
KB	Kahn-Briat

LCAO	Linear combination of atomic orbitals
LDA	Local density approximation
LMTO	Linear muffin-tin orbital
LSDA	Local spn density approximation
LUMO	Lowest-unoccupied molecular orbital
LYP	Lee-Yang-Parr correlation functional
MO	Molecular orbital
NMO	Natural magnetic orbital
OMO	Orthogonal magnetic orbital
PBE	Perdew-Burke-Ernzerhof functional
PMO	Perturbative molecular orbital
RECP	Relativistic effective core potential
RKKY	Ruderman-Kittel-Kasuya-Yosida
SCF	Self-consistent field
SDFT	Spin density functional theory
SFO	Symmetrized fragment orbital
SOMO	Singly-occupied molecular orbital
STO	Slater-type orbitals
TB	Tight-binding
TZ2P	Triple-ζ, double polarization basis set
VB	Valence bond
VWN	Vosko-Wilk-Nusair functional
XC	Exchange-Correlation

YAeHMOP	Yet-Another-extended-Hückel Molecular Orbital Program
ZORA	Zero-order regular approximation

TABLE OF CONTENTS

CHAPTER Page

CHAPTER Page

LIST OF FIGURES

FIGURE Page

FIGURE Page

FIGURE Page

FIGURE Page

FIGURE Page

LIST OF TABLES

CHAPTER I

INTRODUCTION

Theoretically derived rules for interpreting and designing magnetic molecules and materials that incorporate organic radicals and/or transition metal ions were conceived and refined over many years. They serve an important role guiding experimentalists who synthesize and measure the properties of magnetic materials.[1-16] The synthesis of an expanded class of Prussian blues and interpretation of their magnetic properties by the groups of Girolami, Long, and Verdaguer, for example, was clearly guided by an understanding of the orbital interactions responsible for ferro- and antiferromagnetic coupling in these network solids.[17-30]

Of the elements that produce magnetic materials, the lanthanides provide some of the richest opportunities for enhancing materials' interesting and useful magnetic and conducting properties. However, there exists a need for chemically useful yet physically realistic bonding schemes that can serve to interpret and predict magnetic behavior in polynuclear lanthanide molecules and extended solid-state networks. This dissertation focuses on a semi-quantitative description of *d*-electron mediated *f-f* exchange in lanthanide compounds to construct and check features of a generally applicable qualitative approach to understanding their magnetic behavior.

Before going into any details of what we achieved in this area, let us first introduce the idea of exchange energy, discuss several popular orbital interaction models

---

This dissertation follows the style of *Journal of the American Chemical Society*.

that describe magnetic interactions, and explain the inadequacy of these models for compounds with open *f*-shells. In 1928 Heisenberg used the Pauli exclusion principle, which states that no two electrons can have identical sets of quantum numbers the same, to show that ferromagnetism is caused by electrostatic interactions between the electrons.[31] Together with the Coulomb interaction between electrons, this leads to a scalar isotropic interaction between two spins through which antiparallel (↑↓) (i.e., singlet, S = 0) and parallel (↑↓) (i.e., triplet, S = 1) spin states arise ($J > 0$). This exchange phenomenon can be described by the Heisenberg-Dirac-Van Vleck (HDVV) spin Hamiltonian $\hat{H} = -J_{ij}\hat{S}_i\hat{S}_j$ and $J = E_S - E_T$ (where S and T refer to singlet and triplet, respectively).[32]

An analogous phenomenon arises within dinuclear transition metal complexes in which the unpaired spins on paramagnetic centers are coupled by "superexchange" interactions via diamagnetic bridging ligands. This mechanism, proposed by Kramers[33] and later developed by Anderson[2] in solid-state insulators accounted for substantial magnetic coupling between transition metal ions when the distances between ions are too large for direct magnetic interactions. In short, the bridging anions (ligands) play an intermediary role in the exchange interaction. Qualitative relationships between the signs of spin exchange interactions were first developed by Goodenough,[1] and exteneded by Kanamori[3] and Anderson.[34] According to their rules, we can estimate and predict whether a magnetic interaction between two spins has ferromagnetic or antiferromagnetic character. On the basis of these rules, when the localized electrons on two neighboring transition metal ions occupy orbitals that are directed towards one

another such that the orbitals have reasonably large overlap with the same *p*-orbital of the intermediate ligand (e.g., oxygen (O) is the intervening ligand and the angle TM1-O-TM2 is 180°), the exchange is strongly antiferromagnetic. If the exchange pathway between (half) filled orbitals is through a 90° angle, the exchange is ferromagnetic and relatively weak. When the exchange is due to an overlap between an occupied and an empty orbital, superexchange interaction in a metal dimer is predicted to be weakly ferromagnetic.

Early theoretical studies have elucidated how the relationship between the Heisenberg description of spin exchange interactions and the electronic structures of magnetic systems. In particular, Hay, Thibeault and Hoffmann,[4] and Kahn and Briat[5] formulated semi-empirical models and made it possible to analyze and predict spin exchange interactions in terms of qualitative chemical concepts such as overlap and orbital interaction in molecular complexes, chains, and ring systems. In order to describe these two models, we merely mention the following case where two identical interacting ions (such as a Cu^{2+} d^9 where $S_A = S_B = ½$) are bridged by a ligand (X) and the system has at least C_{2v} symmetry (**1.1**). The emblematic dicopper tetraacetate serves as a convenient example:

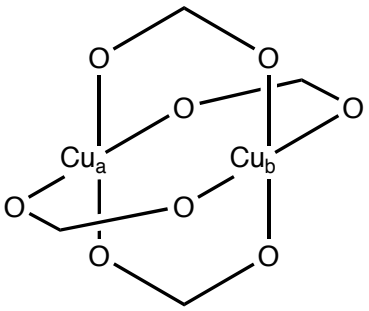

1.1

The combination of the d_a and d_b orbitals leads to two canonical molecular orbitals φ_1 and φ_2 (**1.2**).

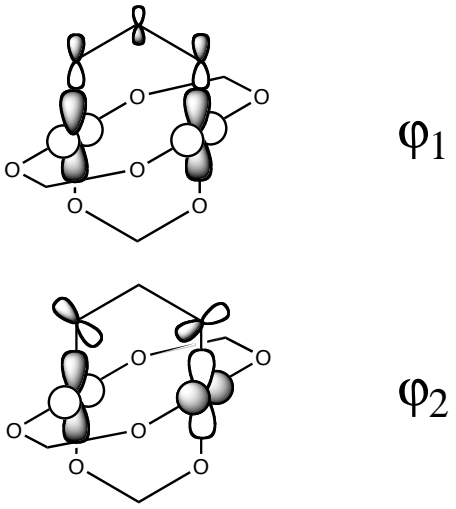

1.2

1.1 HTH Model

Hay, Thibeault and Hoffmann (HTH) developed a molecular orbital (MO)

approach wherein the singlet-triplet splitting is expressed as:

$$E_S - E_T = -J_{12} + \frac{1}{2}\left(J_{11} + J_{22}\right) - \frac{\left(\varepsilon_1 - \varepsilon_2\right)^2}{2K_{12}} \tag{1.1}$$

where ε_1 and ε_2 are the energies of the molecular orbitals φ_1 and φ_2, J_{ij} and K_{ij} are the Coulomb and exchange integrals, respectively, expressed in the molecular orbital basis:

$$\begin{aligned} J_{ij} &= \left\langle \varphi_i(1)\varphi_j(2)\left|r_{12}^{-1}\right|\varphi_i(1)\varphi_j(2)\right\rangle \\ K_{ij} &= \left\langle \varphi_i(1)\varphi_j(2)\left|r_{12}^{-1}\right|\varphi_j(1)\varphi_i(2)\right\rangle \end{aligned} \tag{1.2}$$

Interpretation of experimental data is simpler if Eq. 1.1 is expressed in terms of two-electron integrals involving localized orbitals φ_a and φ_b;

$$\begin{aligned} \varphi_a &= \frac{1}{\sqrt{2}}\left(\varphi_1 + \varphi_2\right) \\ \varphi_b &= \frac{1}{\sqrt{2}}\left(\varphi_1 - \varphi_2\right) \end{aligned} \tag{1.3}$$

which are sometimes called *orthogonal magnetic orbitals* ($\left\langle \varphi_a \middle| \varphi_b \right\rangle = 0$; See Figure 1.1). Using the expressions for φ_a and φ_b, Eq. 1.1 can be rearranged as:

$$E_S - E_T = J = 2K_{ab} - \frac{\left(\varepsilon_1 - \varepsilon_2\right)^2}{J_{aa} - J_{ab}} \tag{1.4}$$

The first and second terms in this equation represent ferromagnetic and antiferromagnetic contributions, respectively:

$$\begin{aligned} J &= J_F + J_{AF} \\ J_F &= 2K_{ab} \\ J_{AF} &= -\frac{\left(\varepsilon_1 - \varepsilon_2\right)^2}{J_{aa} - J_{ab}} \end{aligned} \tag{1.5}$$

If φ_a and φ_b are degenerate (or nearly degenerate), the antiferromagnetic contribution vanishes and a triplet ground state is preferred. However, a significant splitting between these two molecular orbitals yields a singlet ground state. Eq 1.4 suggests that one can calculate the orbital energy difference $\varepsilon_1 - \varepsilon_2$ as a measure of the singlet-triplet energy splitting for these compounds. The HTH model has mainly been applied within the EHTB framework, wherein the singlet-triplet energy differences cannot be calculated (two electron interactions are not included).[11]

1.2 KB Model

In an alternative analysis of the relationship between electronic structure and the exchange coupling mechanism, the exchange may be viewed as the borderline case of a weak chemical bond.[11] In this valence bond interpretation, χ_a and χ_b are defined as the singly occupied molecular orbitals (SOMO) for the M_a-X and X-M_b fragment, respectively, in their local ground state. These *natural magnetic orbitals* are not orthogonal and their overlap integral (see Figure 1.1);

$$S_{ab} = \langle \chi_a | \chi_b \rangle \tag{1.6}$$

plays a key role in predicting the magnitude of exchange interactions in magnetically coupled systems. However, the cutting of the M_a-X-M_b system into two M_a-X and X-M_b fragments with a common bridging region X is not exact and too much weight is placed on the bridge's orbitals.

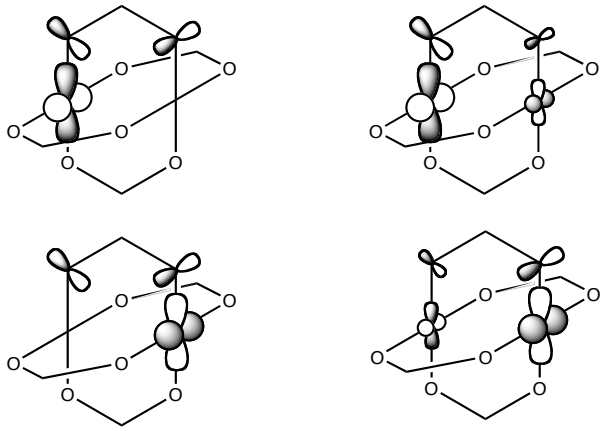

NMOs OMOs

Figure 1.1. Comparison of natural magnetic orbitals (NMOs) and orthogonal magnetic orbitals (OMOs).

The qualitative interpretation of the exchange coupling is now based on the overlap S_{ab} between natural magnetic orbitals. The singlet-triplet splitting is:

$$E_S - E_T = J = 2k + 4h_{ab}S_{ab} - 2S_{ab}^2\left(2h_{aa} + j\right) \tag{1.7}$$

where

$$\begin{aligned} h_{aa} &= \left\langle \chi_a \middle| \hat{h} \middle| \chi_a \right\rangle \\ h_{ab} &= \left\langle \chi_a \middle| \hat{h} \middle| \chi_b \right\rangle \\ k &= \left\langle \chi_a(1)\chi_b(2) \middle| r_{12}^{-1} \middle| \chi_a(2)\chi_b(1) \right\rangle \\ j &= \left\langle \chi_a(1)\chi_b(2) \middle| r_{12}^{-1} \middle| \chi_a(1)\chi_b(2) \right\rangle \end{aligned} \tag{1.8}$$

and $\hat{h}$ is the one-electron Hamiltonian that takes into account the kinetic energy of the electron and its interactions with the nuclei and all the passive electrons. The $2k$ term is always positive and therefore represents a ferromagnetic contribution, and S_{ab}, the overlap integral, and h_{ab}, resonance or transfer integral, are of opposite sign and the

second term in Eq. 1.7 represents the antiferromagnetic contribution to the coupling constant. The third term is considered to be much smaller than the other terms and is often neglected in qualitative analyses. With these approximations, the Eq. 1.7 can be rewritten as:

$$J = J_F + J_{AF} \approx 2k + 4h_{ab}S_{ab} \tag{1.9}$$

If S_{ab} vanishes, we should expect a triplet ground state with $J = 2k$. Also, one can compare the strength of the antiferromagnetic coupling with different bridging ligands, provided that one is able to calculate S_{ab}.

1.3 BS Model

Another popular approach that has come to the forefront of describing magnetically coupled TM systems is the broken symmetry (BS) approach developed as a method to calculate J values by Noodleman[35, 36] and others.[37, 38] The BS approach which aims to unify both Kahn's VB and Hoffmann's MO viewpoints by making use of symmetry breaking and spin projection techniques. Noodleman constructed a (spatially) broken symmetry (BS) state which is not a pure spin state but an artificial state of mixed spin symmetry and lowered space symmetry (a broken-symmetry wave function), which turns out to be very useful for computation within density functional theory (DFT). To impact the flavor of this approach, imagine a system with two paramagnetic centers with one unpaired electron occupying orthogonal magnetic orbitals φ_a and φ_b. Proper spin eigenfunctions for this system are:

$$\Psi_{S,0} = \frac{1}{\sqrt{2}}\left(\left|\varphi_a\bar{\varphi}_b\right| + \left|\bar{\varphi}_a\varphi_b\right|\right)$$
$$\Psi_{T,0} = \frac{1}{\sqrt{2}}\left(\left|\varphi_a\bar{\varphi}_b\right| - \left|\bar{\varphi}_a\varphi_b\right|\right)$$
$$\Psi_{T,+1} = \left|\varphi_a\varphi_b\right| \tag{1.10}$$
$$\Psi_{T,-1} = \left|\bar{\varphi}_a\bar{\varphi}_b\right|$$

The direct calculation of the energy difference between the singlet and triplet states involves at least one wave function, $\Psi_{S,0}$ that cannot be expressed as a single configuration. Noodleman suggested using a broken-symmetry solution:

$$\Phi_{BS} = \left|\varphi_a\bar{\varphi}_b\right| \ \left(or\ \Phi'_{BS} = \left|\bar{\varphi}_a\varphi_b\right|\right) \tag{1.11}$$

for which $M_S = 0$ but Φ_{BS} is a "state" of mixed spin that can be expressed as a combination of $\Psi_{S,0}$ and $\Psi_{T,0}$:

$$\Psi_{BS} = \frac{1}{\sqrt{2}}\left[\Psi_{S,0} + \Psi_{T,0}\right]$$
$$E_{BS} = \frac{1}{2}\left(E_S + E_T\right) \tag{1.12}$$

The expression for the coupling constant is:

$$J = 2\left(E_{BS} - E_T\right) \tag{1.13}$$

For the general case, the overlap S_{ab} between non-orthogonal orbitals must be taken into account:

$$J = \frac{2\left(E_{BS} - E_T\right)}{1 + S_{ab}^2} \tag{1.14}$$

For small overlap $\left(S_{ab}^2 \ll 1\right)$, the expression reduces to Eq. 1.13 and for large overlap $\left(S_{ab}^2 \approx 1\right)$, $E_{BS} \approx E_S$. In Chapter II, we will discuss our extension of the BS model to rare-earth compounds and solids.

1.4 Description of Rare Earth Compounds

To a much greater extent than is true of the *d* orbitals on transition metal atoms, the 4*f* orbitals on lanthanide atoms are highly contracted and their direct participation in magnetic superexchange coupling (mediated by 4*f*-overlap with intervening ligand orbitals) is effectively precluded (Figure 1.2).[6, 39] Nevertheless, there are materials where relatively strong magnetic coupling of lanthanide

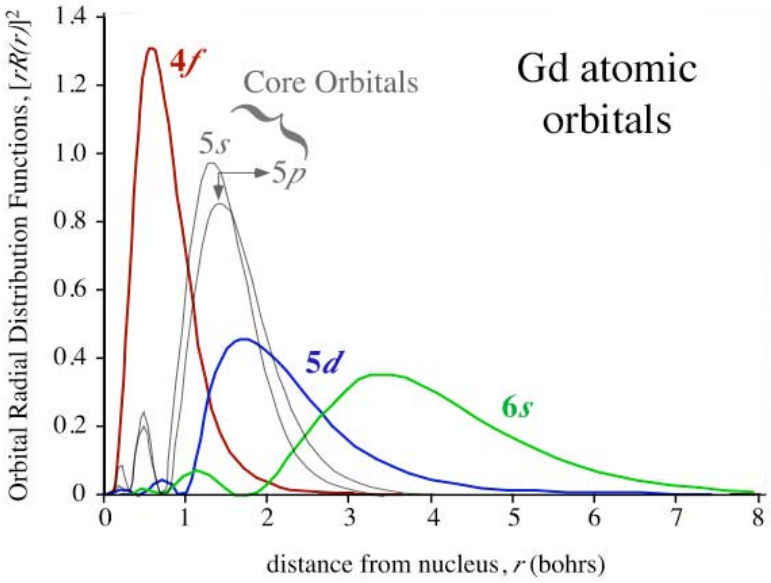

Figure 1.2. Orbital radial distribution in gadolinium.

moments *does* occur: in the elemental metals and in intermetallic compounds, especially those with the "magnetic" transition metals (Fe, Co, and Ni).[40-45] Elemental gadolinium, for example, is a metallic ferromagnet that orders at 292K.[46] Figure 1.3 qualitatively describes how ferromagnetism arises in Gd metal.

Figure 1.3 (left) is the density of states of Gd metal in a hypothetical paramagnetic state where the (primarily) 5*d* electrons partially occupy the conduction band up to the Fermi level and electrons are all spin-paired. The 4*f* electrons, not shown in the plot, are contracted in the atomic cores and randomly oriented with respect to each other. If some of the conduction electrons near the Fermi level are promoted (unpaired)

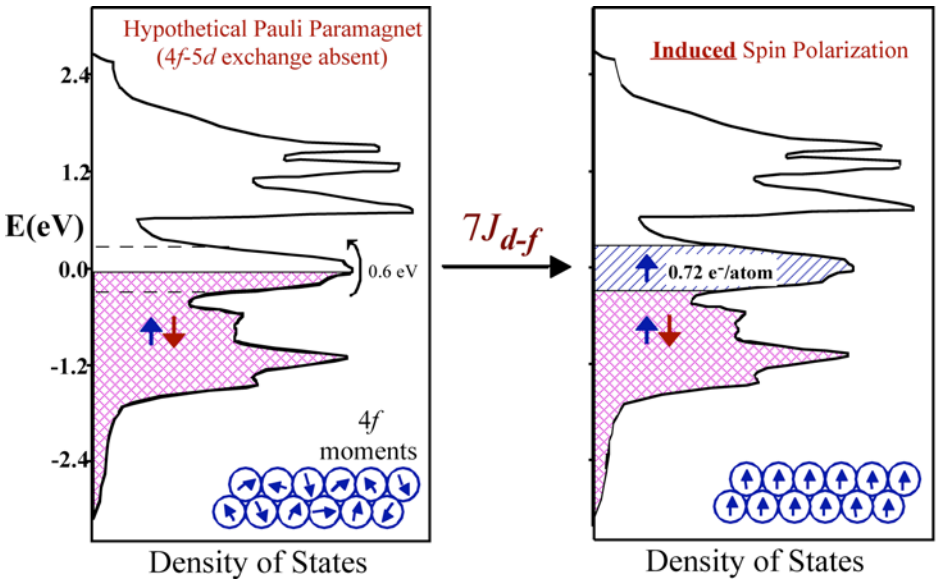

Figure 1.3. Ferromagnetic coupling mechanism of gadolinium metal shown by density of states. Shading of areas refers to occupation of states by electrons.

(Figure 1.3 right), the net unpaired spin density that results and the 4*f* moments on the Gd atoms will align in a cooperative fashion.[47] The stabilization gained by the *d-f* exchange interactions compensates for the energetic cost of promoting the 5*d* electrons. Thus, the $4f^7$ moments are coupled through this indirect mechanism, originally used to describe magnetically dilute alloys, which is called the RKKY interaction.[48-50] The 5*d* conduction (itinerant) electrons mediate 4*f*-4*f* coupling. When the conduction electrons are spin-polarized, as in Fe-rich or Co-rich intermetallic compounds that contain lanthanides (e.g., $Nd_2Fe_{14}B$ and $SmCo_5$), the exchange coupling to the conduction electrons is much stronger — with the lanthanide moment alignment remaining "fixed" by the surrounding polarized spin-density.[51-53] The general characteristics of these systems provide some initial hints as to which molecular systems might offer particular promise.

As the above comments indicate, lanthanide atoms or ions with $4f^n5d6s^2$ or $4f^n5d$ configurations experience substantial *intraatomic* exchange interactions between 4*f* electrons and valence 5*d* and 6*s*. In the case of Gd, the energetic costs of flipping the 5*d* or 6*s* electron in opposition to the $4f^7$ spin are on the order of 0.80 eV and 0.30 eV, respectively (Figure 1.4), well above the thermal energy at room temperature (~0.025 eV).[54]

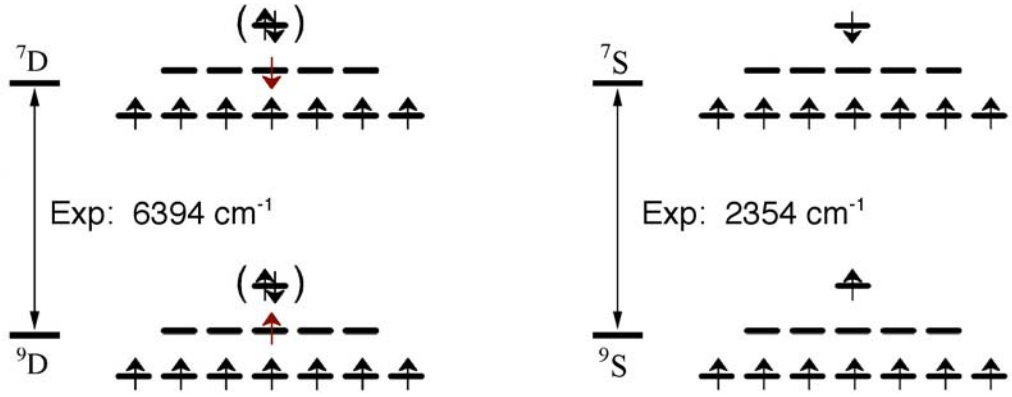

Figure 1.4. The *d-f* and *s-f* exchange interactions for the Gd atom and the Gd^{2+} ion. (The ground state for a Gd^{2+} ion is ^9D and the energy difference between the excited states ^9S and ^7S is used as a comparative example.)

This exchange interaction is intrinsically "ferromagnetic", favoring parallel intraatomic alignment of the valence electrons with the 4*f* electrons. The idea of aligning localized moments through delocalized spins motivated our group to investigate the magnetic properties of lanthanide molecules, clusters, and solids where one or more unpaired and/or delocalized cluster electrons are available. Our computational interest lies in Gd systems (molecules, clusters, and solids) where Gd magnetic moments are subject to significant interatomic exchange coupling *and* are not subject to magnetic anisotropy or spin-orbit splitting of the *f*-shell. The results in this dissertation provide a means for interpreting the results from magnetic measurements on compounds under investigation in our laboratory and other potentially interesting rare-earth compounds where strong *d*-electron mediated *f-f* exchange occurs.

CHAPTER II

THEORETICAL METHODS

This chapter will briefly describe the main features of the commonly used methods of quantum chemistry used in this work. The theoretical details behind these methods can be found in various textbooks and journal articles referenced here, but the practical details of the computational implementations of these methods are sparse in the literature. Both points are emphasized here with the hope that readers will be able to continue the work outlined in this dissertation.

In this work, two types of quantum chemical calculations were used: density functional and semi-empirical methods. Density functional methods[55-58] are based on an approximate functional for the exchange and correlation energy that is dependent on the density and is generally parameterized to fit experimental data. Semi-empirical methods[56, 59] have the same conceptual framework as *ab initio* Hartree-Fock calculations. However since core electrons are not included in the calculation and only a minimal basis set is used, the method is parameterized to experimental data or *ab initio* calculations. Despite the approximations, semi-empirical methods can yield fast estimates for a number of properties. The semi-empirical method used in this study was extended Hückel/tight binding method.

Wave function methods attempt to solve the non-relativistic time-independent Schrödinger equation:[56, 60]

$$\hat{H}\Psi = E\Psi \tag{2.1}$$

where H is the Hamiltonian, Ψ the wave function, and E the energy. In molecular systems, the many-particle Hamiltonian is given by;

$$\hat{H} = -\sum_{i=1}^{N}\frac{1}{2}\nabla_i^2 - \sum_{A=1}^{M}\frac{1}{2M_A}\nabla_A^2 - \sum_{i=1}^{N}\sum_{A=1}^{M}\frac{Z_A}{r_{iA}} + \sum_{i=1}^{N}\sum_{j>i}^{N}\frac{1}{r_{ij}} + \sum_{A=1}^{M}\sum_{B>A}^{M}\frac{Z_A Z_B}{r_{AB}} \tag{2.2}$$

for N electrons and M nuclei where, nuclei are represented by A and B, electrons are represented by i and j, ∇^2 is the Laplacian, M_A is the ratio of the mass of nucleus A to the mass of an electron and r is the distance between the two particles specified by the indices. The first and second terms in Eq. 2.2 are the kinetic energy operator for the electrons and the nuclei, respectively. The third term represents the electron-nuclear Coulombic attraction and the fourth and fifth terms represent the electron-electron and nuclear-nuclear Coulombic repulsion, respectively.

Exact solution of the Schrödinger equation for an atomic or molecular system more complicated than a hydrogen ion is impossible, but it may be simplified using the Born-Oppenheimer approximation. This approximation states that the electrons are constantly moving in the field of fixed nuclei. Therefore, the nuclei experience zero kinetic energy and the potential energy due to nucleus-nucleus repulsion is a constant. Incorporating the Born-Oppenheimer approximation, Eq. 2.2 can then be represented as;

$$\hat{H} = \hat{H}_{elec} + \hat{H}_{nuc} \tag{2.3}$$

$$\hat{H}_{elec} = -\sum_{i=1}^{N}\frac{1}{2}\nabla_i^2 - \sum_{i=1}^{N}\sum_{A=1}^{M}\frac{Z_A}{r_{iA}} + \sum_{i=1}^{N}\sum_{j>i}^{N}\frac{1}{r_{ij}} = \hat{T}_{elec} + \hat{V}_{Ne} + \hat{V}_{ee} \tag{2.4}$$

$$\hat{H}_{nuc} = -\sum_{A=1}^{M} \frac{1}{2M_A} \nabla_A^2 + \sum_{A=1}^{M} \sum_{B>A}^{M} \frac{Z_A Z_B}{r_{AB}} = \hat{T}_{nuc} + \hat{V}_{nuc} \tag{2.5}$$

where $\hat{H}_{elec}$ and $\hat{H}_{nuc}$ are the electronic and nuclear Hamiltonian, respectively.

The electronic Schrödinger equations can be represented by:

$$\hat{H}_{elec} \Psi_{elec} = E_{elec} \Psi_{elec} \tag{2.6}$$

where Ψ_{elec} is the electronic wave function and E_{elec} is the electronic energy. The electronic wave function describes the motion of the electrons and *explicitly* depends on the electronic coordinates but depends *parametrically* on the nuclear coordinates.[61] The total energy, E_{tot}, is then the sum of E_{elec} and the constant nuclear repulsion term $\hat{V}_{nuc}$:

$$E_{tot} = E_{elec} + \sum_{A=1}^{M} \sum_{B>A}^{M} \frac{Z_A Z_B}{r_{AB}} \tag{2.7}$$

With the basics introduced, the details regarding extended Hückel/tight binding and density functional methods will now be discussed.

2.1 Extended Hückel/Tight Binding Method

As mentioned earlier, extended Hückel theory is a semi-empirical method and it uses only valence electrons and linear combination of atomic orbitals (LCAO) method to generate the electronic structure of molecules. This discussion borrows heavily from Lowe and Cramer. [56, 59] The approach is similar to ordinary Hückel theory except that the Hamiltonian and overlap matrices are composed in different ways.

The basis functions use Slater-type orbitals (STOs) for the radial part of the atomic orbital (AO) wave function, defined as:

$$R_n(r,\zeta) = r^{n-1}e^{-\zeta r} \tag{2.8}$$

where n is the principle quantum number and ζ is the Slater exponent. The ζ values for the basis set are parameters supplied by the user and were initially obtained by set of rules developed by Slater to fit experimental atomic spectra.

The diagonal elements of the Hamiltonian matrix are the appropriate orbital energies of the atoms as in the original Hückel method, i.e. the formation of the secular determinant for the secular equation:

$$\begin{vmatrix} H_{11}-ES_{11} & H_{12}-ES_{12} & \cdots & H_{1N}-ES_{1N} \\ H_{21}-ES_{21} & H_{22}-ES_{22} & \cdots & H_{2N}-ES_{2N} \\ \vdots & \vdots & \ddots & \vdots \\ H_{N1}-ES_{N1} & H_{N2}-ES_{N2} & \cdots & H_{NN}-ES_{NN} \end{vmatrix} = 0 \tag{2.9}$$

The off-diagonal elements are calculated using the Wolfsberg-Helmholz relation;

$$H_{ij} = \frac{C_{ij}}{2}\left(H_{ii}+H_{jj}\right)S_{ij} \tag{2.10}$$

where the diagonal elements of the Hamiltonian, H_{ii}, are parameters supplied, C_{ij} is an empirical constant and S_{ij} is the overlap integral between AOs ϕ_i and ϕ_j. The H_{ii}'s are related to the Valence State Ionization Potentials (VSIP) of the atomic orbitals of the free atoms. Thus the energy associated with the matrix element is the average of the VSIPs for the two orbitals *i* and *j* times the extent to which the two orbitals overlap in space. The constant C_{ij} is typically 1.75 for *all* matrix elements, but can be weighted as a function of the H_{ii}'s.

Once the overlap matrix, **S**, and the Hamiltonian matrix, **H**, have been generated, the secular equation;

$$\mathbf{HC} = \mathbf{SC}\vec{E} \tag{2.11}$$

which is a matrix approximation of the Schrödinger equation, is solved to provide the eigenvalues (molecular orbital energies), $\vec{E}$, and the eigenvectors (LCAO coefficients), **C**. The extended Hückel total energy, E_{tot}, is given by:

$$E_{tot} = \sum_{i=1}^{N} n_i E_i \tag{2.12}$$

Extended Hückel theory is a versatile method for solving complicated systems that are computationally inexpensive. However, the one-electron model has a major drawback in that there is no mechanism to take into account electron spin. Therefore, the method follows the Aufbau principle that two electrons fill levels starting at the lowest available energy state until all electrons are accounted for.

The EHTB method is generally considered to be the crudest of the semi-empirical methods applied to a wide range of molecules. Nevertheless, it is useful, when carefully parameterized, for producing orbital energies and other one-electron properties.

The extended Hückel programs used in this work were YAeHMOP[62] and CAESAR[63], both available free of charge via the World Wide Web.

2.2 Density Functional Method

Density Functional theory (DFT) offers a powerful and elegant method for calculating the ground-state total energy and electron density of a system of interacting

electrons. The theory is based on the electron density, rather than wave functions, for obtaining information about atomic and molecular systems. For a more thorough discussion, the reader is encouraged to read Koch and Holthausen, and Cramer, the main sources used in this section.[55, 56] Although DFT conceptual roots lie in the Thomas-Fermi model,[64, 65] it was not until the Hohenberg-Kohn (HK) theorems provided the theoretical foundation on which modern day density functional theory is based.[55, 56, 66] The HK theorems relate to any system consisting of electrons moving under the influence of an external potential $V_{ext}(\vec{r})$.

Theorem 1. *The external potential, V_{ext}, and hence the total energy, is a unique functional of the electron density* $\rho(\vec{r})$.

The complete ground state energy is a functional of the ground state electron density and the energy functional $E_0[\rho_0]$ can be written in terms of the external potential $V_{ext}(\vec{r})$;

$$E_0[\rho_0] = \int \rho_0(\vec{r}) V_{ext}(\vec{r}) d\vec{r} + F_{HK}[\rho_0] \tag{2.13}$$

$$F_{HK}[\rho_0] = T[\rho_0] + E_{ee}[\rho_0] \tag{2.14}$$

where $F_{HK}[\rho_0]$ is the HK functional that is unknown, but otherwise universal functional of the electron density $\rho(\vec{r})$, $T[\rho_0]$ and $E_{ee}[\rho_0]$ are the functionals of the kinetic energy and electron-electron interaction, respectively. The Hamiltonian for the system can be written such that the electron wave function Ψ that minimizes the expectation value gives the ground state energy;

$$E[\rho(\vec{r})] = \left\langle \Psi \middle| \hat{H} \middle| \Psi \right\rangle \tag{2.15}$$

and

$$\hat{H} = \hat{F} + \hat{V}_{ext} \tag{2.16}$$

$$\hat{F} = \hat{T} + \hat{V}_{ee} \tag{2.17}$$

where $\hat{F}$ is the electronic Hamiltonian consisting of a kinetic energy operator, $\hat{T}$, and an electron-electron interaction operator, $\hat{V}_{ee}$. The electron operator $\hat{F}$ is the same for all *N*-electron systems, so $\hat{H}$ is completely defined by the number of electrons *N* and the external potential $V_{ext}(\vec{r})$ (i.e. the electron attraction to the nuclei).

The proof of the first theorem is based on *reductio ad absurdum*, where one assumes that two different potentials, $V_{ext,1}(\vec{r})$ and $V_{ext,2}(\vec{r})$ give rise to the same density $\rho_0(\vec{r})$. The associated Hamiltonians, $\hat{H}_1$ and $\hat{H}_2$, will therefore have different ground state wave functions, $\hat{H}_1$ and $\hat{H}_1$, that yield $\rho_0(\vec{r})$. Using the variational principle, together with Eq. 2.15 yields

$$E_1^0 < \left\langle \Psi_2 \middle| \hat{H}_1 \middle| \Psi_2 \right\rangle = \left\langle \Psi_2 \middle| \hat{H}_2 \middle| \Psi_2 \right\rangle + \left\langle \Psi_2 \middle| \hat{H}_1 - \hat{H}_2 \middle| \Psi_2 \right\rangle \tag{2.18}$$

or because the two Hamiltonian differ by $V_{ext}(\vec{r})$;

$$E_1^0 < E_2^0 + \int \rho(\vec{r}) \left[V_{ext,1} - V_{ext,2} \right] d\vec{r} \tag{2.19}$$

where E_1^0 and E_2^0 are the ground state energies of $\hat{H}_1$ and $\hat{H}_2$, respectively. Interchanging the subscripts for Eq. 2.19 leads to an equivalent expression. Adding the interchanged inequality leads to the result:

$$E_1^0 + E_2^0 < E_2^0 + E_1^0 \tag{2.20}$$

which is a contradiction and as a result, the ground state density uniquely determines the external potential $V_{ext}(\vec{r})$ to within an additive constant.

Theorem 2. *The ground state energy can be obtained using the variational principle: the density that minimizes the total energy is the exact ground state density.*

As shown earlier, $\tilde{\rho}(\vec{r})$ determines its own $\tilde{\hat{H}}$ and therefore $\tilde{\Psi}$. The variational principle asserts that this wave function $\tilde{\Psi}$ can now be used as a trial wave function for the Hamiltonian generated from the true external potential, $V_{ext}(\vec{r})$, i.e.

$$\begin{aligned}\left\langle \tilde{\Psi}\middle|\hat{H}\middle|\tilde{\Psi}\right\rangle &= T[\tilde{\rho}] + V_{ee}[\tilde{\rho}] + \int \tilde{\rho}(\vec{r}) V_{ext} dr \\ &= E[\tilde{\rho}] \geq E_0[\rho_0] = \left\langle \Psi_0\middle|\hat{H}\middle|\Psi_0\right\rangle\end{aligned} \tag{2.21}$$

Although extremely powerful, the Hohenberg-Kohn theorems do not offer a way of computing the ground state density of a system in practice. Kohn and Sham[67] introduced a method based on an orbital-density description of DFT that removes the necessity of knowing the exact form of $T[\rho]$. They proposed focusing on the exact kinetic energy of a non-interacting system of electrons as a functional of a set of single-particle orbitals that give the exact density. Kohn and Sham chose to separate $F[\rho(\vec{r})]$ into three parts, so $E[\rho(\vec{r})]$ becomes;

$$E[\rho(\vec{r})] = T_S[\rho] + J[\rho] + E_{XC}[\rho] + E_{Ne}[\rho] \tag{2.22}$$

where $T_S[\rho]$ is defined as the kinetic energy of a non-interacting electron gas as a function of the density, $J[\rho]$ is the electron-electron repulsion (Coulomb) energy term as a function of density, $E_{XC}[\rho]$ is the exchange-correlation term that includes the rest

of the electron-electron interactions, and $E_{Ne}[\rho]$ is the nuclear-electron attraction energy term as a function of density. The ground state density can be written as

$$\rho(\vec{r}) = \sum_{i=1}^{N} |\phi_i(\vec{r})|^2 \tag{2.23}$$

where $\phi_i(\vec{r})$ is the Kohn-Sham orbital.

Applying the variational principle leads to

$$\left(-\frac{1}{2}\nabla^2 + V_{eff}(\vec{r})\right)\phi_i = \varepsilon_i \phi_i \tag{2.24}$$

$$V_{eff}(\vec{r}) = \frac{\partial J}{\partial \rho} + \frac{\partial E_{XC}}{\partial \rho} + V_{Ne} \tag{2.25}$$

whose solutions are the Kohn-Sham orbitals and $V_{eff}(\vec{r})$ is the Kohn-Sham effective potential.

Although DFT is a method based on the electron density in principle, in practice the orbitals and wave functions tend to play nearly as prominent a role in interpretation of results as in wave function-based theory – even if this role is not quite rigorously rooted. This is probably a natural outgrowth of the development of the Kohn-Sham approach.

2.2.1 Exchange-Correlation (XC) Functionals

Although the Kohn-Sham formalism is exact in principle, its application is approximate since the exchange-correlation energy density functional, $E_{XC}[\rho]$, is not known. Fortunately, reasonable approximations to $E_{XC}[\rho]$ are available and can be

separated into an exchange term and a correlation term.[68] The simplest approximation one can make for the exchange-correlation energy is the local density approximation (LDA). In this approximation, the exchange-correlation energy functional is given by;

$$E_{XC}^{LDA} = \int \rho(\vec{r}) \varepsilon_{XC}^{\text{hom}}\left(\rho(\vec{r})\right) d\vec{r} \tag{2.26}$$

where $\varepsilon_{XC}^{\text{hom}}(\rho)$ is the exchange-correlation energy per particle for a homogeneous electron gas which has been evaluated as a function of electron density. The LDA approximation has many shortcomings, such as the neglect of all nonlocal effects and a systematic tendency to underestimate the energy.[57] Accounting for electron density gradients when constructing the functional yields significant improvement upon the LDA. Functionals so obtained are commonly referred to as generalized gradient approximation (GGA) functionals. One commonly used exchange-correlation term is Becke-Lee-Yang-Parr (BLYP) functional,[69-71] which is the functional most often used in this work. Examining the Becke exchange functional, the expression is;

$$E_X = E_X^{LDA} - \beta \sum_{\sigma} \int \rho_{\sigma}^{4/3} \frac{x_{\sigma}^2}{\left(1 + 6\beta x_{\sigma} \sinh^{-1} x_{\sigma}\right)} d(\vec{r}) \; ; x = \frac{|\nabla \rho|}{\rho^{4/3}} \tag{2.27}$$

where β is an empirical parameter, fitted so as to reproduce exact Hartree-Fock exchange energy of the six noble gases, and σ refers to spin. The E_x^{B88} term depends on both the density, ρ, and the gradient of the density ($\nabla\rho$). The Lee-Yang-Parr (LYP) correlation functional abandons the use of a uniform electron gas to estimate the energy. The correlation is expressed as:

$$E_C = (1 - c_C) E_C^{VWN} + c_C E_C^{LYP} \tag{2.28}$$

where E_C^{VWN} and E_C^{LYP} are complicated functions that that can be found in references 70 and 72, respectively. The Vosko-Wilk-Nusair (VWN) functional depends on ρ_α and ρ_β and has 12 empirical parameters to fit the correlation energy of jellium by Monte Carlo methods for a number of different densities. While the VWN function[72] is almost exact for jellium, it overestimates correlation energy when applied to atoms and molecules.[73] The LYP functional is based on the Colle-Salvetti formula[74] which presented an approximate correlation energy formula for the Helium atom in terms of the electron density and second order Hartree-Fock density matrix. Lee, Yang, and Parr turned this into a functional dependent upon the density, gradient, and Laplacian and containing four parameters that were derived from the He atoms. The use of the LYP functional yields much better correlation energies than VWN alone.[56]

In DMol[3] from the Cerius2® or Materials Studio® suite of programs,[75-77] the choice of functional is limited to Local Spin Density Approximation (LSDA) or a pure GGA. One very popular method is the so-called hybrid functional which includes an admixture of Hartree Fock (exact) exchange to the GGA functional. Recent studies suggest that it is better to use a hybrid functional for these problems, like B3 (Becke 3 parameter)[78] + LYP correlation (B3LYP), rather than a pure GGA functional because the hybrid functionals avoid a large suppression of correlation effects. Hybrid functionals suffer less from self-interaction errors and have less non-dynamical correlation effects.[79-81] Their accuracy in describing the magnetic coupling of transition metal complexes has been shown for several models.[9-11, 25, 82-106] BLYP tends to overcompensate for the electron correlation, leading to an overestimation of the *J* values.[86] However, it is not

clear whether this applies to systems with *d-f* exchange. The evaluation of molecules using hybrid functionals takes significantly more computer time (10 to 100 times longer) than traditional GGA functionals. According the author of DMol[3], the improvement of calculated reaction enthalpies by B3LYP vs. PBE is very small and given the amount of computer time, it is not worth it to include hybrid functionals for DMol[3].[107]

Many authors have found that the key factor in improving the description of the magnetic coupling lies in the choice of the exchange functional rather than correlation.[86, 108] LDA (or LSDA) has been shown to strongly overestimate the values of magnetic coupling. For antiferromagnetic models, there is a general tendency to produce quite large overlaps but it cannot be interpreted as the strongly delocalized limit, rather it is a failure of LDA to properly describe the broken symmetry determinant (see section 2.3 for description).[37] Using GGA functionals, orbitals still tend to be too delocalized but this tendency is much smaller. Of the available GGA functionals at my disposal, we used (almost) exclusively BLYP. The only other non-local functional available is BPW91 (Becke 88 exchange and Perdew-Wang (1991) correlation[109]). BPW91 tends to behave like the LDA approach in describing the broken symmetry determinant using more delocalized orbitals, but to a lesser extent than LDA. Also, it is difficult to achieve SCF convergence of the broken symmetry determinant for Gd-containing molecules and solids. Previous studies which examined varying the functional and its effects on magnetic coupling, BLYP is the best functional of the pure-GGA functionals.[86]

2.2.2 Relativistic Effects

It is important to include relativistic effects in calculations of rare-earth-containing compounds. [57, 110-115] There are two classes of effects that much be considered: kinematic (scalar relativistic) and spin-orbit coupling.

Kinematic effects[110] derive from the high velocity of electrons near the nucleus. These effects are more pronounced for the heavier elements and can be easily understood by comparing the average radial velocity, *v*, of a 1*s* electron. The average speed of the 1*s* electron in a hydrogen atom is $\sim 2 \times 10^6$ m·s^{-1}; it must have sufficient kinetic energy to avoid being pulled into the nucleus. The 1*s* electron of gold, for example, must travel at $\sim 1.6 \times 10^8$ m·s^{-1} ($\approx 0.53c$) in order to avoid falling into the Z = 79 nucleus.[114] The radius of this orbital, in non-relativistic calculations, is the Bohr radius:

$$r_{Bohr} = \frac{4\pi\varepsilon_0\hbar^2}{Ze^2m} \tag{2.29}$$

where e is the charge of an electron, Z is the nuclear charge, and m is the mass of an electron. In a relativistic scenario, one must replace the mass by the relativistic mass:

$$m = m_0\gamma = \frac{m_0}{\sqrt{1-\frac{v^2}{c^2}}} \tag{2.30}$$

One thus introduces a factor of γ when comparing the relativistic and non-relativistic Bohr radii.

This affects the valence *s* orbitals in two ways. First, the outer orbitals need to contract in order to satisfy the orthogonality requirement with the now smaller 1*s* core

orbital. Furthermore, the valence *s* and *p* orbitals have significant contributions near the core, and thus one must consider the kinematic effects in this region of space. Relativistic effects lead to *s* and *p* ($p_{1/2}$) orbitals that are spatially smaller and lower in energy. Such effects are referred to as "direct relativistic effects." This results in a better shielding of the nucleus for the *d* and *f* orbitals, which are not penetrating the core. These orbitals experience "indirect relativistic effects"; *d* and *f* orbitals are spatially enlarged and higher in energy.

In a fully relativistic tratment, one solves the Dirac equation;[57, 116]

$$-i\frac{\partial\Psi(\vec{r},t)}{\partial t} = \hat{H}_D\Psi(\vec{r},t) \tag{2.31}$$

and the Dirac Hamiltonian is;

$$\hat{H}_D = c\vec{\alpha}\cdot\mathbf{p} + m_0c^2\vec{\beta} \tag{2.32}$$

where **p** is the momentum operator, *c* is the speed of light, m_0 is the rest mass of the electron and $\vec{\alpha}$ and $\vec{\beta}$ are 4×4 matrices. The Dirac equation is four-dimensional, and the relativistic wave function contains 4 components accounting for an intrinsic magnetic moment (spin up and spin down) and the different particles (electron and positron). The relativistic wave function is;

$$\Psi = \begin{pmatrix} \Psi_{L\alpha} \\ \Psi_{L\beta} \\ \Psi_{S\alpha} \\ \Psi_{S\beta} \end{pmatrix} \tag{2.33}$$

where Ψ_L and Ψ_S are the large and small components of the wave function and α and β indicate the spin functions.

The time-independent Dirac equation can be given by:

$$\left[c\vec{\alpha}\cdot\vec{\pi}+\vec{\beta}'mc^2+\mathbf{V}\right]\Psi=E\Psi \tag{2.34}$$

where $\vec{\alpha}$ and $\vec{\beta}'$ are block matrices. For an electron moving in a potential V, the equation for the upper (L) and lower (S) two components is:

$$\begin{aligned} c(\vec{\sigma}\cdot\vec{\pi})\Psi_S+\mathbf{V}\Psi_L&=E\Psi_L \\ c(\vec{\sigma}\cdot\vec{\pi})\Psi_L+(-2mc^2+\mathbf{V})\Psi_S&=E\Psi_S \end{aligned} \tag{2.35}$$

where σ denotes the Pauli spin matrices and π is the generalized momentum operator. The latter equation can be written into the form:

$$\Psi_S=\frac{\vec{\sigma}\cdot\vec{\pi}}{E+2mc^2-V}\Psi_L \tag{2.36}$$

Because solving the Dirac equation can be very time consuming, there are several ways to explicitly or implicitly include relativistic effects in calculations. One method is to obtain a Hamiltonian from a Foldy-Wouthuysen (FW) transformation of the Dirac equation, which allows one to approximate the four-component Dirac equation by a two-component equation,[57, 116] a description of which is beyond the scope of this thesis.[117] This results in the Hamiltonian which contains the large components;

$$\hat{H}_{Pauli}=\hat{H}_{Nonrel}-\frac{\vec{\pi}^4}{8m^3c^2}-\frac{\nabla^2V}{8mc^2}-\frac{1}{4mc^2}\sigma_0\left(\nabla V\times\vec{\pi}\right) \tag{2.37}$$

known as the Pauli Equation. The first term contains the usual non-relativistic kinetic and potential energy operators, the three correction terms are (*i*) the mass-velocity (MV) correction; (*ii*) the Darwin correction (D); and (*iii*) the spin-orbit correction (SO). The mass-velocity corrections result from the relativistic mass increase ($m = m_0\gamma$). The

Darwin term is much more difficult to interpret because it has no simple classical counterpart. Firstly, the motion of a free electron consists of two parts; an average motion that can be observed experimentally and a highly oscillatory motion that has a frequency of order ($2mc^2/h$) and amplitude of order ($\hbar/mc$). This rapidly varying motion was given then name *Zitterbewegung* (literally, jitter motion). The Darwin term may then be understood in terms of *Zitterbewegung*, whereby the electron does not move smoothly but instead undergoes extremely rapid small-scale fluctuations (by a distance scale of order $\hbar/mc$), causing the electron to see a smeared-out Coulomb potential of the nucleus. Therefore, the potential energy the electron experiences is not strictly at a particular position, but rather an "average" at that point.[116] The spin-orbit interaction results from the coupling of the spin-magnetic moment of the electron with the magnetic field due to its own orbital motion in the electric field due to the nucleus. The MV and D operators are termed scalar relativistic corrections.

The Pauli method suffers from singular behavior at the nucleus. Also, for heavy atoms with a frozen core basis, it fails to give acceptable results. An alternative method which avoids divergence near the nucleus is the Zero-Order Regular Approximation (ZORA) to the Dirac equation:

$$H_{ZORA} = \sum_i p_i \frac{c^2}{2mc^2 - V} p_i + \frac{mc^2}{\left(2mc^2 - V\right)^2} \sigma \cdot \left(\nabla V \times \mathbf{p}\right) + V \qquad (2.38)$$

Its derivation (and the derivation of the Pauli equation) is beyond the scope of this thesis, but can be found in detail in references 57 and 118. The important distinction between these two methods is that instead of the non-relativistic expression for the kinetic energy,

an approximate relativistic expression for the kinetic energy is used for the ZORA method. Thus the Hamiltonian that is used in the SCF calculation is a relativistic Hamiltonian. Calculations using the ADF program employed the ZORA approximation of relativistic effects.

Another approximation is to use relativistic effective-core pseudopotentials (RECPs), where the core electrons are replaced by a pseudopotential that was determined based on full relativistic atomic calculations.[55, 119] These RECPs simulate the effects the core-electrons would have had on the valence electrons had they been present. The advantage of using an RECP is twofold: In addition to implicitly recovering the bulk of the relativistic effects in an otherwise non-relativistic calculation, the RECP reduces the computational size of the problem by eliminating the core electrons. This method is used in the DMol^3 program.

2.2.3 Computational Details

This section discusses the practical implementation of the density functional programs. As alluded to in the previous sections, two programs were used in this work, DMol^3 from the Cerius2® or Materials Studio® suite of programs, [75-77] or Amsterdam Density Functional (ADF).[120, 121] The methods described were used in all calculations unless otherwise noted.

2.2.3.1 DMol^3

DMol^3 uses numerical functions on an integration grid as its atomic basis and it can perform both all electron or pseudopotential calculations. This program was used for single-point and solid-state calculations. The convergence criterion for the energy was set at 10^{-6} au. In all calculations, we have employed 302 radial points, generated with a harmonic function with l = 29 (called a "fine grid" in DMol^3). To check the influence of the grid on the accuracy of the results, we performed some test calculations increasing the size up to l = 41. The difference in the 2J values computed with the two grids was ~ 0.002 cm^{-1}, so the use of the fine grid was deemed to be acceptable (using models based on [{Gd(OAc)$_3$(H$_2$O)$_2$}$_2$] and Gd[Gd$_6$I$_{12}$Co]). As mentioned earlier, all calculations used the BLYP functional.[69-71] The double numerical basis including *d*-polarization functions, DND, was employed in DMol^3 calculations for all atoms. The size of the DND basis is comparable to Gaussian 6-31G* basis sets, but the numerical basis set yields greater accuracy than a Gaussian basis set of the same size because it is numerically optimized.[75] Ruiz *et al.* recently showed that for determination of magnetic coupling constants for transition-metal complexes, numerical basis sets are accurate and reliable alternatives to Gaussian basis functions.[122] A small frozen-core effective potential (ECP) was used for Gd (1*s*-3*d*) and Y (1*s*-3*d*) and a large effective core for I (1*s*-4*f*). If the ECP option is used, DMol^3 allows no user discretion concerning which atoms have "large" or "small" ECPs and no control over the size of the frozen core. DMol^3 applies scalar relativistic corrections (Darwin and mass-velocity) using effective

core potentials as mentioned in section 2.2.2.[123] All calculations included open-shell configurations and the symmetry was lifted.

2.2.3.2 ADF

ADF is a first-principles software package especially suited for inorganic compounds that utilizes Slater-type orbitals as basis functions. This program was primarily used for single-point energies and (partial) geometry optimizations if experimental data was not available. Spin-unrestricted calculations were performed with an accuracy parameter of 6.0 and energy convergence criterion of 10^{-6} au. The electronic configurations were described at the DFT/BLYP level with triple-ζ, double polarization (TZ2P) small core basis sets using the ZORA method for all atoms. The Dirac utility was used to generate relativistic frozen core potentials for the scalar ZORA calculations.[118, 124] For geometry optimizations, the Hessian matrix used was the Broyden-Fletcher-Goldfarb-Shanno (BFGS) method and the energy convergence criterion was set to 10^{-4} au. Symmetry was used in single-point calculations *only*.[125] All optimized geometries were verified by frequency calculations.

2.3 Broken Symmetry Approach

The exchange interaction between two paramagnetic centers is phenomenologically described using the Heisenberg-Dirac-Van Vleck (HDVV) spin Hamiltonian;[31, 126, 127]

$$\hat{H} = -J_{ij}\hat{S}_i\hat{S}_j \tag{2.39}$$

where J_{ij} is the magnetic coupling constant describing the spin exchange between different spin states and $\hat{S}_i$ and $\hat{S}_j$ are the total spin operators for atoms *i* and *j*. The effective Hamiltonian is defined such that the sign of the magnetic coupling constant, J_{ij}, is positive for ferromagnetic coupling and negative for an antiferromagnetic interaction.[128]

In the simplest example of a magnetically coupled system, a dimer where $S_1 = S_2 = 1/2$, the four basis spin determinants are $|\alpha\alpha\rangle$, $|\beta\beta\rangle$, $|\alpha\beta\rangle$, and $|\beta\alpha\rangle$. Since $\hat{H}$, the total spin operator $\hat{S}^2$, and the *z*-component of the spin operator, $\hat{S}_z$, commute, it is possible to determine a set of eigenfunctions relating all three operators. The eigenfunctions of $\hat{S}^2$ and $\hat{S}_z$ are denoted as $|S,M_s\rangle$ and it is straightforward to show that $|1,1\rangle = |\alpha\alpha\rangle$ and $|1,-1\rangle = |\beta\beta\rangle$, whereas determinants $|0,0\rangle$ and $|1,0\rangle$ consist of a linear combination of $|\alpha\beta\rangle$ and $|\beta\alpha\rangle$. It is simple to show that the single and triplet states are also eigenfunctions of the HDVV Hamiltonian with energies of $3/4J$ and $-1/4J$, respectively. Therefore, the coupling constant, *J*, may then be obtained as the energy difference between the singlet and triplet states.

The spin eigenfunction of the high spin state for $|S\ M_S\rangle$ is a single Slater determinant (where *S* is the total spin and M_S is its *z*-component). Any lower spin state eigenfunction is expressed as linear combinations of Slater determinants and therefore is not amenable to direct calculation in the usual implementation of density functional theory. Noodleman[35] proposed an alternative approach, in which unrestricted, or spin-

polarized, functions are evaluated within the density functional formalism and the expectation value(s) for broken symmetry solution(s) are used in calculating the energy of the low-spin state(s). The coupling constant of dinuclear complex is evaluated using the energy difference between the high spin state and the computed expectation value (energy) of the low-spin, broken symmetry determinant. For the case in which $S_i = S_j$, the coupling constant may be obtained by use of equation 2.40;

$$E_{HS} - E_{LS} = -2JS_i\left(S_i + \frac{1}{2}\right) \tag{2.40}$$

where E_{HS} is the energy that corresponds to the state with the highest total spin, E_{LS} corresponds to the state with the lowest total spin ($S = 0$, for a homodinuclear complex), and S_{i} is the total spin on each metal atom. Experience has shown that estimating the energy of the low-spin state by making use of the computed "energy" for the broken symmetry solution for transition metal complexes, without performing any spin projection, leads to good agreement with experimental data for a large variety of compounds with exchange coupled electrons. [13, 84, 87, 99, 105, 129-134]

In extended systems, all possible pairwise interactions are considered, yielding the HDVV spin Hamiltonian

$$\hat{H} = -\sum_{i<j} J_{ij}\hat{S}_i\hat{S}_j; \tag{2.41}$$

the summations usually include only neighbors (i and j) that are in proximity to each other. In many cases, it is difficult or impossible to find the eigenfunctions of the HDVV spin Hamiltonian. A common alternative for computation of the magnetic coupling constant is to make use of the simpler Ising Hamiltonian ($\hat{H}^I$), where the total

spin operators are replaced by their *z*-components:[83, 108, 135]

$$\hat{H}^{I} = -\sum_{i<j} J'_{ij} \hat{S}_{z,i} \hat{S}_{z,j} \tag{2.42}$$

J'_{ij} values are calculated directly from energy differences between the states of maximum and minimum M_s, the so-called "ferromagnetically coupled" and "antiferromagnetically coupled" states, respectively. In the Ising Hamiltonian, it is common to assign eigenvalues of +1 (α) and –1 (β) to the "pseudospin", so that the magnitudes of the Ising and Heisenberg coupling constants differ by quantities on the order of $\hat{S}_i \hat{S}_j$. Eigenfunctions of $\hat{H}^{I}$ are not generally eigenfunctions of $\hat{S}^2$, but are eigenfunctions of $\hat{S}_z$, retaining M_s as a quantum number. Considering again the case where $S_1 = S_2 = 1/2$, a pure ($M_s = 1$) component of the ferromagnetic state is explicitly described as the determinant $|\alpha\alpha\rangle$ since it is a spin eigenfunction. In contrast, the antiferromagnetic state cannot be described because there are two determinants with $M_s = 0$ ($|\alpha\beta\rangle$ and $|\beta\alpha\rangle$) and neither is an eigenfunction of the total spin operator $\hat{S}^2$.

The Ising Hamiltonian can be connected to all the unrestricted formalisms based on the single determinant approach of spin-density functional theory (SDFT) via the broken-symmetry approach. The single determinantal nature of SDFT poses problems because it does not allow the calculation of a pure low-spin eigenfunction. As in the treatment using the Ising Hamiltonian, the single determinant description of the high-spin states is straightforward (because high-spin states are eigenfunctions of $\hat{S}^2$ and $\hat{S}_z$ and therefore suffer no spin contamination). A broken-symmetry approach allows one to

calculate spin-state energy differences using the results of a single-determinantal function.[35, 36] Dai and Whangbo explored the relationship of the spin dimer approach using broken-symmetry Heisenberg Hamiltonian and the magnetic solid approach using the Ising Hamiltonian.[136] They showed that a description of the spin-exchange interactions of a magnetic solid treated with a Heisenberg spin Hamiltonian can be extracted from broken-symmetry SDFT calculations that are most directly consistent with the Ising spin Hamiltonian. In our results, we have employed a broken-symmetry approach to evaluate the magnetic coupling constants between Gd centers.

2.3.1 Application to Gadolinium Compounds

The 5*d* and 6*s* valence orbitals of lanthanide atoms are diffuse, but in an important sense the 4*f* electrons are essentially core electrons – in highly contracted orbitals that preclude appreciable overlap with neighboring atoms.[137] Because such 4*f* overlaps are so small, superexchange coupling (mediated by overlap with intervening ligand orbitals) between neighboring lanthanide centers is largely precluded. Because of their core-like radial extension, lanthanide 4*f* electrons can not be viewed as typical "band electrons". In rare-earth intermetallic compounds, an indirect pathway involving the localized 4*f* electrons and the conduction band electrons is responsible for magnetic ordering. When the conduction electrons are spin-polarized, as in Fe-rich or Co-rich compounds (e.g., $Nd_2Fe_{14}B$ and $SmCo_5$ and other related permanent magnets), the exchange coupling to the conduction electrons can be significant. Elemental gadolinium is a metallic ferromagnet with an ordering temperature of T_c = 292 K.[46] Within the bulk

metal, stabilizing 4*f*-5*d* exchange induces some spin-polarization of 5*d* electrons in the vicinity of the Fermi level that cooperatively aligns the 4*f* moments.[138] This indirect exchange mechanism, which was originally treated in magnetically dilute systems (RKKY exchange),[48-50] produces an *effective* 4*f*-4*f* coupling and is responsible for the observed magnetic properties.

Of course, in any real system where one might have a single *f* electron on adjacent lanthanide centers (e.g., a bimetallic cerium complex), spin-orbit coupling within the 4*f*-shell would have to be accounted for in addition to interatomic *f*-*f* exchange. Thus, for handling interatomic spin exchange interactions in the rare-earth elements, gadolinium offers the least complicated starting point. For its ground configuration, $[Xe]4f^7 5d^1 6s^2$, the ground state and lowest excited states are derived by coupling the 5*d* electron (^{2}D) with the ^{8}S state of the $4f^7$ core to give a ^{9}D ground state and an excited ^{7}D state. Loosely speaking, these states respectively correspond to the *d*-electron spin either aligning with or against the exchange coupled spins of the f^7 core and the results of SDFT calculation of the atom are discussed in Chapter III. We concerned ourselves entirely with systems containing $4f^7$ gadolinium centers, where spin-orbit coupling effects are absent in first order (for the ^{8}S state of the $4f^7$ core) and can therefore be safely neglected.

In applying the symmetry-broken approach to a molecule with two Gd centers, SDFT is first used to calculate the energy of $|\uparrow_7,\uparrow_7\rangle$ and $|\uparrow_7,\downarrow_7\rangle$. The former spin eigenfunction represents a state with all seven of the *f*-electrons on both Gd atoms are spin up and the latter expression, $|\uparrow_7,\downarrow_7\rangle$, represents a determinant where all seven *f*-

electrons on one Gd atom are spin up and all seven on the other Gd atom are spin down, which is a combination of pure spin eigenfunctions with S = 0, 1, …7 and $M_s = 0$. The energy of the high spin state can be identified with the energy obtained with the HDVV Hamiltonian ($\hat{H} = -J\hat{S}_1 \bullet \hat{S}_2$): $E_{|\uparrow_7,\uparrow_7\rangle} = -49/4\ J$. Overlaps between *f* orbitals on neighboring atoms are very small, e.g., $\langle\downarrow_7,\uparrow_7|\uparrow_7,\downarrow_7\rangle \approx 0$, so $|\uparrow_7,\downarrow_7\rangle$ can be expressed as a combination of pure states using the Clebsch-Gordan coefficients without overlap corrections and obtain from that an energy expression in terms of the set of pure state energies, $\{E_S\}$:[139]

$$E_{|\uparrow_7,\downarrow_7\rangle} = \frac{3}{24}E_0 + \frac{7}{24}E_1 + \frac{7}{24}E_2 + \frac{49}{264}E_3 + \frac{7}{88}E_4 + \frac{7}{312}E_5 + \frac{1}{264}E_6 + \frac{1}{3432}E_7 \qquad (2.43)$$

The HDVV Hamiltonian yields an energy expression in terms of the set of pure state energies ($E_S = J(S(S+1))$):

$$E_{|\uparrow_7,\downarrow_7\rangle} = \frac{49}{4}J \implies \frac{49}{2}J = E_{|\uparrow_7,\downarrow_7\rangle} - E_{|\uparrow_7,\uparrow_7\rangle} \qquad (2.44)$$

An identical value for $E_{|\uparrow_7,\downarrow_7\rangle}$ is obtained from the expectation value, $\left\langle\uparrow_7\downarrow_7\middle|\hat{H}\middle|\uparrow_7\downarrow_7\right\rangle$, *directly* and this is how one can correlate computed SDFT energies with coupling parameters *in practice*; the point of these comments being a demonstration of the equivalence of this procedure with the broken-symmetry approach (see Figure 2.1).

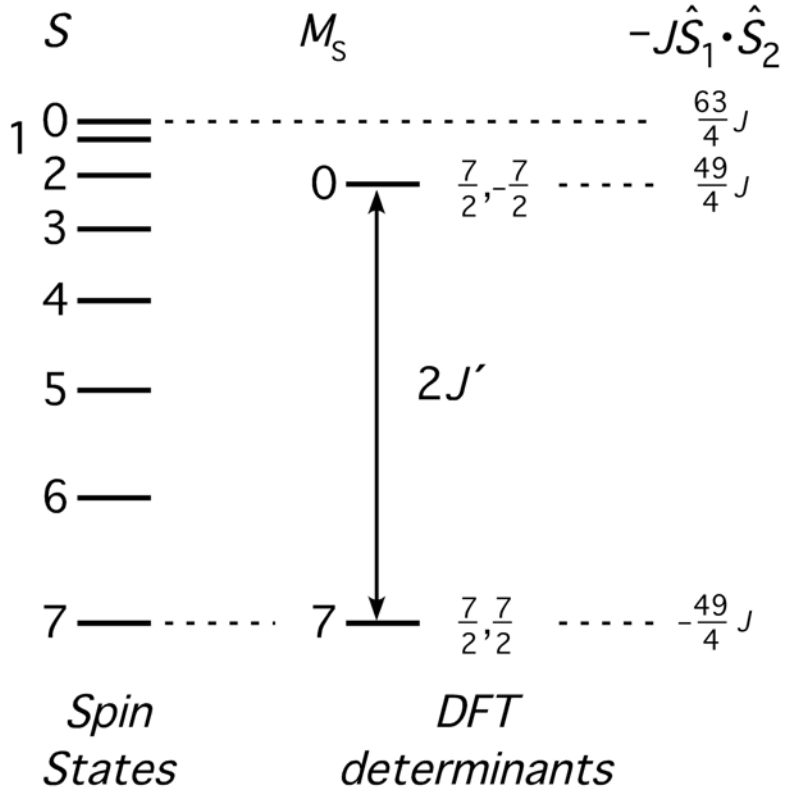

Figure 2.1. Pure spin state "ladder" and determinants used in DFT for a Gd_2 system (J, $J' > 0$).

When we refer calculated energies differences $E_{|\uparrow_7,\uparrow_7\rangle}$ and $E_{|\uparrow_7,\downarrow_7\rangle}$ to exchange couplings (J') in the Ising Hamiltonian, the "pseudospin" vector takes only two values, +1 (α) and –1 (β), and as a result we obtain:

$$2J' = E_{|\uparrow_7,\downarrow_7\rangle} - E_{|\uparrow_7,\uparrow_7\rangle} \tag{2.45}$$

Ising exchange constants were used in Chapters III and VI, and to make an identification to Heisenberg coupling constants, it is clear that $J = (4/49)\, J'$.

CHAPTER III

BENCHMARK SYSTEMS*

This chapter will focus on magnetic ordering of several benchmark systems including the Gd atom, a molecular model based on GdI_2, and the pseudo-one-dimensional chain compound, Gd_2Cl_3.[43, 44, 140] Because these systems have been well characterized in the literature,[40, 42-44, 54, 141-158] they offers us important benchmarks for testing the use of the broken symmetry SDFT method for evaluating magnetic coupling in Gd compounds.

A common theoretical/computational method of determining the strength of exchange is based on a spin dimer analysis of the extended solid.[159] In this approach, one constructs truncated model dimers, and results from the computational studies are used to supply the pairwise-coupling parameters in model Hamiltonians (e.g., Heisenberg or Ising) describing the magnetic properties of the solid. Even if the quantum mechanical method is adequate to tackle this task, several issues arise in evaluating the approach, namely the appropriateness of the selected model Hamiltonian and the possible uncertainty introduced from structural truncation into the computed parameters. Can the magnetic coupling energy of the solid really be expressed as a sum of pairwise-additive effective exchange interaction energies? If the comparison of experimental data to theory only relies on magnetic susceptibilities, how much confidence can we have in a

semi-empirical spin-dimer treatment that may include scaling the magnitude of all the exchange parameters as part of the treatment? The use of SDFT band structure calculations pursues an approach that is more general than the spin-dimer approach. Indeed, we shall see that these calculations shed light on the question of whether magnetic coupling should be described in terms of pairwise interactions in reduced Gd-rich compounds.

3.1 4*f*-5*d* Exchange in the Gadolinium Atom

Before directly considering molecules and solids, we present results using SDFT calculations on the Gd atom. Particularly relevant is a comparison between theory and experiment for the energy gap between the electronic ground state (^{9}D) and the first excited state (^{7}D) within the ground configuration ([Xe]$4f^7 5d^1 6s^2$). Qualitatively, this calculation yields the exchange energy penalty required to flip the 5*d*-electron spin in opposition to the $4f^7$ spins. The energy difference is calculated using the two determinants, $\Phi_{\uparrow_7,\uparrow}$ and $\Phi_{\uparrow_7,\downarrow}$, where the subscript notation indicates the spin of the seven 4*f* electrons and the single 5*d* electron separately; $\Phi_{\uparrow_7,\uparrow}$ is a spin-eigenfunction, but the spin-contamination of $\Phi_{\uparrow_7,\downarrow}$ must be accounted for.

The $f^7 d^1$ configuration yields five distinct ^{7}D states, but four of these derive from coupling the *d* electron (^{2}D) with sextet excited states of the $4f^7$ core (^{6}P, ^{6}D, ^{6}F, ^{6}G) and spectroscopic data show that such states lie very high in energy. To a good approximation then, the spin-contamination of $\Phi_{\uparrow_7,\downarrow}$ is accounted for by constructing an

$S = 3$ spin-eigenfunction that is orthogonal to the ^{9}D ground state, since it is the only other state with a $4f^7(^8\mathrm{S})$ core. The components of ^{9}D with $M_S = 4$ and $M_S = 3$ are

$$\Psi\left(^9D,4\right) = \Phi_{\uparrow_7,\uparrow}$$

$$\Psi\left(^9D,3\right) = \sqrt{\frac{1}{8}}\Phi_{\uparrow_7,\downarrow} + \sqrt{\frac{7}{8}}\left[\frac{1}{\sqrt{7}}\sum_{i=1}^{7}\Phi_{\uparrow_6\downarrow_i,\uparrow}\right] \tag{3.1}$$

where the second function can be simply derived from the first by operating with a spin-lowering operator. For the orthogonal components of ^{7}D with $M_S = 3$, we can write

$$\Psi\left(^7D,3\right) = \sqrt{\frac{7}{8}}\Phi_{\uparrow_7,\downarrow} + \frac{1}{\sqrt{8}}\left[\frac{1}{\sqrt{7}}\sum_{i=1}^{7}\Phi_{\uparrow_6\downarrow_i,\uparrow}\right] \tag{3.2}$$

which, as can be readily confirmed, is a spin-eigenfunction with $S = 3$. From these two expressions, we obtain an expression for $\Phi_{\uparrow_7,\downarrow}$ in terms of the pure state functions:

$$\Phi_{\uparrow_7,\downarrow} = \sqrt{\frac{7}{8}}\Psi(^7D,3) - \sqrt{\frac{1}{8}}\Psi(^9D,3) \tag{3.3}$$

Assuming this approximate relation applies, we can use the exact electronic Hamiltonian (excluding spin-orbit coupling) to evaluate $E_{\uparrow_7,\downarrow} = \left\langle \Phi_{\uparrow_7,\uparrow} \middle| \hat{H} \middle| \Phi_{\uparrow_7,\uparrow} \right\rangle$, which leads to a simple expression for the energy difference between the ^{9}D ground state and the lowest ^{7}D excited state in terms of energies calculated with SDFT:

$$E_{\uparrow_7,\downarrow} = \frac{7}{8}E(^7D) + \frac{1}{8}E(^9D) \tag{3.4}$$

$$E(^7D) - E(^9D) = \frac{8}{7}\left[E_{\uparrow_7,\downarrow} - E(^9D)\right] = \frac{8}{7}\left[E_{\uparrow_7,\downarrow} - E_{\uparrow_7,\uparrow}\right]$$

The calculated gap using the BLYP functional and the double numeric basis sets discussed in the computational section is 5693 cm^{-1}, about 89% of the spectroscopically

measured gap of 6394 cm^{-1} (after averaging over spin-orbit splitting in both states) using DMol[3] (See Figure 3.1) (The energy gap using ADF is 4816 cm^{-1}, or 75% of the

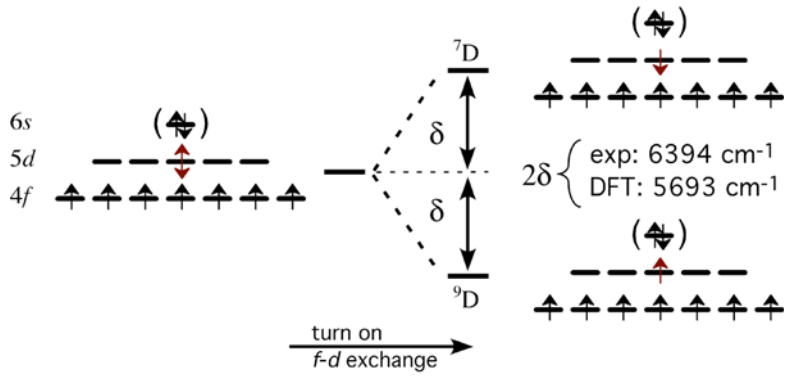

Figure 3.1. Electronic splitting of the Gd atom as a function of 4*f*-5*d* exchange perturbation.

measured gap).[54, 160] A final complication that should be mentioned arises from a well-known artifact of DFT: although both the ^{9}D and ^{7}D states are orbitally degenerate, the energies computed for these states with all current functionals in fact depends slightly on which *d* orbital is actually occupied.[55] In our case, we examined the difference of occupying one of the four spatially equivalent "cloverleaf" orbitals (i.e., not d_{z^2}) in both states, and the energy difference given reflects this choice.[161]

3.2 GdI_2

GdI_2 is a metallic ferromagnet with an ordering temperature at 292K and has a

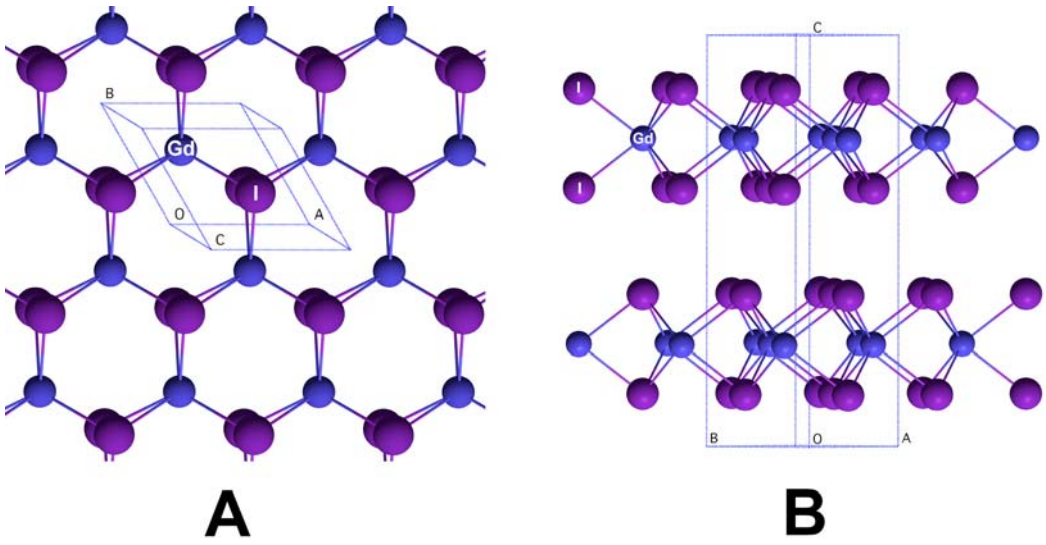

Figure 3.2. Structure of GdI_2. Side A depicts a single layer of GdI_2 viewed down the three-fold axis. Side B presents a perspective view of GdI_2 along [110].

MoS_2-type structure, shown in Figure 3.2.[44, 142] The compound is prepared is a solid state reaction between Gd metal and GdI_3; conducted in a tantalum tube that was jacketed in a silica tube and heated to 1100 K for 3 weeks, then quenched to room temperature.[143] The crystal structure consists of two GdI_2 layers where each gadolinium atom centers an I_6 trigonal prism and is surrounded by 6 other Gd atoms at 4.075 Å in the plane. Figure 3.3 depicts the *d*-orbital ligand field splitting of for a metal atom in a trigonal prismatic arrangement.[158] The three low-lying $\{ d_{x^2-y^2}, d_{xy}, d_{z^2} \}$ orbitals combine to form three-center bonding orbitals with one delocalized *d*-electron in each of the triangular cavities within the layer, shown in **3.1**. The $\{d_{xz}, d_{yz}\}$ pair of orbitals are directed toward the ligands and contain the greatest amount of Gd-I σ antibonding character.

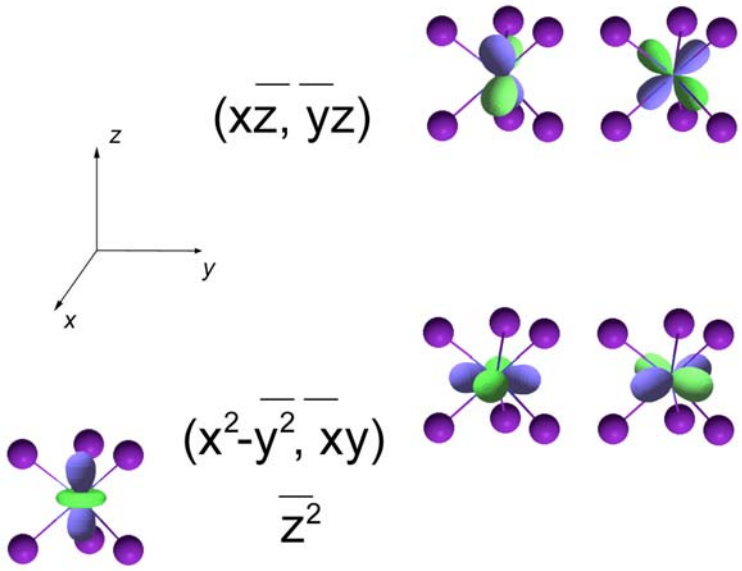

Figure 3.3. *d*-orbital ligand field splitting diagram for a metal atom in a trigonal prismatic environment typically found in solid-state compounds, i.e., where the L-L distances are all nearly equal.

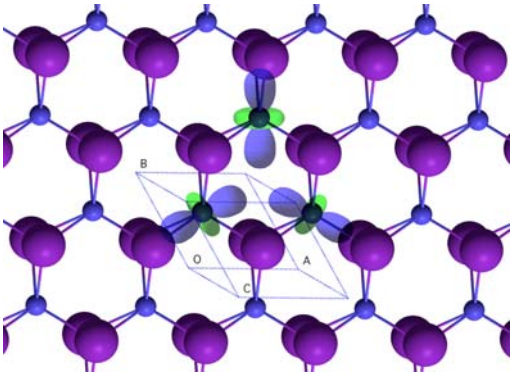

3.1

Figure 3.4 shows a spin projected DOS plot containing a single and the ferromagnetic structure of GdI_2 from DFT.[162, 163] In the single layer compound, the narrow bands at -7.3 eV and -1.8 eV correspond to the *f*-shell, which are split into spin-

Figure 3.4 shows a spin projected DOS plot containing a single and the ferromagnetic structure of GdI_2 from DFT.[162, 163] In the single layer compound, the up (α) and spin-down (β) states, respectively. Interestingly, the *d* bands are split such that they "feel"

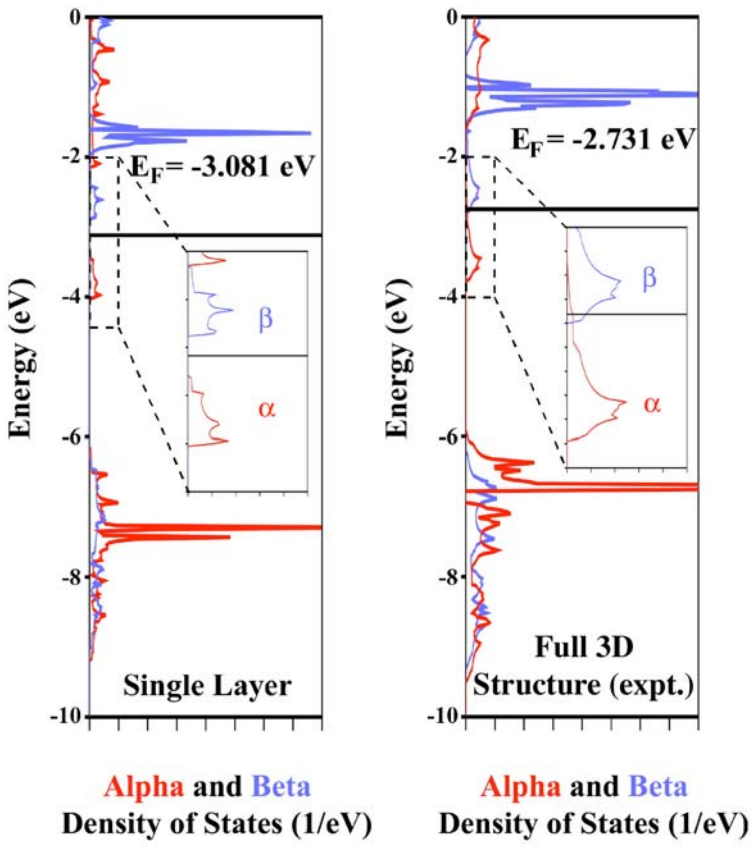

Figure 3.4. DOS plot of a single layer and the ferromagnetic crystal structure of GdI_2. The inset of each plot shows a close up of the plot near the Fermi level.

the exchange potential of the *f*-shell, similar to the effect found for the Gd atom. The *d* states of Gd around E_F have a bandwidth of less than 2 eV and DFT predicts that the 2-D sheet is a semiconductor with a band gap of ~0.4 eV. The occupied I *p* bands are centered about 4.5 eV below E_F and are barely affected by the Gd 4*f* potential. Interestingly, calculations on the ferromagnetic crystal structure predict metallic behavior and the bands near the Fermi level contain a small amount of β-spin *d* bands. Also, the I α-spin *p* bands appear to be expanded, in comparison to the single layer DOS. Previous LMTO calculations also predict metallic behavior for the solid where the Fermi level splits the α- and β-spin *d*-band.[44] Our calculations predict that GdI_2 is a ferromagnetic conductor, but if they layers could be separated (perhaps by intercalation of molecules), the material might become semiconducting. The strength of the interlayer interaction is larger than we might have expected. Perhaps the d_{z^2} orbital on the Gd atom interacts with the I atom from the above layer, but since the relevant Gd-I distance is 5.708 Å, this interaction is quite weak. The distance between iodide atoms between the layers is 4.542 Å and is outside the mean van der Waals radii.[164] However, our results from the single layer model are encouraging and show the singly-occupied three-center bond will polarize the 4*f* moment to achieve ferromagnetic coupling between Gd centers. The GdI_2 systems inspired us to devise polynuclear cluster models with similar magnetic coupling.

3.2.1 Molecular Model Inspired by GdI_2

To build a meaningful model based on GdI_2, important considerations include preservation of 3-center bonding character found in Gd_3 triangles and maintenance of the tricapped-trigonal-prismatic coordination environment around Gd. Hence, our model consists of 3 gadolinium atoms, 6 bridging iodide ligands, and 12 phosphine oxide ligands, OPH_3 (Figure 3.5). Phosphine oxide ligands act both to replace the coordination provided by six iodide ions lost upon "excising" the clusters from the layers and to create a metal-ligand bond where further metal-metal bonding occurs in the open cavities sites of the periodic structure. Use of neutral phosphine oxide ligands allows for an overall cationic charge of the models, $[Gd_3I_6(OPH_3)_{12}]^{n+}$, n = 3 – 1, when 0, 1, or 2 *d*-electrons respectively occupy the 3-center bond orbital. Partial geometry optimization of the yttrium analog was performed in order to obtain the correct position of the phosphine oxide ligands. In addition, we also studied the model where one Gd atom was replaced with a Y to give $[YGd_2I_6(OPH_3)_{12}]^{n+}$, n = 3 – 1 with the same electronic configuration as before. Hegetschweiler and coworkers synthesized trinuclear clusters, $[Ln_3(H_{-3}L_i)_2(H_2O)_6]^{3+}$ (Figure 3.6), supported by ligands, L_i, designed to hold lanthanide metal ions in close proximity (L_1 = 1,3,5-triamino-1,3,5-trideoxy-*cis*-inositol (taci) and L_2 = 1,3,5-trideoxy-1,3,5-tris(dimethylamino)-cis-inositol (tdci)).[165] As discussed below, these molecules have direct bearing on benchmark computational studies we have already completed — if we can reduce them.

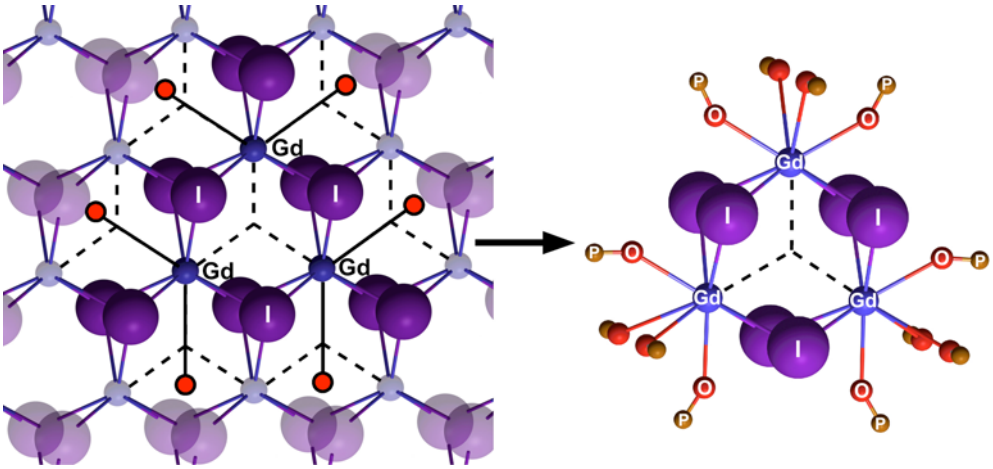

Figure 3.5. Assembly of model cluster compound from the "parent" GdI_2 structure. Dashed lines indicate 3c-bonding locations. Hydrogen atoms located on the model were omitted for clarity.

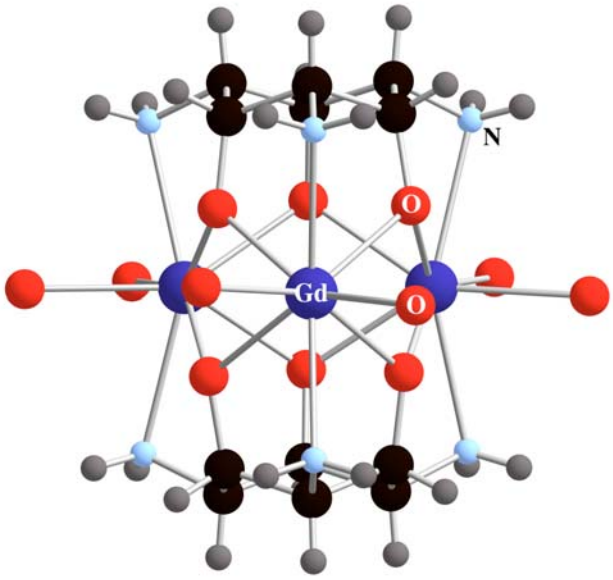

Figure 3.6. Structure of $[Gd_3(H_{-3}L)_2(H_2O)_6]^{3+}$; H atoms on H_2O not shown. *d*(Gd-Gd) = 3.72 Å, shorter than in GdI_2 (4.08 Å) and as short as in Gd_7CoI_{12}.

3.2.2 Magnetic Coupling in $[Gd_3I_6(OPH_3)_{12}]^{n+}$

Calculated relative spin state energies for $[Gd_3I_6(OPH_3)_{12}]^{n+}$ (Table 3.1) illustrate that in both the d^0 and d^2 (closed-shell) clusters, antiferromagnetic coupling is observed. This coupling is essentially negligible in the d^0 system, but is substantial in the d^2 system. For the open-*d*-shell (d^1) system, the ferromagnetically coupled state is strongly favored. These same results are also observed for $[YGd_2I_6(OPH_3)_{12}]^{n+}$, also presented in in Table 3.1.

Table 3.1. Relative spin state energies (cm^{-1}) of $[Gd_3I_6(OPH_3)_{12}]^{n+}$ and $[YGd_2I_6(OPH_3)_{12}]^{n+}$.

	$4f^7$ Spin Arrangements	3+ (d^0)	2+ (d^1)	1+ (d^2)
$[Gd_3I_6(OPH_3)_{12}]^{n+}$	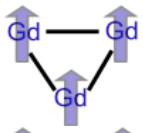	4	0, S = 11 2534, S = 10	240
	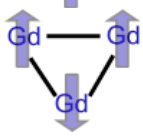	0	755, S = 4 1590, S = 3	0
$[YGd_2I_6(OPH_3)_{12}]^{n+}$	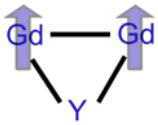	2	0, S = 15/2 2287, S = 13/2	236
	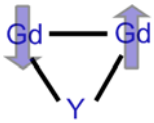	0	1459, S = 1/2	0

Evaluation of the Heisenberg magnetic coupling constants can be carried out in a straightforward fashion by expressing the energy difference between different "spin patterns" as a sum of pairwise interactions:

$$E_{HS} - E_{BS} = -3J\left(\frac{49}{2}\right) \tag{3.5}$$

For Gd_3 model cations with 3+ and 1+ charges, DFT calculations estimate the values of the magnetic coupling constant, *J*, for $n = 3$ and $n = 1$ as –0.054 cm^{-1} and –3.265 cm^{-1}, respectively. Because the YGd_2 model only contains one pairwise interaction, the estimated values of the magnetic coupling constant are 0.082 cm^{-1} and 9.63 cm^{-1} for $n = 3$ and $n = 1$, respectively. A few qualitative conclusions are obvious: (a) To a good approximation, d^0 systems exhibit negligible exchange coupling of their $4f^7$ moments; (b) Closed shell d^n-systems favor antiferromagnetic coupling of $4f^7$ moments; (c) For this system, the open-*d*-shell configuration exhibits strong ferromagnetic coupling of the $4f^7$ moments. These qualitative features can be interpreted using a perturbative molecular orbital (PMO) model that focuses the influence of the $4f^7$-*d* exchange interaction on the *d*-based molecular orbitals.

We can treat the Gd_3 trinuclear cluster model in the same spirit as with the Gd atom and adopt the simple 3-center bond model shown in Figure 3.7 to account for the 3 MO's of this bonding system. This analysis can also be applied to $[YGd_2I_6(OPH_3)_{12}]^{n+}$. ΔE represents the gap between the bonding orbital and the degenerate antibonding orbitals and δ represents the (de)stabilization that a(n) (un)like spin *d*-electron

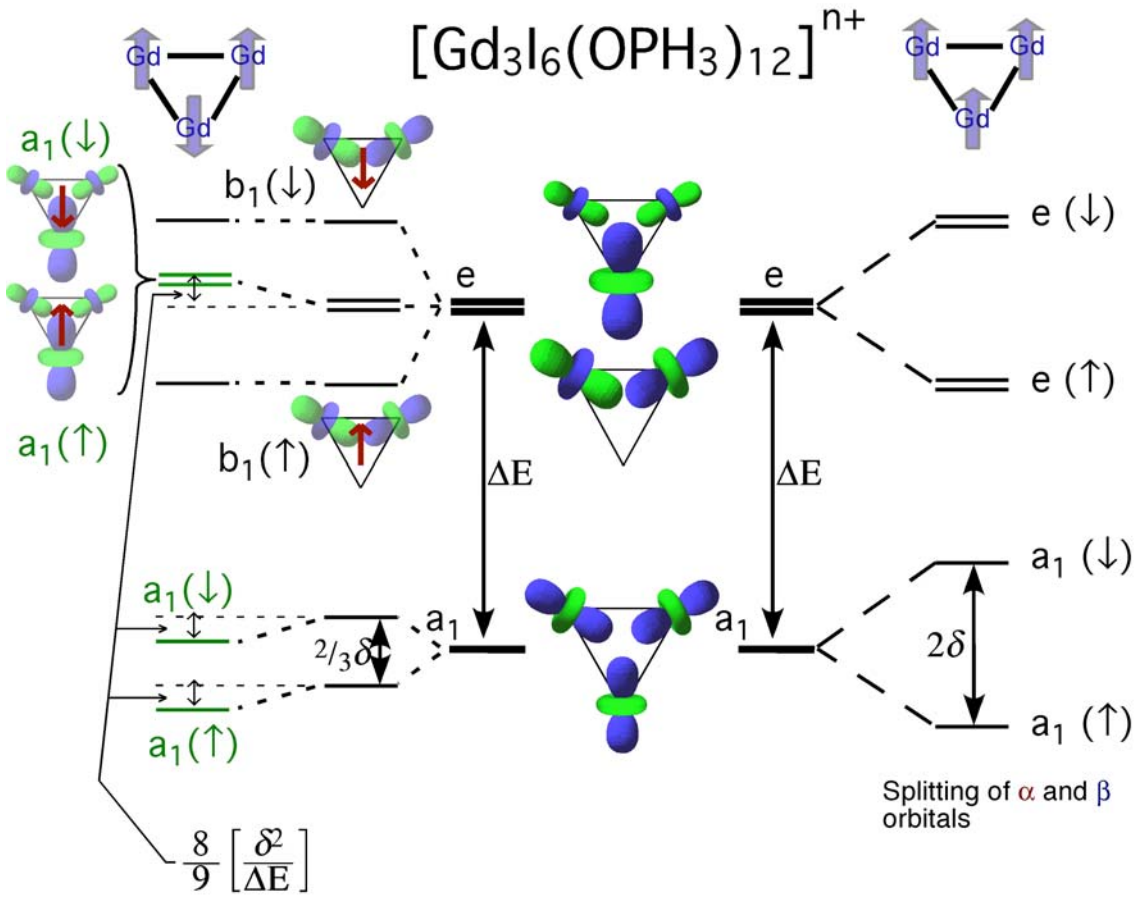

Figure 3.7. Treatment of 4*f*-5*d* exchange interaction in the model $[Gd_3I_6(OPH_3)_{12}]^{n+}$ as a perturbation to the 3-center bonding.

experiences upon "turning on" the $4f^7$-*d* exchange perturbation. Orbital plots clearly demonstrate that the *d*-electron(s) in the d^1 (d^2) systems reside in a delocalized 3-center bond orbital—underlining the plausibility of this treatment. For simplicity, the MO's are assumed to be a linear combination of Gd *d*-orbitals with no ligand contribution or 6*s*-hybridization taken into account.

In the all-spin-aligned "ferromagnetic" case, 4*f*-moment ordering is simply induces a 1st-order splitting the α- and β-spin molecular orbitals, and since the exchange potential felt by the *d* electrons maintains symmetry, no symmetry breaking occurs and no 2nd order perturbation effects are limited to mixing of the occupied a_1' orbital with orbitals of the same symmetry. When one of the 4*f*-moments is flipped antiparallel with the others ("ferrimagnetic" case), the exchange perturbation lowers the symmetry and mixing between the bonding and antibonding MO's is thereby induced, yielding a 2nd-order stabilization of both α and β spins (manifest in polarization of each *d*-spin orbital toward $4f^7$ centers of like spin).

In summary, when one has a closed *d*-shell system (like the d^2 trinuclear cluster), antiferromagnetic coupling is inevitably favored because antiferromagnetic $4f^7$-spin patterns inherently *break symmetry* and mix unoccupied orbitals into the occupied orbitals. Spatially, this allows for the stabilizing effect of spin polarization to occur. Any f^7 spin ordering that is effective at inducing 5*d*/6*s* spin-polarization will tend to have lower energy because such spin-polarization allows the delocalized electrons to spend more time in the vicinity of the like-spin *f*-electrons. In general, there is no reason to expect that such a mechanism of coupling should produce a spin-state energy ordering that conforms to a model built upon pairwise exchange coupling. With two parameters, δ and ΔE, we can achieve a satisfactory fit the SDFT energies as shown in Table 3.2 calculated for 6 different spin patterns (i.e., determinants) for $[Gd_3I_6(OPH_3)_{12}]^{n+}$ (n = 1, 2) systems.

Table 3.2. Energy comparison between DFT results and a two-parameter fit for $[Gd_3I_6(OPH_3)_{12}]^{n+}$ (n = 2, 1).

Complex	Number of Unpaired Electrons	DFT Energy (cm^{-1})	Two-Parameter Energy (cm^{-1})
$[Gd_3I_6(OPH_3)_{12}]^{2+}$	22	0	0
	8	755	778
	6	1666	1590
	10	2534	2475
$[Gd_3I_6(OPH_3)_{12}]^{1+}$	0	0	0
	14	240	180

3.3 Gd_2Cl_3

Gd_2Cl_3 has a structure wherein linear chains of *trans*-edge-sharing metal octahedra are bridged at the apices of the metal chains and capped on triangular faces by chlorine atoms, as shown in Figure 3.8.[146, 166] It is prepared by adding stoichiometric amounts of Gd and $GdCl_3$ to a tantalum tube and heating to 890 K for 30 days upon which the reaction vessel is quenched to room temperature.[146] As pointed out in previous studies, the structure may be formally described as a condensation M_6X_8 octahedral clusters to form single chains.[140] Nevertheless, the "octahedra" are quite distorted: the Gd-Gd distances on the shared edges are significantly shorter (3.37 Å) than Gd-Gd distances parallel with the chain propagation axis (*b* = 3.90 Å); Gd-Gd distances between basal and apical atoms range from 3.71 to 3.78 Å. Gd_2Cl_3 is a semiconductor with bandgap of ~ 0.85 eV,[167] as inferred from resistivity measurements; a presence of a

gap is consistent its the measured photoelectron spectrum and published electronic structural calculations.[150]

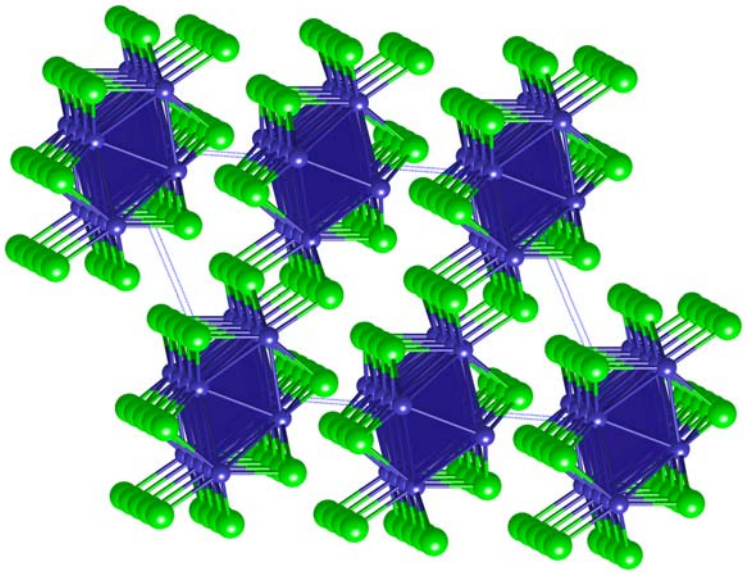

Figure 3.8. Perspective view of Gd_2Cl_3 down [101].

Previous band structure calculations indicate that the sesquichlorides have three low-lying, overlapping occupied *d* bands that contain the metal-metal bonding of the shared edge and these bands split off from the remainder of the *d* block, giving a gap of ~0.7 eV.[152] The semiconducting behavior is consistent with 6 metal *d* valence electrons per Gd_4Cl_6 unit cell available for metal-metal bonding in the structure. A semilocalized bonding picture of isotypic Y_2Cl_3 extracted from the band structure revealed the metal-

metal bonding orbitals consist of two 4c-2e bonds and one 2c-2e bond per unit cell, further clarifying both the structure-property relationships of these compounds.[158]

Although Gd_2Cl_3 has been studied using EPR, NMR, and magnetic susceptibility measurements,[40] the results of neutron diffraction experiments on single crystals of Gd_2Cl_3 provided the most detailed information concerning a 3-D antiferromagnetic phase transition at 26.8 K leading to a magnetic supercell (*a*, *b*, *2c*).[42] Within the 1D chains, the moments of the Gd atoms at the condensed octahedra sites are aligned along the chain direction, but are in an antiparallel arrangement across the short Gd-Gd bond shared by the octahedra as depicted in Figure 3.9. The moments on the apex atoms do

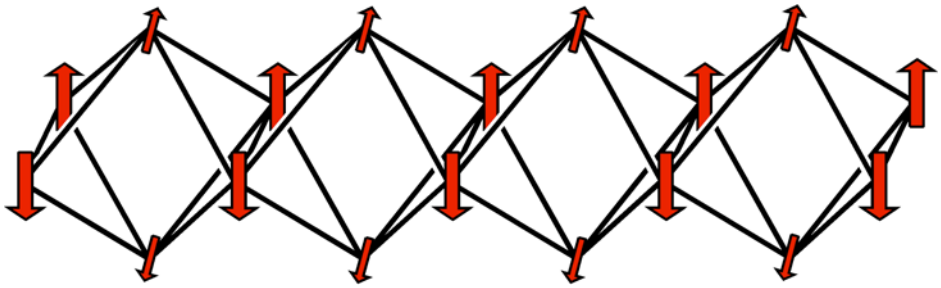

Figure 3.9. Intrachain magnetic ordering according to neutron diffraction results.[42]

not order, as one might expect, given the geometric frustration that should occur in relation to the spin ordering from the basal atoms. Adjacent chains are coupled antiferromagnetically.

3.3.1 Model Structure

While a study of the 3-D magnetic ordering in Gd_2Cl_3 would be desirable, we have limited our investigation to the ordering in 1-D chain models of Gd_2Cl_3. To build a meaningful 1-D model, important considerations include preservation of the bonding character found in the chains of condensed octahedra and maintenance of the coordination environment around Gd. In the structure of Gd_2Cl_3, each metal center is coordinated to the chloride atom of 2 adjacent 1-D condensed chains forming a 2-D sheet, allowing for additional interactions through the basal and apical Gd-Cl-Gd bridges. However, since interactions within the chains are likely to control the 1-D magnetic structure, only those contacts will be included in our model structure. Hence, our unit cell consists of 8 gadolinium atoms, 12 chloride ligands, and 4 phosphine oxide ligands, OPH_3, as shown in Figure 3.10. Our model preserves the metal backbone of the

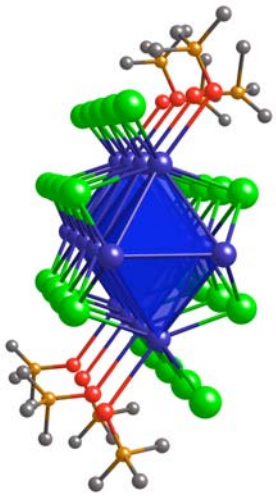

Figure 3.10. Model structure of Gd_2Cl_3.

chain and the chloride ligands that both cap the triangular side faces of the octahedra and bridge between two octahedra within the chain. Each chain was separated by a distance of 12.57 Å along the *c* direction and 11.87 Å along the *a* direction. Phosphine oxide ligands fill the coordination site provided by the apical Gd-Cl contacts lost upon separating the chains. Doubling of the unit cell in the chain direction (*b*) was necessary for two reasons: (1) crowding of adjacent phosphine oxide ligands is avoided by alternating their orientation within the doubled cell; (2) necessary flexibility in calculations of alternative antiferromagnetic spin arrangements is thereby enabled. Partial geometry optimizations for the positions of the phosphine oxides were performed using an analogous yttrium model system, $Y_4Cl_6(OPH_3)_2$; this resulted in Ln-O-P angles of 38.8° and 120° to prevent close H-H contacts. The closest H-H distance is 2.97 Å, well beyond van der Waals contact. Use of neutral phosphine oxide ligands allows one to avoid unphysical charge density accumulation that would have accompanied the use of anionic ligands.

3.3.2 Magnetic Ordering in the Model Structure of Gd_2Cl_3 Using SDFT

In order to directly assess the ability of the broken-symmetry SDFT approach to reproduce the magnetic ordering pattern observed in Gd_2Cl_3, we carried out electronic band calculations for nine competing spin patterns: one ferromagnetic, one ferrimagnetic, and seven antiferromagnetic. The calculated relative energies for such patterns are shown in Figure 3.11.[168] In each case we also show the symmetry of the potential that the 4*f* electron "cores" impose on the motion of the 5*d* and other valence

electrons. As we shall argue below, the origin of the differences computed in all our calculations is the *d*-band mixing induced by the perturbation of intraatomic 4*f*-5*d* exchange. Since the atomic calculations underestimate the magnitude of that exchange by ~11% (see Section 3.1), we expect that calculated energy differences for this model are probably an underestimation of the "true" differences between the spin patterns.

The most important and consistent characteristic of the results in Figure 3.11 is a preference for antiferromagnetic spin patterns in comparison to the ferro- or ferrimagnetically-coupled spin arrangements. The lowest energy calculated pattern is in correspondence with the experimentally observed spin-ordering as far as the basal atoms are concerned, i.e., antiparallel spin alignment prevails for atoms across the basal planes of the condensed octahedra (The lack of significant magnetization on the apical atoms cannot be modeled in our calculation). Interestingly, the 2nd lowest calculated pattern reproduces the observed basal spin-ordering. The difference between these two calculated spin patterns is the apical spin arrangements and the energy difference is nominal (22.9 cm^{-1}). Spin patterns in which 4f^7 spins alternate along the chain propagation axis in the basal plane (with 2*b* periodicities) all lie higher in energy.

Label, Pseudosymmetry,[a] Relative SDFT Energy,[b] Ising Energy Expression	Spin Patterns
Ferromagnetic, $D_{2h}(b)$ 1738.3 cm^{-1} $-2J'_1-4J'_2-16J'_3-4J'_4$	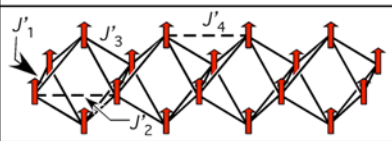
Ferrimagnetic, $C_{2v}(b)$ 729.2 cm^{-1} $-2J'_1-4J'_2-4J'_4$	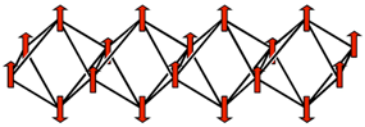
Antiferro V, $C_s(2b)$ 458.1 cm^{-1} $-2J'_1+4J'_2-4J'_4$	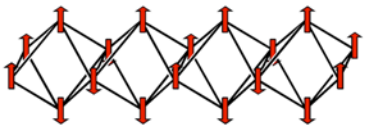
Antiferro IV, $C_s(2b)$ 449.2 cm^{-1} $-2J'_1+4J'_2+4J'_4$	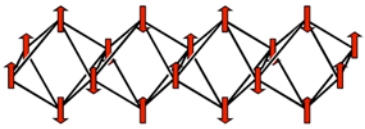
Antiferro IIIa, $C_2(2b)$ 311.3 cm^{-1} $+2J'_1+4J'_2+4J'_4$	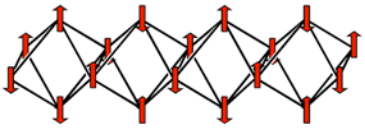
Antiferro III, $C_2(2b)$ 281.2 cm^{-1} $+2J'_1+4J'_2-4J'_4$	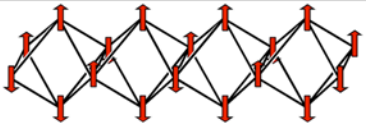
Antiferro II, $D_{2h}(b)$ 89.5 cm^{-1} $-2J'_1-4J'_2+16J'_3-4J'_4$	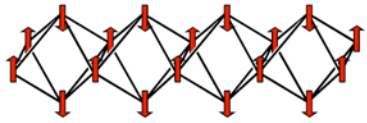
Antiferro Ia, $C_s(2b)$ 22.7 cm^{-1} $+2J'_1-4J'_2+4J'_4$	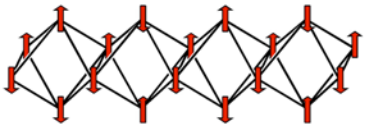
Antiferro I, $C_s(b)$ 0.0 cm^{-1} $+2J'_1-4J'_2-4J'_4$	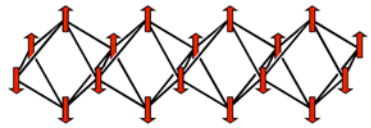

[a] "Pseudosymmetry" refers to the highest point symmetry of the spin-dependent potential the 4*f* electron moments exert on the valence electrons. Labels "*b*" and "2*b*" refer to the periodicity of potential along the *b* (chain) axis.

[b] Relative energy and Ising expressions are given per $Gd_8Cl_{12}(OPH_3)_4$ cell.

Figure 3.11. Nine spin patterns, energies, and Ising expressions for the model of Gd_2Cl_3.

SDFT calculations and the broken symmetry approach have been successfully applied to the estimation of the exchange coupling constants for a variety of binuclear transition metal complexes, with good agreement between computed and experimental values.[9] From the computed results in Figure 3.11, let us examine whether we can extract values for the Ising exchange parameters for this system. Under the (Ising) hypothesis of exchange interaction additivity, it is a simple matter to assign to each spin pattern an expression for the magnetic energy of each spin pattern, as shown in Figure 3.11. The energy associated with any one spin-pattern, A, can be written as:

$$E_{\text{spin pattern A}} = -\sum_{i<j} Z_{ij} \hat{S}_{z,i} \hat{S}_{z,j} J'_{ij} \tag{3.6}$$

where $\hat{S}_{z,i}$ and $\hat{S}_{z,j}$ are respective pseudo-spins (+1 and –1) on sites of types *i* and *j* for pattern A, J'_{ij} is the magnetic coupling constant between them, and $Z_{i,j}$ is the number of *i-j* neighbors. Energy differences are readily evaluated. In the present case, four magnetic constants have been considered, namely J'_1, J'_2, J'_3, and J'_4, as defined in Figure 3.11. (To scale these values for the Heisenberg Hamiltonian, all J'_i values need to be multiplied by 49/2.) J'_1 and J'_2 represent the basal-to-basal couplings across the octahedra and along the chain propagation axis, respectively. J'_3 represents the exchange coupling between apical-basal atom pairs and J'_4 represents the coupling between two apical atoms along the chain. Because the ferrimagnetic spin pattern gives rise to an asymmetric charge density in which structurally equivalent apical atoms have differing total charge, we dropped it from consideration in evaluating magnetic coupling constants (its inclusion does not alter the fundamental nature of our conclusions, however). Of the

remaining eight spin patterns, one may compute seven energy differences using the lowest energy spin pattern from the SDFT results and each difference may be set equal to an Ising parameter expression. We attempted to use a linear least squares fitting to determine the four magnetic constants. The J' values predict ferromagnetic coupling for J'_1 (2.08 ± 31.53 cm^{-1}) and J'_3 (4.48 ± 30.19 cm^{-1}), and antiferromagnetic coupling for J'_2 (-51.53 ± 15.77 cm^{-1}) and J'_4 (-165.41 ± 51.49 cm^{-1}). Although the sign of J' values sufficiently reproduce the experimentally determined magnetic structure along the basal plane, the ordering of the spin-patterns shown in Table 3.3 *are not* reproduced with the Ising parameters.

Table 3.3. Comparison of spin pattern energies with a "best fit" Ising model (J') for 1-D model of Gd_2Cl_3.

$E_A - E_{AntiferroI}$	$\Sigma_{i,j} Z_{i,j} J'_{i,j}$	EHTB Energy difference (cm^{-1})	Ising energy difference (cm^{-1})
$E_{Ferro} - E_{AntiferroI}$	$-4J'_1 - 16J'_3$	1738.3	-79.94
$E_{AntiferroV} - E_{AntiferroI}$	$-4J'_1 + 8J'_2$	458.1	-420.60
$E_{AntiferroIV} - E_{AntiferroI}$	$-4J'_1 + 8J'_2 + 8J'_4$	449.2	-1743.87
$E_{AntiferroIIIa} - E_{AntiferroI}$	$8J'_2 + 8J'_4$	311.3	-1735.54
$E_{AntiferroIII} - E_{AntiferroI}$	$8J'_2$	281.2	-412.28
$E_{AntiferroII} - E_{AntiferroI}$	$-4J'_1 + 16J'_3$	89.2	63.29
$E_{AntiferroIa} - E_{AntiferroI}$	$8J'_4$	22.7	-1323.27

One might presume that we could identify and order the pairwise coupling parameters in magnitude so that we could to correlate our SDFT results. After obtaining coupling constants that well represent the four energy differences, the calculated

energies of the patterns not used in each case (ferrimagnetic and other dropped pattern) is poor. We conclude that the Ising model provides an inappropriate description of *d*-electron-mediated *f-f* exchange interactions. Assuming the broken symmetry approach is valid for determining parameters in a Heisenberg model (i.e., that the discussion of Gd_2 dimer complex given in Chapter II can be generalized to the band case), a Heisenberg model would also be inadequate. If Gd_2Cl_3 were metallic, this would probably be expected since it is commonplace to treat metallic systems by considering the effect of exchange on electrons near the Fermi surface.[44, 47, 144] It is perhaps more surprising that these pairwise exchange models fail even for this closed shell (semiconducting) compound. Whatever the limitation of our present treatment (e.g., basis set or the use of the BLYP functional), we can reasonably assume that an improvement in theory is unlikely to produce results that revive a pairwise exchange model, with the possible exception of a model includes significant anisotropic exchange.

Previous analysis had postulated that 1D magnetic correlations in Gd_2Cl_3 persist at temperatures well above the 3D ordering temperature of 26.8 K.[41] While this suggestion is intuitively appealing, our results leave us unable to evaluate it plausibility. As we have seen, pairwise exchange parameters are elusive and without them, the excitation energies that accompany local spin fluctuations are difficult to estimate with the results we have at hand.

In view of the forgoing discussion and the closed *d*-shell (semiconducting) nature of our $Gd_4Cl_6(OPH_3)_2$ model chains (and Gd_2Cl_3 itself), we should not be surprised that all the low energy spin patterns are antiferromagnetic. We can identify features in

density of states (DOS) plots obtained with various $4f^7$-spin patterns that show how the extended chain system and trinuclear cluster are analogous; see Figure 3.12. As

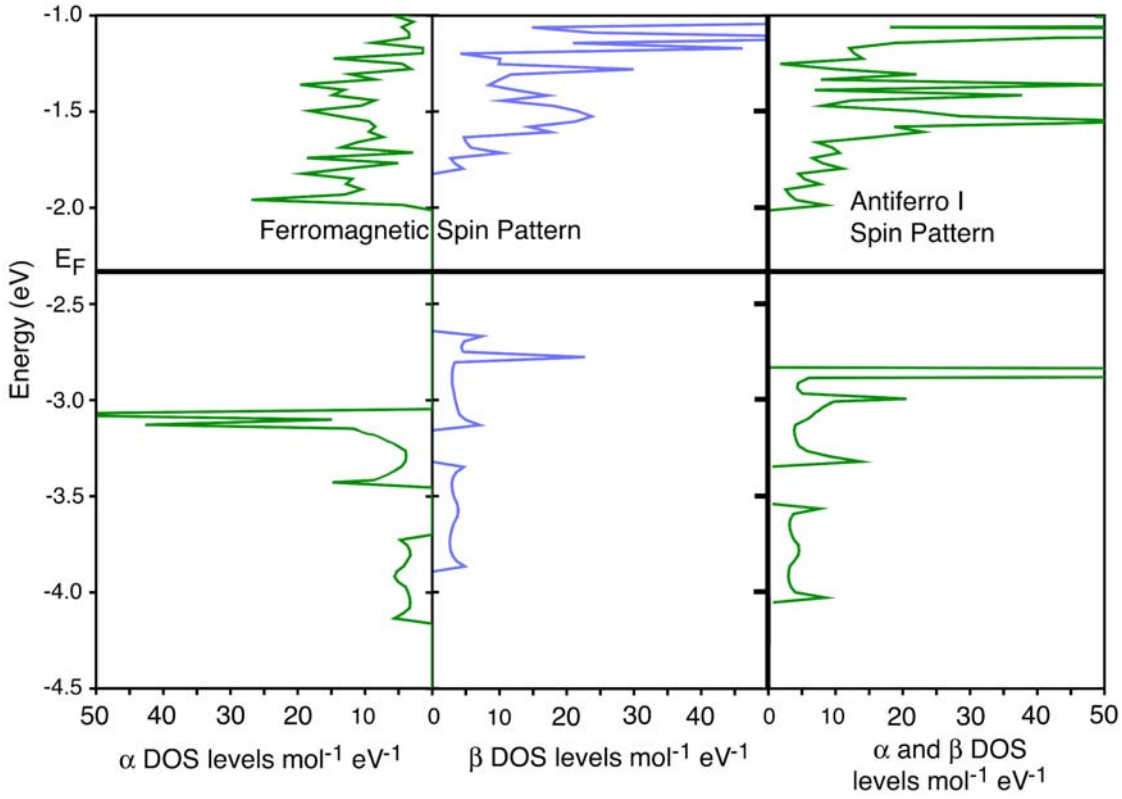

Figure 3.12. DOS plots of the Ferro and Antiferro 1 spin pattern.

expected, the bands in the vicinity of the Fermi level are Gd-localized. The results amplify those of previous tight-binding calculations of both Gd_2Cl_3 and its yttrium analog: three doubly-occupied 5*d* bands (per Gd_4Cl_6 unit cell) are separated by a significant gap from the rest of the low-lying unoccupied metal hybridized *d* and *s* bands.[148, 152, 158] The calculated gap ranges from 0.68 to 1.0 eV for different

antiferromagnetic spin patterns with the gap for Antiferro I equal to 0.82 eV, in good agreement with the 0.85 eV band gap seen experimentally for Gd_2Cl_3. The α- and β-DOS plots for all the antiferromagnetic cases are identical because although the α- and β-electrons localize on different atoms, the α- and β-spin distributions are spread over symmetry equivalent sets of atoms. Examination of the α- and β-DOS plots for the ferromagnetic spin pattern shows a stabilization and destabilization of the α- and β-electrons, respectively. Since the exchange potential felt by the *d* electrons maintains symmetry, the $4f^7$-spin patterns induce little mixing between valence and conduction band orbitals. In our qualitative perturbation analysis then, this semiconducting ferromagnetic-ordered system experiences no overall stabilization because the 1^{st}-order stabilization of α-spin *d* bands is cancelled by destabilization of β-spin *d* bands and there is little 2^{nd}-order stabilization. In contrast, while the antiferromagnetic alternatives experience no net 1^{st}-order splitting between α- and β-spin *d* bands, both α- and β-spin *d* bands are stabilized in 2^{nd}-order by the valence-conduction band mixing induced by symmetry breaking.

While DOS plots are useful in illustrating the distinction between the ferro- and antiferromagnetic cases, we gain no further insight into the specific ordering among the antiferromagnetic alternatives. Though a specific "orbital explanation" for the calculated ordering is not apparent, it is nevertheless instructive to examine the 5*d* and 6*s* spin polarizations (i.e., the local differences in α- and β-spin populations). These are given for all of the calculated spin patterns obtained via Mulliken population analysis

(summed over all *k*-points calculated) and gathered in Table 3.4. On each Gd atom, for every spin pattern, the 5*d* and 6*s* spin polarizations mirror the spin orientations of $4f^7$ core for that atom — hence we have given only the polarization magnitudes in Table 3.4.

Table 3.4. Average Gd 5*d* and 6*s* spin density for each spin pattern of Gd_2Cl_3.

Spin Arrangement	Basal Spin Density	Apical Spin Density	Relative Energy (cm^{-1})
Ferro	0.087 (0.0005)	0.034 (0.0009)	1738.2
Ferri	0.193 (0.0061)	0.219 (0.1567)	729.2
AntiferroV	0.294 (0.0013)	0.227 (0.0009)	458.1
AntiferroIV	0.295 (0.0014)	0.227 (0.0008)	449.2
AntiferroIIIa	0.326 (0.0019)	0.227 (0.0021)	311.3
AntiferroIII	0.326 (0.0017)	0.227 (0.0019)	281.2
AntiferroII	0.294 (0.0017)	0.295 (0.0006)	89.5
AntiferroIa	0.417 (0.0006)	0.234 (0.0012)	22.7
AntiferroI	0.417 (0.0005)	0.235 (0.0018)	0

We have combined 5*d* populations with 6*s* populations because they track with each other, though the 6*s* polarization is consistently smaller. Typically, total 5*d* populations are about 2.3-2.7 times larger than the 6*s* populations, while the polarization for 5*d* populations are 5-6 times larger than the polarizations of the 6*s* populations. (This reflects the fact that the intraatomic exchange interaction between the 4*f* electrons and the more diffuse 6*s* electrons is typically about one-third that of the 4*f*-5*d* interaction.)

The data in Table 3.4 is unambiguous in confirmation of our perturbation-theoretic interpretation. The symmetry-breaking antiferromagnetic patterns all induce much greater spin-polarization than is seen in the ferromagnetic case. Beyond that, however, we can see that the extent of spin-polarization is monotonically correlated with the relative stability of each spin-pattern; the greatest spin-polarization is seen in the computed ground state pattern. One concern regarding comparison of these results with experiment is the significance of the apical atom spin-polarizations — recall that spin-polarized neutron diffraction results showed no evidence of magnetic order on the apical atom positions.[42] Examination of two spin orderings which differ only that the apical atom $4f^7$-spins alternate, for example in Antiferro pattern I and Ia, reveals they have similar energies and exhibit virtually identical spin-polarization magnitudes. The clear implications are that apical-basal interactions are indeed "frustrated", even if a pairwise interaction model is not a strictly appropriate means to reveal it, and that the kind of apical-apical communication that would favor ordering is also not present.

3.3.3 Calculations of the 1-D Gd_2Cl_3 Model Using EHTB Method

3.3.3.1 Semilocalized Bonding Description

We have carried out electronic band calculations for the 1D model of Y_2Cl_3 at the semi-empirical and first principles levels of theory to gain some insight into the semilocalized bonding description of this material. While the best scenario would be to use DFT results to provide these descriptions, unfortunately DMol^3 does not provide projected DOS plots for atoms or orbitals and the program does not produce band

dispersion plots. Since the 4*f* orbitals on a lanthanide atom generally play a minor role in bonding, our first goal was to adapt EHTB parameters to simulate DFT results of the nonmagnetic yttrium analog to describe the bonding in a solid.[169] Referring back to the Gd atom, the nonmagnetic case is analogous to the averaged effect of 4*f*-5*d* exchange interaction. To determine the ionization potential and Slater exponents for the yttrium atom, we compared general characteristics of DOS plots in an attempt to match band gaps, bandwidths, and local maxima and minima. A comparison between total DOS plots are depicted in Figure 3.13 showing the Y basal and apical atom *d*-orbital contribution and band dispersion plot along the chain propagation axis in the tight-binding case. The bandwidths and band gaps for the EHTB

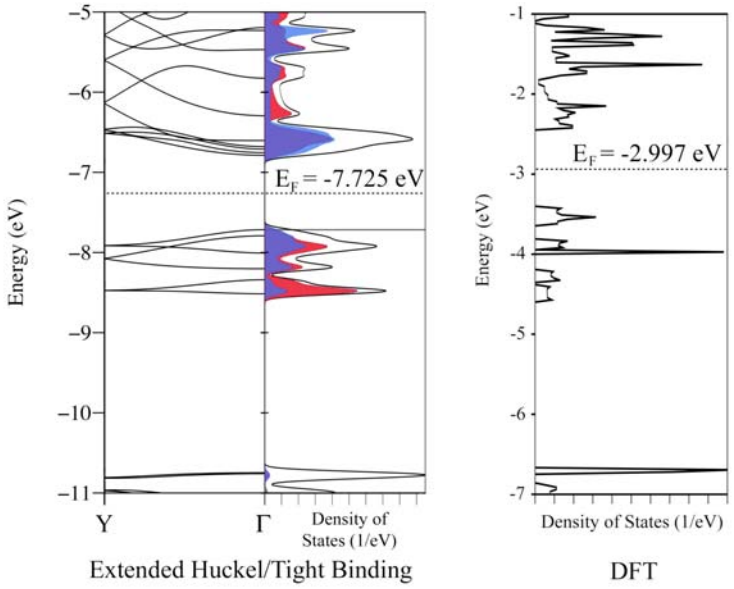

Figure 3.13. Density of States plot for Y_2Cl_3 for EHTB and DFT. Red (light gray) projected plot indicates the basal Y atom DOS and blue (dark gray) projected plot is apical Y atom. The band dispersion plot is along the chain propagation axis.

model are in good agreement with the DFT results. The band gap at the Fermi level for the DFT model is ~1.0 eV and EHTB calculations predicts a gap of ~0.7 eV. The DOS plots obtained from EHTB show that the states near the Fermi level are Y-based. While the band dispersion plot depicts 6 bands, there are only three bands below the Fermi level. Because the unit cell is doubled for the Gd_4Cl_6 units, a folding effect occurs in the bands. The *d*-orbital projected DOS plots for the basal and apical Y atoms are shown in Figures 3.14 and 3.15, respectively. The lowest band clearly has σ-bonding character between the pair of basal Y atoms, as described in reference 158.[158, 170] The two remaining bands are not well localized and are not easy to discriminate. A schematic bonding picture is shown in **3.2** and shows π character with respect to bonding between the pair of basal metal centers and considerable apical-basal bonding as well. At the Fermi level, the band has significant σ-bonding character along the chain propagation axis from both atoms.

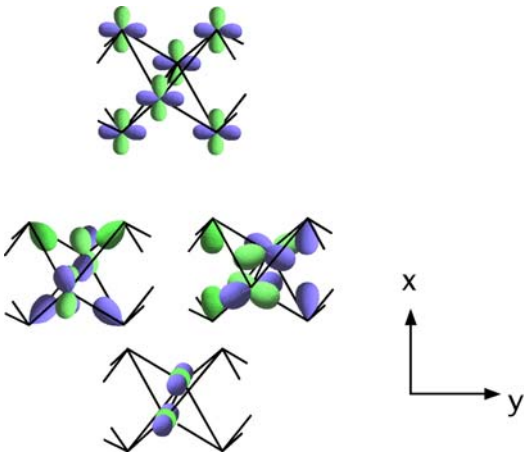

3.2

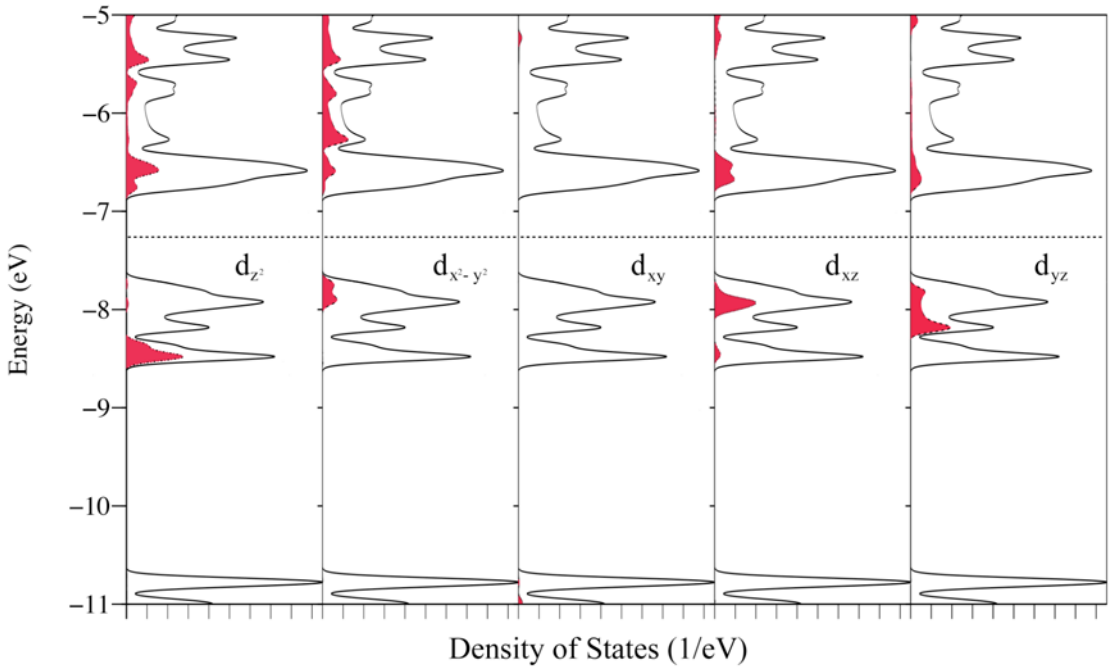

Figure 3.14. *d*-orbital projected DOS plots of the basal Y atom for the 1D model of Y_2Cl_3.

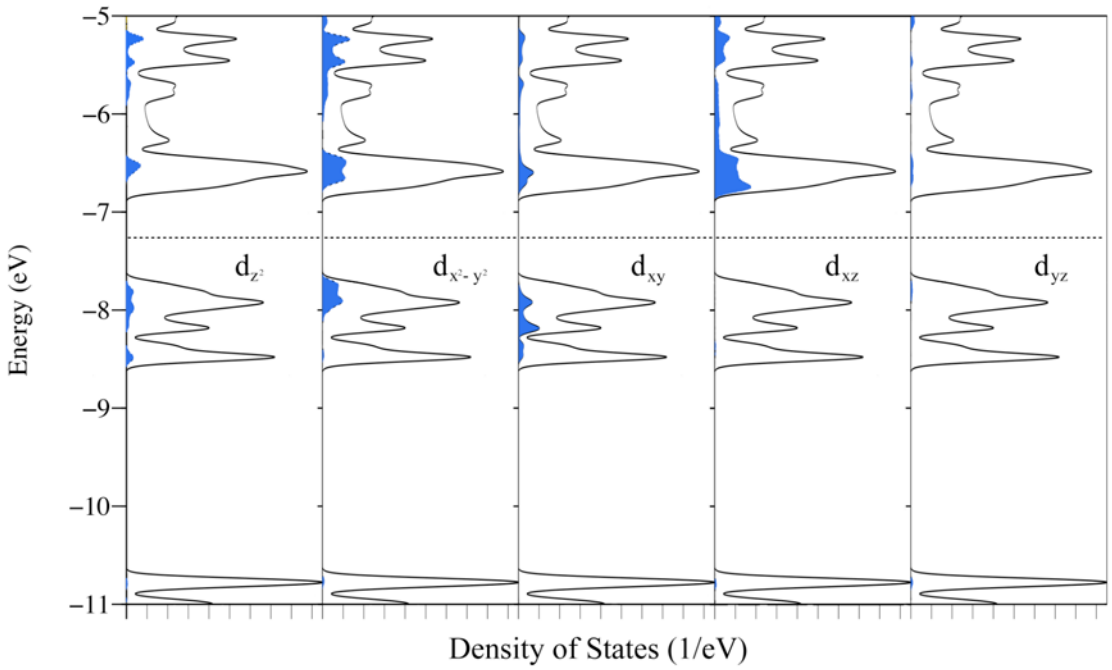

Figure 3.15. *d*-orbital projected DOS plots of the apical Y atom for the 1D model of Y_2Cl_3.

3.3.3.2 Magnetic Coupling Results

Using results obtained from DFT band calculations, we have been able to provide a semilocalized bonding description of the nonmagnetic Y_2Cl_3. We then asked ourselves if we could use EHTB to interpret the magnetic properties of Gd-containing compounds, specifically Gd_2Cl_3. Using DFT DOS plots for the lowest energy antiferromagnetic spin pattern, Antiferro1, we adjusted *d*- and *s*-orbital parameters for EHTB calculations (H_{ii}'s) to simulate the exchange effects exerted by the 4*f* moments to the Gd atom 5*d*- and 6*s*-orbital energies in the EHTB calculations. A full description of this procedure can be found in Appendix A.

Results from the EHTB calculations in comparison to DFT can be found in Figure 3.16. We carried out eight tight binding calculations using 256 ***k***-points: one ferromagnetic spin pattern, and seven antiferromagnetic spin patterns.[171] The ferrimagnetic case was not included in our comparison because of its asymmetric charge density and its energy is considered to be higher than the antiferromagnetic spin patterns. Results in Figure 3.16 show a preference for the lowest energy antiferromagnetic spin pattern as predicted by DFT calculations. The energy difference between Antiferro I and Antiferro Ia are essentially the same, and the ferromagnetic spin pattern is the highest in energy for both methods. The similarity ends there: The ordering from DFT results is not reproduced by the EHTB method and the energy differences are well below that from DFT. However, it is encouraging to note that only four sets of spin patterns switch position in the EHTB case. Figure 3.17 depicts the DOS plots for the lowest energy antiferromagnetic spin pattern and the ferromagnetic pattern. The correspondence

between EHTB and DFT methods is good: the calculated band gap using EHTB is smaller for the ferromagnetic case, but it reproduces DFT results.

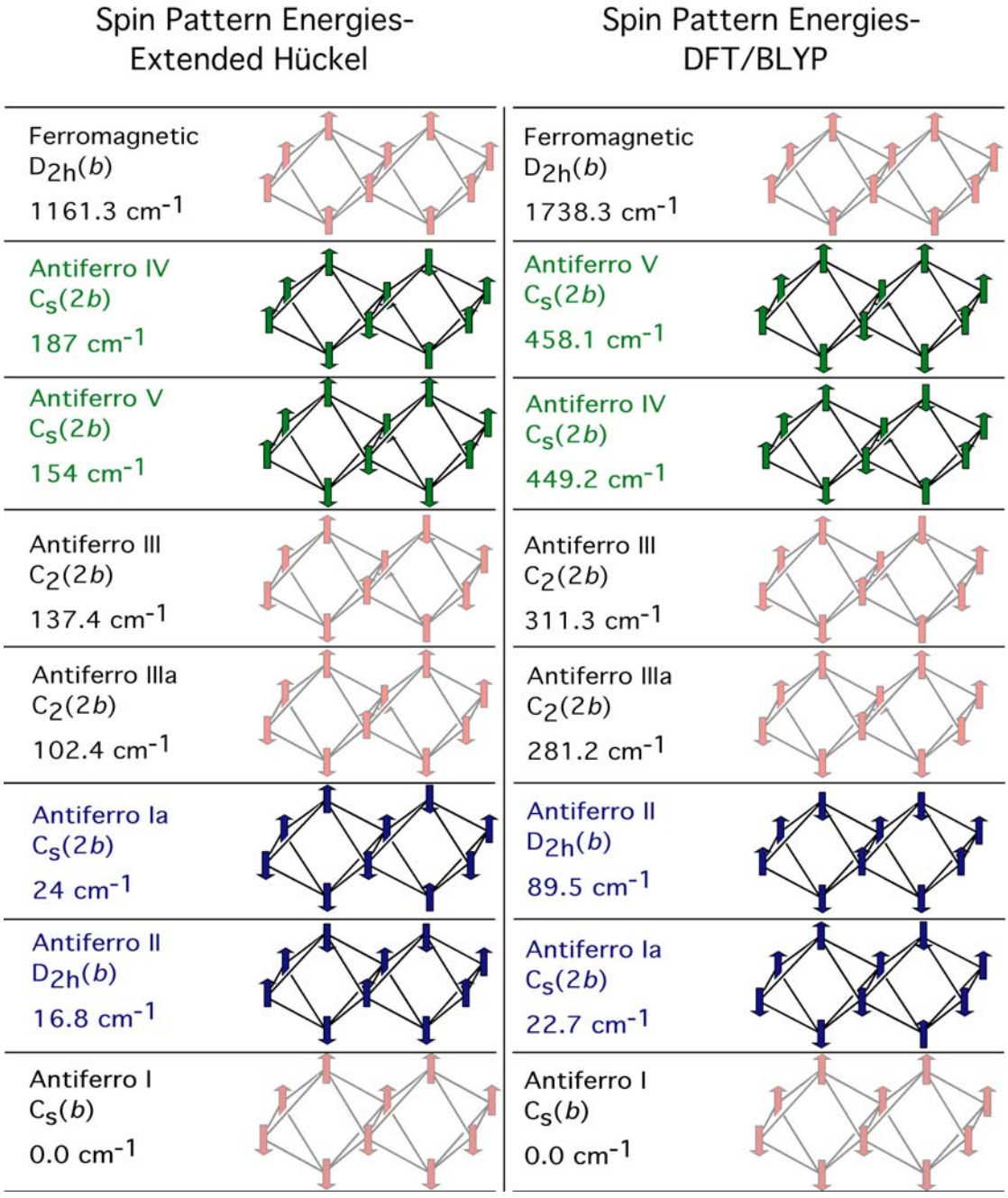

Figure 3.16. Comparison of EHTB and DFT results of eight spin patterns and energies for the 1D model of Gd_2Cl_3.

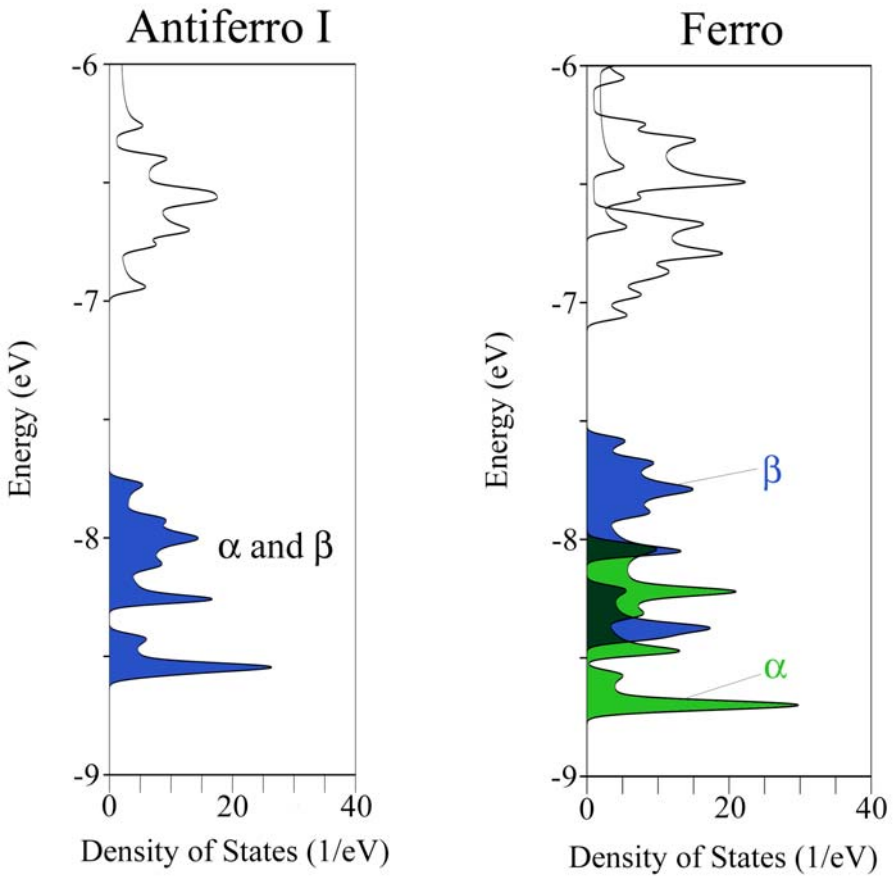

Figure 3.17. EHTB DOS plots for AntiferroI and Ferro spin patterns for the 1D model of Gd_2Cl_3.

CHAPTER IV

GADOLINIUM DINUCLEAR COMPLEXES*

In this chapter, we subject dinuclear gadolinium complexes with bridging carboxylate, phenoxide, and diazenido bridging ligands to theoretical scrutiny with the purpose of learning how intervening ligands in these complexes influence the magnetic coupling between the gadolinium $4f^7$ (^{8}S) ion cores. As the preceding comments indicate, our purpose is to elucidate electronic factors that might be transferable to polynuclear lanthanide-containing molecules and materials that might exhibit magnetic ordering.

4.1 Computational Details

Geometries used in calculations of phenoxide- and carboxylate-bridged dinuclear compounds were based on structures of related compounds determined by X-ray crystallography. When necessary, experimental structures were slightly idealized to achieve inversion symmetry. Partial geometry optimizations were performed on the two models mimicking the heptadentate amino phenoxide Gd complex bis((μ_2-tris(((2-Hydroxybenzyl)amino)ethyl)amine)-gadolinium), ($[Gd(AmPh)]_2$), in which the models contain either one bridging phenoxide group, Ph = 3 and Ph = 1, or a bridging enolate group, Ph = 0 (refer to Figure 4.3 for notation). In both cases, the Gd-L distances and

angles were kept at experimentally determined values and only the ligands were optimized.

Since no diazenido-bridged dinuclear gadolinium complexes have been reported, its structure was obtained from a yttrium analog by multiplying observed Y–L distances by a scale factor of 1.029 – the ratio of the two metals' 8-coordinate crystal radii – to obtain Gd–L distances.[172] Geometries of the yttrium diazenido complexes were also optimized at the DFT/BLYP level. Partial geometry optimizations for the one-electron oxidized product were performed using both experimental and optimized geometries, keeping constant the distances and angles of the bis(silyl)amide and solvent ligands. Both yielded the same geometry. In discussions referring to van der Waals radii, standard radii were taken for C (1.70 Å), Si (2.10 Å), and N (1.55 Å).[164] For yttrium, the v-d-W radius (2.42 Å) was obtained using the relation $R_{vdw} = R_{cov} + 0.80$ Å with $R_{cov} = 1.62$ Å. A standard Mulliken population analysis was carried out to obtain total atomic populations and charges.

4.2 Benchmark Systems: Alkoxo-Bridged Gd(III) Dinuclear Complexes

4.2.1 $[Gd(OAc)_3(H_2O)_2]_2$

$[\{Gd(OAc)_3(H_2O)_2\}_2]\cdot 4H_2O$ (**1**) has a structure wherein two of the six carboxylate units bridge each gadolinium to form a planar four-membered ring.[173] In the bridging acetate ligands, the oxygen atoms not involved in the central Gd_2O_2 parallelogram bind to one Gd center, as shown in Figure 4.1. Two additional acetate

ions and water molecules complete the coordination environment around each Gd^{3+} ion. The distance between the gadolinium ions within the dinuclear unit is 4.206 Å, and the angles at the oxygen bridgeheads are 115.48°. $[\{Gd(OAc)_3(H_2O)_2\}_2]$ exhibits ferromagnetic coupling; the effective moment (per Gd) reaches 9.07 μ_B at 1.74 K, and the susceptibility data is fit with $J = 0.03$ cm^{-1}.[174]

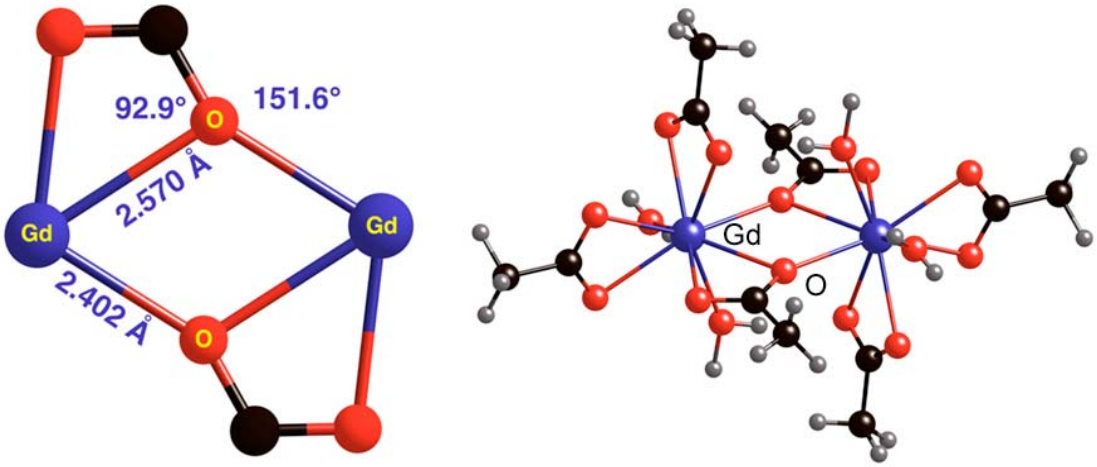

Figure 4.1. Structure of $[Gd(OAc)_3(H_2O)_2]_2$ detail of the Gd_2O_2 core.

4.2.2 $[Gd(AmPh)]_2$

$[Gd(AmPh)]_2 \cdot 2CHCl_3$ (**2**) is a homodinuclear complex containing two 8-coordinate Gd ions, each of which is coordinated by (tris(((2-hydroxybenzyl)amino)ethyl)amine (AmPh), a triply-deprotonated heptadentate Schiff base ligand (Figure 4.2).[175] One phenolate arm on each ligand acts as a bridge between

the two metal centers, which are separated by 3.984 Å; the angle at the oxygen bridgeheads is 113.12°. The molecule is centrosymmetric and the Gd_2O_2 parallelogram is nearly rhombic (the two Gd–O distances are 2.391(2) and 2.384(2) Å). The complex exhibits antiferromagnetic coupling with a decrease in the magnetic moment with temperature such that the moment (per Gd) falls to 7.30 μ_B at 4.2 K (derived coupling constant, $J = -0.045$ cm^{-1}).

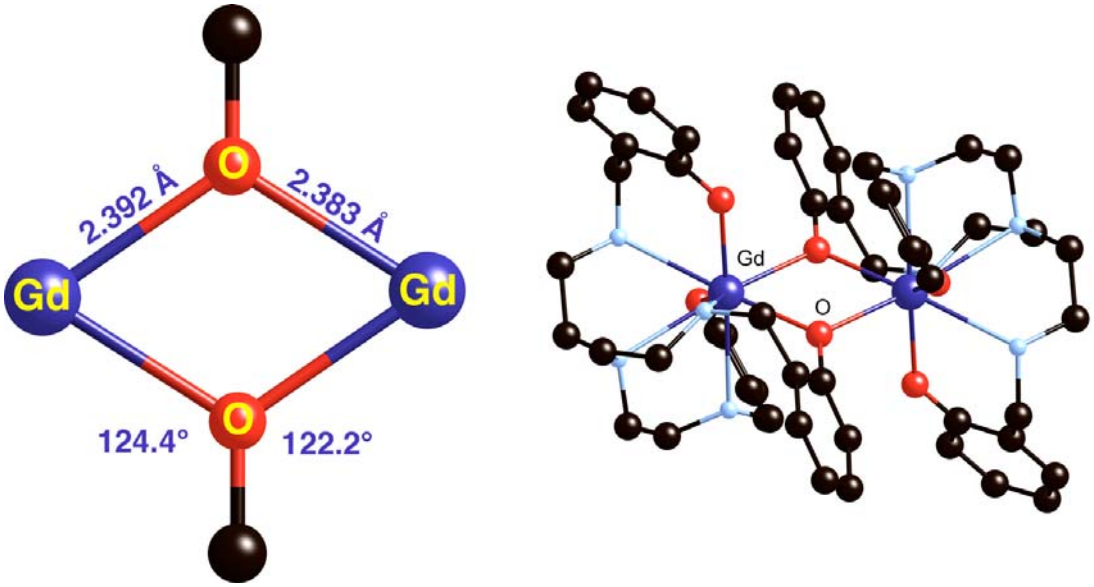

Figure 4.2. Structure of $[Gd(AmPh)]_2$ and detail of the Gd_2O_2 core.

The experimental and calculated exchange coupling constants for complexes **1** and **2** and related models are shown in Table 4.1. Though they lack quantitative accuracy, our calculations successfully predict the qualitative nature of the coupling (i.e., the sign of *J*) and give good agreement for the magnitude of the coupling in every case, which is

always very small. To check the applicability of our computational models to correctly evaluate coupling constants in real compounds, we calculated *J* for different model structures using the experimentally determined structural data for both compounds. Results for other carboxylate derivatives based on **1** indicate that electron-withdrawing groups exert little influence on the strength of exchange; all of the cases computed are predicted to have coupling constants very similar to that found for acetate bridges.[176]

Table 4.1. Exchange coupling constants $2J$ (cm^{-1}) calculated as the S = 0 – S = 7 energy difference for the structures of the oxo–bridged Gd(III) dinuclear complexes and related model structures.

Complex	J_{Calcd}	J_{Exptl}
$[Gd(O_2CH)_2(\mu\text{–}O_2CR)(H_2O)_2]_2$		
R = CH_3	0.053	0.039
R = CF_3	0.046	
R = H	0.040	
$[Gd(AmPh)]_2$		
Ph = 3	–0.116	–0.045
Ph = 1	–0.116	
Ph = 0	–0.121	

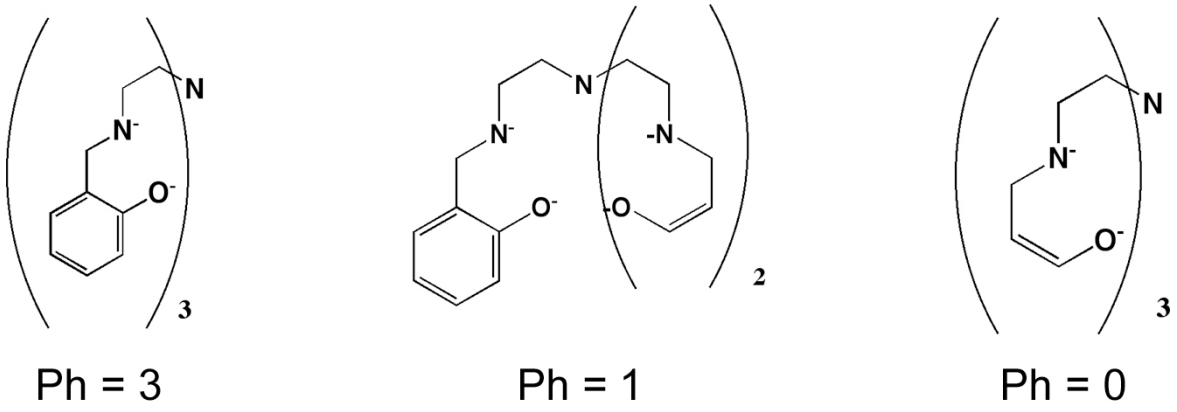

Figure 4.3. Model structures for $[Gd(AmPh)]_2$. Ph = 3 refers to a ligand with three phenoxide groups, Ph = 1 to a Gd_2-bridging ligand with one phenoxide group, and Ph = 0 refers to a bridging ligand with no phenoxide moieties.

For the models of complex **2** (see Figure 4.3), simplifying only the terminal phenoxide groups of the heptadentate ligand and maintaining the phenolate bridge yields a computed constant of –0.116 cm^{-1}, that is larger than experimentally observed (– 0.045 cm^{-1}), but correctly predicts antiferromagnetic coupling. Similarly, when replacing the bridging phenoxide group with a model using enolate bridges, one observes a larger calculated coupling constant (–0.121 cm^{-1}) than experimental model, however, it correctly predicts weak antiferromagnetic coupling of comparable magnitude as the other calculated coupling constants.

The important distinction between these two classes of complexes is in the geometries of the Ln_2O_2 carboxylate (phenolate) bridges. The central Ln_2O_2 cores of the phenolate-bridged complexes, **2**, show near-D_{2h} symmetry: all the Ln-O bond distances are nearly equal, and the Ln–O–C(ring) angles are all within 2˚ of their mean values. In

contrast, the Ln_2O_2 cores of the carboxylate bridged molecules, **1**, have approximate C_{2h} symmetry: the Ln–O lengths show significant alternation within the Ln_2O_2 ring and the lines containing the exo-O–C do not radiate outward from the center of the ring (see Figures 4.1 and 4.2). The differences computed in all our calculations seem to correlate with the donor ability of the ligand and the break in symmetry. In addition to a large in-plane displacement, the oxygen bridgehead angles are also important for assessing the coupling exhibited by the Gd centers (**4.1**). Small increases in Gd-O-Gd angle, θ, appear to favor ferromagnetic exchange. Also, as the in-plane angle, φ, tends toward 120°, the system exhibits antiferromagnetic character. These small changes, however, are not as substantial as the ligand effect on lowering the symmetry.

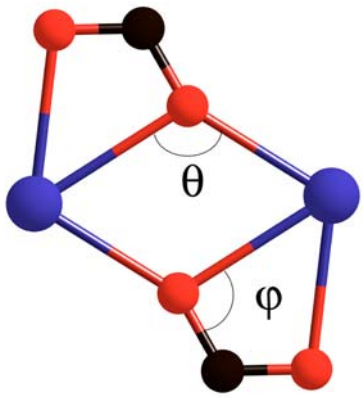

4.1

4.2.3 Magnetostructural Correlations in Alkoxo-Bridged Gd(III) Dinuclear Complexes

Gd-O distances for other alkoxo-bridged Gd(III) dinuclear complexes range between 2.940 and 2.324 Å. To investigate the correlation between the Gd–O distance and magnetic coupling, we calculated the coupling constant for several model structures with a Gd_2O_2 ring.[173, 175, 177-180] The calculated values of 2*J* in Table 4.2 show that as the Gd–O distances become more unequal, antiferromagnetic coupling is replaced by ferromagnetic coupling. The sign of the coupling constants in these complexes are correctly reproduced in all four cases, and they are all predicted to have small magnitudes. Further analysis of all the experimental structures reveals magneto-structural correlations in the Gd dinuclear complexes. Both the theoretical results and experimental data show the correlation between the rhombus for the Gd_2O_2 ring, and the sign and magnitude of magnetic coupling.

While it is reassuring that we obtain generally good agreement between computed coupling constants experimental data for the complexes so far considered, the magnitudes of these couplings are quite small.[181] With net couplings of such small magnitude, it is difficult to extract any qualitative chain of reasoning that "explains" the results discussed so far. Furthermore, it seems likely that as long as we remain focused on hard, saturated oxygen-based donors as bridging ligands, strategies for increasing the magnitude of the Gd–Gd coupling will remain obscured. We therefore turn our attention to dinuclear lanthanide complexes synthesized in Evans' group: those containing diazenido bridges and lower Gd^{III} coordination numbers.

Table 4.2. Exchange coupling constants $2J$ (cm^{-1}) calculated from the (S = 0) – (S = 7) energy difference for various oxo–bridged Gd(III) dinuclear complexes.

Compound	θ/°	φ/°	Gd···Gd (Å)	Gd–O (Å)	J_{exp}	J_{calc}	Ref.
$[Gd_2(mal)_2(H_2O)_6]$	116.71	92.59	4.277	2.426/ 2.597	0.048	0.057	177
$[Gd_2(acetylsal)_4]_\infty$	114.3	94.0	4.187	2.439/ 2.545	0.037	0.075	178
$[\{Gd(OAc)_3(H_2O)_2\}_2]$	115.48	92.88	4.206	2.403/ 2.570	0.03	0.039	173
$[Gd_2(O_2Fc)_2(O_2Fc)_4(MeOH)_2]$	112.44	83.39	4.409	2.349/ 2.941	0.006	0.003*	179
$[Gd(AmPh)]_2$	113.12	124.41	3.984	2.383/ 2.392	–0.045	–0.116	175
$[\{Gd(Hsabhea)(NO_3)\}_2]$	107.61	121.01	3.764	2.324/ 2.341	–0.198	–0.482	180

* Within our accuracy limitation, this is not significantly different from zero.

4.3 Dinitrogen Complexes

Evans and coworkers have synthesized a class of molecules in which Ln centers are coordinated by two bis(trimethylsilyl)amide ligands and a single THF molecule: $\{[(Me_3Si)_2N]_2(thf)Ln\}_2(N_2)$; ($Ln^{III}$ = Gd, Tb, Er, Ho, Y, Lu, Tm, Dy, Nd) as shown in **4.2**.[182-184] These molecules have a structure in which dinitrogen bonds in a μ-η^2:η^2-N_2 fashion where the N–N distances are 1.258–1.305 Å, indicating that the bridging dinitrogen is most appropriately described as a diazenido ligand, N_2^{2-}. Despite the fact that the synthesis of some of these compounds involved divalent lanthanide reagents (in the case of thulium, dysprosium, and neodymium), *all* the lanthanide centers in this set of molecules should be regarded as trivalent with $4f^n$ (n_{La} = 0, n_{Ce} = 1, etc) core

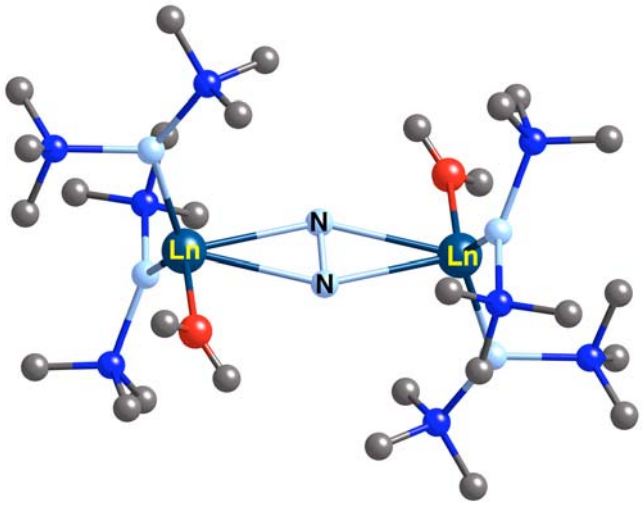

2. Ln = Gd, Tb, Er, Ho, Y, Lu, Tm, Dy, Nd

4.2

configurations and bearing a 3+ core charge. The same valence description applies to a second class of diazenido-bridged complexes wherein two *t*-butoxide ligands and two THF molecules are bound to each lanthanide center: $[(2,6\text{-}t\text{Bu}_2\text{C}_6\text{H}_3\text{O})_2(\text{thf})_2\text{Ln}]_2((\mu\text{-}\eta^2\text{:}\eta^2\text{-}\text{N}_2)$ with Ln^{III} = Tm, Dy, Nd.

Most lanthanide compounds are 8- or 9-coordinate; the Ln centers in both classes of complex are 5- and 6-coordinate. These relatively low Ln coordination numbers are important in stabilizing the diazenido ligand in these complexes (Figure 4.4, only half of the dinuclear complex is shown). Importantly, this relative coordinative unsaturation is compensated by the π-donation of amide and by back donation from the diazenido ligand. Thus, the ligand bulk, low coordination numbers, and bridging diazenido ligands are interrelated. As we shall see, these circumstances conspire to enhance the magnetic

coupling of Gd centers through the bridge.

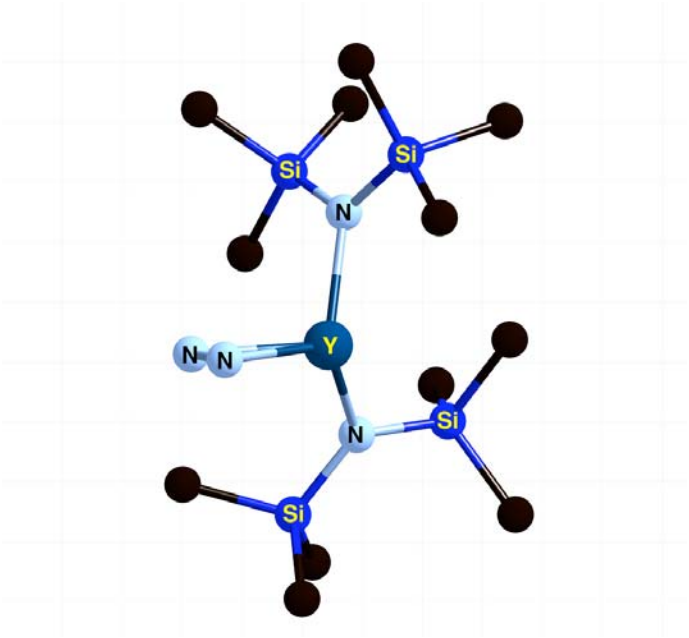

Figure 4.4. $\{[(Me_3Si)_2N]_2(thf)Ln\}_2(N_2)$; the thf ligand is omitted.

4.3.1 Yttrium Geometry Optimization

A geometry optimization on the yttrium complexes revealed only minor differences between optimized and experimental structures. All relevant bond distances and angles are shown in Table 4.3. The computed dinitrogen distance (1.256 Å) is about 1% shorter than observed experimentally (1.268(3) Å) and the computed Y-N distances (2.340 and 2.369 Å) are about 2% longer than those observed experimentally (2.296(2) Å and 2.317(2) Å). All other metal-ligand distances are slightly longer (0.03 Å) than experiment and the largest discrepancy in bond angles is ~2°. There are no precedents in

the literature to which we can draw comparisons for yttrium complex geometry optimizations using BLYP functional, but bond distances for tris(bis-dimethylsilyl)amido samarium using the hybrid B3LYP functional are also slightly longer than experiment for lanthanide systems.[185-190] All angles and bond lengths in the disilylamide ligands are normal; there are no indications that would suggest that C-H bonds are donating significantly to the Y centers. We therefore replaced the $Si(Me)_3$ groups with simpler SiH_3 groups in our calculations.

Table 4.3. Selected experimental and DFT optimized bond distances (Å) and angles (deg) for $\{[(H_3Si)_2N]_2(solv)Y\}_2(N_2)^{0,+1}$. [191]

	Experimental Geometry	Geometry Optimization	$1\text{-}e^-$ Oxidation
		Bond Distances (Å)	
Y—N3 (diazenido)	2.296	2.340	2.502
Y—N4	2.317	2.369	2.537
N4—N3	1.268	1.256	1.182
Y-O			
thf	2.390	2.487	2.368
OMe_2*	2.465	2.487	2.411
H_2O*	2.504	2.470	2.430
		Bond Angles (deg)	
N3—Y—N4 (diazenido)	31.90	30.94	27.12

*Experimental Ln-OMe_2 and Ln-H_2O distances were determined from partial geometry optimizations varying only the Ln-Solv distance.

To better assess the effect that the experimental and calculated metal-diazenido distances have on bonding in the Ln_2N_2 core, relevant Mulliken charges and populations are shown in Table 4.4. First, it appears that there is a modestly greater charge

separation for the optimized geometry than for the experimental geometry. Population analysis shows greater overall Y *d*-electron density at the experimental structure, indicating a potential underestimation of backbonding from the diazenido bridge to the yttrium in the optimized structure.[192]

Table 4.4. Comparison of overall Mulliken charges and populations, and percent SFO populations of various atomic orbitals for experimental and DFT geometry-optimized structures for $\{[(H_3Si)_2N]_2(thf)Y\}_2(N_2)$.

	Geometries	
	Experimental	Optimized
Y—N (diazenido) distance (Å)		
Y—N3	2.296	2.340
Y—N4	2.317	2.369
Mulliken Charges		
Y	1.7763	1.8014
N	–0.4710	–0.5038
Orbital Populations		
Y 4*d*	1.0661	1.0021
N 2*s*	1.7583	1.7547
N 2*p*	3.6418	3.6776
SFO Gross Population (%)*		
HOMO (eV)	–4.121	–3.931
N–*p*	67.33	68.28
Y–*d*	21.88	23.38
LUMO (eV)	–2.698	–2.525
N–*p*	86.61	86.38
Y–*d*	8.13	8.10

*SFO = Symmetry Adapted Combination of Fragment Orbitals

4.3.2 Calculated Gd Exchange Coupling

The calculated values of *J* for $\{[(Me_3Si)_2N]_2(thf)Gd\}_2(N_2)$ and models $\{[(H_3Si)_2N]_2(Solv)Gd\}_2(N_2)$ with different solvent ligands are presented in Table 4.5.

For both geometries, calculations predict antiferromagnetic couplings that, while weak, are significantly stronger than that for the oxygen-bridged complexes. Caution is advisable in drawing quantitative conclusions since we see significant variations in computed *J* values when the geometric details of the structures are also varied. In addition, changes in the oxygen donors (H_2O, $O(Me)_2$, and THF) exert little effect on the computed *J* coupling constant. We are particularly interested in whether ligands with unpaired delocalized electrons might effectively couple lanthanide magnetic moments. With this in mind, we performed calculations for a 1-electron oxidized complex, $\{[(Me_3Si)_2N]_2(thf)Y\}_2(N_2)^{+1}$. There is, as yet, no experimental evidence for the existence of such species, so we performed a geometry optimization on the $N(SiH_3)_2$ derivative complex, then varied the solvent ligand, keeping the core structure fixed. Not surprisingly, upon oxidation the N–N distance shortened to 1.182 Å and the Y–N distances is lengthened to 2.602 Å and 2.560 Å. The computed distances in the latter are probably too long since they were too long in the neutral parent molecule. Replacing Y with Gd, the calculated *J* values for the different model structures are shown in Table 4.5. The results show that the compounds favor ferromagnetic exchange with much stronger coupling than for the neutral molecule. Again, changing solvent ligands yielded only slight changes in the magnitude of computed coupling constant. Previous researchers have correlated changes in exchange coupling constants with the basicity of nitrogen-containing terminal ligands in hydroxo-bridged copper (II) binuclear complexes, but from among the computational variations we've investigated, we find no

obvious correlations between the pK_a of the solvent molecules and magnetic couplings.[82, 193-196]

Table 4.5. Calculated exchange coupling constant (J/cm^{-1}) and Gd Mulliken populations for the complexes $\{[(R_3Si)_2N]_2(Solv)Gd\}_2(N_2)^n$ (R = Me, H) (n = 0, +1), with various solvent ligands.

Compound	***J*(cm^{-1})**	***s-d* Mulliken Populations**		
		P_{BS}[b]		P_{HS}[c]
		$\underline{4f^7\uparrow}$	$\underline{4f^7\downarrow}$[d]	$\underline{4f^7\uparrow}$
Experimental				
$[\{[(Me_3Si)_2N]_2(thf)Gd\}_2(N_2)]$	–0.112	0.142	0.142	0.132
$[\{[(H_3Si)_2N]_2(Solv)Gd\}_2(N_2)]$[a]				
OMe_2	–0.042	0.151	0.151	0.141
thf	–0.048	0.151	0.151	0.144
H_2O	–0.055	0.152	0.152	0.143
Geometry Optimization				
$[\{[(Me_3Si)_2N]_2(thf)Gd\}_2(N_2)]$	–0.129	0.143	0.143	0.133
$[\{[(H_3Si)_2N]_2(Solv)Gd\}_2(N_2)]$				
OMe_2	–0.188	0.153	0.153	0.142
thf	–0.203	0.154	0.154	0.142
H_2O	–0.207	0.155	0.155	0.143
1-Electron Oxidized Species				
$[\{[(H_3Si)_2N]_2(Solv)Gd\}_2(N_2)]^{+1}$				
OMe_2	2.74	0.196	0.054	0.197
thf	2.64	0.201	0.056	0.197
H_2O	2.95	0.200	0.060	0.197

[a] Uses an experimental distance for Si-H = 1.350 Å. Gd-OMe_2 and Gd-H_2O distances were determined from partial geometry optimizations varying only the Gd-Solv distance.
[b] P_{BS}: Summed 6*s* and 5*d* spin populations for the broken symmetry calculation, $|\uparrow_7,\downarrow_7\rangle$.
[c] P_{HS}: Summed 6*s* and 5*d* spin populations for the high spin calculation, $|\uparrow_7,\uparrow_7\rangle$.
[d] The spin polarizations have the same sign as their respective 4*f* electrons.

4.3.3 Interpretation of the Results

The $4f^7$-exchange field can be viewed, to a good approximation, as a kind of *contact* interaction — exerting its *direct* influence only on orbitals centered on the Gd atom. The valence 5*d* and 6*s* electrons penetrate to some extent into the atomic core, where they experience the effect of this exchange field. The more contracted 5*d* electrons penetrate to a greater extent than the 6*s* electrons, and consequently experience greater exchange interaction with the $4f^7$-core. This local character of the $4f^7$-exchange field suggests a simple perturbative molecular orbital (PMO) model can be used to model the perturbation that the $4f^7$ cores exert on electrons that reside in molecular orbitals with 5*d*-, and 6s-character – and thereby controls magnetic exchange couplings in polynuclear Gd compounds. We have previously outlined our perturbative model in Chapter II.

4.3.3.1 *d*-Electron Mediated Exchange

We can treat the Gd diazenido dimer model in the same spirit just described and adopt a simple *d*-metal-*p*-ligand bonding scheme to account for the frontier molecular orbitals of this bonding system. Shown in Figure 4.5 is a molecular orbital diagram for the Gd_2N_2 moiety. Only the Gd-N bonds are drawn; the MOs are given D_{2h} representation labels, though that symmetry is only approximate. Figure 4.6 shows a perturbative analysis using these Gd_2N_2 orbitals. ΔE represents the gap between the HOMO and the higher lying antibonding orbitals. Orbital plots shown in Figure 4.7

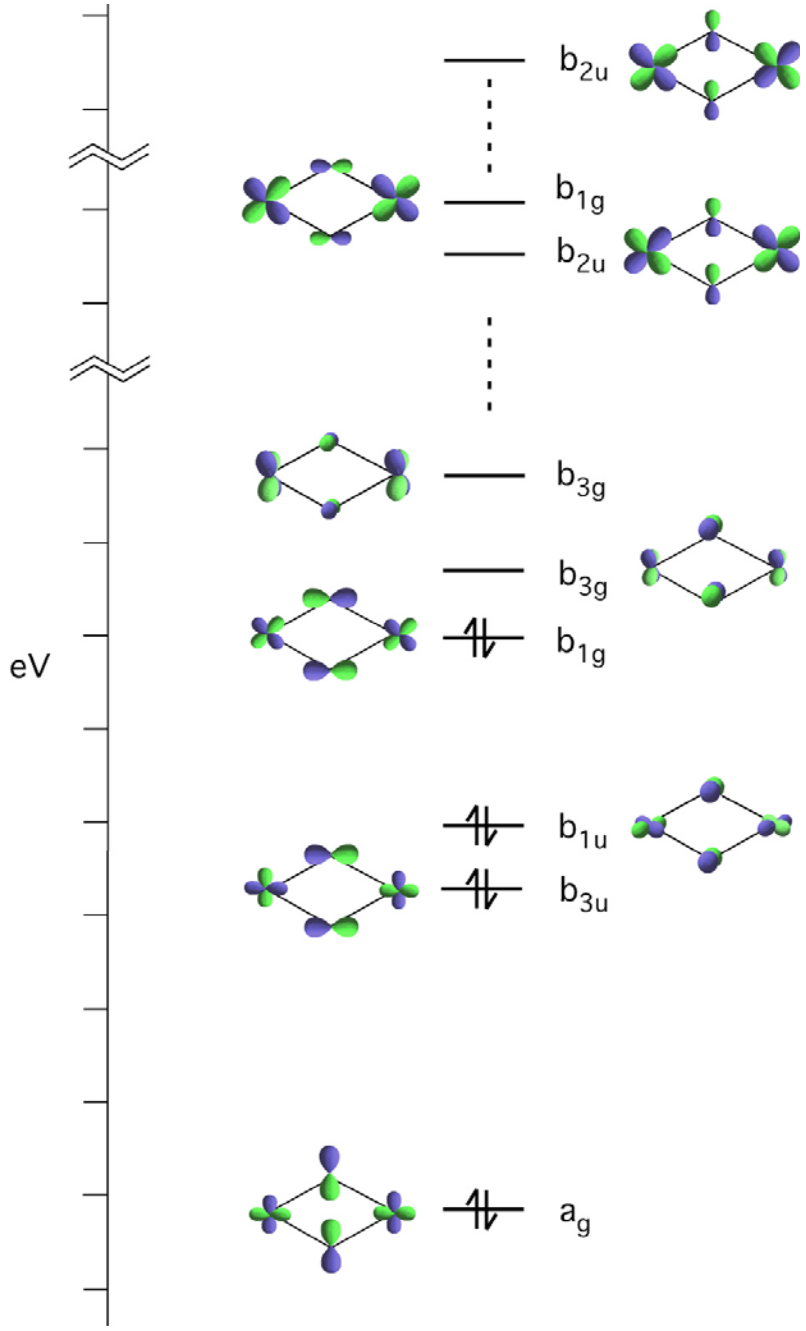

Figure 4.5. Molecular orbital diagram for the Gd_2N_2 moiety. Also shown are the pertinent unoccupied orbitals.

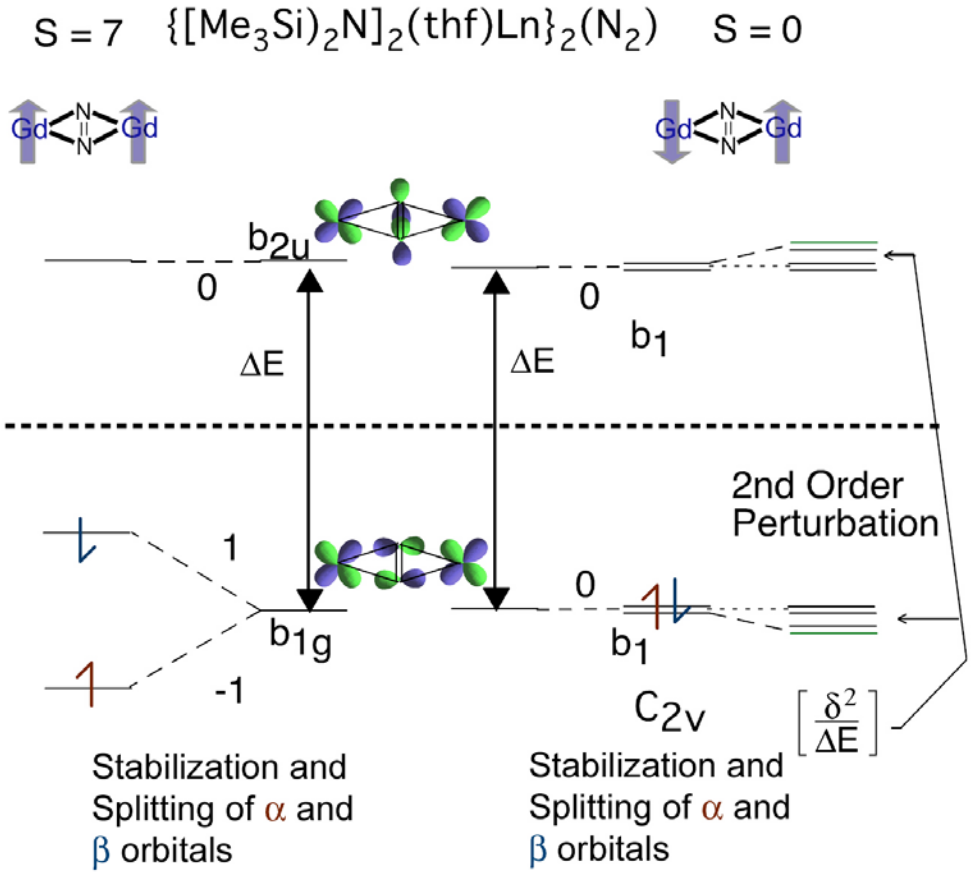

Figure 4.6. Treatment of the exchange interaction in $\{[(H_3Si)_2N]_2(thf)Gd\}_2(N_2)$ as a second-order perturbation to the system.

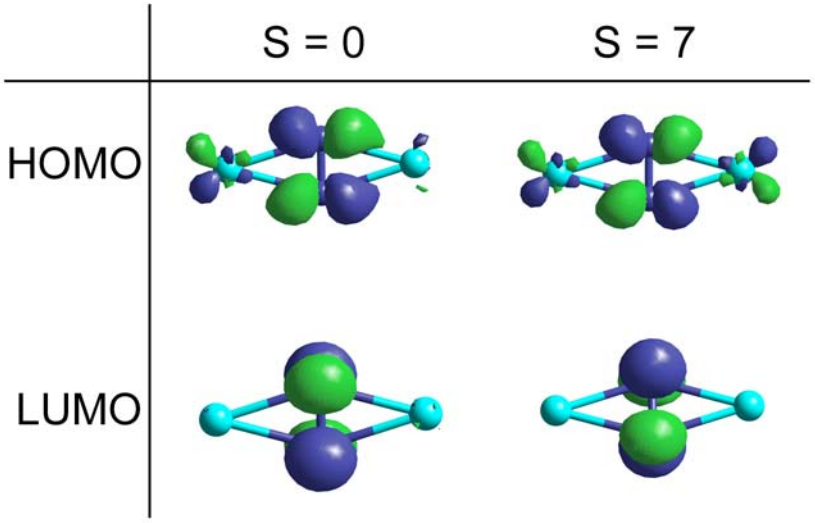

Figure 4.7. HOMO and LUMO orbital plots for $\{[(Me_3Si)_2N]_2(thf)Gd\}_2(N_2)$ S = 0 and S = 7 (disilylamide and THF ligands omitted for clarity).

clearly demonstrate that appreciable *d*-electronic character in the HOMO – underlining the plausibility of this treatment.

In the all-spin-aligned S = 7 case, the 4*f*-moments induce a 1st-order splitting the α- and β-spin molecular orbitals. Because the symmetry of the exchange potential felt by the Gd 5*d* and 6*s* electrons is unchanged, no 2nd order mixing occurs among orbitalsof different symmetry. When the 4*f*-moments are oppositely oriented, the exchange potential felt by the 5*d* and 6*s* electrons has a reduced (near-C_{2v}) symmetry. Mixing between the HOMO and frontier MO's is thereby induced, yielding a 2nd-order stabilization of both α and *β* spins (manifest in polarization of each electron toward its like spin $4f^7$ center).

The default expectation for a closed *d*-shell system is antiferromagnetic coupling because antiferromagnetic $4f^7$-spin patterns inherently *break orbital symmetry for each spin* and will mix unoccupied orbitals into the occupied orbitals of like spin, allowing for stabilization via spin polarization. Indeed, in any otherwise-closed-shell system, f^7 spin ordering that is effective at inducing 5*d*/6*s* spin-polarization will tend to have lower energy because such spin-polarization always reflects the fact that the delocalized electrons spend more time in the vicinity of like-spin *f*-electrons.

The one-electron oxidized case is clear cut: the unpaired delocalized electron is stabilized in first order with its spin aligned with both 4*f* moments, and the magnitude of the stabilization is much greater than seen for the second-order effects. The effects of polarization can be seen in the orbital plots on Figure 4.8 for the S = 15/2 spin state vs. the S = 1/2 spin pattern.

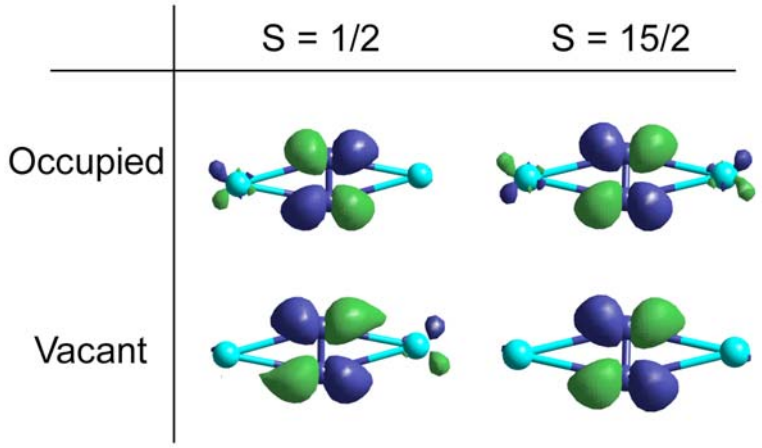

Figure 4.8. HOMO and LUMO orbital plots for $[\{[(Me_3Si)_2N]_2(thf)Gd\}_2(N_2)]^{1+}$ S = 1/2 and S = 15/2 (Gd and N atoms only shown for clarity).

4.3.3.2 Spin Density Distribution

The preceding analysis reveals a direct correlation between the sign and magnitude of the exchange coupling constant when examining the Mulliken spin densities on both the bridging atoms and the metal. It is instructive to examine the spin density distribution for the disilylamide Gd dimer complex (i.e., the local differences in α- and β-spin populations). The most relevant atomic spin densities obtained from our calculations are presented in Table 4.5. For both spin patterns, the 5*d* and 6*s* Gd spin polarizations mirror the spin orientations of $4f^7$ core for that atom — hence we have given only the polarization magnitudes in Table 4.5. We have combined 5*d* populations with 6*s* populations because they track with each other; the 6*s* polarization is consistently about 2.3 times smaller than the total 5*d* populations. The data in Table 4.5 confirm our perturbation-theoretic interpretation. For the closed-shell system, the symmetry-breaking antiferromagnetic pattern induces a much greater spin-polarization than is seen in the ferromagnetic case. In the one-electron case, the spin density shows that the unpaired spin is polarized to its like-spin gadolinium neighbor.

CHAPTER V

GADOLINIUM CLUSTER COMPOUNDS*

This chapter focuses on the theoretical investigations of the series of compounds $Gd(Gd_6ZI_{12})$ (Z = Co, Fe or Mn) [45], $CsGd(Gd_6CoI_{12})_2$,[197] $Gd(Gd_6ZI_{12})$ (Z = N, C, or B),[41] and the reduced clusters of $Gd_{10}X_{18}C_4$ (X = Cl, Br, or I).[152, 198-200] These solids are comprised of reduced gadolinium clusters that are cross-linked by halide bridges. In addition, we examine the discrete cluster $Gd_5(\mu_5\text{-}O)(\mu_3\text{-}OPr^i)_4(\mu\text{-}OPr^i)_4(OPr^i)_5$ and a theoretical model of $Gd_6(\mu_6\text{-}O)(\mu_3\text{-}OPr^i)_8(OPr^i)_6$, which show promise as discrete high-spin molecules.[201-203] Varying the electron counts allows us to investigate the effect that unpaired delocalized electrons have on magnetic coupling within the clusters.

5.1 $Gd[Gd_6ZI_{12}]$

The rhombohedral $R[R_6ZX_{12}]$ structure ($R\bar{3}$ or $R3$) has been determined for R = Sc, Y and many of the lanthanides where X = Cl, Br, or I and Z = main group or transition metal element. [45, 204-207] We have focused on the Gd-containing clusters, $Gd[Gd_6ZI_{12}]$ because of these compounds offer a range of cluster electron counts, minimal anisotropy, and well understood magnetic description. There is one cluster per cell (Figure 5.1); all 12 Gd-Gd edges of the cluster are bridged by one of two

*Reproduced in part with permission from Journal of the American Chemical Society, accepted for publication. Unpublished work copyright 2006 American Chemical Society.

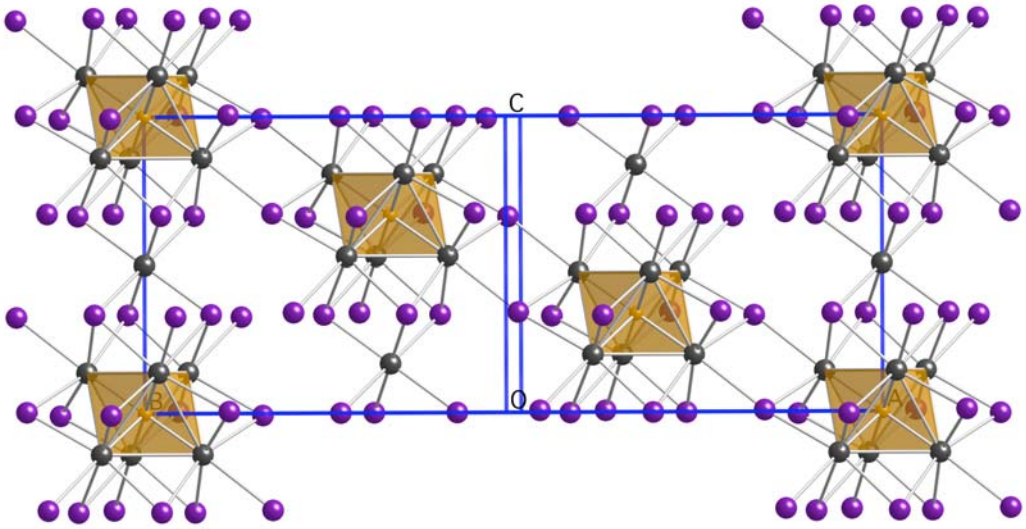

Figure 5.1. Perspective view of the [110] plane of $Ln[Ln_6ZI_{12}]$ in a hexagonal setting. The shaded clusters represent the Ln_6Z units.

crystallographically distinct iodide atoms. Six iodine atoms bridge the "waist" edges of each Gd_6 octahedron and simultaneously form exo bonds to metal vertices of adjacent clusters ($X^{i\text{-}a}$). The other six halide atoms bridge Gd-Gd edges at the "top" and "bottom" triangular faces of the Gd_6 trigonal antiprism (I^i). The seventh Gd atom, located midway between the $(Gd_6Z)I_{12}$ clusters along the *c* axis, binds to six I^i atoms that form a trigonal antiprism. Because it does not participate in metal-metal bonding, it can be regarded as Gd^{III} ion. Using the established notation, the structures are thus described as $Gd^{3+}[Gd_6Z(I^i)_6(I^{i\text{-}a})_{6/2}(I^{a\text{-}i})_{6/2}]^{3-}$ where *a* and *i* refer to ausser or axial and inner or bridging ligands. In the centric ($R\bar{3}$) structures, the symmetry of the Gd_6ZI_{12} clusters

deviates very slightly from D_{3d} and the departure from octahedral symmetry is small enough that an O_h approximation is still useful in discussing their electronic structure.

Compounds of the R[R_6ZI_{12}] structure type are versatile in that they incorporate a variety of interstitial elements (Z), including several of the metals of Groups 7–11 and the main group atoms B, C, N.[41, 45, 204, 205] Interstitials are essential to the formation and stability of these clusters; formally, they provide electrons to the electron-deficient R_6 cage, but more importantly, the R–Z bonding is undoubtedly much stronger than the R–R bonding. The electronic structure of these clusters has been discussed many times, but we will briefly review it here in order to place magnetic results in context.[208] Figure 5.2 shows a molecular orbital diagram for the [Gd_6ZX_{12}] clusters where Z is a transition metal (left) and a main group element (right); levels that have predominately Gd 5*d* character are displayed. In O_h symmetry, first-row transition metal interstitial t_{2g}/e_g (3*d*) and a_{1g} (4*s*) orbitals interact with the cluster orbitals of like symmetry to form bonds with the surrounding Gd cluster (the 4*p*-t_{1u} orbitals are less important). The highest occupied t_{1u} orbital **(5.1)** is predominantly delocalized over the Gd_6 cage and is only slightly stabilized by a small contribution of Z-atom 4*p* orbitals. Likewise, main group interstitial t_{1u} (2*p*) and a_{1g} (2*s*) orbitals will form bonds with the Gd cluster, leaving the t_{2g} orbital **(5.1)** as the highest occupied orbital. The electronic requirements for the Gd_6Z octahedron is illustrated in Figure 5.2, which yields a closed-shell cluster-based-electron count of 18 (14) for a transition metal (main group) atom. The optimal bonding configuration is achieved when Z = Co (N), such as in the compound Gd[Gd_6CoI_{12}] (Gd[Gd_6NI_{12}]), and the HOMO is fully occupied with a t_{1u}^6 (t_{2g}^6) configuration.

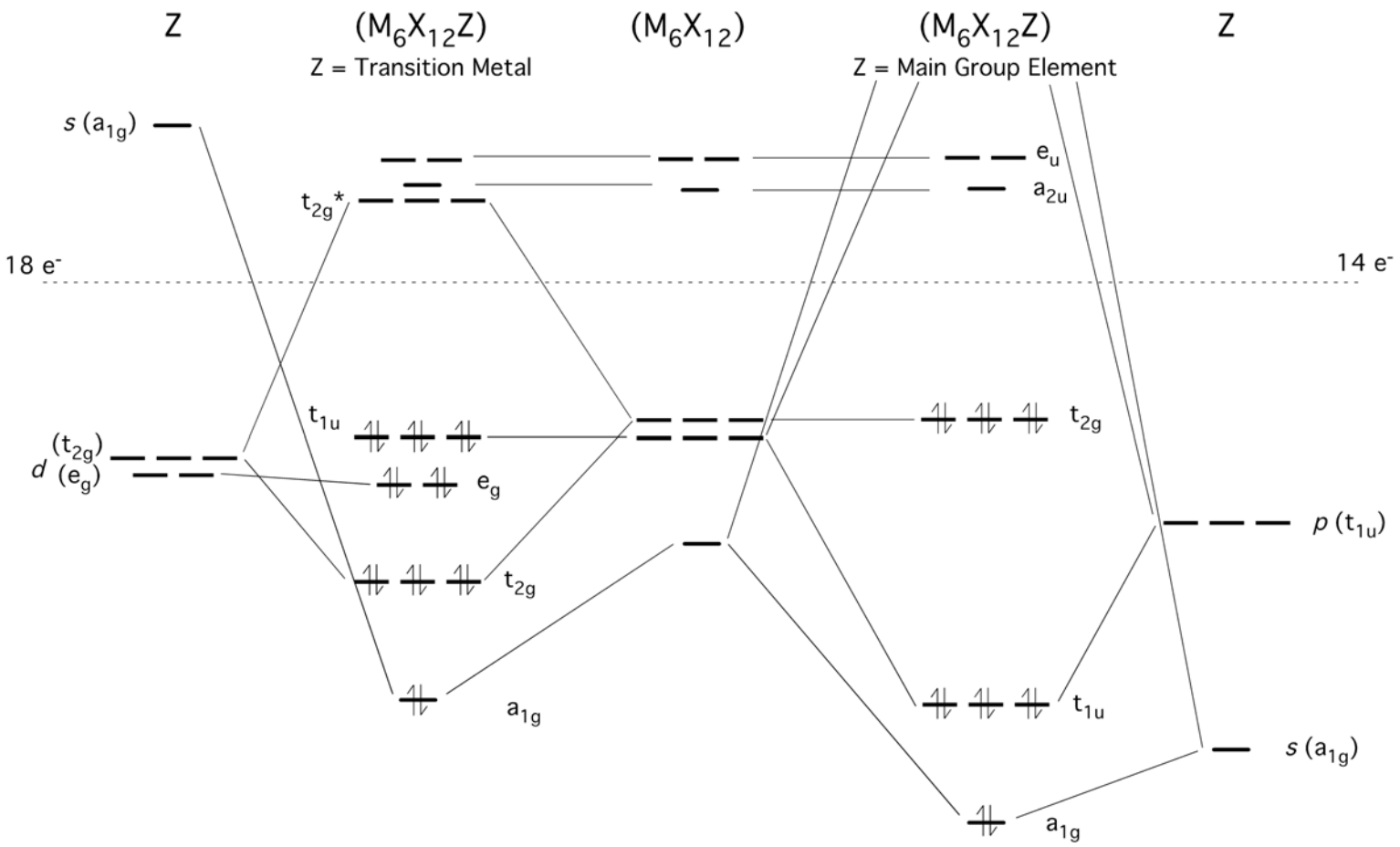

Figure 5.2. Schematic orbital interaction diagram of M_6X_{12} octahedral clusters with a transition metal element (left) and a main group element (right) as the interstitial atom. The electronic configurations shown are those for 18 CBEs (left) and 14 CBEs (right).

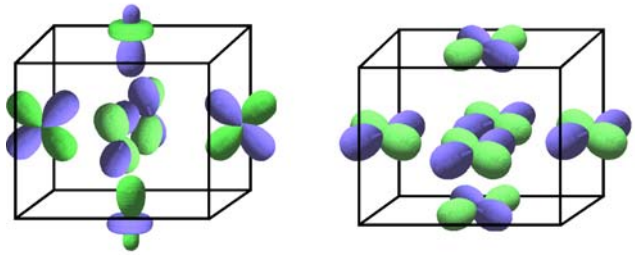

5.1

5.1.1 Gd[Gd_6ZI_{12}] (Z = Co, Fe, Mn)

Our research lab has measured the magnetic susceptibilities of Gd-containing clusters with transition metal interstitial atoms, Gd[Gd_6ZI_{12}] (Z = Co, Fe, and Mn), and have determined single crystal structures of these compounds in order to establish structural details-which may in turn have an effect on the electronic and magnetic properties. The synthesis of these compounds consists of combining stoichiometric proportions of GdI_3, ZI_2 (Z = Co, Fe, Mn) and Gd metal in a Nb tube outfitted with a silica jacket and heated to 850°C for 16 days. Figure 5.3 depicts the χT vs T plot for Gd[Gd_6ZI_{12}] (Z = Co, Fe, Mn) and CsGd[Gd_6CoI_{12}]$_2$. In summary, $[Gd_6CoI_{12}]^{3-}$ exhibits approximate Curie-Weiss behavior (when subtracting the structurally isolated Curie-like Gd^{III} contribution) and is most closely consistent with that of independent spins on the Gd atom. The $[Gd_6FeI_{12}]^{3-}$ and $[Gd_6MnI_{12}]^{3-}$ systems possess one and two unpaired electrons, respectively, and the effective magnetic moment per cluster unit is significantly increased at high temperatures in comparison with the Co centered

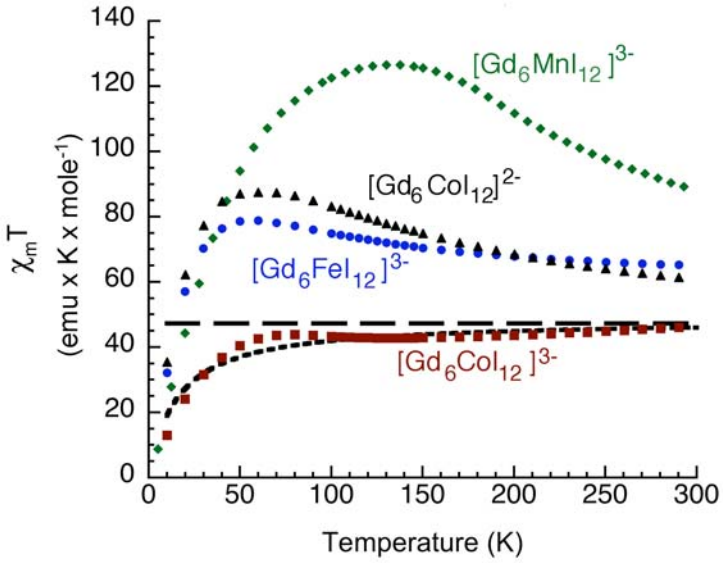

Figure 5.3. $\chi_m T$ vs. T for $Gd(Gd_6CoI_{12})$, $Gd(Gd_6FeI_{12})$, $Gd(Gd_6MnI_{12})$ and $CsGd(Gd_6CoI_{12})_2$ at a 3.5 Tesla applied field. $\chi_m(Gd^{III})$ was subtracted from data for $CsGd(Gd_6CoI_{12})_2$ and the resultant was divided by two to yield a per cluster susceptibility for $[Gd_6CoI_{12}]^{2-}$. The Curie constant (47.25 emu K mol^{-1}) for an "ideal" cluster with six uncoupled Gd^{III} centers (S = 7/2; g = 2) is shown as the long-dashed line. The Curie-Weiss fit to $[Gd_6CoI_{12}]^{3-}$ is shown as the short-dashed line. [209]

compound. Then at low temperatures, the susceptibility for $[Gd_6ZI_{12}]^{3-}$ (Z = Fe, Mn) is suppressed.[209] The increase at high temperatures can be attributed to relatively strong exchange interactions between the unpaired electrons in the HOMO and the electrons in the 4*f* orbitals, as we will discuss below. Since the clusters in these compounds are not structurally isolated, we should also expect intercluster coupling to exert an important effect on these compounds' magnetic properties.

5.1.1.1 Model Description

It is instructive to first turn our attention to the strong *intra*cluster magnetic coupling in clusters of this type. We investigated the model $[Gd_6CoI_{12}](OPH_3)_6$ as shown in Figure 5.4 (Model A). The model retains the $[Gd_6FeI_{12}]^{3-}$ cluster core structure, but possesses a half-filled t_{1u}^3 HOMO configuration. The use of a half-filled t_{1u} subshell allows us to avoid computational complications that arise when one attempts to obtain a converged density with an orbitally degenerate cluster bonding configuration.[210]

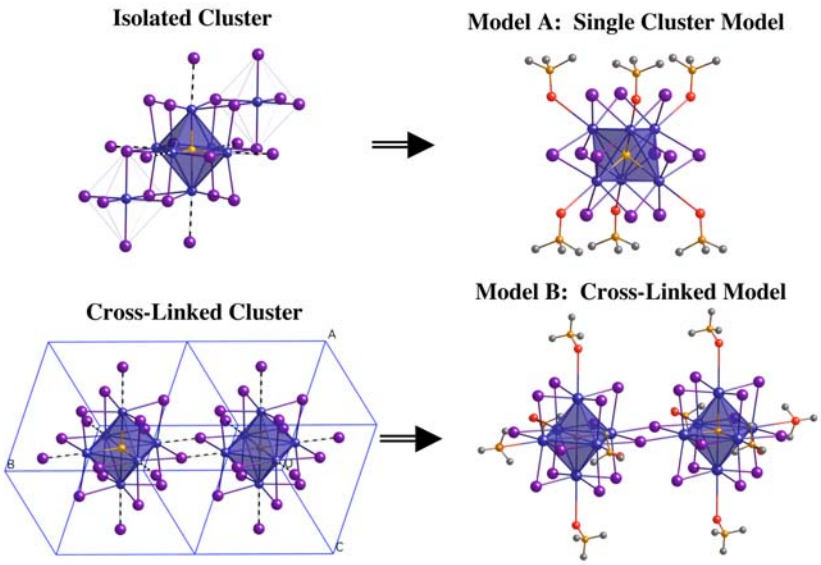

Figure 5.4. Relationship between the single cluster model (A) and cross-linked cluster model (B) and the parent $Gd[Gd_6ZI_{12}]$ structure.

Phosphine oxide ligands are used to fill the coordination sites provided by the Gd–I contacts lost upon separating the clusters and avoid unphysical charge density

accumulation obtained when anionic capping ligands are used. These ligands are also a logical choice from a synthetic point of view since they readily coordinate to rare earth atoms.[211] A model system in which two clusters are crosslinked was constructed in the same spirit as the single-cluster model and results from calculations should provide an estimate for the magnitude of the *inter*molecular interactions that occur in the solid state (Model B in Figure 5.4). The two-cluster model maintains the clusters' solid state structure and phosphine oxide ligands again serve as terminating ligands. Partial geometry optimizations for the positions of the phosphine oxides were performed using an analogous yttrium model systems, $[Y_6CoI_{12}](OPH_3)_6$ and $[Y_6CoI_{12}]_2(OPH_3)_{10}$, resulting in structures with D_{3d} and C_i symmetries, respectively. In calculations probing the manner in which the unpaired cluster bonding electrons (CBEs) mediate the coupling of the $4f^7$-moments, we have restricted our attention to the ground state, $^4A_{1u}$, from the t_{1u}^3 (CBE) configuration.

5.1.1.2 Magnetic Coupling in $[Gd_6CoI_{12}](OPH_3)_6$

We carried out electronic structure calculations for 20 competing spin patterns on the single cluster model, but shall focus our attention the cases where electrons in the three (5*d* character) electrons in the HOMO are all spin-up (i.e., $S = M_S = 3/2$). The calculated energies for those 10 patterns are shown in Figure 5.5.[212] In each case, we also indicate the symmetry of the potential that the 4*f* spin-patterns impose on the valence electrons. Since the DFT calculations underestimate magnitude of the $4f^7$-5*d* exchange interaction for the Gd atom by ~11% (Chapter III), and because the exchange

interactions in these molecular cases have their origin in the same intra-atomic $4f^7$-5*d* exchange interaction, it is reasonable to assume that the spin pattern energy differences calculated here are underestimated by a similar margin.

The results from single cluster calculations indicate a remarkably strong preference for ferromagnetic coupling within the cluster. The lowest energy calculated spin pattern is that with all of the 4*f* spins aligned parallel to the three spin-up valence CBEs. Figure 5.5 shows that if the Gd 4*f* moments are successively "flipped" over, the energy increases in incremental steps of ~1480 cm^{-1} (range: 1380–1600 cm^{-1}) for each opposing Gd moment. The spatial relationship between flipped moments has little direct effect; energy differences between *cis*- and *trans*- (C_{2v} and D_{4h}) or between *fac*- and *mer*- (C_{3v} and C_{2v}) spin patterns differ by less than 10 cm^{-1}.

We have previously demonstrated the effectiveness of using a perturbative molecular orbital (PMO) model which describes the perturbation that the $4f^7$ exchange field exerts on electrons in molecular orbitals with 5*d*- and 6*s*-character to interpret 5*d*/6*s*-electron-mediated *f-f* exchange.[213-215] Applying this approach to the model compound $Gd_6CoI_{12}(OPH_3)_6$, we now turn our attention to the cluster MOs shown in Figure 5.6. In our analysis, we compare two cases: The potential exerted by the six Gd $4f^7$ moments possessing O_h symmetry (all 4*f* moments aligned) and the case of flipping two *trans*-$4f^7$ moments which imposes a spin-dependent D_{4h} symmetry potential on the CBEs (using local symmetry of the cluster). Orbital plots clearly demonstrate that the three unpaired CBEs reside in a delocalized t_{1u} orbital (Figure 5.7). The $4f^7$ moment ordering induces a first-order splitting into α- and β-spin molecular orbitals, but no

Label, Pseudosymmetry, Relative SDFT Energy	Spin Patterns	Label, Pseudosymmetry, Relative SDFT Energy	Spin Patterns
S = 39/2, O_h 8892.0 cm^{-1}		S = 3/2, C_{2v} 4246.4 cm^{-1}	
S = 25/2, C_{4v} 7291.1 cm^{-1}		S = 17/2, C_{2v} 2797.1 cm^{-1}	
S = 11/2, C_{2v} 5747.6 cm^{-1}	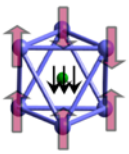	S = 17/2, D_{4h} 2787.1 cm^{-1}	
S = 11/2, D_{4h} 5747.0 cm^{-1}		S = 31/2, C_{4v} 1380.5 cm^{-1}	
S = 3/2, C_{3v} 4252.7 cm^{-1}	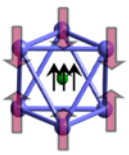	S = 45/2, O_h 0.0 cm^{-1}	

Figure 5.5. 10 spin patterns and energies for the model $[Gd_6CoI_{12}](OPH_3)_6$.

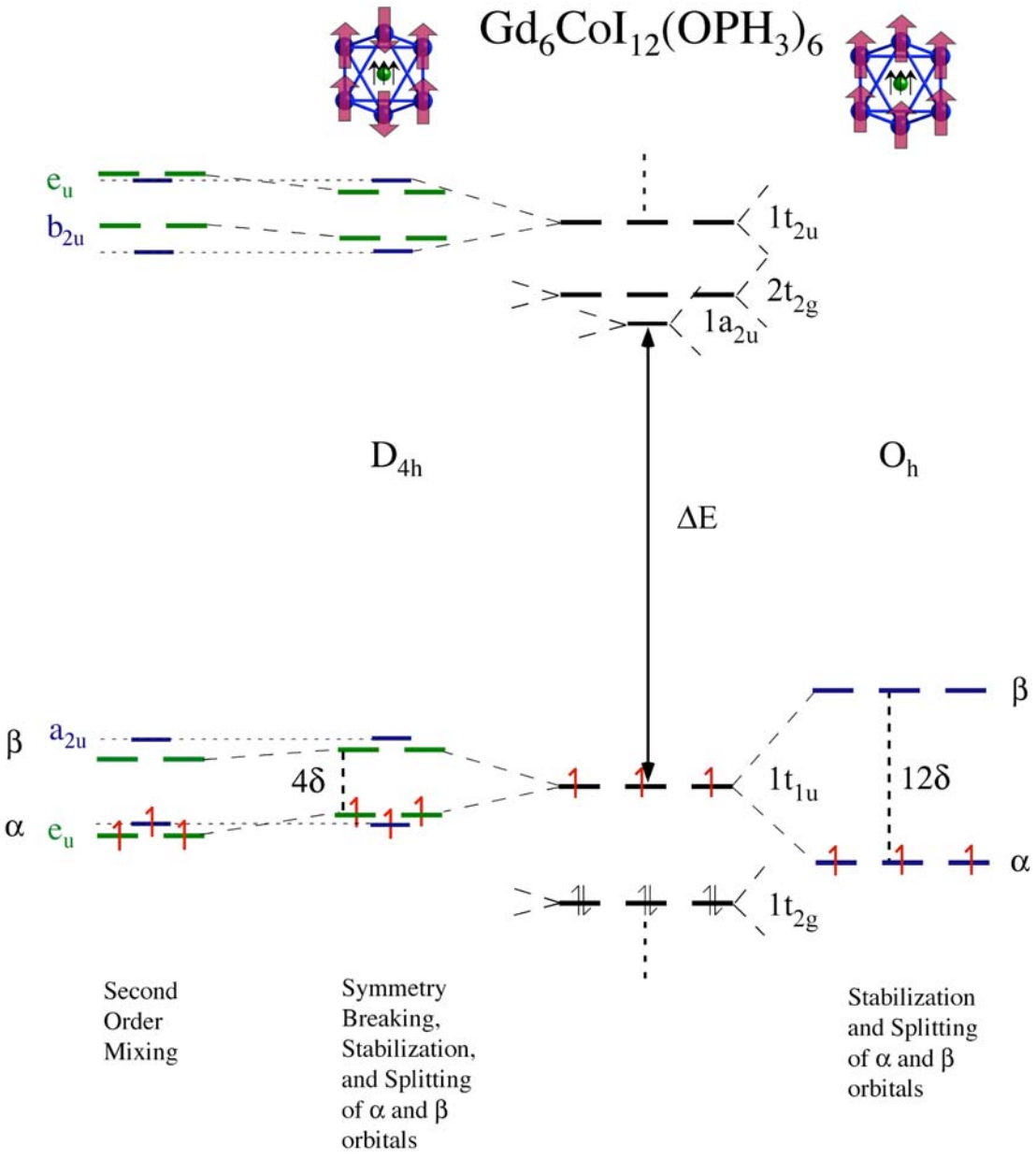

Figure 5.6. Perturbative analysis of *d*-electron mediated *f-f* exchange for the $Gd_6I_{12}Co(OPH_3)_6$ model.

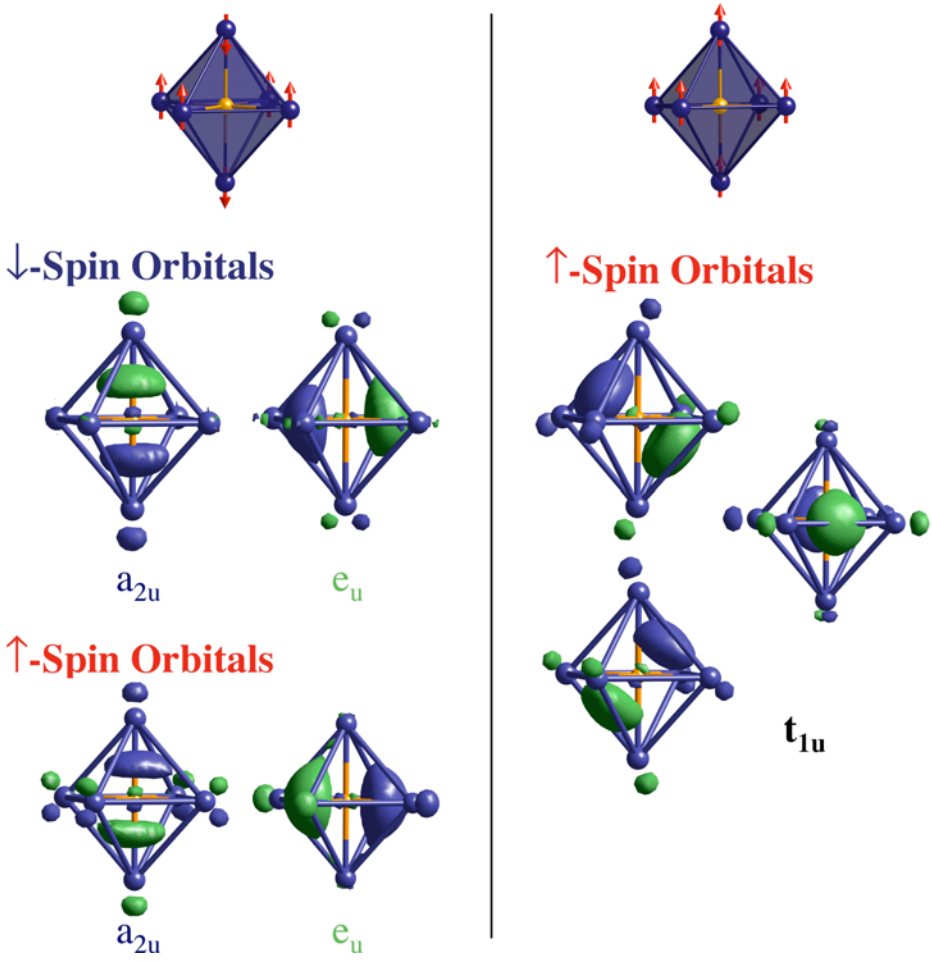

Figure 5.7. Molecular orbital plots for the D_{4h} and O_h model of $Gd_6I_{12}Co(OPH_3)_6$.

symmetry breaking occurs since the exchange potential maintains symmetry. In the O_h cluster, the first-order splitting induced by the exchange perturbation yields a maximum possible stabilization for the three unpaired electrons. Second-order effects are minimal since only energetically distant cluster orbitals of t_{1u} symmetry can "rehybridize" to alter the form of the HOMO. First-order effects on the D_{4h} cluster will also stabilize the CBEs in the HOMO, but to a lesser extent, since those electrons are relatively destabilized by the two gadolinium atoms with opposed-spin 4*f* moments. The exchange perturbation lowers the symmetry and some mixing between the bonding and antibonding MOs is induced, yielding a second-order stabilization of both the α and β spin-orbitals. However, these second order effects are not strong enough to lower the energy of the system very much.

One can construct a simple coupling model to account for the calculated relative energies of the spin-patterns (Table 5.1). Given that energy differences between 10 spin-patterns is almost wholly dependent on the number of flipped $4f^7$ moments – and not their stereochemistry, we can evaluate the exchange coupling constants by assuming that the gadolinium moments communicate solely through the Co interstitial atom with a single *J* value of +137.96 (0.93) cm^{-1}. The Hamiltonian associated with this calculated *J* value is simple:

$$\hat{H} = -J\sum_{i=1}^{6} S_{Gd}S_{Co} \qquad S_{Gd} = \frac{7}{2};\ S_{Co} = \frac{3}{2} \tag{5.1}$$

Table 5.1. Possible equations used in calculating Heisenberg coupling constants (*J*'s) for $Gd_6CoI_{12}(OPH_3)_6$.

$\Delta E_{A\text{-}S=45/2}$	$\sum_{i,j} Z_{i,j} J_{i,j}$	DFT Energy Difference (cm^{-1})	Heisenberg Energy Difference (cm^{-1})
$\Delta E_{S=31/2\text{-}S=45/2}$	$2J_1$	1380.5	1448.6
$\Delta E_{S=17/2(D_{4h})\text{-}S=45/2}$	$4J_1$	2787.1	2897.2
$\Delta E_{S=17/2(C_{2v})\text{-}S=45/2}$	$4J_1$	2797.1	2897.2
$\Delta E_{S=3/2(C_{2v})\text{-}S=45/2}$	$6J_1$	4246.4	4345.8
$\Delta E_{S=3/2(C_{3v})\text{-}S=45/2}$	$6J_1$	4252.7	4345.8
$\Delta E_{S=11/2(D_{4h})\text{-}S=45/2}$	$8J_1$	5747.0	5794.4
$\Delta E_{S=11/2(C_{2v})\text{-}S=45/2}$	$8J_1$	5747.6	5794.4
$\Delta E_{S=25/2\text{-}S=45/2}$	$10J_1$	7291.1	7243.0
$\Delta E_{S=39/2\text{-}S=45/2}$	$12J_1$	8892.0	8691.6

This reproduces the trends in the calculated energies and predicts strong ferromagnetic coupling between the Gd centers through the Co "bridge" (Figure 5.8), but it is not to be taken seriously insofar as the "Co" is concerned. The delocalized unpaired t_{1u} electrons have a limited amount of cobalt character, as we shall discuss below.

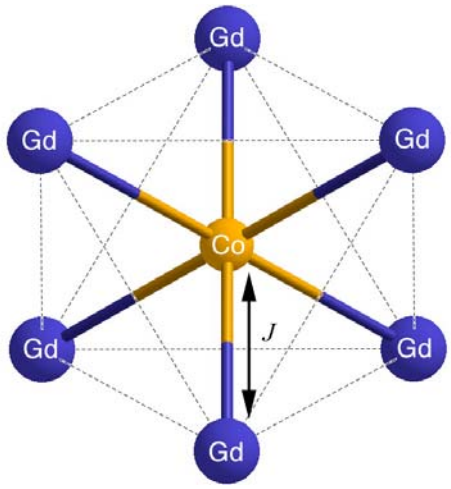

Figure 5.8. Provisional Heisenberg coupling constant for $Gd_6I_{12}Co(OPH_3)_6$.

From our previous work on the Gd atom, we might expect the energy difference between the high-symmetry state (S = 45/2) and the next lowest state (S = 31/2) to be approximately one-half the energy difference between the ^{9}D and ^{7}D for the Gd atom, assuming that the three unpaired metal-metal bonding electrons are delocalized in 5*d*-orbitals spread equally over six Gd atoms. Instead, the energy difference is approximately one fourth that of the ^{9}D – ^{7}D difference. While it is difficult to pinpoint the origin of the "discrepancy", the Co interstitial atom has appreciable spin density in the HOMO, as seen in the Mulliken populations in Table 5.2. The Co 4*p* orbital spin density increases upon successive "flipping" of the 4*f* moments. The symmetry breaking patterns all induce much greater spin polarizations and the Co 4*p* mixing helps the HOMO electrons to avoid the opposed-spin Gd atoms. Also, the Gd 6*s* character increases in the t_{1u}–type orbitals for successive spin patterns. The more 6*s* character will reduce the coupling because the 6*s*-4*f* exchange is ~75% less than the 5*d*-4*f* exchange.

Table 5.2. Magnitudes of Co 4*p* and Gd 5*d* and 6*s* spin populations for $Gd_6CoI_{12}(OPH_3)_6$. All values are computed with precision within ±0.002.

Spin Pattern	P_{Co}	P_{Gd} ($4f\uparrow$)[a]		P_{Gd} ($4f\downarrow$)		Relative Energy (cm^{-1})
	4*p*	5*d*	6*s*	5*d*	6*s*	
S = 45/2	0.495	0.468	0.087	---	---	0
S = 31/2	0.500	0.468	0.091	-0.197	-0.028	1380.5
S = 17/2, D_{4h}	0.506	0.468	0.095	-0.205	-0.026	2787.1
S = 17/2, C_{2v}	0.506	0.479	0.092	-0.191	-0.028	2797.1
S = 3/2, C_{2v}	0.514	0.468	0.099	-0.201	-0.029	4246.4
S = 3/2, C_{3v}	0.513	0.479	0.096	-0.186	-0.032	4252.7
S = 11/2, D_{4h}	0.522	-0.198	-0.033	0.470	0.103	5747.0
S = 11/2, C_{2v}	0.522	-0.197	-0.033	0.482	0.100	5747.6
S = 25/2	0.533	-0.194	-0.038	0.486	0.104	7291.1
S = 39/2	0.545	-0.194	-0.042	---	---	8892.0

[a] Positive spin populations have the same sign as their respective 4*f* moments.

5.1.1.3 Magnetic Coupling in $(Gd_6CoI_{12})_2(OPH_3)_{10}$

In order to determine *inter*cluster coupling effects, we performed two calculations using the model $(Gd_6CoI_{12})_2(OPH_3)_{10}$, which maintains the *inter*cluster bonding found in the solid state compound. Since the difference between the ferromagnetically coupled single cluster and the next lowest spin state was ~1400cm^{-1}, we only considered the cross-linked models that contain *intra*cluster ferromagnetic coupling, assuming all other configurations will be much higher in energy. Figure 5.9

illustrates the energy difference between S = 45 and S = 0 in our cross-linked cluster model, which 50 times lower than of the single cluster.

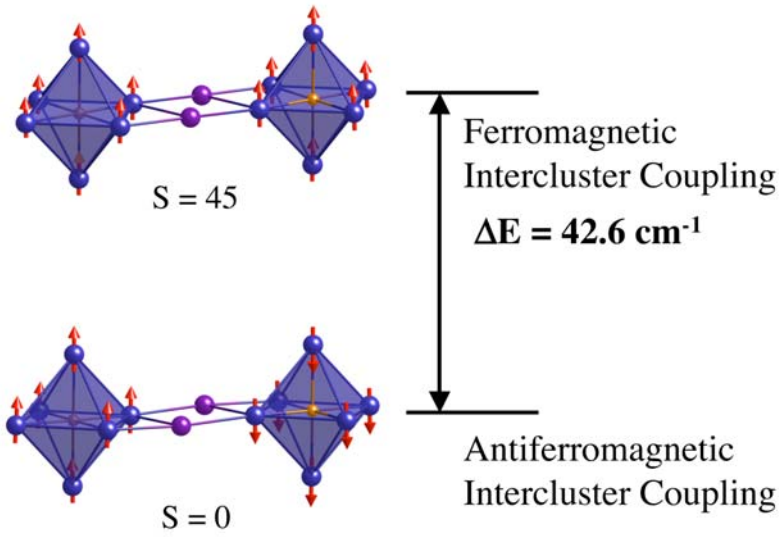

Figure 5.9. Energy difference between S = 0 and S = 45 for the cross-linked model.

The most important aspect of this result is a preference for antiferromagnetic coupling between clusters at low energy. We can evaluate the exchange coupling constants by assuming that the gadolinium clusters communicate through the iodide bridges with a single J value. The associated Hamiltonian is:

$$\hat{H} = -JS_{Cluster1}S_{Cluster2} \qquad S_{Cluster1} = S_{Cluster2} = \frac{45}{2} \tag{5.2}$$

and the magnetic coupling constant is calculated to be –0.084 cm^{-1}; indicating relatively *weak* antiferromagnetic coupling between the Gd centers through the iodide bridges.

5.1.2 $CsGd[Gd_6CoI_{12}]_2$

The structure of $CsGd(Gd_6CoI_{12})_2$, recently synthesized in our group, is a cubic and well described as an intergrowth of $Gd(Gd_6CoI_{12})$ and $Cs(Er_6CI_{12})$ types (Figure 5.10).[45, 216] The clusters in $CsGd(Gd_6CoI_{12})_2$ possess 17 electrons for metal-metal

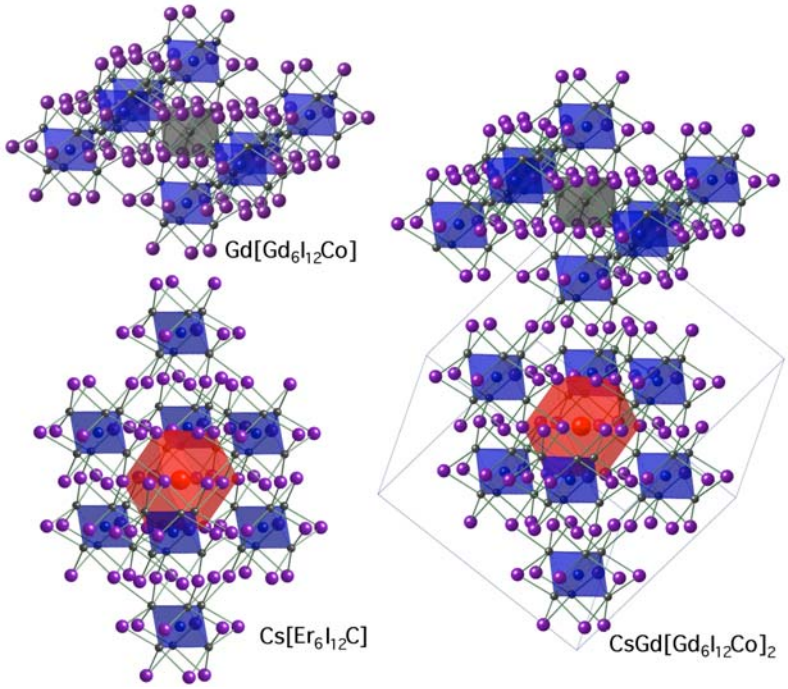

Figure 5.10. Illustration of the intergrowth of $Gd[Gd_6CoI_{12}]$ and $Cs[Er_6CI_{12}]$ (left) to form $CsGd[Gd_6CoI_{12}]_2$ (right). (Crystal structure courtesy of Luke Sweet). The cuboctahedron at (0.5, 0.5, 0.5) is a CsI_{12} coordination polyhedron and octahedron at (0, 0, 0) is $Gd^{III}I_6$.

bonding, and this compound therefore offers a useful control for our implicit hypothesis concerning the influence of open-5*d*-shell character on the magnetic properties of these compounds. Although these clusters are Co-centered (as in $Gd(Gd_6CoI_{12})$), the clusters

are isoelectronic to the Fe-centered clusters in $Gd(Gd_6FeI_{12})$. The magnetic susceptibility plot for $CsGd[Gd_6CoI_{12}]_2$ is similar to that for $Gd(Gd_6FeI_{12})$, with the downturn we have attributed to intercluster antiferromagnetic coupling occurring at a slightly higher temperature than for $Gd(Gd_6FeI_{12})$. Theoretical calculations have been performed on the yttrium-containing compound, $CsY(Y_6CoI_{12})_2$, using the EHTB method.[217] While it would be instructive to study the Gd-containing solid using our spin pattern approach using DFT, it is difficult to achieve SCF convergence on the yttrium analog because of the large number of atoms in the unit cell (160 atoms). In order to compare EHTB results, we also performed calculations on its closest match, $Y(Y_6FeI_{12})$, a 17-electron cluster system DOS results for $Y(Y_6FeI_{12})$ and $CsY(Y_6CoI_{12})_2$ are depicted in Figure 5.11. The intercluster linking of the two compounds is responsible for the similar ~0.3 eV bandwidth at the Fermi level except that the t_{1u} band is doubly peaked in $CsY[Y_6CoI_{12}]_2$. The Fermi level cuts through the band and the bandwidth may be large enough that these compounds would be conductors. Shown in Figure 5.12 is the band dispersion plot for $CsY(Y_6CoI_{12})_2$. The widening of this band in Gd-containing analogs should weaken the otherwise very strong ferromagnetic coupling that we have predicted for a truly discrete $Gd_6ZI_{12}^{n-}$ cluster with a t_{1u}^3 configuration because the coupling is maximized for the $^4A_{1u}$ ground state. Achieving that state in a crosslinked solid requires that the t_{1u} electrons be unpaired over the entire band and thus entails an effective “promotion energy” cost.

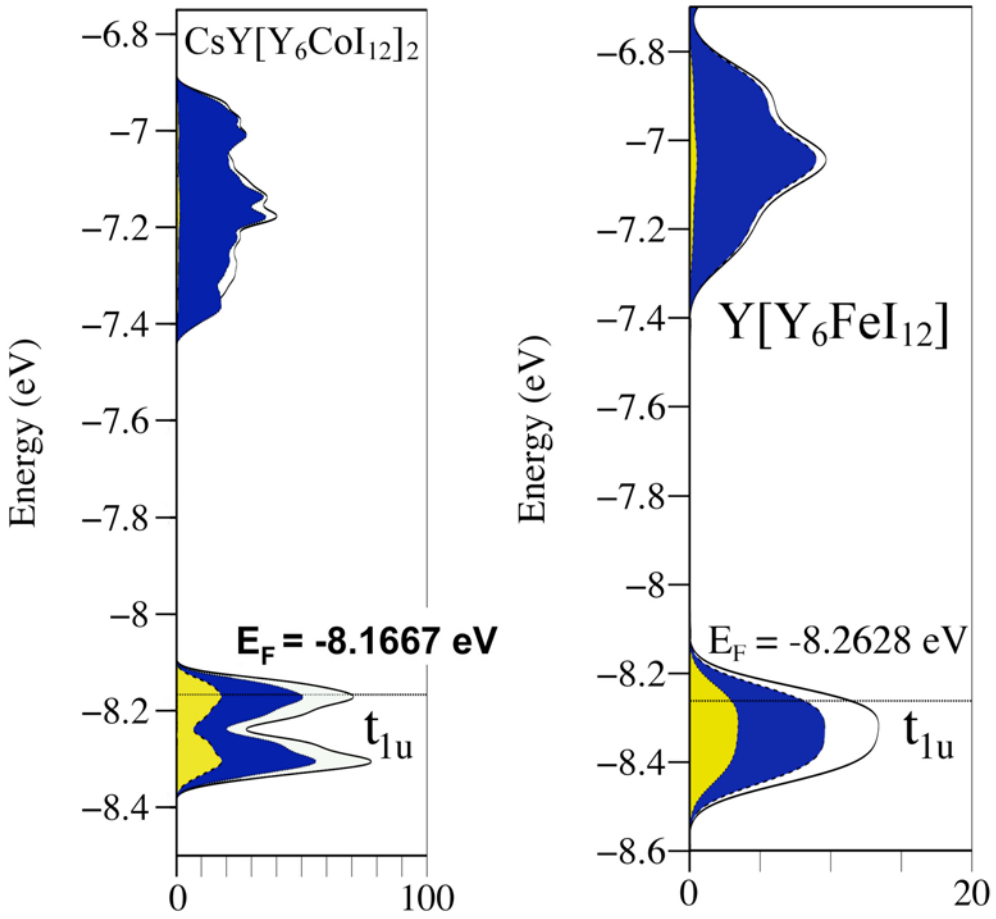

Figure 5.11. DOS plots for $CsY[Y_6CoI_{12}]_2$ and $Y[Y_6FeI_{12}]$ using EHTB for the energy range bracketing the Fermi level. Y_6 projected DOS depicted in blue (dark gray), Co/Fe projected DOS depicted in yellow (light gray).

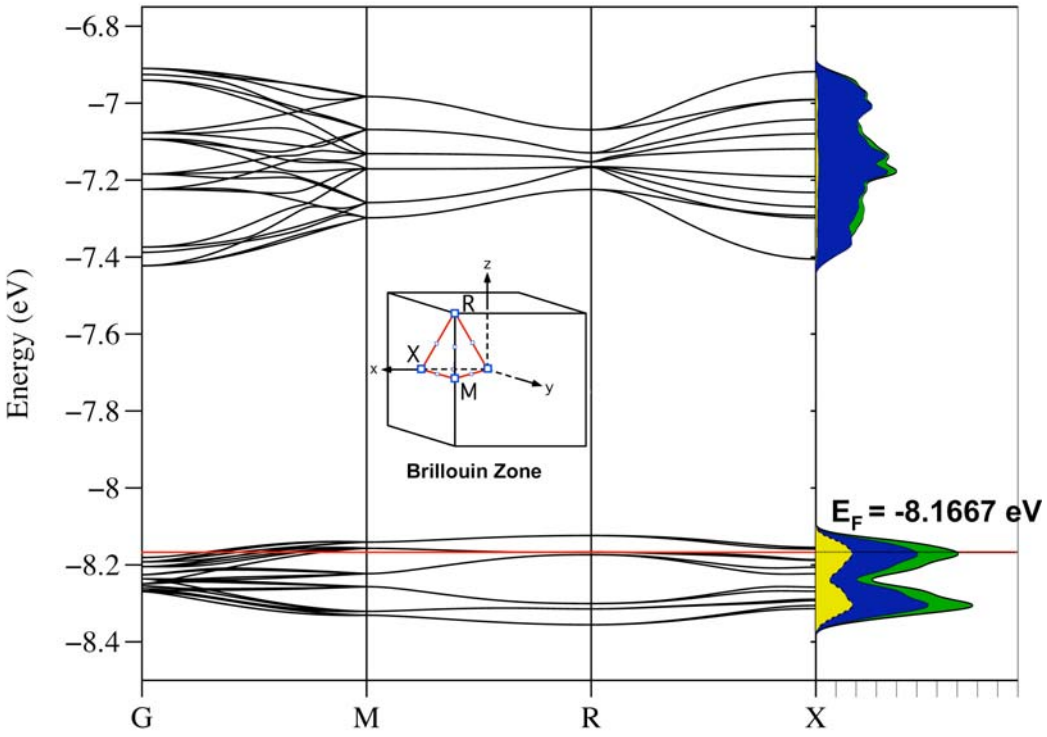

Figure 5.12. Band dispersion plot and DOS near the Fermi level for $CsY(Y_6CoI_{12})_2$.

5.1.3 $Gd[Gd_6ZI_{12}]$ (Z = B, C, N)

A natural extension of previous computational work is the study of $[R_6Z]$ clusters centered by main group atoms (Z = B, C, N). The identity of the interstitial atom Z is intimately related to the valence electron deficiency ('holes' in the HOMO and magnetic properties of the clusters, as discussed for the interstitial transition metal atom case. Insertion of Z into the empty cluster does not change the net number of bonding MO's but does add additional electrons and stabilizes MOs that would otherwise be involved in R-R bonding. The electronic requirements for a single metal-metal bonded octahedron with main group interstitials leads to optimal CBE count of 14, corresponding to a closed-shell configuration. The number of valence electrons available for metal-metal bonding for B, C, and N are 12, 13, and 14 e^-, respectively, for $Gd[Gd_6ZI_{12}]$. According to our description of transition metal-centered clusters, we would expect the nitrogen-containing cluster to exhibit Curie-Weiss behavior at high temperatures and then antiferromagnetic coupling. For open-shell configurations, we expect *intra*molecular ferromagnetic coupling through *d*-electron mediated *f-f* exchange. The compound $Gd[Gd_6CI_{12}]$ has been reported in the literature, but there is some discrepancy concerning the Gd-C distance.[41, 218] The distance of 2.673 Å reported by Simon seems far too long since the Gd-Z distance should scale with the size of the Z element. Although the crystal by Meng exhibited twinning problems, the Gd-C contacts were within a range of 2.51 to 2.54 Å.[218] We therefore chose the Gd-N distance of our model to be 2.518 Å. To study the *intra*molecular interactions, we examined the model $[Gd_6NI_{12}](OPH_3)_6$, where phosphine oxide ligands serve in the same capacity as before

and the model compound has a t_{2g}^3 HOMO configuration. As with the case of $[Gd_6CoI_{12}](OPH_3)_6$, we carried out electronic structure calculations for 20 competing spin patterns, but shall only focus our attention on the cases where the HOMO electrons are all spin up (i.e. $S = M_S = 3/2$.).[219] The 10 calculated spin pattern energies are depicted in Table 5.3.

Table 5.3. Ten spin pattern energies and symmetry imposed by the 4*f* moments for $Gd_6NI_{12}(OPH_3)_6$.

Spin	Symmetry	Energy (cm^{-1})
S = 45/2	O_h	0
S = 31/2	C_{4v}	1944.0
S = 17/2	C_{2v} (*cis*-)	3911.0
S = 17/2	D_{4h} (*trans*-)	4101.2
S = 3/2	C_{3v} (*fac*-)	5922.0
S = 3/2	C_{2v} (*mer*-)	6117.5
S = 11/2	C_{2v} (*cis*-)	8159.7
S = 11/2	D_{4h} (*trans*-)	8404.5
S = 25/2	C_{4v}	10496.4
S = 39/2	O_h	12914.4

Similar to the $[Gd_6CoI_{12}](OPH_3)_6$ case, results from single cluster calculations predict a strong preference for ferromagnetic coupling and the lowest energy spin pattern is the scenario of all 4*f* spins aligned parallel to the three spin-up valence electrons. Successive "flipping" of the 4*f* moments yields an incremental increase in energy of ~2000 cm^{-1}. This value is increased by ~25% compared to the Co-centered clusters. The

energy difference between *cis*- and *trans*- (C_{2v} and D_{4h}) and *fac*- and *mer*- (C_{3v} and C_{2v}) spin patterns differ by ~200 cm^{-1}, substantially larger than seen for the Co-centered clusters, which exhibited very small energy differences between different 4*f* –spin pattern stereochemistries. In an attempt to trace the origin of these differences, we compare the Mulliken populations for both compounds. Table 5.4 depicts the Mulliken spin populations for the 5*d* and 6*s* character of $[Gd_6NI_{12}](OPH_3)_6$. Recall that the Co-centered clusters showed significant Co 4*p* character, which acts to stabilize higher energy spin patterns. In addition, these cluster models exhibited an increase in the amount of Gd 6*s* character in the t_{1u}–type orbitals for successive spin patterns. Neither of these factors applies to the N-centered clusters. Firstly, the amount of 6*s* character is small and varies only slightly throughout the spin patterns. Secondly, the 3*s* orbitals of the N atom make a negligible contribution to the stabilization of higher energy spin patterns for the C_{2v} models (since t_{2g} must split into $A_1+B_1+B_2$ in C_{2v}). The gap between the N 2*p* and 3*s* orbital is much larger than that of the 3*d* and 4*p* for Co. Therefore, the coupling mainly arises from Gd 5*d* occupation. We expected that the energy difference between the high-symmetry spin pattern and the next lowest pattern still to be approximately one-half difference between the ^9D and ^7D. The energy difference is approximately ~40% of the ^9D-^7D difference, which may be attributable to the small amount of spin density located in the Gd 6*s* orbital.

Table 5.4. Magnitudes of Gd 5*d* and 6*s* spin populations for $Gd_6NI_{12}(OPH_3)_6$. All values are computed with precision within ±0.002.

Spin Pattern	P_{Gd} ($4f\uparrow$)[a]		P_{Gd} ($4f\downarrow$)		Relative Energy (cm^{-1})
	5*d*	6*s*	5*d*	6*s*	
S = 45/2	0.573	0.041	---	---	0
S = 31/2	0.583	0.041	-0.305	0.018	1944.0
S = 17/2, C_{2v}	0.594	0.041	-0.390	0.018	3911.0
S = 17/2, D_{4h}	0.594	0.041	-0.339	0.015	4101.2
S = 3/2, C_{3v}	0.633	0.044	-0.315	0.018	5922.0
S = 3/2, C_{2v}	0.608	0.041	-0.346	0.018	6117.5
S = 11/2, C_{2v}	-0.355	0.015	0.650	0.044	8159.7
S = 11/2, D_{4h}	-0.356	0.015	0.623	0.041	8404.5
S = 25/2	-0.367	0.015	0.669	0.044	10496.4
S = 39/2	-0.381	0.015	---	---	12914.4

[a] Positive spin populations have the same sign as their respective 4*f* moments.

We were able to construct a simple magnetic coupling model to account for the relative energies of the spin patterns, using the same model as before, assuming that the Gd atoms communicate through the N interstitial atom. Equation 5.3 depicts the Hamiltonian associated with this calculated *J* value:

$$\hat{H} = -J\sum_{i=1}^{6} S_{Gd}S_N \qquad S_{Gd} = \frac{7}{2};\ S_N = \frac{3}{2} \tag{5.3}$$

With a single *J* value of +198.6 (2.0) cm^{-1}, we can reproduce the trends from the calculated energies and predict strong ferromagnetic coupling between Gd atoms

through the "N" bridge (Table 5.5). Of course, the N atom plays no real role in achieving coupling, since the delocalized t_{2g} electrons contain no nitrogen character.

Table 5.5. Possible equations used in calculating Heisenberg coupling constants (*J*'s) for $Gd_6NI_{12}(OPH_3)_6$.

$\Delta E_{A\text{-}S=45/2}$	$\sum_{i,j} Z_{i,j} J_{i,j}$	DFT Energy Difference (cm^{-1})	Heisenberg Energy Difference (cm^{-1})
$\Delta E_{S=31/2\text{-}S=45/2}$	$2J_1$	1944.0	2085.9
$\Delta E_{S=17/2(C_{2v})\text{-}S=45/2}$	$4J_1$	3911.0	4171.9
$\Delta E_{S=17/2(D_{4h})\text{-}S=45/2}$	$4J_1$	4101.2	4171.9
$\Delta E_{S=3/2(C_{3v})\text{-}S=45/2}$	$6J_1$	5922.0	6257.8
$\Delta E_{S=3/2(C_{2v})\text{-}S=45/2}$	$6J_1$	6117.5	6257.8
$\Delta E_{S=11/2(C_{2v})\text{-}S=45/2}$	$8J_1$	8159.7	8343.7
$\Delta E_{S=11/2(D_{4h})\text{-}S=45/2}$	$8J_1$	8404.5	8343.7
$\Delta E_{S=25/2\text{-}S=45/2}$	$10J_1$	10496.4	10429.7
$\Delta E_{S=39/2\text{-}S=45/2}$	$12J_1$	12914.4	12515.6

We can use our perturbative MO approach to describe how the 4*f* exchange field can affect the electrons in the cluster MOs with 5*d*- or 6*s*-character (Figure 5.13). As in the case of the Co-centered model, we compared the case in which the potential of the 4*f* moments possess O_h symmetry, and the case of flipping two *trans*-4*f* moments which imposes D_{4h} symmetry. The analysis is similar to the Co-containing species and we will only discuss the prominent differences between the two compounds. First of all, the O_h cluster exhibits second-order effects in addition to first order splitting because of a low-lying unoccupied t_{2g} antibonding cluster orbital. Secondly, second-order effects also stabilize *all* CBEs in the HOMO of the D_{4h} cluster. Orbital plots clearly demonstrate that the three unpaired CBEs reside in a delocalized t_{2g} orbital (Figure 5.14).

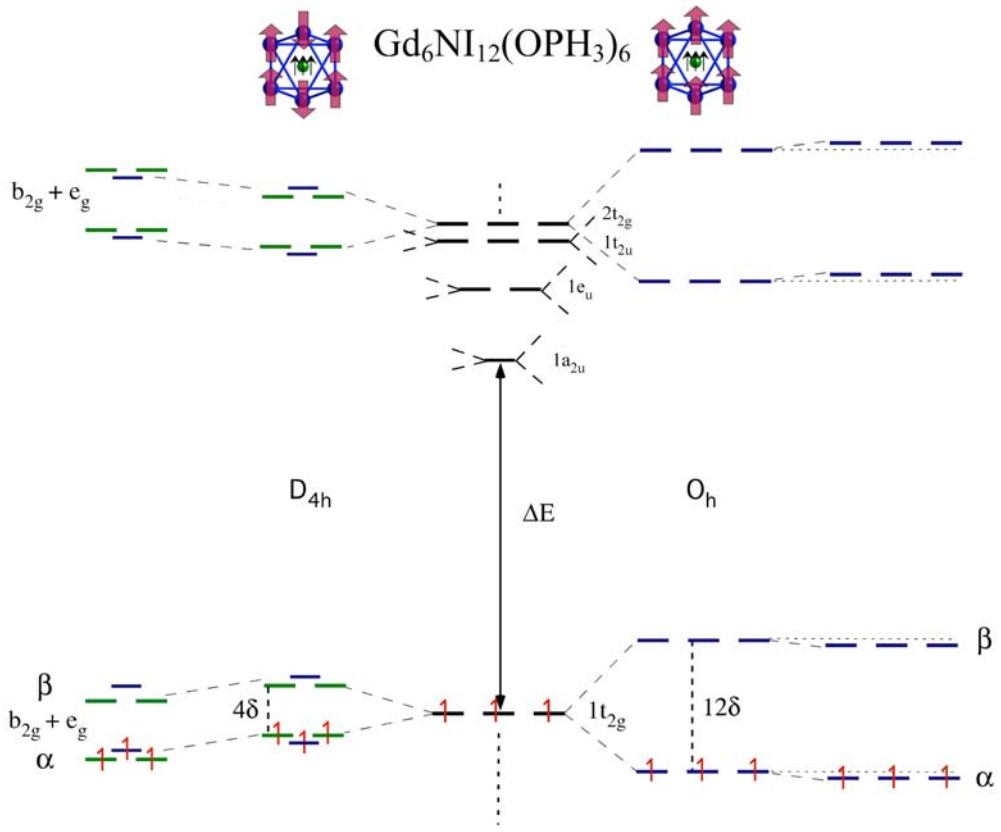

Figure 5.13. Perturbative treatment of the cluster MOs for $[Gd_6NI_{12}](OPH_3)_6$.

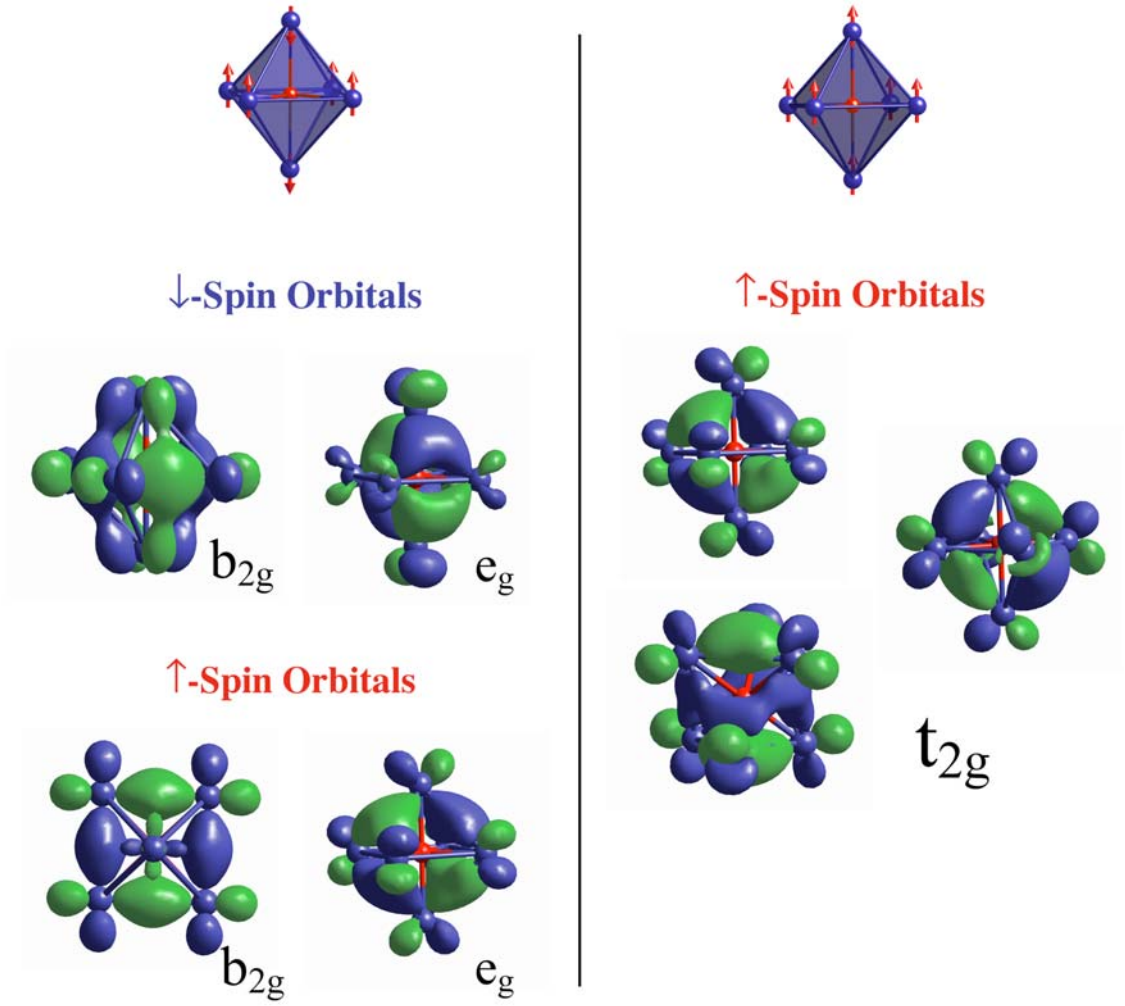

Figure 5.14. Molecular orbital plots of the D_{4h} and O_h model for $[Gd_6NI_{12}](OPH_3)_6$.

5.2 Bioctahedral Clusters

Long-term goals for studying rare-earth clusters include isolation of discrete cluster subunits and a comprehensive study of their magnetic behavior. Of possible candidates for interesting magnetic behavior, bioctahedral clusters of $Gd_{10}Cl_{17}C_4$ and $Gd_{10}I_{16}C_4$ have the most potential. The clusters are the first step of condensation of the closely related M_6X_{12}-type clusters. The metal atoms form a Gd_{10} unit by connecting two Gd_6 octahedra via a common edge. Both octahedra are centered by C_2 groups and the free edges are coordinated by X atoms, similar to the coordination seen in M_6X_{12}-type clusters (Figure 5.15).[152, 198, 200] The first in this series, $Gd_{10}Cl_{18}C_4$ (A), forms discrete cluster units whereas neighboring $Gd_{10}Cl_{17}C_4$ (B) and $Gd_{10}I_{16}C_4$ (C) units are linked via one and two halide bridges, respectively. Each cluster has approximate D_{2h} symmetry (within 0.01 Å). More importantly, upon moving through this series of compounds, the number of valence electrons for Gd-Gd bonding increases from 0 in $Gd_{10}Cl_{18}C_4$ to 1 and 2 electrons in $Gd_{10}Cl_{17}C_4$ and $Gd_{10}I_{16}C_4$, respectively. Addition of these electrons should induce *f-f* coupling, making these systems an interesting subject for further study.

Previous tight-binding studies indicate that the addition of electrons to the $Gd_{10}Cl_{18}C_4$ cluster decreases the distance at the Gd-Gd shared edges (3.21 to 3.12 Å for $Gd_{10}Cl_{18}C_4$ and $Gd_{10}Cl_{17}C_4$, respectively) and no observable change in C-C distance (~1.47 Å).[41, 152, 199] The C_2 group with a formal charge of –6 is stable only because of strong mixing with the *d* orbitals of the surrounding Gd anions. Electrical and magnetic studies on $Gd_{10}Cl_{17}C_4$ show that the compound behaves as an antiferromagnetic

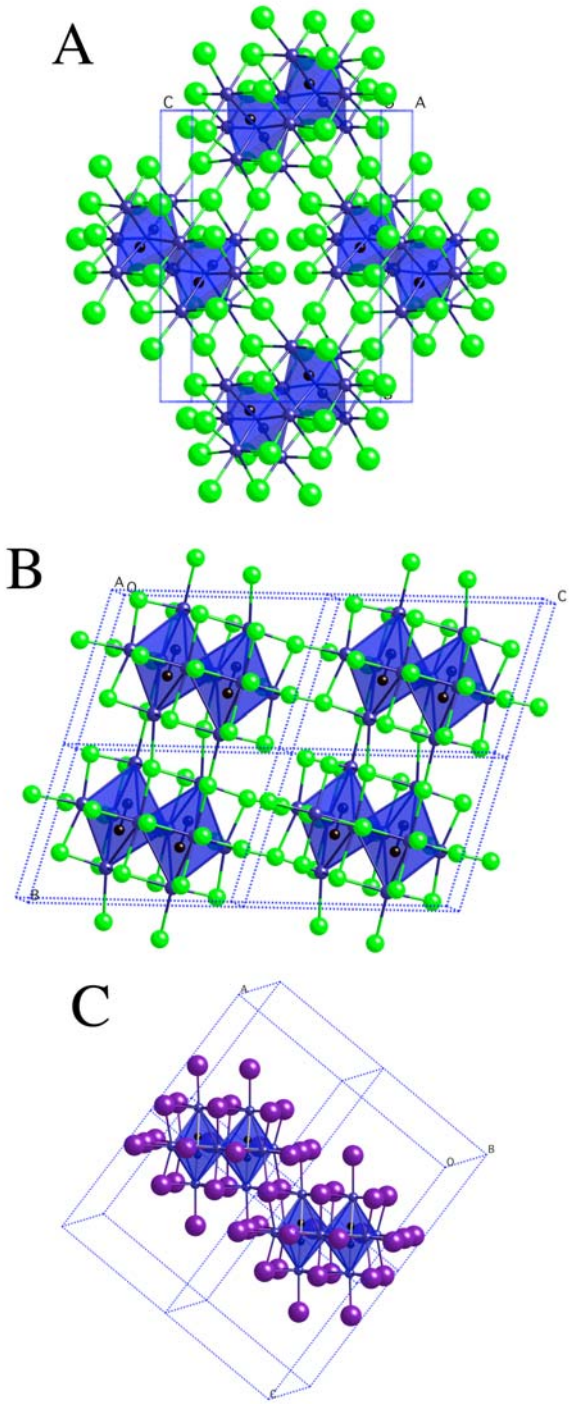

Figure 5.15. Arrangement of $Gd_{10}X_{18}C_4$ units in $Gd_{10}Cl_{18}C_4$ (A), $Gd_{10}C_{17}C_4$ (B) and $Gd_{10}I_{16}C_4$ (C).

semiconductor with ordering occurring at 25 K.[41] The results that do not correlate to our premise that open-*d*-shell systems exhibit ferromagnetism, we assume that antiferromagnetic ordering results from intermolecular coupling. Hence, upon excision, we expect the 4*f*-moments in $Gd_{10}Cl_{17}C_4$ should couple ferromagnetically.

DFT calculations were performed on the yttrium analog of these compounds and resulting DOS plots are presented in Figure 5.16.[220] The DFT results are remarkably

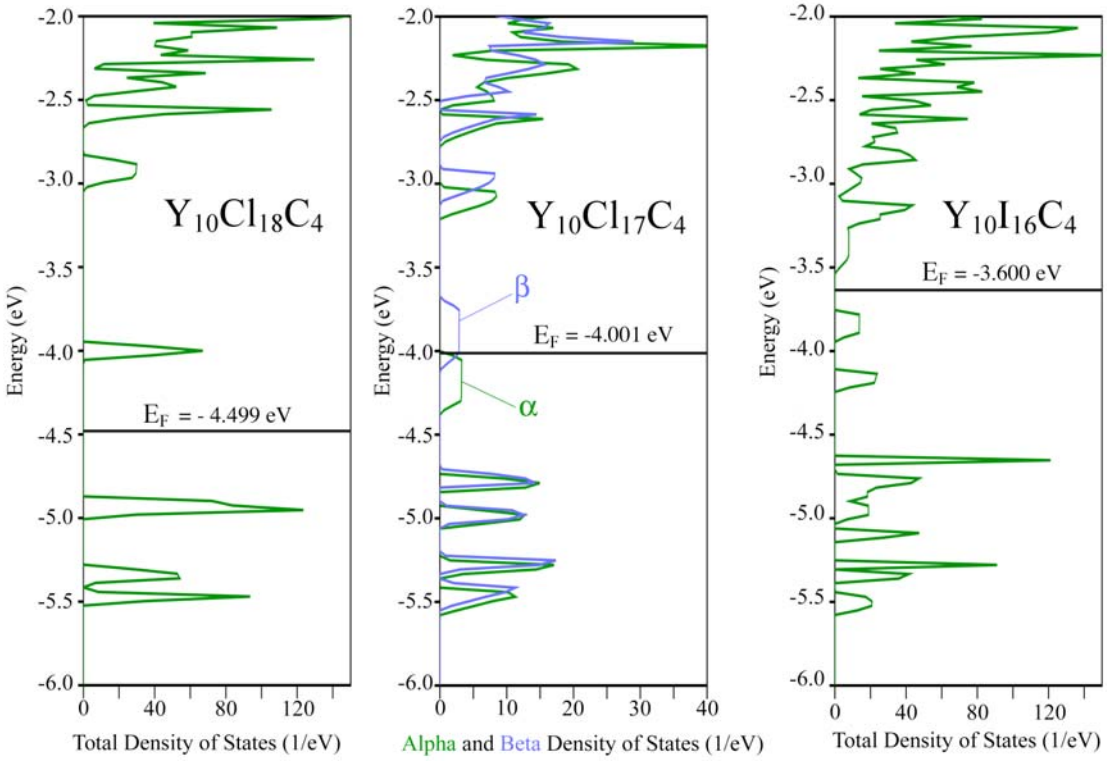

Figure 5.16. DOS plots for $Y_{10}Cl_{18}C_4$, $Y_{10}Cl_{17}C_4$, $Y_{10}I_{16}C_4$.

similar to tight-binding results performed by Bullett on $Gd_{10}Cl_{18}C_4$ and $Gd_{10}Cl_{17}C_4$.[152] The bands from approximately –4.5 eV to –5.5 eV are composed of the π_g levels with

some Y *d*-orbital character. Tight-binding results by Bullett reveal that the orbital composition of the "π_g" state contains 50% Gd, 5% Cl, and 45% C.[152] The halide *p* levels range from –8 eV to –12eV and this region also presumably contains the π_u and $3\sigma_g$ orbitals of C_2^{6-} although they cannot identified because their energies overlap with the halide *p* levels. The lowest unoccupied band contains a metal-metal bonding orbital, split off about 1 eV from the main Y *d* bands (which will mix with the $3\sigma_u$ orbital on C). To rationalize this, if each C_2 group in $Y_{10}I_{16}C_4$, was assigned an effective negative charge of –7, this would imply half-occupancy of the $3\sigma_u^*$ orbital, which is very high in energy. Consequently, in $Y_{10}Cl_{17}C_4$ and $Y_{10}I_{16}C_4$ there is a M-M bonding band that is partially or fully occupied, respectively.

5.2.1 Model Description

We investigated the model $[Gd_{10}Cl_{18}C_4](OPH_3)_8$ (A) and $K[Gd_{10}Cl_{17}C_4](OPH_3)_8$ (B), shown in Figure 5.17. The model retains the $Gd_{10}Cl_{18}C_4$ and $Gd_{10}Cl_{17}C_4$ cluster core structure and phosphine oxide ligands fill the coordination sites provided by the Gd–Cl contacts lost upon separating the clusters. Partial geometry optimizations for the positions of the phosphine oxides were performed using an analogous yttrium model system, $[Gd_{10}Cl_{18}C_4](OPH_3)_8$, resulting in structure with D_2 symmetry. Potassium cation and its position were chosen based on SCF convergence difficulties. The system had problems achieving SCF convergence when cesium was used as the model cation and when the cation was placed in the (0,0,0) position. At the (0.5,0.5,0) position, the K

cation was at a distance of ~4.2 Å, well beyond the van der Waals radii for a K-Cl interaction.

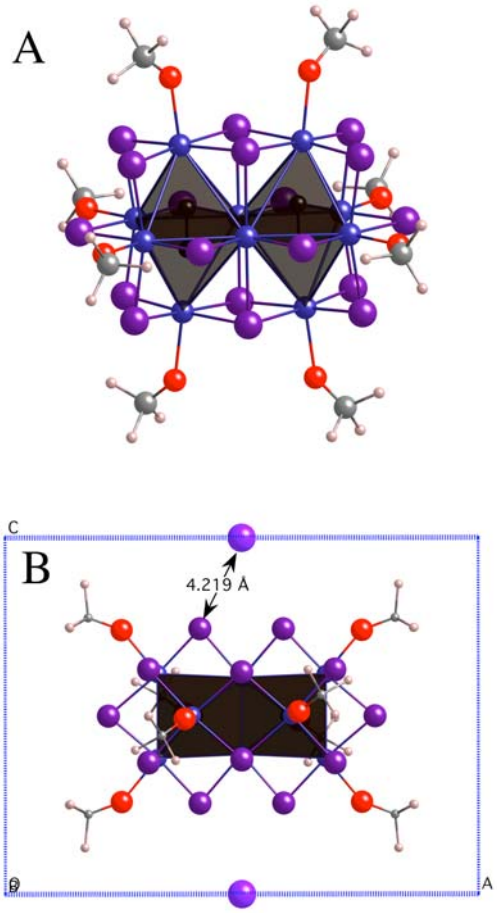

Figure 5.17. Single cluster models for $Gd_{10}Cl_{18}C_4$ (A) and the [1,0,1] view for $Gd_{10}C_{17}C_4$ (B).

5.2.2 Magnetic Interactions on Models of $[Gd_{10}Cl_{18}C_4]$ and $[Gd_{10}Cl_{18}C_4]^-$

We carried out electronic structure calculations for 12 competing spin patterns on the single cluster model, and the calculated energies and pseudosymmetries imposed by

the 4*f* moments are shown in Figure 5.18. Because of the large number of patterns with the same spin and pseudosymmetry, an additional label is provided for further clarification. These spin patterns do not represent a complete list (96 spin pattern

Label, Pseudosymmetry, Relative SDFT Energy	Spin Patterns	Label, Pseudosymmetry, Relative SDFT Energy	Spin Patterns
S = 35, D_{2h} 166.1 cm^{-1}	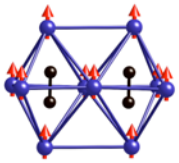	S = 21 (apical1), C_{2v} 72.0 cm^{-1}	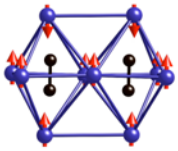
S = 28 (basal2), C_s 128.2 cm^{-1}	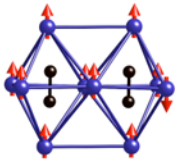	S = 28 (basal1), C_{2v} 63.7 cm^{-1}	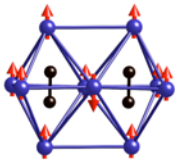
S = 28 (apical), C_s 110.7 cm^{-1}	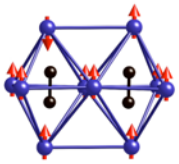	S = 21 (apical3), C_{2h} 53.7 cm^{-1}	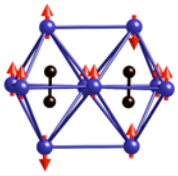
S = 21 (apbas2), C_1 88.5 cm^{-1}	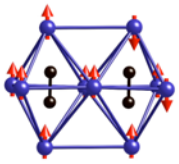	S = 0, C_s 51.7 cm^{-1}	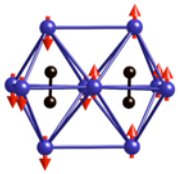
S = 21 (basal2), C_{2v} 79.7 cm^{-1}	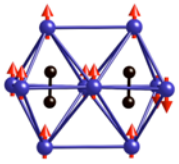	S = 21 (apbas1), C_1 25.3 cm^{-1}	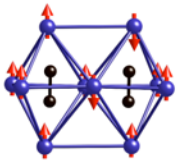
S = 21 (apical2), C_{2v} 77.7 cm^{-1}	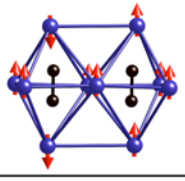	S = 21 (basal1), D_{2h} 0.0 cm^{-1}	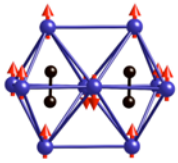

Figure 5.18. Spin pattern energies for the model $Gd_{10}Cl_{18}C_4(OPH_3)_8$.

combinations in total), but are rather a selection of possible lowest energy spin patterns. Notably, the energies of calculated spin patterns are all in a range of about ~100 cm^{-1}. Of the patterns calculated, the lowest energy pattern is one in which 4*f*-moments of the shared Gd-Gd edge are opposed to moments on the other Gd atoms. It is difficult to propose an analysis explaining why $S = 21$ (basal1) is the lowest energy spin pattern, but other conclusions can be drawn. Presented in Figure 5.19 is a MO plot of the HOMO and LUMO orbitals for the $S = 35$ (high-spin) system.

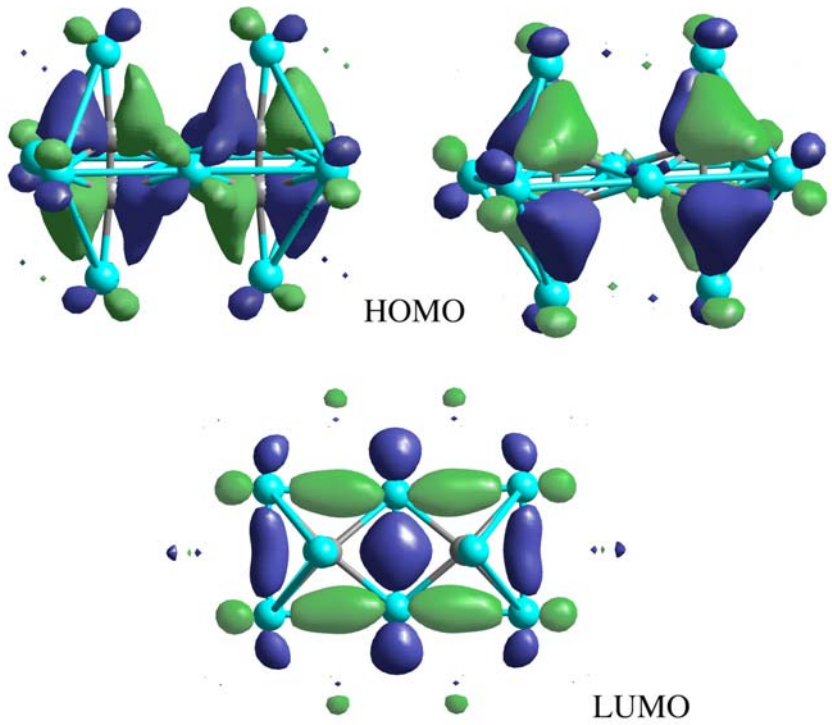

Figure 5.19. HOMO and LUMO MO plots for $S = 35$ system. Phosphine oxide and chloride ligands are hidden for clarity.

These plots resemble contour plots for the same orbital in LMTO-ASA calculations on

$Gd_{10}I_{18}C_4$.[199] The HOMO plot reveals that the "π_g" orbitals contain a large amount of Gd *d*-orbital character, as discussed in the band structure analysis for the solid state compounds. This conclusion is underscored by the Mulliken population analysis (Table 5.6) which reveals that the lowest spin pattern yields the greatest *d*- and *s*- contributions on the minority spin Gd *and* least amount of C 2*p* character.[221] The LUMO of the model

Table 5.6. Magnitudes of the average C 2*p* and Gd 5*d* and 6*s* spin populations for $[Gd_{10}Cl_{18}C_4](OPH_3)_8$. All values are computed with precision within ±0.002.

Spin Pattern	P_C	P_{Gd} ($4f\uparrow$)[a]		P_{Gd} ($4f\downarrow$)		Relative Energy (cm^{-1})
	2*p*	5*d*	6*s*	5*d*	6*s*	
S = 21 (basal1)	-0.058	0.112	0.026	0.138	0.031	0
S = 21 (apbas1)	-0.062	0.111	0.025	0.134	0.031	25.3
S = 0	0.000	0.113	0.026	0.113	0.026	51.7
S = 21 (apical3)	-0.066	0.110	0.026	0.129	0.023	53.7
S = 28 (basal1)	-0.086	0.109	0.025	0.141	0.030	63.7
S = 21 (apical1)	-0.066	0.110	0.026	0.128	0.032	72.0
S = 21 (apical2)	-0.066	0.107	0.026	0.114	0.023	77.7
S = 21 (basal2)	-0.078	0.112	0.027	0.112	0.027	79.7
S = 21 (apbas2)	-0.072	0.111	0.026	0.119	0.025	88.5
S = 28 (apical)	-0.090	0.108	0.025	0.129	0.023	110.7
S = 28 (basal2)	-0.096	0.109	0.025	0.109	0.029	128.2
S = 70	-0.115	0.107	0.025	---	---	166.1

[a] Positive spin populations have the same sign as their respective 4*f* moments.

$[Gd_{10}Cl_{18}C_4](OPH_3)_8$ shows that, if occupied, it would give rise to Gd-Gd bonding in the basal plane. The metal-metal bonding is strongest between the atoms that share a common edge and the orbitals on the apical atoms contribute very little to this orbital.

Results from the calculations on the model $K[Gd_{10}Cl_{18}C_4(OPH_3)_8]$ are shown in Table 5.7 and of the 12 spin patterns attempted, 10 achieved SCF convergence. The labeling is similar to the previous model except the spin values are increased by 1/2. Of the spin patterns, the six lowest in energy predict ferromagnetic coupling among the basal plane. Figure 5.20 depicts the lowest energy spin pattern arrangement. Unlike

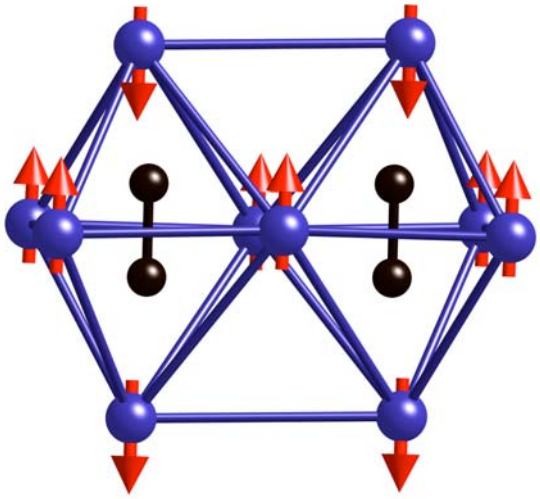

Figure 5.20. Lowest spin pattern arrangement (S = 15/2) for the model compound $K[Gd_{10}Cl_{18}C_4(OPH_3)_8]$.

previous cluster models which predict a strong preference for ferromagnetic coupling for an open shell cluster, the six lowest energy spin patterns are all within ~5 cm^{-1} of each other and do not predict a ferromagnetic arrangement as the lowest energy spin pattern.

However, the result is not surprising because all of these patterns differ in the apical 4*f*-moment arrangement, which is not involved in metal-metal bonding of the occupied orbital. What is more surprising is that the model does not predict strong coupling at all upon "flipping" the 4*f* moments on the basal atoms. As mentioned earlier, it was difficult to achieve SCF convergence for models of $[Gd_{10}Cl_{18}C_4]^-$ and perhaps the model should be revised before continuing.

Table 5.7. Ten spin pattern energies and symmetry imposed by the 4*f* moments for $K[Gd_{10}Cl_{18}C_4(OPH_3)_8]$.

Spin	Pseudosymmetry	Relative Energy (cm^{-1})
S = 15/2	D_{2h}	0
S = 43/2 (apical3)	C_{2h}	0.60
S = 43/2 (apical1)	C_{2v}	1.30
S = 43/2 (apical2)	C_{2v}	1.87
S = 57/2 (apical)	C_s	2.76
S = 71/2	D_{2h}	4.87
S = 43/2 (apbas2)	C_1	11.79
S = 57/2 (basal2)	C_s	13.20
S = 43/2 (basal2)	C_{2v}	20.55
S = 43/2 (basal1)	D_{2h}	41.76

5.3 Gadolinium Oxoalkoxides

The rare-earth oxoalkoxides, $R_5(\mu_5\text{-}O)(\mu_3\text{-}OPr^i)_4(\mu\text{-}OPr^i)_4(OPr^i)_5$ (R = Er, Gd),[201, 203, 222] are of interest as potential precursors of single molecule magnets. The compound is prepared by adding a stoichometric proportions of RCl_3 (R = Gd, Er), H_2O and $KOPr^i$ to 2-propanol and toluene. Upon stirring for 48 hours, the KCl is centrifuged from solution and the reaction produces 90-95% $R_5(O)(OPr^i)_{13}$. Figure 5.21 shows the

structure of $R_5(\mu_5\text{-}O)(\mu_3\text{-}OPr^i)_4(\mu\text{-}OPr^i)_4(OPr^i)_5$ which contains a trigonal pyramid of R atoms that surround a central oxygen atom and are capped on the four triangular faces and the four basal edges with isopropoxide ligands. Terminal isopropoxide ligands are bound to each R center as well. The oxygen atom that centers these clusters is probably derived from water; the clusters apparently assemble around hydroxide/oxide ions in highly basic isopropoxide/isopropanol solutions.

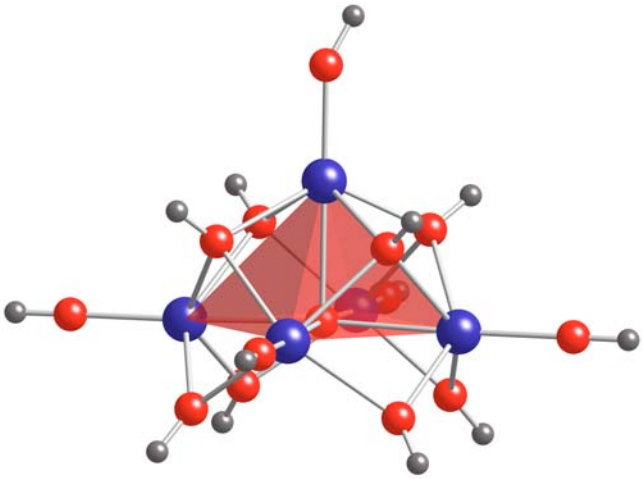

Figure 5.21. Structure of $R_5(O)(OPr^i)_{13}$ (R = Gd, Er) where *iso*-propoxide ligands are truncated for clarity.

In $Gd_5(O)(OPr^i)_{13}$, Gd is in the 3+ oxidation state but the Gd atoms are brought into close proximity in surrounding the μ_5-O atom (d(Gd-μ_5-O) = 2.405 (12) Å for the basal atoms and 2.387 (11) Å for the apical atom). The metal-oxygen distances are as follows: μ_5-Gd-O > μ_3-Gd-O > μ-Gd-O > Terminal Gd-O. The Gd-μ_3-O distances depend on whether the Gd atom is apical or basal, the former being shorter. The Gd-Gd

contacts (3.389 (2) Å around the basal atoms and 3.525 (2) Å for basal-apical distances), are *shorter* than those observed in $Gd(Gd_6I_{12}C)$ ($d(Gd\text{-}Gd)_{avg}$ = 3.56 Å) where Gd-Gd bonding orbitals are occupied. In addition, the cationic nature of the cluster core, $[Gd_5(\mu_5\text{-}O)(\mu_3\text{-}OPr^i)_4(\mu\text{-}OPr^i)_4]^{5+}$, suggests that this cluster or a suitable derivatives might be reduced such that one or more R-R bonding orbitals are occupied to yield a cluster with enhanced *d*-electron mediated *f-f* exchange coupling.

5.3.1 Model Structure

We investigated the three different models, $Gd_5(\mu_5\text{-}O)(\mu_3\text{-}OH)_4(\mu\text{-}OH)_4(OH)_5$, $Gd_5(\mu_5\text{-}O)(\mu_3\text{-}OH)_4(\mu\text{-}OH)_4(OPH3)_5^{5+}$, $Gd_5(\mu_5\text{-}O)(\mu_3\text{-}OCH_3)_4(\mu\text{-}OCH_3)_4(OPH_3)_5^{5+}$. Initial calculations performed on the $Gd_5(O)(OH)_{13}$ model indicate that the HOMO-LUMO gap is ~3.8 eV with the LUMO containing more ligand-localized character and no appreciable metal-metal bonding. Unfortunately, no orbitals with Gd *d*-electron character appear within 1 eV of the LUMO, leaving one to believe that upon reduction, magnetic behavior will not be induced and decomposition is likely. Given these results, we decided to try (1) replacement of the terminal hydroxy ligands on the model with phosphine oxide (Figure 5.22) and (2) addition of another metal atom to create an $[R_6Z]$ core (Figure 5.23). Previous experimental results have indicated that both of these models are viable synthetic target molecules.[203] The former approach increases the overall positive charge on the cluster, thereby advantageously shifting the reduction potential. The Gd_5 model retains the cluster core structure and phosphine oxide ligands were used to increase the overall cationic charge. Partial geometry optimizations for the

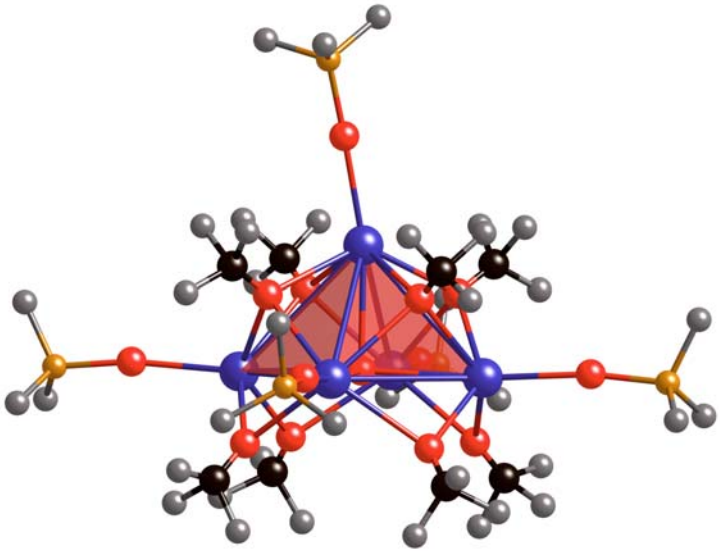

Figure 5.22. Model structure of $Gd_5(\mu_5\text{-}O)(\mu_3\text{-}OCH_3)_4(\mu\text{-}OCH_3)_4(OPH_3)_5^{5+}$.

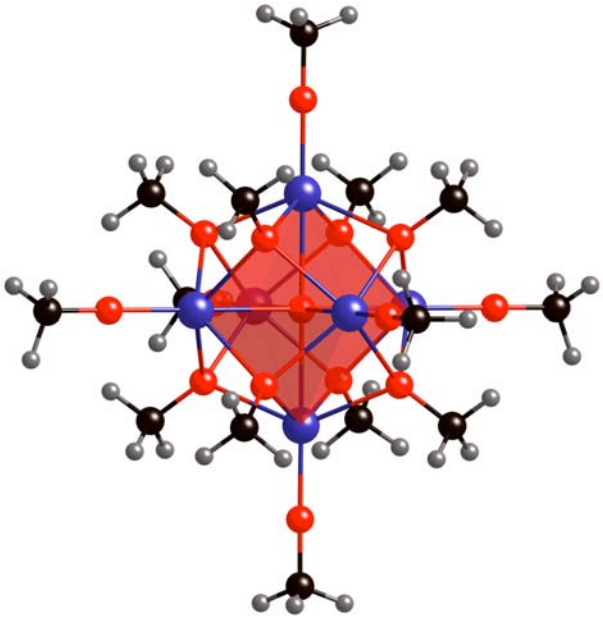

Figure 5.23. Model structure of $Y_6(\mu_6\text{-}O)(\mu_3\text{-}OCH_3)_8(OCH_3)_6^{2+}$ and $Y_6(\mu_6\text{-}O)(\mu_3\text{-}OCH_3)_8(OPH_3)_6^{8+}$.

positions of the phosphine oxides and methoxides were performed using an analogous yttrium model system, resulting in structure with C_s symmetry; the cluster core retains C_{4v} symmetry.

Geometry optimizations for $Y_6(O)(OCH_3)_{14}^{2+}$ and $Y_6(O)(OCH_3)_8(OPH_3)_6^{8+}$ yielded the structure in Figure 5.23. The model structures of Y_6 retain the structure of the original model $Gd_5(O)(OCH_3)_8(OPH_3)_5^{5+}$ except adding either a Y-OCH_3 or Y-OPH_3 apex. The optimization yields a cluster core with O_h symmetry and Y-interstitial O distance of 2.47 Å and 2.510 Å ($\leq$ 0.12 Å longer than Gd-μ_5-O distances in $Gd_5(O)(OPr^i)_{13}$) for $Y_6(O)(OCH_3)_{14}^{2+}$ and $Y_6(O)(OCH_3)_8(OPH_3)_6^{8+}$, respectively. Because of the three-fold symmetry about the terminal ligands, these compounds have C_1 symmetry. Interestingly, the slightly bent apical phosphine oxide ligand (167º) in $Gd_5(O)(OCH_3)_8(OPH_3)_5^{5+}$ straightened to a 180º in the Y_6 structures.

5.3.2 Electronic Structure of Model Structures

The electronic structures of $Gd_5(O)(OCH_3)_8(OPH_3)_5^{5+}$ and $Y_6(\mu_6\text{-}O)(\mu_3\text{-}OCH_3)_8(OCH_3)_6^{2+}$ and M_6X_8 cluster compounds are similar. The latter clusters have been the subject of many theoretical investigations,[223, 224] but we provide a detailed discussion here with emphasis on the effects of an interstitial atom. For the sake of our discussion, we will first compare the electronic structure of an M_6X_8-type compound and $Y_6(O)(OCH_3)_{14}^{2+}$, but it should be noted that the same analysis applies to another possible model, $Y_6(O)(OCH_3)_8(OPH_3)_6^{8+}$. We use the cluster core symmetries in our analysis. Figure 5.24 shows a molecular orbital scheme for the $[M_6X_8]X_6^{n+}$-type cluster

(for example: $[Mo_6S_8]^{4-}$, $[Mo_6Cl_{14}]^{2-}$, and $[Re_6S_8Cl_6]^{4-}$);[225-230] levels that have predominately M *d* character are displayed. Because a detailed discussion of the orbital description can be found elsewhere, we will only briefly describe salient features of the electronic structure. When referring to these clusters, we will adopt the convention that each metal atom has a local coordinate system such that each M center's "*z*-axis" is normal to the faces of the cube and the d_{xy} orbitals are directed towards the ligands. Generally, these clusters are 24 electron species in rhenium chalcogenide compounds, 20-24 e^- species in molybdenum halides and chalcogenides, and have as few as 19 e^- in $Nb_6I_8^{3+}$.[227, 231-233] We see that only 4 levels are filled in Figure 5.24, consistent with the assignment of 8 electrons in $Y_6(O)(OCH_3)_{14}^{2+}$ and as we point out below, those 8 e^- actually reside in the interstitial oxygen atom 2*s* and 2*p* orbitals. The $[M_6X_8]X_6^{n+}$ MO diagram changes for analogous $Y_6(OCH_3)_{14}^{4+}$ where the frontier orbitals are affected by the face-capping and terminal -OCH_3 ligands and the LUMO becomes the e_g set of orbitals (Figure 5.25). Addition of the interstitial O^{2-} atom to $Y_6(OCH_3)_{14}^{4+}$ will result in bonding/antibonding a_{1g} and t_{1u} orbitals, depicted in Figure 5.25. As expected, the a_{1g} and t_{1u} are strongly stabilized by the interaction with the oxide anion and these bonding orbitals almost exclusively contain interstitial oxygen character. The subsequent antibonding a_{1g} and t_{1u} orbitals are located within the metal-metal bonding region and the "new" LUMO becomes a_{1g}, shown in Figure 5.26. This orbital consists of a "z^2s" hybrid, shown in **5.2**, which is a consequence of the interaction with the interstitial oxide anion in the cluster. Approximately 0.3 eV higher in energy contains the e_g set of orbitals. The HOMO-LUMO gap is 4.129 eV and 5.116 eV for $Y_6(O)(OCH_3)_{14}^{2+}$and

$Y_6(O)(OCH_3)_8(OPH_3)_6^{8+}$, respectively.

The electronic structure of $Gd_5(O)(OCH_3)_8(OPH_3)_5^{5+}$ is shown in Figure 5.27 and is markedly different from the electronic structure of $Y_6(O)(OCH_3)_{14}^{2+}$. Firstly, the LUMO for the compound is b_1, which is comprised of part of the e_g set from an O_h cluster. Secondly, the HOMO-LUMO gap is 0.944 eV, much smaller than proposed O_h cluster compounds. Given these results, this molecule is a candidate for reduction experiments to determine if *d*-electron mediated *f-f* exchange is possible.

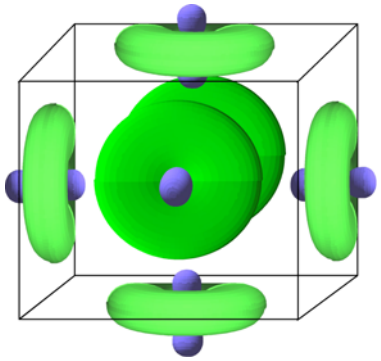

5.2

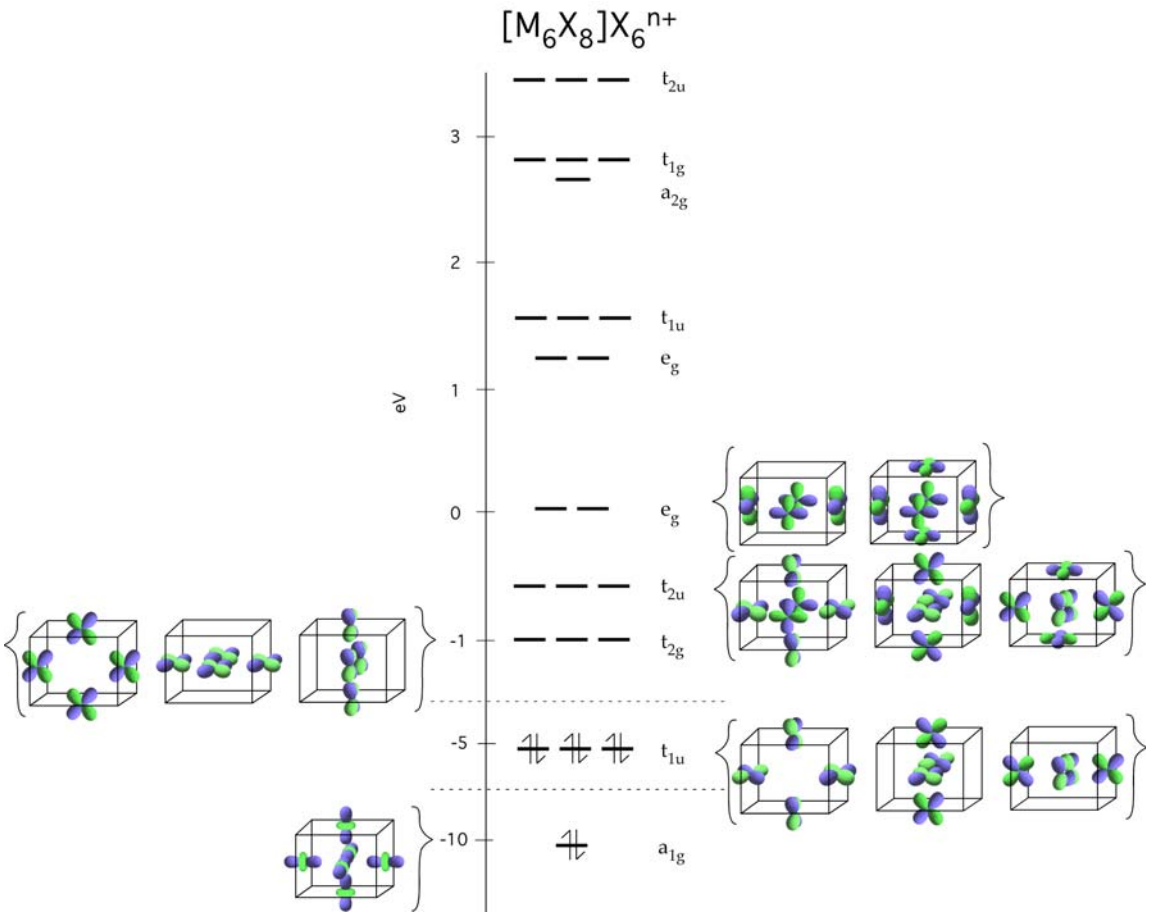

Figure 5.24. MO diagram for $[M_6X_8]X_6^{n+}$. Included are the M-M bonding orbitals.

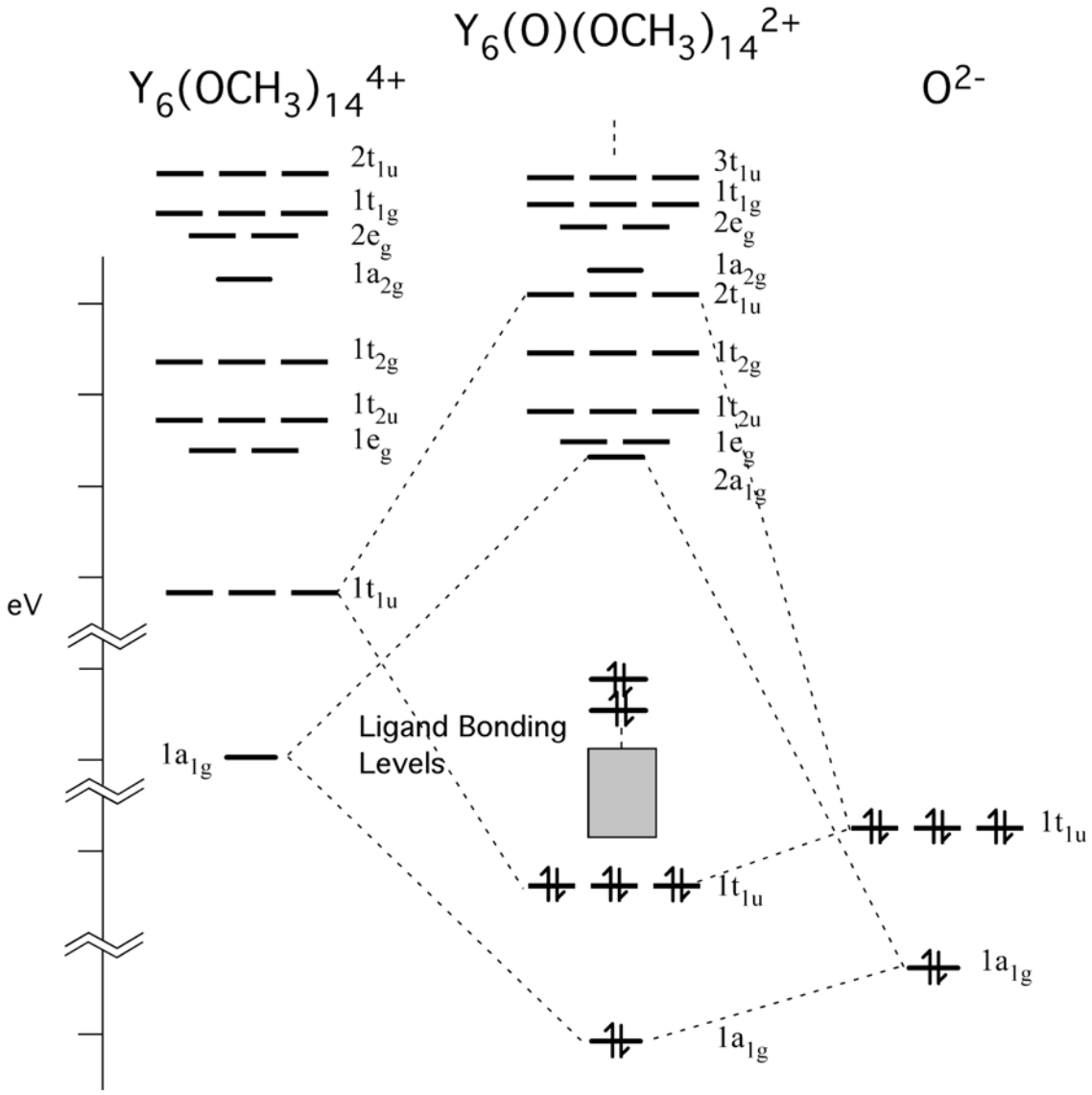

Figure 5.25. MO diagram for $Y_6(O)(OCH_3)_{14}^{2+}$.

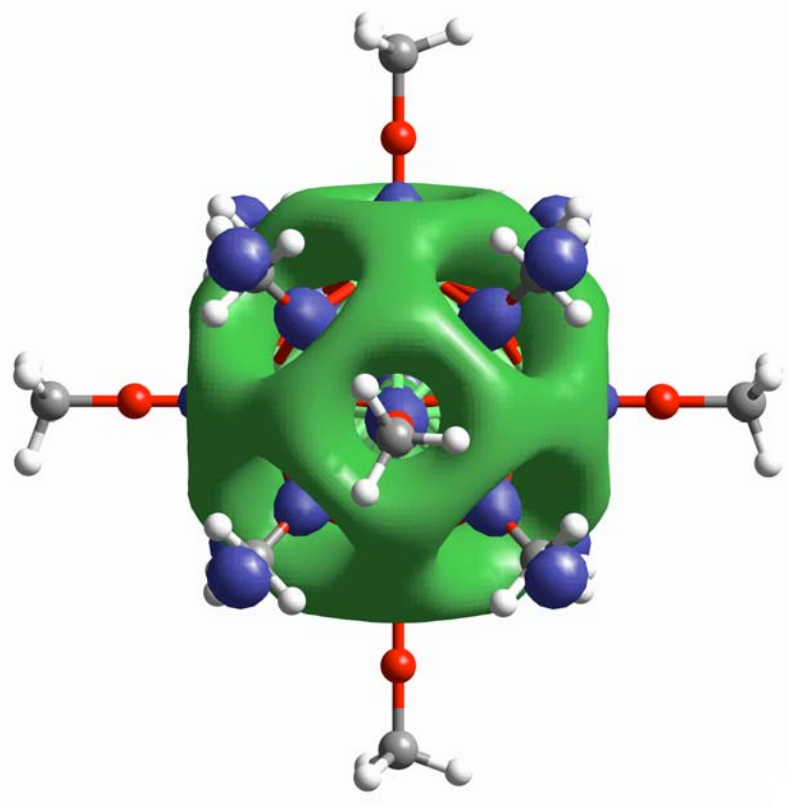

Figure 5.26. Molecular orbital plot of the LUMO a_{1g} orbital.

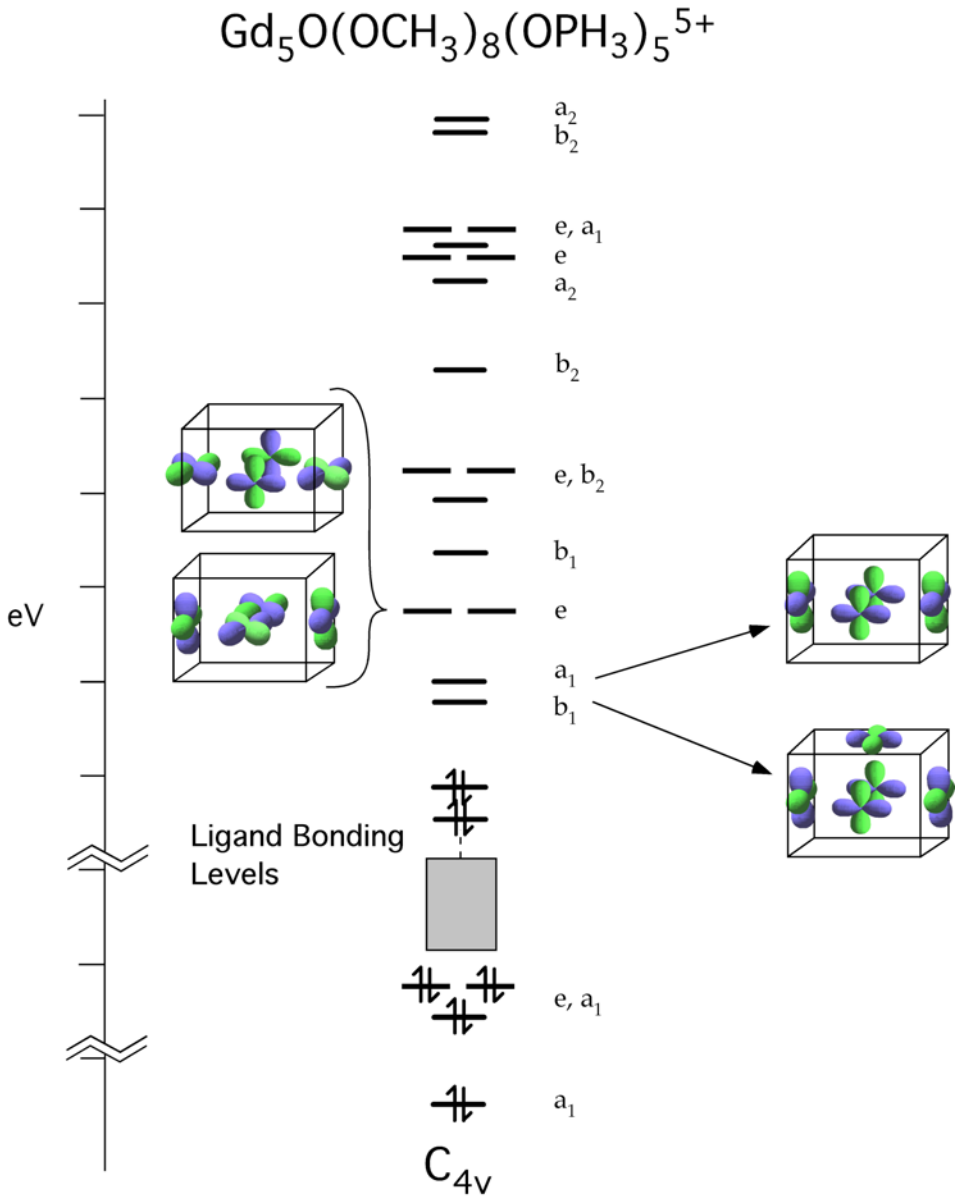

Figure 5.27. Electronic structure of $Gd_5(O)(OCH_3)_8(OPH_3)_5^{5+}$. Pertinent orbitals are displayed.

CHAPTER VI

SOLID STATE MATERIALS*

This chapter focuses on using semi-empirical calculations with parameters chosen to reproduce first principles benchmark results, to simulate *d*-electron mediated *f*-*f* exchange in extended Gd conducting systems. Unfortunately, it is difficult perform our spin pattern approach using DFT on metallic rare-earth extended systems. Therefore, we set out to developed other means of describing the possible spin patterns of these solids using a carefully parameterized Extended Hückel tight binding (EHTB) approach. For a qualitative description, the spin dimer approach based on EHTB calculations has reproduced relative strengths of the spin-exchange interactions determined from first principles electronic structure calculations for a variety of magnetic transition metal oxides.[234-239] To test our method, we studied benchmark systems where the magnetic structure of Gd-containing solids was known using neutron diffraction techniques. Of the rare earth atoms, Gd poses a problem because natural Gd is almost opaque to neutrons due to the high absorption cross sections of ^{155}Gd and ^{157}Gd.[240] However, it is possible to obtain a magnetic structure for Gd-containing solids using compounds isotopically-enriched with ^{158}Gd or ^{160}Gd,[241-244] hot neutrons with a wavelength of 0.58 Å which reduce the absorption cross-sections for heavy neutron absorbers,[245-249] Mössbauer studies on the ^{155}Gd isotope,[250, 251] and/or using new powder neutron

*Reproduced in part with permission from Journal of the American Chemical Society, to be submitted. Unpublished work copyright 2006, American Chemical Society.

diffractometers which help to correct for heavy neutron absorbers.[252, 253] Indeed, we shall see that these calculations shed light on the question of whether one can simulate *d*-*f* exchange in metallic Gd compounds.

6.1 Computational Details

Electronic structure calculations for YB_2C_2, α-Y_2S_3, Y_5Si_4 and Y_5Ge_4 were performed using density functional theory with the Becke exchange functional and Lee-Yang-Parr correlation functional (BLYP).[69, 70] All density functional calculations presented here were performed using the DMol^3 program from the Materials Studio® or Cerius® suite of programs. The double numerical basis including *d*-polarization functions, DND, was employed in DMol^3 calculations for all atoms. Ruiz *et al.* recently showed that for transition-metal complexes, numerical basis sets are accurate and reliable alternatives to Gaussian basis functions.[122] For yttrium, a small frozen-core (1*s*2*s*2*p*3*s*3*p*3*d*) effective potential was used. All calculations included scalar relativistic effects and open-shell configurations. Because there are no fractional coordinates obtained from the neutron diffraction experiment to distinguish between the boron and carbon positions for YB_2C_2 or GdB_2C_2, we used lattice parameters for GdB_2C_2 and fractional coordinates from TbB_2C_2.[252, 254] The criterion for the energy convergence in DFT calculations was set at 10^{-6} a.u. Band calculations were carried out for YB_2C_2 using a mesh of 405 ***k***-points throughout the Brillouin to obtain density-of-states (DOS) and band structure plots of high resolution. DOS plots were generated using Cerius2®

and band dispersion plots were generated using the viewkel routine from YAeHMOP.[62] Band calculations were carried out for α-Y_2S_3, Y_5Si_4, and Y_5Ge_4 using a mesh of 27 ***k***-points throughout the Brillouin to obtain density-of-states (DOS).

Extended Hückel tight binding (EHTB) calculations were carried out with the program YAeHMOP on YB_2C_2, "GdB_2C_2", α-Y_2S_3, "α-Gd_2S_3", Y_5Si_4, "Gd_5Si_4", Y_5Ge_4, and "Gd_5Ge_4" (where (5*d*/6*s*)-*f* spin polarization is simulating in the Gd-containing compounds using a Y model to be described below). The exponents (ζ's) and valence shell ionization potentials (H_{ii}'s in eV) are listed in Appendix B. Double-zeta Slater-type orbitals were used to represent Y 4*d* atomic orbitals. The band dispersion and density of states (DOS) diagrams were generated with the viewkel routine.

6.1.1 Models of GdB_2C_2

For systems with a "small" tetragonal cell (i.e., for the observed antiferromagnetic spin pattern and for the ferromagnetic calculations), we used a 936 ***k***-point mesh in the irreducible wedge of the Brillouin zone. ***k***-points meshes in supercells were chosen such that they were consistent with this mesh (468 ***k***-points for the tetragonal $1 \times 1 \times 2$ supercell, 432 ***k***-points for the orthorhombic $2 \times 2 \times 1$ supercell). In this context, "consistent" means that the supercell ***k***-points map on to the subcell ***k***-points and therefore energies of the small-cell spin patterns scale exactly (with volume) when recomputed in the supercells. We performed test calculations with a smaller mesh (550 ***k***-points in the irreducible wedge of the small tetragonal cell) and the spin-pattern energy differences were within 28 cm^{-1} of the energy differences reported here. 28 cm^{-1}

may therefore be regarded as a pessimistic upper bound on the precision with which the spin-pattern energies given in Figure 6.4 are computed.

6.1.2 Models of α-Gd_2S_3, Gd_5Si_4, and Gd_5Ge_4

We used a 1000 ***k***-point mesh for the models of α-Gd_2S_3, Gd_5Si_4, and Gd_5Ge_4 using EHTB in the irreducible wedge of the orthorhombic Brillouin zone. We used the chemical unit cell for these models and no supercells were attempted.

6.2 GdB_2C_2

6.2.1 LnB_2C_2 Geometric and Magnetic Structures

LnB_2C_2 phases possess a three-dimensional structure in which 2-D layers of Ln atoms alternate with 2-D 4.8^2 B_2C_2 nets (in which B_2C_2 rhombi are crosslinked by B–C bonds). Viewing the structure down the *c*-axis, the Ln atom is positioned between the centers of 8-membered B_4C_4 rings. Despite the relative simplicity of this structure, two important structural characteristics of the LnB_2C_2-type have been debated in the literature. For many years, it was unclear (*i*) whether the B_2C_2 rhombi were crosslinked by B–C bonds (as just described) or by B–B and C–C bonds (Figure 6.1) and (*ii*) whether the B/C atoms in successive layers were stacked directly or alternately in the *z*-direction (and the *c*-axis was thereby doubled).[255-258] Single crystal X-ray diffraction studies on YB_2C_2, CaB_2C_2, and LaB_2C_2 reported B–B and C–C contacts within the 8-

membered ring and a second B/C net at z = 1/2 rotated by 90° with respect to that at z = 0 to give a (*a*, *a*, *2c*) tetragonal cell (Figure 6.1b).[257, 259]

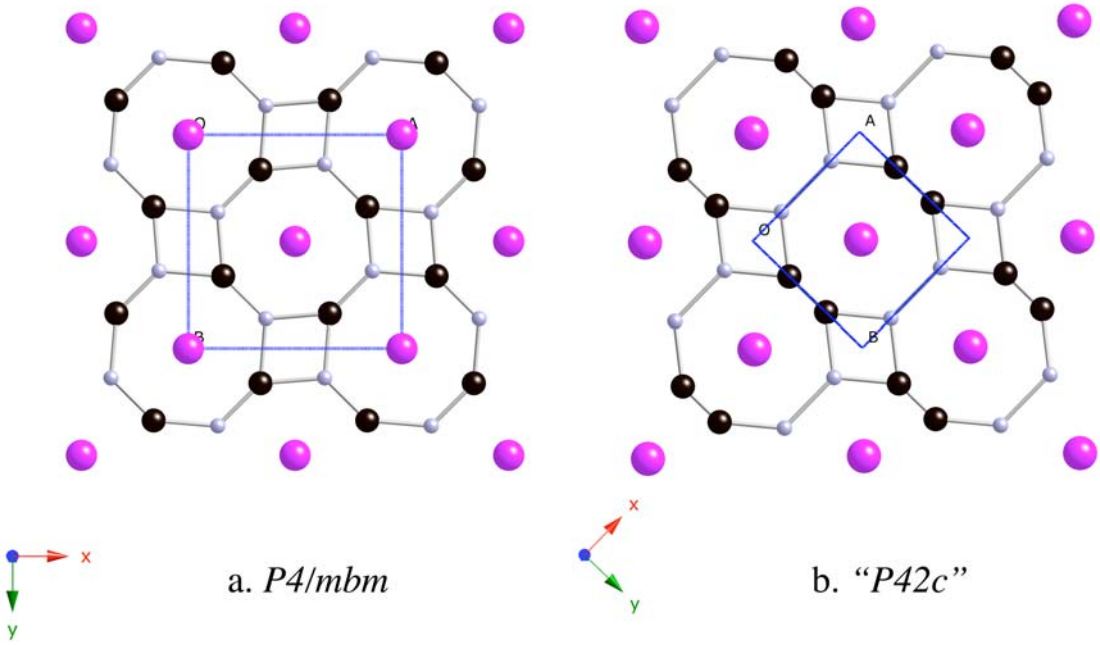

Figure 6.1. Alternative models for LnB_2C_2 (Ln = La, Ce, Pr, Nd, Tb, Dy, Ho, Er, Tm, Lu) with the unit cells shown.

However, more recent neutron diffraction experiments have established that these compounds possess a network structure with B–C bonds between and within the B_2C_2 rhombi and showed no doubling of the *c* axis (Figure 6.1a).[254, 258] The bonding connectivity in this structural model is that originally proposed by Smith, though Smith had not refined the B and C positional parameters.[256] This structure is also consistent with that predicted by Burdett *et al.*, who used extended Hückel theory to analyze the B–

C bonding arrangements in CaB_2C_2 and LaB_2C_2. In both cases, the alternating B–C bonded network structure was predicted to enjoy a strong energetic advantage.[260] These predictions have been very recently borne out in a detailed DFT investigation of the structures of these compounds.[261]

Aside from these structural questions, the tetragonal rare-earth diborocarbide compounds have interesting magnetic and conducting properties.[252, 262-267] The metallic conducting behavior is consistent with the electronic configuration of these rare earth diborocarbides written as $R^{3+}(B_2C_2^{2-})e^-$, where the $B_2C_2^{2-}$ sheets, like graphite and hexagonal boron nitride, possess filled π-bonding bands. The additional electron partially fills a broad band(s) with mixed $B_2C_2(\pi^*)$-R(*d*) parentage. YB_2C_2 and LuB_2C_2 are superconductors with respective transition temperatures, T_c, of 3.6 K and 2.4 K.[268] Other LnB_2C_2 compounds show magnetic ordering transitions below 30 K and are not superconducting. DyB_2C_2 and HoB_2C_2 are known to undergo antiferroquadrupolar (AFQ) ordering then below T_N, the antiferromagnetic ordering coexists with the AFQ order.[263, 265, 267, 269, 270] AFQ ordering yield supercell structures that are determined using resonant X-ray scattering and neutron diffraction techniques.[263-265, 269] Among the LnB_2C_2 compounds, TbB_2C_2 is unique in that it is the only one known to exhibit field-induced AFQ ordering.[266]

GdB_2C_2 presents the simplest computational problem with magnetic consequences; Gd lacks an orbital moment, hence the magnetic anisotropy is very small. The magnetic exchange coupling is usually strongest for Gd compounds among isostructural rare earth compounds, and it has no quadrupolar moment. Neutron

diffraction experiments on a crystalline powder sample of GdB_2C_2 showed an antiferromagnetic phase transition at 47.5 K; the magnetic cell is the same as the unit cell (*a*, *a*, *c*), but with reduced symmetry (magnetic space group: P4/m).[252] The magnetic moments are antiferromagnetically ordered in the *ab* plane and are aligned along the *c* axis (Figure 6.2). We have previously shown that first principles calculations based on density functional theory (DFT) can correctly treat magnetic

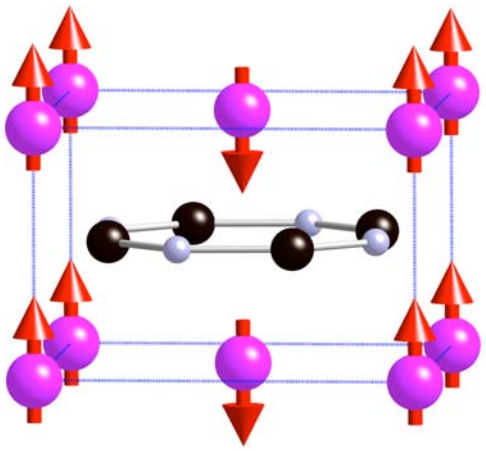

Figure 6.2. Magnetic structure of GdB_2C_2.

coupling that arises from *d*-electron mediated *f*-*f* exchange on Gd compounds and solids.[213-215] However, due to computational difficulties of DFT in our study of our spin pattern approach on Ln conductors, semi-empirical calculations, with parameters chosen to reproduce first principles benchmark results, have been developed to simulate *d*-

electron mediated *f-f* exchange in these extended systems. This allows us to circumvent convergence difficulties at reasonable computational cost.

6.2.2 Spin-Dependent Tight Binding Model

To gain some insight into the electronic structure of this material, we have carried out electronic band calculations for YB_2C_2 at the semi-empirical and first principles levels of theory. Despite its semi-empirical nature, the extended Hückel tight binding (EHTB) approach has been successful in providing a semiquantitative description of the magnetic coupling found in transition metal magnetic molecules and solids.[234, 271] In our EHTB calculations, the 4*f* orbitals on a lanthanide atoms are not explicitly included and it is generally understood that they play a minor role in bonding. Nevertheless, an adaptation of the method provides a means for interpreting the magnetic properties of Gd-containing compounds. In outline, our procedure is as follows: We use density functional (DFT) band calculations, which take into account the two-electron interactions, to provide a semiquantitative description of a nonmagnetic member of this series of compounds (i.e., YB_2C_2). Parameters for EHTB calculations (H_{ii}'s) were adjusted to simulate as closely as possible the DFT band structure for this compound. Then the exchange effects exerted by the 4*f* moments are included as a spin-dependent perturbation to the Gd atom 5*d*- and 6*s*-orbital energies (H_{dd} and H_{ss}) in the EHTB calculations. In effect, a Gd atom with *up-spin* (down-spin) 4*f* electrons, labeled "Gd^+"("Gd^-") in Appendix B, are assigned more(less) negative 5*d*/6*s* orbital energies for *up-spin* 5*d*/6*s* electrons in the tight-binding approach. Of course, the situation is

reversed for *down-spin* 5*d*/6*s* electrons, which are assigned less(more) negative 5*d*/6*s* orbital energies in the vicinity of an *up-spin* (down-spin) 4*f* center. The orbital energies and exponents were adjusted to improve the match between EHTB and DFT-BLYP band structures of Gd_2Cl_3, as described in Section 3.3.3.

The tight-binding calculations are carried out as follows: (a) for a ferromagnetic spin-patterns (all up-spin Gd centers), two EHTB calculations are performed: one for with parameters appropriate for up-spin 5*d*/6*s*-electrons and one for down-spin 5*d*/6*s*-electrons. The Fermi levels for the two calculations are set equal and chosen such that the total number of electrons for the system is appropriate; (b) for an antiferromagnetic 4*f*-spin-pattern where all the Gd atoms are crystallographically equivalent (and the magnetic structure is equivalent to its antistructure), only a single EHTB calculation is required since the up- and down-spin 5*d*/6*s* electron band structure is the same. In this case, of course, the *local* spin 5*d*/6*s* polarizations are *not* the same, but when summed over all atoms, the up- and down-spin 5*d*/6*s* populations are the same; (c) for an antiferromagnetic 4*f*-spin-pattern where all the Gd atoms are not crystallographically equivalent, the up- and down-spin 5*d*/6*s* electron band structure are not the same and two EHTB calculations must be performed and handled as in the ferromagnetic case. Some of the spin-patterns for Gd_2Cl_3, as previously reported, fell into this category but this scenario did not occur in this solid.[214]

Preliminary calculations using the standard EHTB parameters yielded good correspondence between the EHTB band structure for $B_2C_2^{2-}$ (CaB_2C_2 without Ca atoms included) and the CaB_2C_2 DFT band structure. It was therefore deemed reasonable to

expect that only modest changes of the yttrium parameters would be necessary to improve the agreement between DFT and EHTB for YB_2C_2. To determine the ionization potential and Slater exponents for the yttrium atom, we compared characteristics of density of states (DOS) plots in an attempt to match band gaps, bandwidths, and local maxima and minima. The resulting total DOS are depicted in Figure 6.3, with projected DOS showing the contribution by the Y *d*-orbitals in the

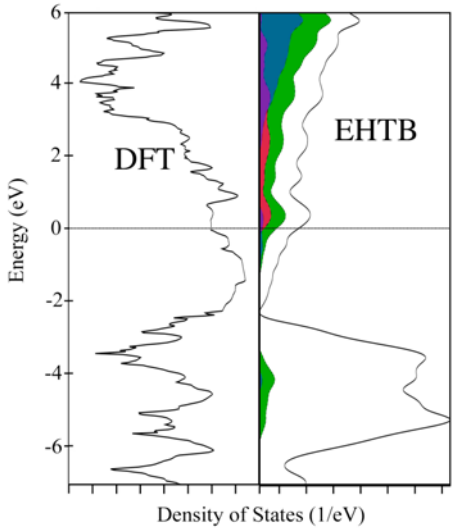

Figure 6.3. Density of States plot for YB_2C_2 for DFT and EHTB. Green (light gray): $d_{x^2-y^2}$, d_{xy}; blue (dark gray): d_{z^2}; red (gray): d_{xz}, d_{yz}.

tight binding case.[272] The bands near the Fermi level (for which a good match is crucial for success of this approach), the correspondence between the EHTB and DFT calculations is good; the borocarbide σ and π bands have approximately the same bandwidths and the conduction band begins at about the same relative energies. The

DOS curves obtained from the EHTB calculations clearly indicate that the states in the vicinity of the Fermi level are have predominantly yttrium *d* character, with some stabilization provided by mixing from the borocarbide π* bands. These bands arise mainly from the $x^2–y^2/xy$ type orbitals (the *d* orbitals 'in the *ab*-plane') on yttrium, plus the π* orbitals of the borocarbide net. The calculated dispersion curves for these bands along several symmetry lines of the Brillouin zone (BZ) are shown in Figure 6.4 for YB_2C_2 using EHTB and DFT computations. Figure 6.5 depicts the tetragonal Brillouin

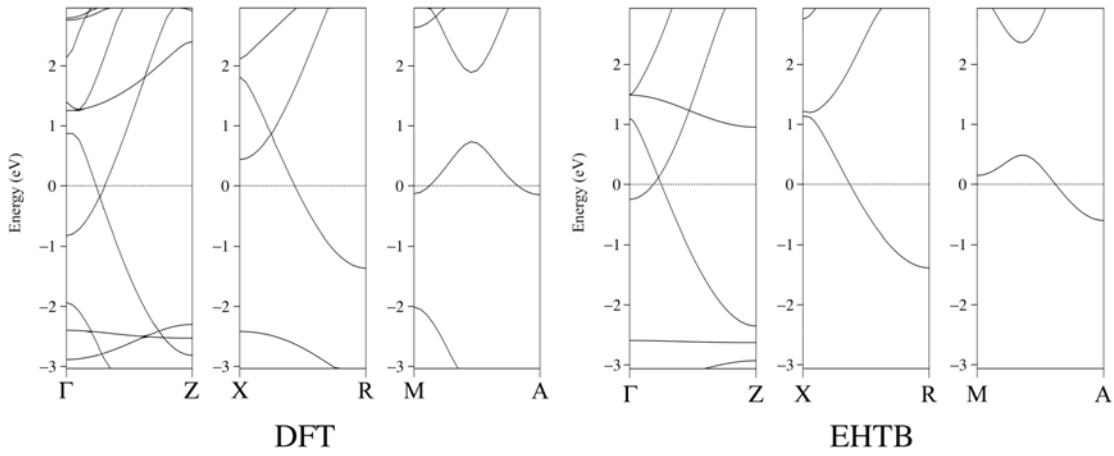

Figure 6.4. Band structure of YB_2C_2 using DFT and EHTB.

zone. The bands calculated by both methods "run" the same way, and except for small energy differences at the high symmetry points, the two methods yield very similar results (See Appendix E for a full band structure). At the Fermi level, they exhibit dispersion of about 3.5 eV along the *c* direction (Γ–Z direction of the BZ) and 0.5 eV in

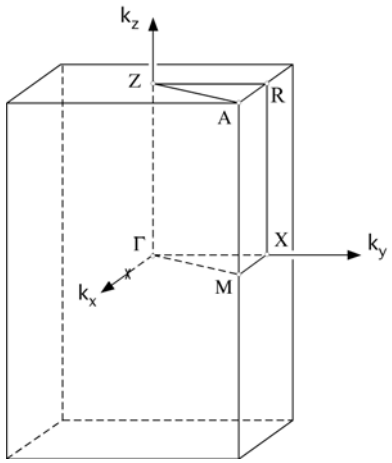

Figure 6.5. Brillouin zone for a tetragonal cell.

the *ab* plane (X–M and R–A directions of the BZ). While band cut by the Fermi level have primarily x^2–y^2/*xy* character (with a π* borocarbide admixture), near Γ the yttrium-based band with z^2 character descends to cross the Fermi level. A comparison of Mulliken charges for YB_2C_2 from DFT and EHTB methods reveal that the EHTB charge distribution is characteristically more highly polarized, but they are in accord with the trends found in DFT.[273]

Figure 6.6 depicts approximate[274] Fermi surfaces (FS) as they emerge from DFT and EHTB calculations on YB_2C_2. In both cases, the large undulating surface results from a cut through the x^2–y^2/*xy*/π* band, and the pocket of electrons surrounding the Γ point results from a cut through a small segment of the z^2 band that dips below the Fermi level at the BZ center. The close similarity between the two surfaces reveals the closeness with which the parameterized EHTB calculations reproduce the DFT calculations.

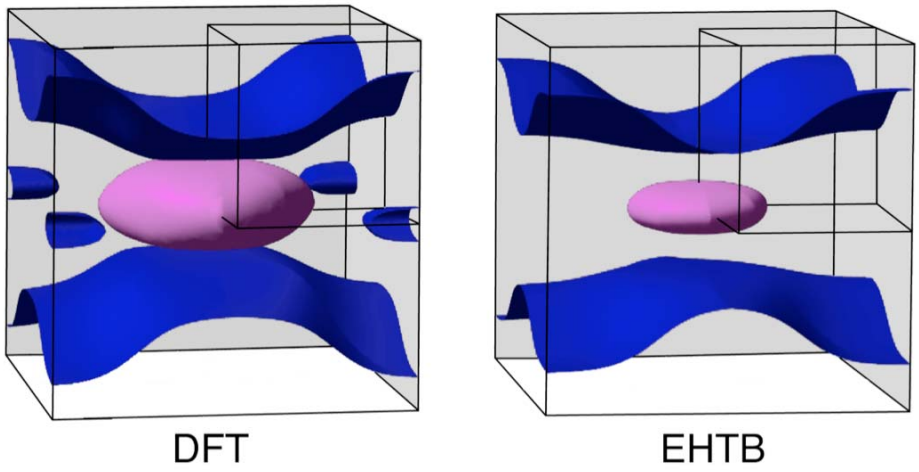

Figure 6.6. Fermi surface for YB_2C_2 using DFT and EHTB. The dark blue (dark gray) refers to the large undulating surface and the violet (light gray) refers to the pocket of electrons.

6.2.3 Magnetic Ordering in GdB_2C_2

In our study of the magnetic ordering in "GdB_2C_2", we performed calculations on 6 competing spin patterns. These include the observed antiferromagnetic ordering pattern, with a magnetic unit cell commensurate with the structural cell (*a*, *a*, *c*); a ferromagnetic pattern; and two additional spin-patterns for each of two different supercells, (*a*, *a*, *2c*) and (*2a*, *2a*, *c*), shown in Figure 6.7. The calculated relative energies for the patterns are shown in Figure 6.8. In each case, we indicate the periodicity and space group imposed by the 4*f* exchange potential. The results in

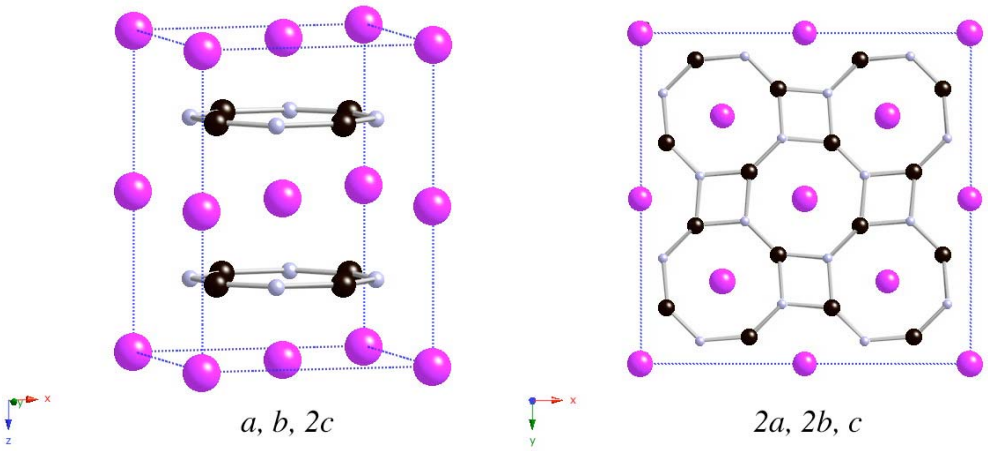

Figure 6.7. Proposed magnetic superstructures for "GdB_2C_2".

Figure 6.8 show a preference for an antiferromagnetic spin pattern corresponding to the experimentally observed spin ordering with adjacent magnetic moments parallel along the *c* axis and antiparallel within the *ab* plane. The second- lowest energy pattern is the ferromagnetic case. The exchange potential of both these spin-patterns is consistent with the 4/*m* symmetry in the Gd atoms, situated as they are between the B_4C_4 rings. The other spin patterns, in which the 4*f* spins change the translational periodicity, lie higher in energy. For two of those spin patterns, the symmetry of magnetic cell (and therefore, the exchange potential) is reduced from tetragonal to orthorhombic.

Label, Supercell, Relative EHTB Energy Ising Expression	Spin Patterns	Label, Supercell, Relative EHTB Energy Ising Expression	Spin Patterns
Antiferro II (2x2x1) (*2a*, *a*, *c*) $Pmc2_1$ 794.7 cm^{-1} $-2J'_3$	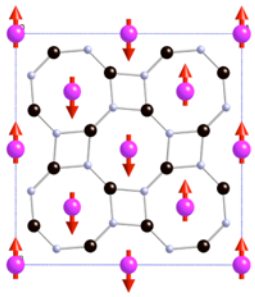	Antiferro II (1x1x2) (*a*, *a*, *2c*) P4/mbm 111.8 cm^{-1} $-4J'_1-4J'_2+2J'_3$	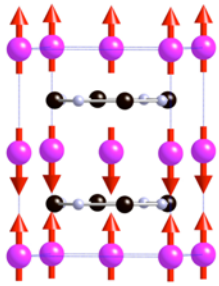
Antiferro III (2x2x1) (*2a*, *2a*, *c*) Pmma 780.9 cm^{-1} $-4J'_1-2J'_3$	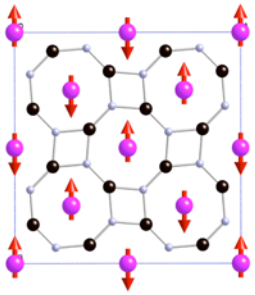	Ferromagnetic (1x1x1) (*a*, *a*, *c*) P4/mbm 108.5 cm^{-1} $-4J'_1-4J'_2-2J'_3$	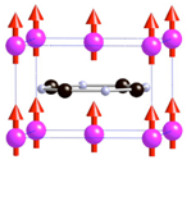
Antiferro III (1x1x2) (*a*, *a*, *2c*) P4/mnc 251.8 cm^{-1} $-4J'_1+4J'_2+2J'_3$	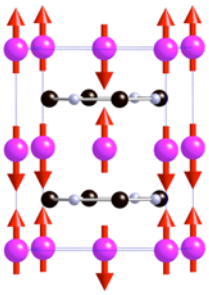	Antiferro I (1x1x1) (*a*, *a*, *c*) P4/m 0.0 cm^{-1} $-4J'_1+4J'_2-2J'_3$	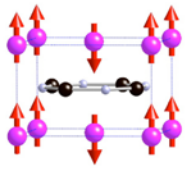

Figure 6.8. Proposed spin patterns for "GdB_2C_2" using P4/*mbm* symmetry.

It is interesting to evaluate whether the relative energies of the spin patterns can be described in terms of Ising coupling constants (J'), as shown in Figure 6.9. Six spin

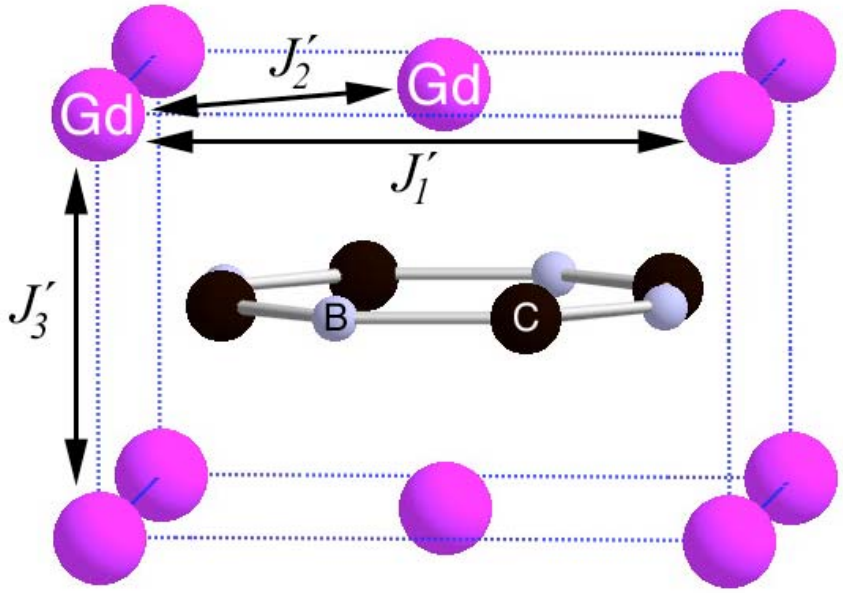

Figure 6.9. Provisional Ising coupling constants for "GdB_2C_2".

patterns yield five independent energy differences and these energy differences can also be expressed in terms of expression involving Ising coupling parameters. We attempted the use of a linear least squares fit to "determine" the three magnetic coupling constants. The *J′* values predict ferromagnetic coupling for J'_1 (112.05 ± 34.0 cm^{-1}) and J'_3 (35.83 ± 54.4 cm^{-1}), and antiferromagnetic coupling for J'_2 (-9.63 ± 26.9 cm^{-1}). Though the sign of *J′* values is sufficient to reproduce the experimentally determined magnetic structure, even the *ordering* of the spin-patterns shown in Table 6.1 is not reproduced with the Ising parameters. Just as we concluded in our study of Gd_2Cl_3,[214] an Ising model is clearly inappropriate for describing the *d*-electron mediated magnetic interaction between the 4*f* moments.

Table 6.1. Comparison of spin pattern energies with a "best fit" Ising model (J') for "GdB_2C_2".

$E_A - E_{Antiferro1}$	$\Sigma_{i,j} Z_{i,j} J'_{i,j}$	EHTB Energy difference (cm^{-1})	Ising energy difference (cm^{-1})
$E_{Ferro} - E_{Antiferro1}$	$-8J'_2$	108.5	77.0
$E_{Antiferro3(1\times1\times2)} - E_{Antiferro1}$	$4J'_3$	251.8	143.3
$E_{Antiferro2(1\times1\times2)} - E_{Antiferro1}$	$-8J'_2+4J'_3$	111.8	220.3
$E_{Antiferro3(2\times2\times1)} - E_{Antiferro1}$	$8J'_1-4J'_2$	780.9	934.9
$E_{Antiferro2(2\times2\times1)} - E_{Antiferro1}$	$4J'_1-4J'_2$	794.7	486.7

In previous work, we have been able to describe the magnetic coupling of *d*-electron mediated *f-f* exchange using our perturbative-theoretic approach.[213-215] To briefly introduce our approach using the simple example, imagine a Gd atom with a $4f^7 5d^1 6s^2$ configuration where the $5d^1$ electron experiences an average (spin-independent) field from the up-spin $4f^7$ electrons (left side of Figure 6.10). Upon turning on the effect

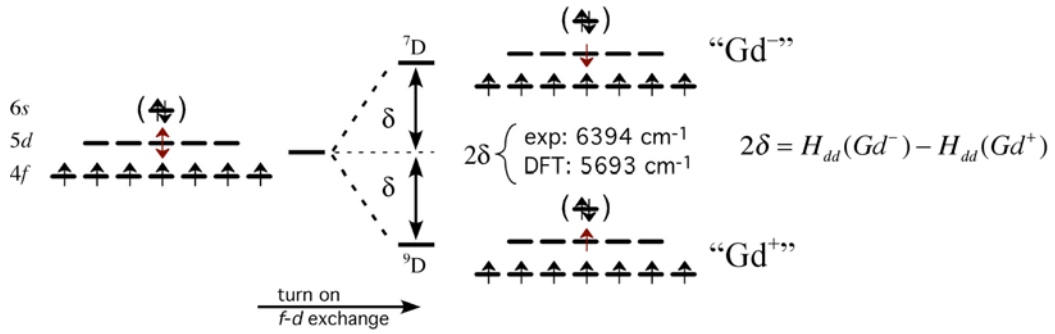

Figure 6.10. Electronic splitting of Gd atom as a function of 4*f*-5*d* exchange perturbation. The labels "Gd^+" and "Gd^-" represent the stabilization/destabilization effect that we simulate in our EHTB calculations.

of exchange, the *d*-electron with its spin aligned (against) the $4f^7$ shell is stabilized (destabilized) by an energy δ. This is the stabilization/destabilization effect of the *s*- and *d*-shell that we simulate in our EHTB calculations. SDFT/BLYP underestimates the spectroscopically measured gap by 11%.[54] Applying this same language to our "GdB_2C_2" system, Figure 6.11 shows the band dispersion plot for the lowest energy antiferromagnetic spin pattern (Antiferro1 from Figure 6.8). It is also important to note that the "α" and "β" spin bands in this case are identical because although the *d*-electrons experience a relative stabilization and destabilization when in the vicinity of like- and unlike-spin $4f^7$ moments, the $4f^7$ moments distributed over symmetry-equivalent sets of atoms.

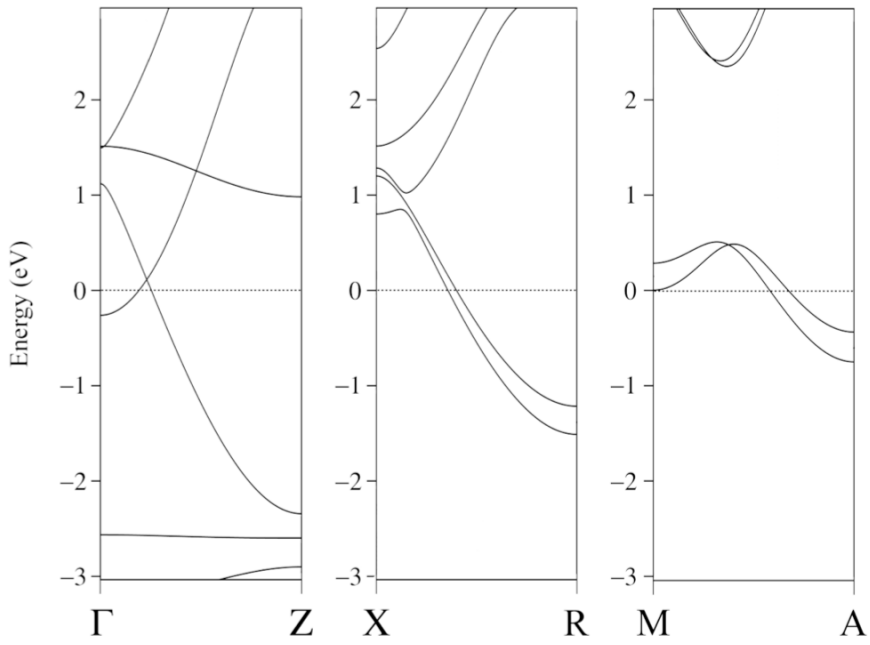

Figure 6.11. Band structure for the lowest energy spin pattern (Antiferro1) for GdB_2C_2.

The band dispersion curves are similar to that for the unperturbed (spinless) YB_2C_2 plot (Figure 6.4), but curves plotted along XR and MA are split from their averaged (spinless) position. In contrast, the ferromagnetic spin pattern induces an exchange energy stabilization and destabilization of bands with spins respectively aligned with and against the $4f^7$ moments. Our "Gd^+" and "Gd^-" parameters provide a simulation of this effect. To understand the interaction in the lowest energy antiferromagnetic spin pattern, imagine the YB_2C_2 band diagram (from Figure 6.4) as a qualitative representation of the magnetic structure, not taking into account the *d-f* exchange perturbation. Then upon applying the "Gd^+" and "Gd^-" spin arrangement, the space group symmetry lowers from *P*4/*mbm* to *P*4/*m*, thereby distinguishing the two erstwhile "yttrium" atoms. The nearest-neighbor interactions along the *c* axis are ferromagnetic and bands along ΓZ remain degenerate because the *d*-character maintainsthe same interaction with the borocarbide π* rings. However, the antiferromagnetic ordering in the *ab* plane splits the bands along XR and MA as a result of differing bonding effects of the "Gd^+" and "Gd^-" combinations with the borocarbide π* rings.

The electronic instabilities can sometimes be related to the topology of a compound's Fermi surface. If a large area of the Fermi surface can be translated by a vector $\boldsymbol{q}$ and superimposed on another region of the surface, then the FS is said to be "nested" by the vector $\boldsymbol{q}$. Ignoring the pocket of electrons from the z^2 band around Γ (see Figure 6.6), the undulating sheets would seem to be superimposable on one another by a vector of (0.5, 0.5, 0.52) (using DFT) or (0.5, 0.5, 0.44) (using EHTB) To see this,

focus on the center of the lower sheet, and the corner of the upper sheet. However, the curvatures of the two sheets are different enough that this "nesting" is rather poor. The presence of the z^2 "pocket" further disrupts any potential nesting. If "Fermi surface nesting" were apparent then we might have expected to observe an antiferromagnetic spin pattern with an enlarged unit cell commensurate, or nearly commensurate, with the nesting vector. As it happens, it is difficult to rationalize a spin pattern preference based on Fermi surface arguments.

It is of interest to ask whether the incorrect "*P*42*c*" structure type would be expected to exhibit magnetic ordering consistent with the observed neutron diffraction results. We performed calculations on four competing spin patterns (Figure 6.12), which included the antiferromagnetic ordering observed in the *P*4/*mbm* structure, a ferromagnetic pattern and three additional antiferromagnetic spin-patterns. Interestingly, the wrong structure type produces the wrong magnetic ordering. The lowest spin pattern predicts antiferromagnetic alignment along the *ab* plane, the lowest pattern predicts antiferromagnetic coupling along the *z*-axis.

Label, Magnetic cell, Relative EHTB Energy	Spin Patterns
Ferromagnetic (a, b, c) $P4_2/mcm$ 335.4 cm^{-1}	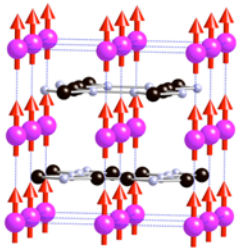
Antiferro I ($2a$, $2b$, $2c$) $P4_2/nnm$ 0.0 cm^{-1}	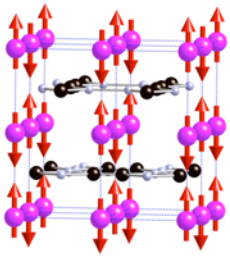
Antiferro II ($2a$, $2b$, c) $P4_2/mcm$ 56.8 cm^{-1}	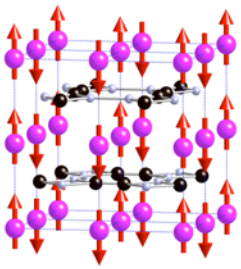
Antiferro III (a, b, $2c$) $P4_2/mcm$ 13.7 cm^{-1}	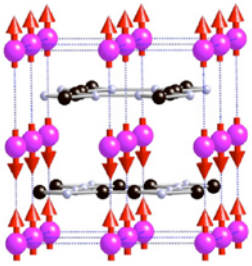

Figure 6.12. Proposed spin patterns for "GdB_2C_2" using "*P*42*c*" symmetry.

6.3 α-Gd_2S_3

α-Gd_2S_3 has an orthorhombic structure (*Pnma*) wherein two types of cation polyhedra which are linked to form a three-dimensional structure. [275-277] The crystal structure of α-Gd_2S_3 projected onto the *ac* plane is shown in Figure 6.13.

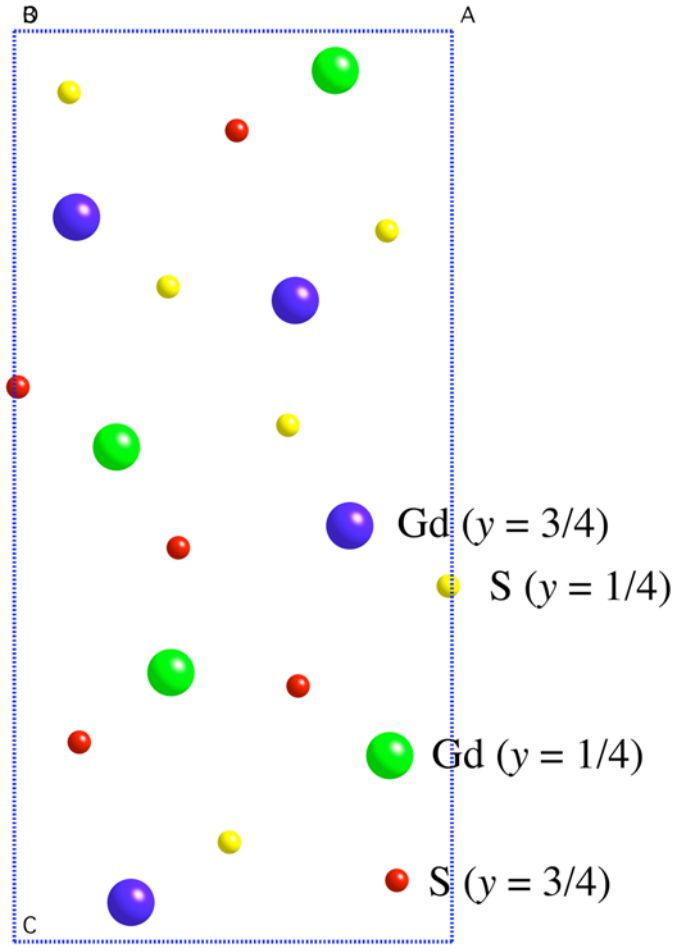

Figure 6.13. The crystal structure of α-Gd_2S_3 projected onto the *ac* plane. Gd atoms are large circles and S atoms are small circles. The light circles represent the atoms at y = ¼ and the dark circles represent the atoms at y = ¾.

One cation forms an eight-coordinate bicapped trigonal prism with the surrounding sulfur atoms (Figure 6.14A) and seven sulfur atoms form a distorted monocapped trigonal prism around the other cation (Figure 6.14B).

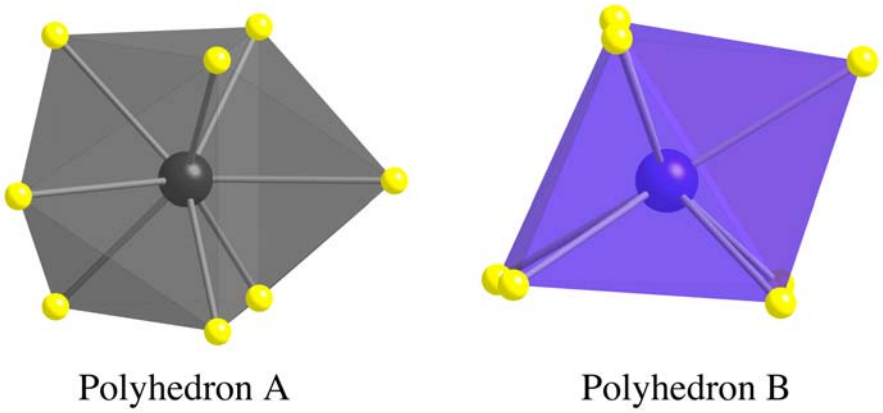

Figure 6.14. Coordination polyhedra in Gd_2S_3. Left: GdS_8 bicapped trigonal prisim. Right: GdS_7 monocapped trigonal prism.

There are five structure types for Ln_2S_3 (Ln = lanthanides), two of which are known for Gd_2S_3: α-Gd_2S_3 and γ-Gd_2S_3 which has the Th_3P_4-type structure (*I*43*d*) where 1/9 of the sites of the metal sublattice are unoccupied.[278-280] Until recently, interest in the magnetic and electrical properties at low temperatures have focused on the γ-type structure. Although γ-Gd_2S_3 exhibits Néel temperature near 4 K, Gd-doping of can lead to giant magnetoresistance (GMR) or an antiferromagnet-ferromagnet transition along with semiconductor-metal transition.[281-283]

Researchers have recently reported the results of electrical resistivity and magnetic measurements for α-Gd_2S_3 that exhibit an antiferromagnetic transition at T_N = 10 K and semiconducting behavior for electronic transport along the *b*-axis show semiconducting behavior.[277] These reports contradict previous results which predicted Curie-Weiss behavior down to 4.2 K with a Weiss constant of -8 K and very weak interactions between the gadolinium atoms.[275, 276] However, magnetic results have been confirmed from an anomaly at T_N = 9.8 K in heat capacity measurements which indicate the occurrence of long-range magnetic ordering.[284] They report that the crystal exhibits anisotropic behavior in the T dependence of χ on the basis of a coupled two-leg spin ladder model and the observation of a novel phase transition in α-Gd_2S_3 to be due to geometric frustration.[277, 284] To determine the magnetic structure and the effects of geometric frustration, neutron diffraction experiments were performed on powder samples of α-Gd_2S_3 and determined that the magnetic cell is the same as the chemical unit cell.[244] Results show that magnetic moments align ferromagnetically along the *b* axis and researchers proposed the ordering in the *ac* plane by matching observed magnetic intensities with those predicted for various alternative spin pattern arrangements (Figure 6.15).[244] Independent synchrotron X-ray diffraction studies in zero and non-zero applied fields supports these findings.[285] A study of this system using our spin pattern approach is ideal since two independent studies determined the same magnetic structure.

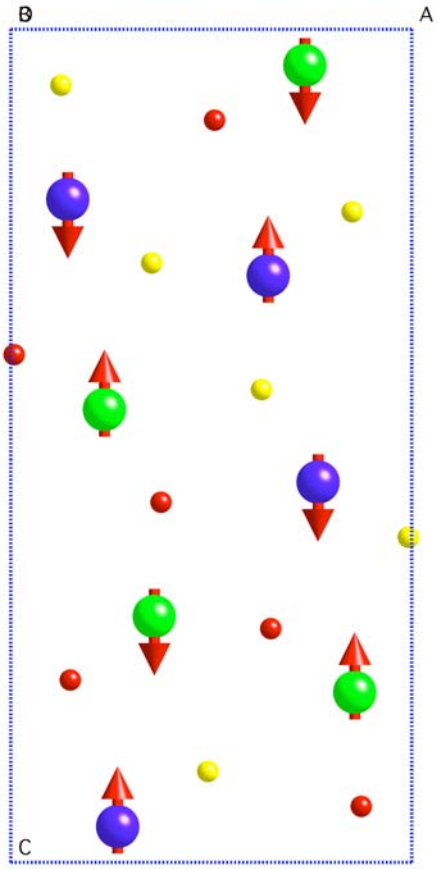

Figure 6.15. Magnetic structure of α-Gd_2S_3 in the *ac* plane.

Figure 6.16 shows the resulting DOS for electronic structure calculations using the yttrium analog, Y_2S_3, at the semi-empirical and first principles level of theory.[286] The DOS plots yields the expected semiconducting behavior, with an energy gap of ~2.4 eV separating the S *p*-levels from the Y *d*-levels.

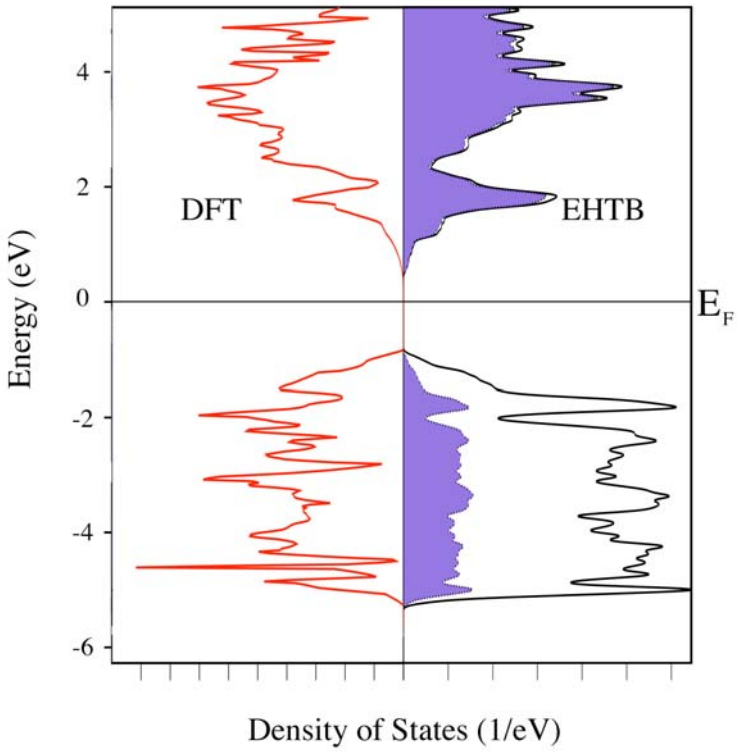

Figure 6.16. DOS plot for α-Y_2S_3 for DFT and EHTB calculations. The contribution from Y is shaded blue.

Based on the magnetic cell, there are 19 possible antiferromagnetic spin pattern arrangements for α-Gd_2S_3.[244] For our study, we carried out electronic band calculations using EHTB for eight spin patterns of "α-Gd_2S_3": one ferromagnetic and seven antiferromagnetic. The antiferromagnetic spin patterns were chosen based on the possible magnetic structure consistent with the chemical space group *Pnma*.[244] Two calculations were necessary for the ferromagnetic and Antiferro7 spin patterns. The results from Figure 6.17 show a preference for the magnetic structure predicted

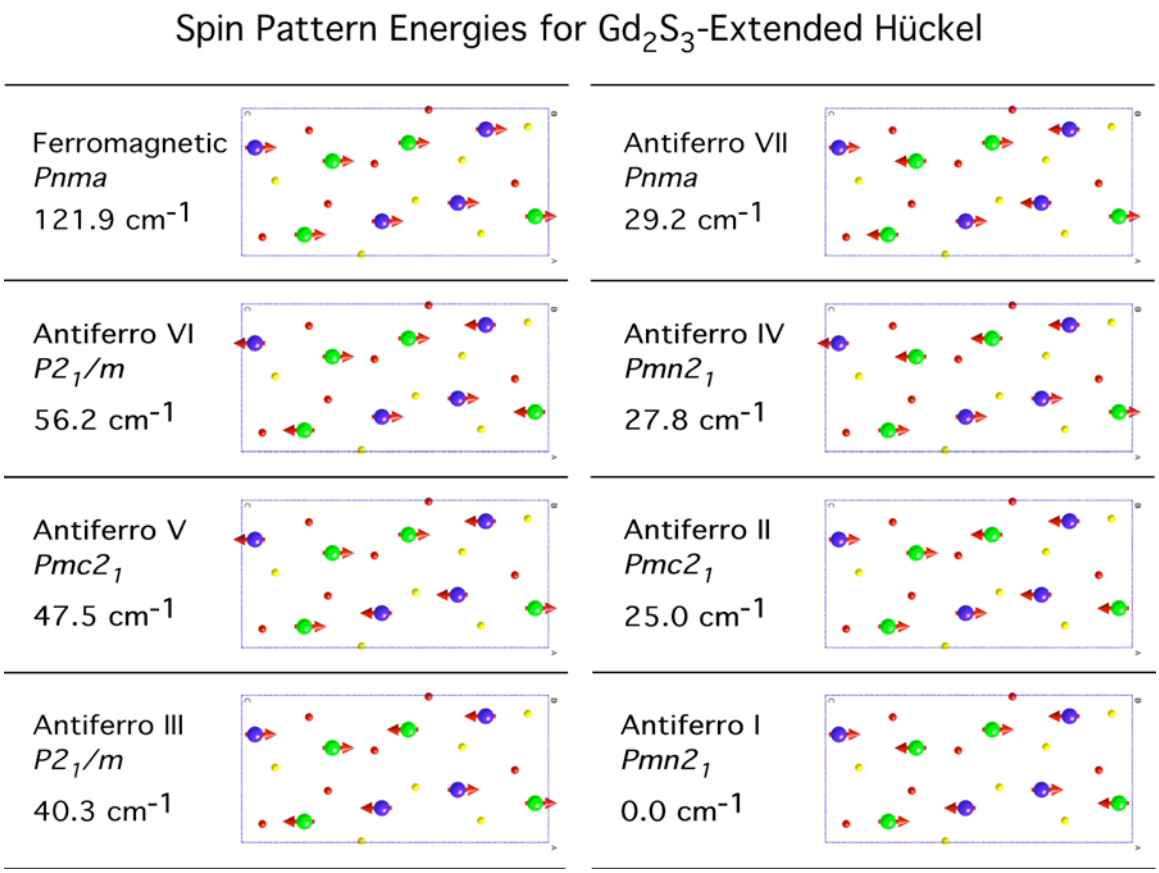

Figure 6.17. Proposed spin patterns for "α-Gd_2S_3".

from group theoretical arguments. The Gd moments adopt antiferromagnetic alignment among atoms within their respective *ac*-planes. Although we were unable to achieve SCF convergence for this solid using DFT for multiple ***k***-points, results from ***k*** = 0 show a preference for observed antiferromagnetic spin pattern (Table 6.2), but the meaning of results based on a single ***k***-point are questionable.

Table 6.2. Comparison of EHTB and DFT results (***k*** = 0) of eight spin patterns and energies for the model of Gd_2S_3.

Spin Pattern	EHTB (cm^{-1})	BLYP/DFT (***k*** = 0) (cm^{-1})
AntiferroI	0	0
AntiferroII	25.0	215.3
AntiferroIV	27.8	211.8
AntiferroVII	29.2	244.3
AntiferroIII	40.3	158.7
AntiferroV	47.5	320.1
AntiferroVI	56.2	128.8
Ferro	121.9	439.6

In view of our foregoing discussions, it is not surprising that α-Gd_2S_3 orders antiferromagnetically given the nature of the solid (no *d*-electrons). In the same spirit of our analysis for Gd_2Cl_3, Figure 6.18 compares the DOS plots for the ferromagnetic and lowest energy antiferromagnetic spin pattern. Our calculations predict semiconducting behavior and calculated gap is nearly equal (~2.2 eV) for antiferro1 and ferro spin patterns. Examination of the "Gd^+" and "Gd^-" DOS plots for the ferromagnetic spin patterns shows a slight stabilization and destabilization of the α- and β- electrons, respectively, however the effect is not nearly as dramatic as in previously discusses systems.

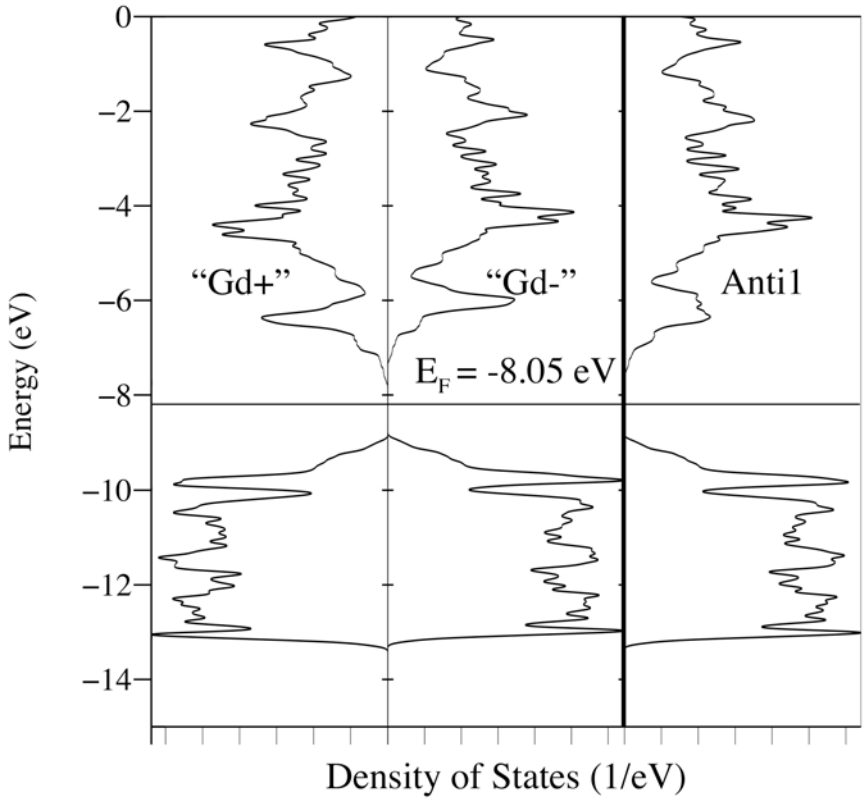

Figure 6.18. DOS plots of the ferro and antiferro1 spin patterns.

6.4 Gd_5Si_4 and Gd_5Ge_4

Gd_5Si_4 exhibits one of the highest Curie temperatures (T_C = 336 K) for a Gd-nonmagnetic element compounds whereas the isotypic Gd_5Ge_4 orders antiferromagnetically at T_N = 15 K.[287] Both compounds crystallize in the orthorhombic Sm_5Ge_4-type structure and their structures can be described as a stacking of successive T_2 (*G*), Gd_4 (*S*), and Gd_2T_4 (*C*) nets up the crystallographic *b* axis where T = Si, Ge (Figure 6.19; compositions indicate the contents per cell).[288] Because a detailed

discussion of the structural features can be found elsewhere, we will only briefly describe the salient features.[288]

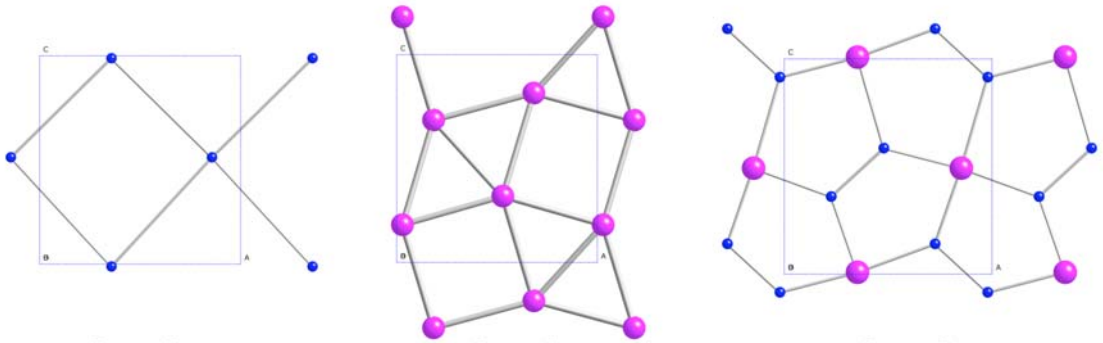

Figure 6.19. The three types of networks found in Gd_5Si_4 and their elevations along the *b* axis. Large circles: Gd; small circles; Si.

Layer *G* contains only two T atoms (M = Si, Ge) which forms a 4^4 network, layer *S* contains four Gd atoms forming a 3^2434 network, and layer C is composed of four T (T = Si, Ge) plus two Gd atoms which form a pentagonal 5^3+5^4 net lying in the mirror plane at y = ¼. Layers *S* and *C* form dual nets and layer *C* is a combination of *G* and *S* where the roles of T (T = Si, Ge) and Gd interchanged. The stacking sequence for $0 \leq y \leq ½$ is *GSCSG* with layer *C* at $y = ¼$ serving as a mirror plane in *Pnma*. A twofold screw operation around the *b*-axis operates on these nets to generate the same stacking sequence for $½ \leq y \leq 1$. The coordination polyhedra for atoms in the layer *C* and are shown in Figure 6.20. The Gd atoms located at $y = ¼$ are surrounded by a distorted cube

of Gd atoms and an octahedron of T atoms (T = Si, Ge), thereby giving the center Gd a coordination number of 14 (Figure 6.20A).[289]

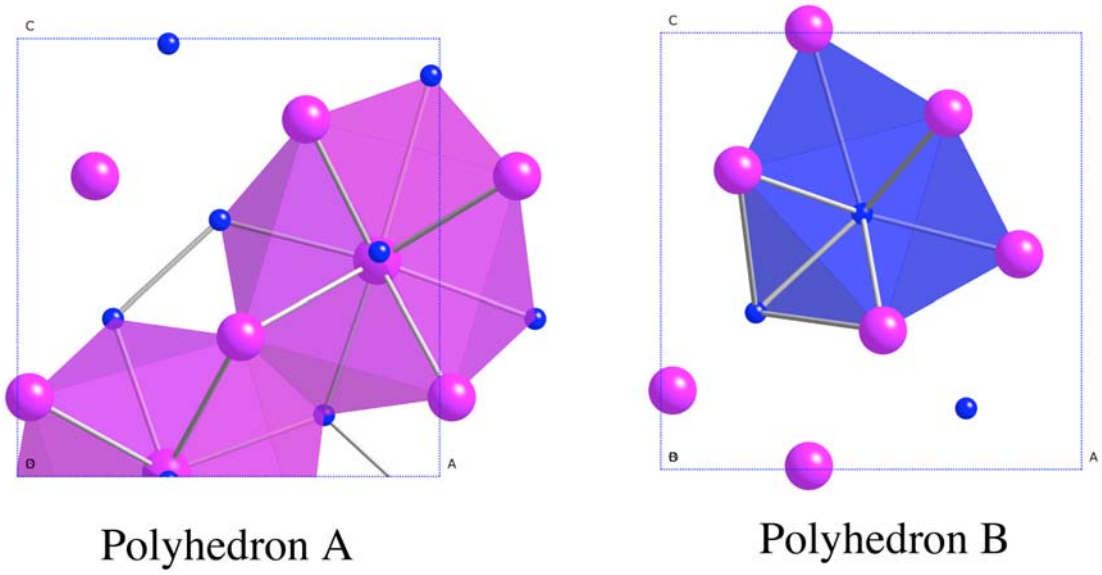

Figure 6.20. Coordination polyhedra found in Gd_5Si_4: (a) Gd coordination, (b) Si coordination.

The T atoms (T = Si, Ge) at y = ¼ are surrounded by 6 Gd atoms in a trigonal prismatic arrangement with 2 Gd and 1 T atom within layer *C* completing the ninefold coordination (Figure 6.20B). Gd_5T_4 (T = Si, Ge) have distinctly layered crystal structures wherein the polyhedra create two-dimensional slabs which are or are not be connected with one another via covalent-like T-T bonds (Figure 6.21). Taking into account the covalent contacts, Gd_5Si_4 and Gd_5Ge_4 can be formulated as $(Gd^{3+})_5(Si_2^{6-})_2(e^-)_3$ and

$(Gd^{3+})_5(Ge_2^{6-})(Ge^{4-})_2(e^-)$, in which three and one extra electron(s), respectively, occupy the low-lying metal-metal bonding band.

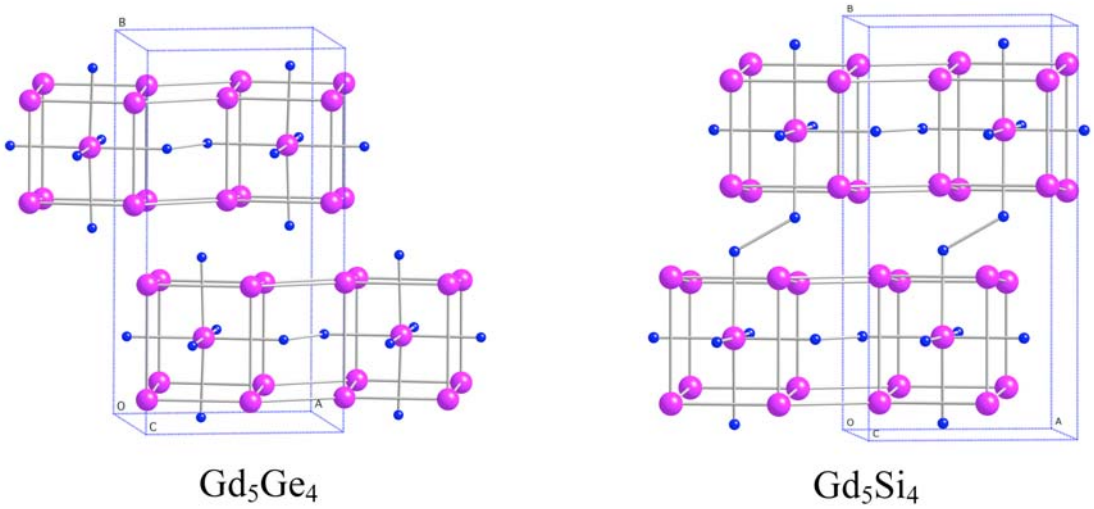

Figure 6.21. Perspective view of Gd_5Ge_4 and Gd_5Si_4 along [110].

Rare-earth (R) silicon/germanium (T) compounds with R_5T_4 compositions have been extensively studied over the past several years for their interesting crystallographic, magnetic and other physical properties.[287, 290-303] These compounds' magnetocaloric properties are of particular interest, demonstrating the feasibility of magnetic refrigeration using magnetic materials with magnetic ordering temperatures near room temperature.[304-310] To improve the efficiency of magnetic refrigerators, materials with Curie temperatures (T_C) even higher than that of elemental Gd (293 K) are called desirable.[307, 311, 312] Among such compounds are Gd_5Si_4 (T_C = 336 K) and Gd_4Bi_3 (T_C =

333 K).[287, 313] The Curie temperature and dramatic magnetocaloric effect observed for Gd_5Si_4 [307] are affected by substitution of Ge for Si; at the $Gd_5(Si_2Gd_2)$ composition, the room temperature crystal structure changes from orthorhombic to monoclinic and T_C drops from ~300K to ~275K. [287, 314] The crystallography and magnetism of $Gd_5(Si_xGe_{4-x})$ systems are closely related and the ferromagnetic state is observed when all slabs are interconnected as in the Gd_5Si_4-type structure.[315] The extensive research on the binary and pseudo-binary phases makes Gd_5Si_4 and Gd_5Ge_4 an attractive system for testing our EHTB spin-pattern approach.

6.4.1 Electronic Structure of Y_5Si_4 and Y_5Ge_4

We carried out electronic structure calculations for the yttrium analog, Y_5Si_4 and Y_5Ge_4, at the semi-empirical and first principles levels of theory and the resulting DOS plots are depicted in Figure 6.22, with the projected DOS of the Y *d*-orbitals in the EHTB case.[316] The bands near the Fermi level are in very close correspondence for both structures. DOS plots clearly show that the states at the Fermi level contain predominantly yttrium *d* character. Comparing Y_5Si_4 first, both DOS plots generated by EHTB and DFT show an energy gap of ~0.5 eV located ~0.5 eV below the Fermi energy. The occurrence of the gap is easily rationalized by formally recognizing the Si_2 units in the structure, $Y_5Si_4 = (Y^{3+})_5(Si_2^{6-})_2(e^-)_3$; three electrons (per formula unit) occupy the bottom of the Y 4*d* bands above the gap. Further information can be extracted from the calculated dispersion curves for these bands along several symmetry lines of the Brillouin zone (BZ) are shown in Figure 6.23 using EHTB. The gap is wider

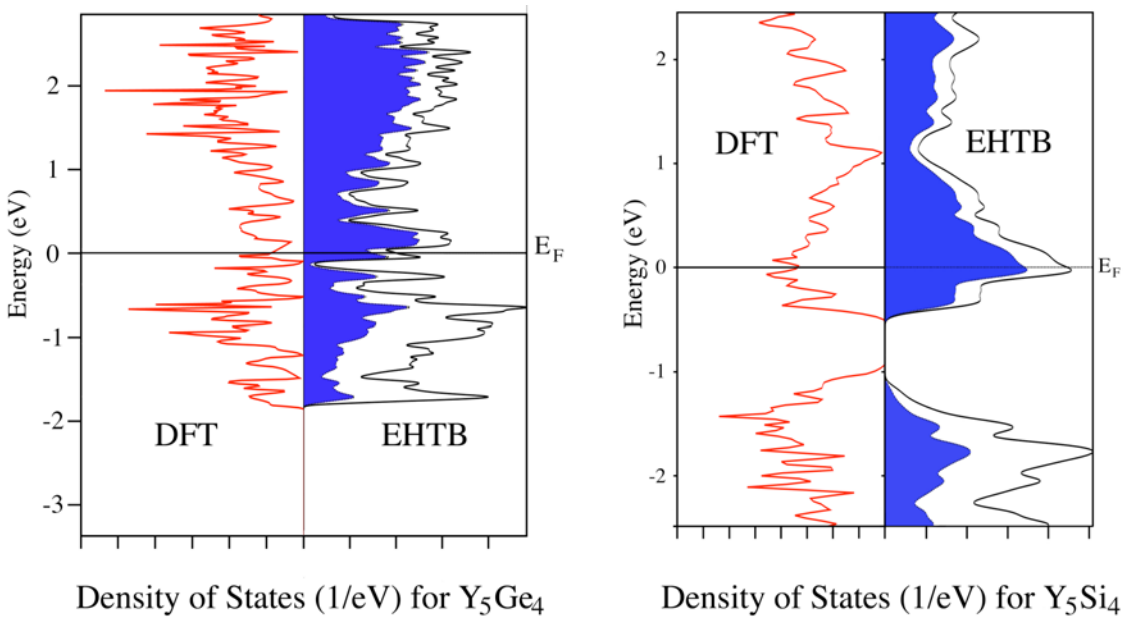

Figure 6.22. Density of States plot for Y_5Ge_4 (left) and Y_5Si_4 (right) for DFT and EHTB calculations. The contribution from Y is shaded blue (black).

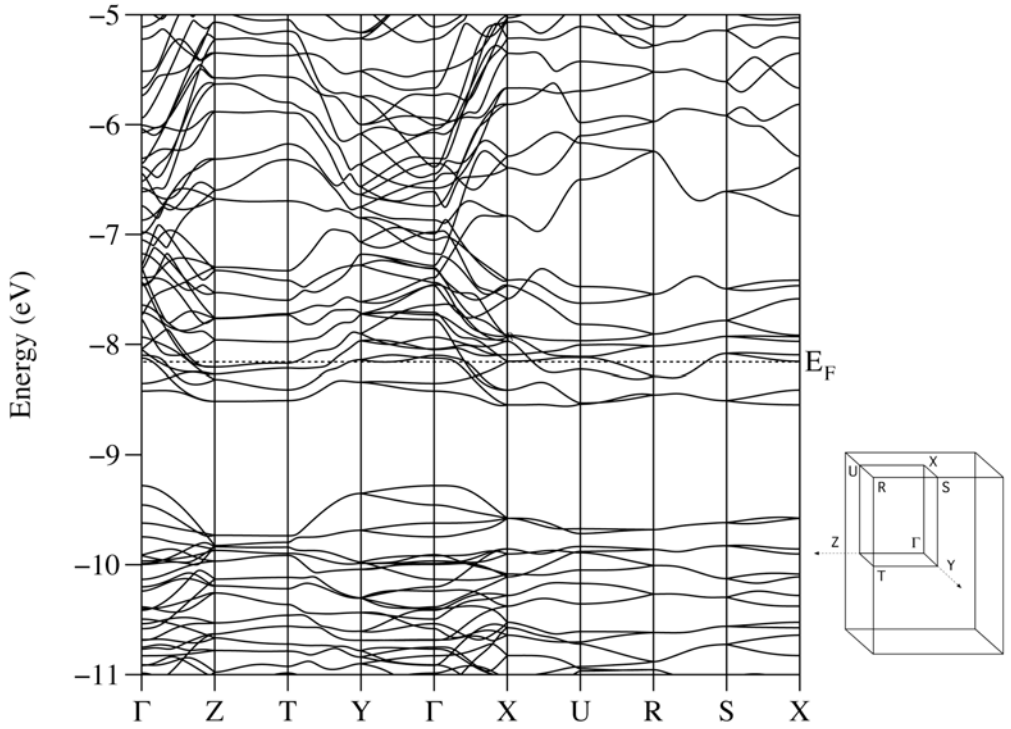

Figure 6.23. Band dispersion plot for Y_5Si_4 using EHTB.

(~1.2 eV) along several points of the BZ and a narrowing of a few bands occurs along the Γ-X and Γ-Y direction.

For the Y_5Ge_4 compound, the Fermi level intersects a very narrow peak and there is a narrow pseudo-gap just below the Fermi energy. The band structure shows a narrowing of bands occurring along the Γ-X direction and the narrow peak consists of four crystal orbitals (Figure 6.24). Levin *et al*. interpreted this peak as arising from the four Gd-Gd σ-bonding orbitals formed from z^2 orbitals due to short Gd-Gd contacts (3.532 Å) between the 2D slabs (Figure 6.25).[315] The band structures are similar to results obtained in previously reported tight-binding linear muffin-tin orbital (LMTO)

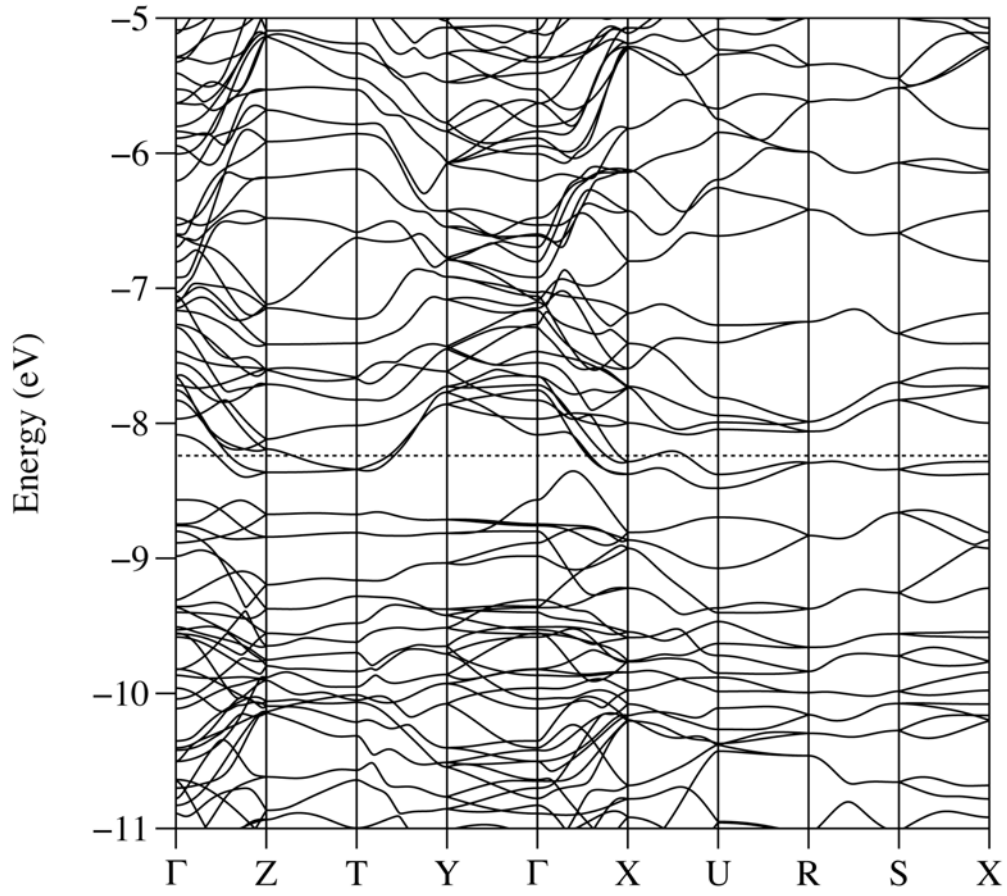

Figure 6.24. Band dispersion plot for Y_5Ge_4 using EHTB.

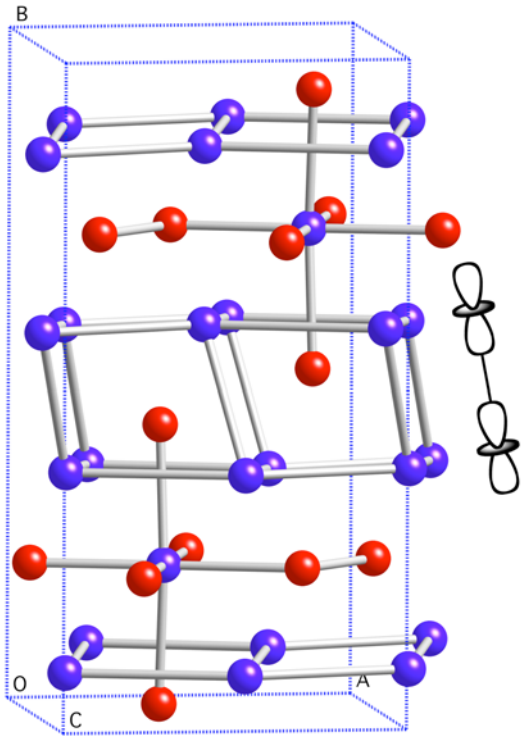

Figure 6.25. Projection of Gd_5Ge_4 along [001] direction emphasizing the Gd-Gd interactions between slabs. The nature of the orbital is illustrated at the right.[315]

calculations on Gd_5Si_4[295] and Gd_5Ge_4,[295, 315] but the former predicted a much narrower gap of ~0.05 eV between the Si *p* and Gd *d* levels below the Fermi level.

6.4.2 Magnetic Ordering in Gd_5Si_4 and Gd_5Ge_4

We performed calculations on 4 competing spin patterns for "Gd_5Si_4" and "Gd_5Ge_4" which included the ferromagnetic pattern and three additional antiferromagnetic patterns, with their calculated relative energies shown in Figure 6.26. As in the case of "GdB_2C_2", we indicate the space group imposed by the 4*f*-electron exchange potential. Results show a preference for the ferromagnetic pattern for "Gd_5Si_4" and the lowest energy pattern for "Gd_5Ge_4" is the case where layers are ordered antiparallel to each other. The spin patterns where the moment of "Gd" atom at y = ¼ is in opposition to the moments on the surrounding distorted cube of "Gd" atoms all lie much higher in energy. Figure 6.27 shows the "Gd^+" and "Gd^-" DOS plots for Gd_5Si_4, respectively modeling densities of states aligned parallel and antiparallel to the $4f^7$ moments. The positions of the "Gd^+" and "Gd^-" gap that separated the Si *p* and "Gd" *d* bands are 1 eV and 0.5 eV below the Fermi level, respectively. Above the gap, each of the spins' DOS functions exhibit a somewhat structured "peak" with a width of ~2 eV. The Fermi level is positioned just below the center of this peak (Figure 6.22) in the nonmagnetic case and when the ferromagnetic exchange is "turned on" the minority spin peak is nearly emptied as the majority spin peak is more fully occupied. These results are similar to previous TB-LMTO calculations on Gd_5Si_4 , though the latter calculations predicted a pseudo-gap separating the Si *p* and Gd *d* bands.[295] In light of the large

Label, Supercell, Relative SDFT Energy	"Gd_5Si_4" Spin Patterns	Label, Supercell, Relative SDFT Energy	"Gd_5Ge_4" Spin Patterns
Ferromagnetic (*a*, *b*, *c*), Pnma 0.0 cm^{-1}	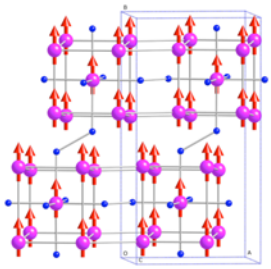	Antiferro I (*a*, *b*, *c*), $Pmc2_1$ 0.0 cm^{-1}	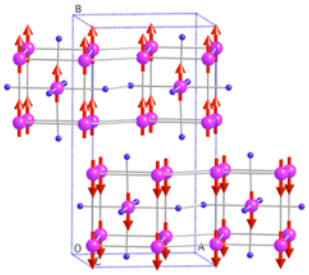
Antiferro I (*a*, *b*, *c*), $Pmc2_1$ 2318.9 cm^{-1}	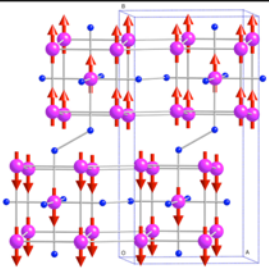	Ferromagnetic (*a*, *b*, *c*), Pnma 54.7 cm^{-1}	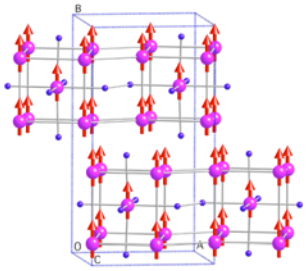
Antiferro II (*a*, *b*, *c*), $Pmc2_1$ 4644.0 cm^{-1}	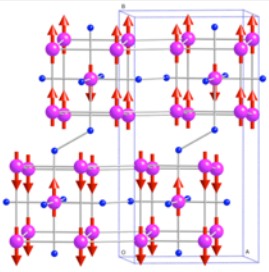	Antiferro III (*a*, *b*, *c*), $Pmn2_1$ 951.9 cm^{-1}	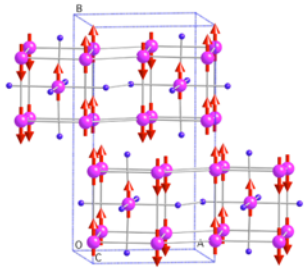
Antiferro III (*a*, *b*, *c*), $Pmn2_1$ 4815.6 cm^{-1}	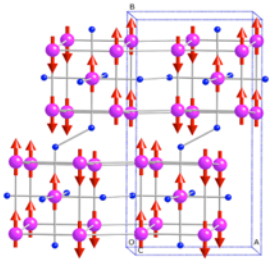	Antiferro II (*a*, *b*, *c*), $Pmc2_1$ 989.4 cm^{-1}	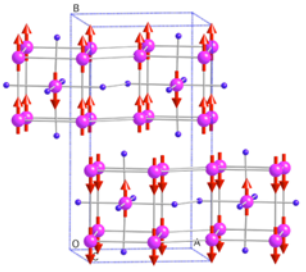

Figure 6.26. Proposed spin patterns for "Gd_5Si_4" and "Gd_5Ge_4".

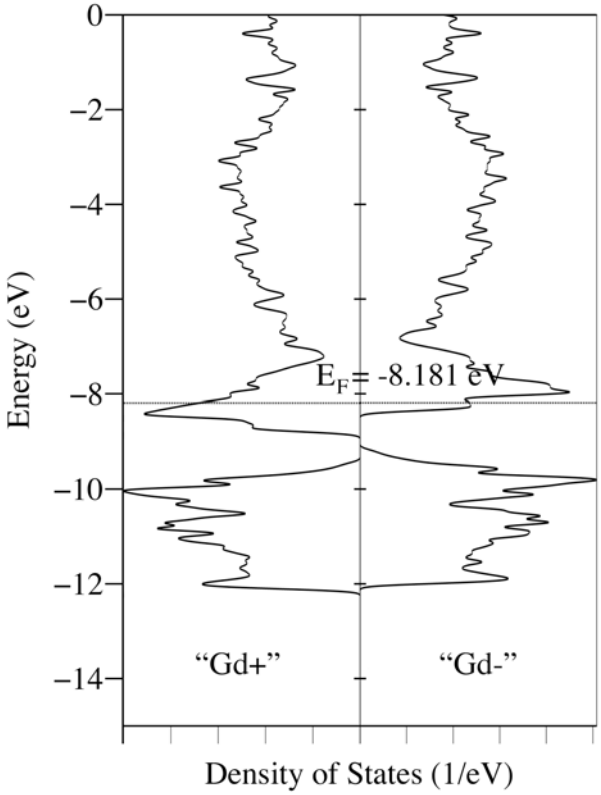

Figure 6.27. DOS plot of "Gd_5Si_4" for the ferromagnetic case.

density of states at the Fermi level (in the unpolarized system), application of the Stoner criterion for ferromagnetic ground state would seem appropriate.[317]

Figure 6.28 depicts the DOS curve for the regions near the Fermi energy of the lowest energy spin pattern (AntiferroI) for Gd_5Ge_4. The Antiferro1 DOS plot appears to be an "average" of both "Gd^+" and "Gd^-". The narrow peak, which was half-filled in the nonmagnetic case, is now fully occupied upon inducing the *d-f* exchange perturbation and consists of primarily the majority spin "Gd^+" atoms. Also, there is a small amount

of minority spin occupied at levels just below the Fermi energy. These results mimic previous calculations using LMTO.[315] Because of the small DOS at the Fermi Energy, the Stoner model would not predict this compound orders ferromagnetically.[317]

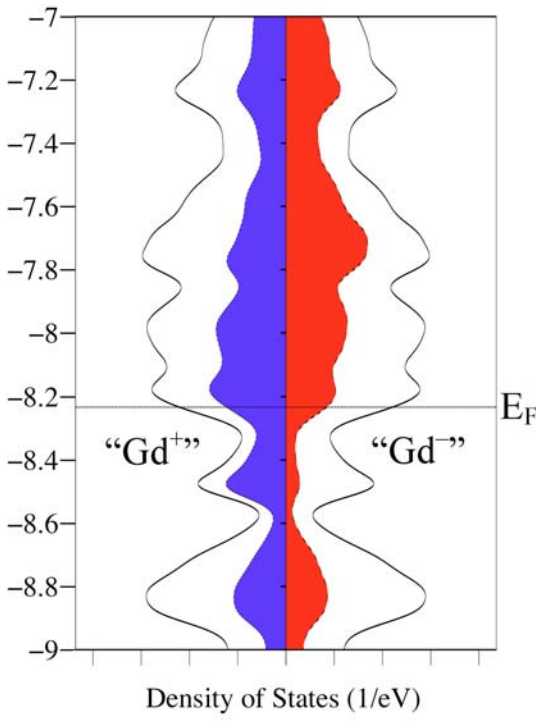

Figure 6.28. Partial DOS curve of "Gd^{+}" and "Gd^{-}" atoms in "Gd_5Ge_4" AntiferroI spin pattern. "Gd" atomic projected DOS curves for a given electron spin. "Gd^{+}" centers represent "Gd" atoms with like-spin *f*-electon moments and "Gd^{-}" centers represent "Gd" atoms with unlike-spin *f*-electon moments.

CHAPTER VII

CONCLUSIONS AND FUTURE WORK

The theoretical results presented in this work have helped us select synthetic targets, interpret magnetic measurements, *and* advance understanding of magnetic coupling phenomena in lanthanide-containing solids. Our computational approach has implications beyond our own research and will advance the area of magneto–structural correlations in lanthanide-based systems. To our knowledge, we are the pioneers in extension of the broken-symmetry approach to the study of magnetic coupling in lanthanide-based compounds.

In this work, we have established: (1) DFT is capable of yielding results that reproduce experiment in treating magnetic coupling/ordering phenomena in gadolinium compounds, often with semi-quantitative accuracy using GGA functionals. These results can be obtained by applying a generalized broken-symmetry interpretation to single-determinantal DFT calculations. (2) For more complex systems (with several Gd centers or in an extended system), computational evaluation of an overdetermining set of competing spin-pattern energies should be used to extract the best set of mutually consistent coupling parameters — or to reveal whether a pairwise scheme of magnetic coupling is *not* appropriate. (3) Perturbational MO theory offers a straightforward way of understanding structure-magnetic exchange correlations in Gd-containing compounds. This amplifies the usefulness of our computational studies because it offers a way going beyond a mechanical evaluation of spin-pattern energies for individual systems to the

point where we may hope to qualitatively predict how to modify real lanthanide-containing compounds to control magnetic properties.

In our seminal model of $[Gd_3I_6(OPH_3)_{12}]^{n+}$, the system was 'designed' as a model for the electronic structure of GdI_2 with variable oxidation states ranging over values for which the cluster is fully oxidized (n = 3) to the point where the 3*c*-bonding system contains a single electron (n = 2) and 3*c*-bonding MO is doubly occupied (n = 1). Qualitative conclusions are: (*i*) Couplings in d^0 systems are small because without significant 5*d* or 6*s* electron density, there is no robust underlying mechanism to facilitate 'through-bond' coupling of rare-earth ions. (*ii*) The coupling in the d^2 complexes (the 3*c*-bond orbital in doubly-occupied) is substantial, and antiferromagnetic. A perturbational MO (PMO) analysis of these systems suggests that this result may be fairly general for closed *d*-shell systems: antiferromagnetic ordering of the f^7 spins lowers the symmetry of the system and induces a stabilizing mixing of empty orbitals into the ground state, ferromagnetic ordering does not lower the symmetry of potential to which the *d*-electrons are subject. (*iii*) The open *d*-shell ion, $\{Gd_3\}^{2+}$ exhibits strong *ferromagnetic* coupling. This coupling originates from local $4f^7$–5*d* exchange interaction with the single up-spin *d* electron that is in a 3*c*-bonding MO that is delocalized over the three rare-earth atoms. The energetic ordering of the spin-states shown is clearly a understood by examining how many of the f^7 spins are parallel with the delocalized 5*d* electron – as in the d^2 case, if one accounts for spin-polarization of the *d*-electron SOMO by the exchange field of the various f^7 spin arrangements, the numerical results can be well accounted for with a PMO analysis.

In a study of the magnetic coupling present in a “real” system, we examined Gd_2Cl_3, an important benchmark system because it is one of the few semiconducting compounds for which neutron diffraction results are available.[41, 42] Using a model $Gd_4Cl_6(OPH_3)_2$ chain, we computed energies for eight alternative spin patterns and reproduced the experimentally observed magnetic ordering of the basal atoms. From the summed magnitudes of the 5*d* and 6*s* spin-populations induced by each of 4*f* magnetic moment patterns, the induced spin-polarizations reflect the valence/conduction band-orbital mixing induced by the 4*f*-5*d* exchange interaction. The extent of spin-polarization is monotonically correlated the relative stability of each spin pattern; the ground state 4*f*-moment pattern is that which most efficiently induces the second-order valence-conduction band mixing. The two lowest energy spin patterns coincide with experimental results on the basal Gd atom sites and differ from each other by only on the apical positions, which are not ordered at 26 K.

Known Gd dimer systems all exhibit weak coupling, since they are all Gd^{III}–Gd^{III} systems that are in linked by two or more bridging ligands in one way or another. The method complements experimental studies in elucidating the compositional and structural origins of magnetic ordering in rare-earth magnetic materials. Analysis of all the experimental structures reveals magneto-structural correlations in the Gd dinuclear complexes. The calculated values of 2*J* show that as the Gd–O distances become more unequal, antiferromagnetic coupling is replaced by ferromagnetic coupling. Computed magnetic coupling constants are in good agreement with the reported values for the oxygen-bridged Gd^{III} compounds, supporting the reliability of this treatment. Moreover,

we have applied a perturbative-theoretic technique using the diazenido-bridged Gd^{III} complexes, which underline the plausibility of this treatment.

In the diazenido system, the ferromagnetic exchange field is totally symmetric in D_{2h} symmetry; in the antiferromagnetically coupled molecule, the exchange field lowers the spin-dependent symmetry experienced by the delocalized electrons to C_{2v}. However, because this perturbation does not couple the HOMO and LUMO, dramatically larger Gd-Gd exchange coupling is precluded. The perturbative analysis suggests that the best strategy for obtaining strongly coupled lanthanide magnetic molecules (solids) consists of finding ligands that effectively minimize the energy gap between the frontier and adjacent orbitals, and mix in some significant Ln 5*d* character to the same in order to yield strongly (ferro- or antiferromagnetically) coupled systems. Our group is currently examining model systems where such coupling can occur.

The study of the models based on $Gd(Gd_6ZI_{12})$ (Z = Co, Fe, Mn) demonstrates the efficacy with which unpaired, delocalized Gd–Gd bonding electrons can couple the spins localized in the 4*f* orbitals of the Gd atoms. Because of the strong exchange interactions between the electrons localized in the 4*f* orbitals in Gd and the valence (5*d* and 6*s*) electrons, strong magnetic communication can occur. Calculations also suggest that *inter*cluster magnetic coupling is also significant. Insertion of main group atoms (Z = B, C, N) into the empty cluster will enhance the coupling between the 4*f* moments since coupling will arise from only Gd 5*d* occupation.

One of the ultimate objectives of this research is the isolation of reduced rare-earth clusters that are truly *discrete*. Two possible candidates that could exhibit

interesting magnetic behavior are the reduced clusters $Gd_{10}Cl_{18}C_4$ and $Gd_5(O)(OPr^i)_{13}$. Studies of the model based on $Gd_{10}Cl_{17}C_4$ predict moderate exchange interactions between the 4*f* moments on the basal atoms with little preference for the ordering of the apical atoms. Electronic structure calculations on the yttrium analog to $Gd_5(O)(OPr^i)_{13}$ predict that upon reduction, the compound could achieve *d*-electron mediated *f-f* exchange.

Finally, we have shown that we can successfully predict the ground state magnetic structure for several metallic and semiconducting Gd-containing compounds using our EHTB method. Results from "GdB_2C_2" not only correctly predict the magnetic structure from several different supercell, but also support previous calculations which predicted an alternating B–C bonded network.[260, 261] We support the spin pattern arrangement for α-Gd_2S_3 which was proposed from an interpretation of a neutron diffraction experiment. We also examined the isotypic compounds Gd_5Si_4 and Gd_5Ge_4 that, because of the connectivity of the two-dimensional slabs, exhibit ferromagnetic and antiferromagnetic ordering, respectively. The most important characteristic of these results is a preference for a ferromagnetic spin pattern for "Gd_5Si_4" and an antiferromagnetic spin pattern for "Gd_5Ge_4". We make a prediction for the spin pattern arrangement for Gd_5Ge_4 wherein the two-dimensional slab exhibit ferromagnetic coupling and the spins in adjacent slabs are antiferromagnetically aligned.

A longer-range goal involves the incorporation of magnetically anisotropic rare-earth atoms by substitution for Gd into the previously calculated clusters. For the 4*f* electrons, spin-orbit coupling is generally stronger than ligand-field effects and the

influence of the ligand field can usually be understood as operating on the lowest spin-orbit states. It also seems likely that most of the effects of interatomic exchange coupling can be considered apart from local spin-orbit and crystal field effects, and the magnitude of *d*-electron mediated exchange coupling between anisotropic centers in a cluster should be estimable from results for Gd_n clusters. Single-ion magnetic anisotropies of Ln centers can be quite large and their orbital components are not generally subject to quenching via Jahn-Teller distortions. The ligand-field splitting of reported by Ishikawa and coworkers for the sandwich compound Tb(phthalocyanine)$_2^-$, [Tb(pc)$_2^-$] (Figure 7.1), demonstrates that such substate splittings can exceed *k*T at room temperature.[318, 319] These investigators have reported that (Tb,Dy)(phthalocyanine)$_2^-$ complexes exhibit SMM behavior.[320-322]

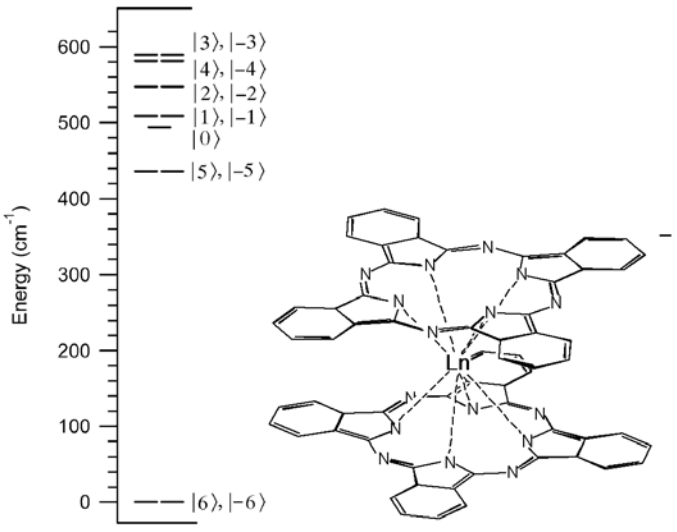

Figure 7.1. [Ln(pc)$_2$]$^-$ complexes; the level diagram applies to the CF (~M_J) states of the Tb complex.

We wish to explore whatever computational tools are available to calculate single ion anisotropies and determine whether there is a way to incorporate single ion anisotropy into a predicted computational scheme. Several challenges arise: Can we correctly handle spin-orbit coupling to give the right orientation of **J** in the absence of exchange? Or upon addition of exchange? A natural starting point would be calculations on the Tb^{3+} ion performed in the same spirit as the Gd atom calculations from Chapter III to provide insight into the magnetic anisotropy. So far, we have performed preliminary calculations on $[Tb(pc)_2]^-$ using scalar relativistic effects and the results are encouraging. These results are necessary before continuing on with a spin-orbit coupling calculation using either the collinear or noncollinear approximation.[323] We were able to achieve SCF convergence for the system with occupation of the minority spin in the $\left\{f_{z^3-3zr^2}\right\}$, $\left\{f_{5yz^2-yr^2}, f_{5xz^2-xr^2}\right\}$, $\left\{f_{xyz}, f_{zx^2-zy^2}\right\}$, or $\left\{f_{y^3-3x^2y}, f_{x^3-3xy^2}\right\}$ orbital(s) (i.e. B_2, E_1, E_2 and E_3 irreducible representation in D_{4d}, respectively) and their calculated energies are in Table 7.1. Initial results show that the lowest energy spin arrangement is where the minority spin occupies the $\left\{f_{z^3-3zr^2}\right\}$ (f^0) orbital. However, one must remember that these are preliminary calculations and that correction for spin-orbit coupling has not been applied. Additional information that can be used to determine the energy of the substates is found in Appendix F. Using the $Y_5O(OR)_{13}$ cluster as an example, another plausible model is the addition of an anisotropic metal atom, such as Tb^{3+}, to construct an R_6Z core (Figure 7.2). Perhaps we could then determine if the Tb ion anisotropy is uniaxial, planar, or cubic when in a cluster.

Table 7.1. Energies (cm^{-1}) and orbital occupation of the minority spin 4*f* electron for $[Tb(pc)_2]^-$.

Energy (cm^{-1})	Orbital Occupation
0	$B_2/\left\{f_{z^3-3zr^2}\right\}$
579.8	$E_1/\left\{f_{5yz^2-yr^2}, f_{5xz^2-xr^2}\right\}$
1479.8	$E_2/\left\{f_{xyz}, f_{zx^2-zy^2}\right\}$
2553.4	$E_3/\left\{f_{y^3-3x^2y}, f_{x^3-3xy^2}\right\}$

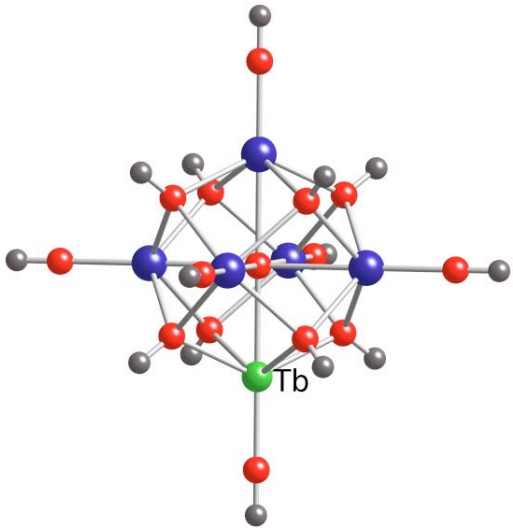

Figure 7.2. Proposed model to study: $Y_5Tb(O)(OH)_{13}$.

REFERENCES

1. Goodenough, J. B., *Magnetism and the Chemical Bond*; Interscience Publishers: New York, NY, 1963; Vol 1.
2. Anderson, P. W., *Phys. Rev.* **1950**, *79*, 350.
3. Kanamori, J., *J. Phys. Chem. Solids* **1959**, *10*, 87.
4. Hay, P. J.; Thibeault, J. C.; Hoffmann, R., *J. Am. Chem. Soc.* **1975**, *97*, 4884.
5. Kahn, O.; Briat, B., *J. Chem. Soc., Faraday Trans.* **1976**, *72*, 1441.
6. Kahn, O., *Molecular Magnetism*; Wiley-VCH: New York, NY, 1993.
7. Christou, G.; Gatteschi, D.; Hendrickson, D. N.; Sessoli, R., *MRS Bulletin* **2000**, *25*, 66.
8. Gatteschi, D., *J. Alloys Compd.* **2001**, *317-318*, 8.
9. Ruiz, E.; Alemany, P.; Alvarez, S.; Cano, J., *J. Am. Chem. Soc.* **1997**, *119*, 1297.
10. Ruiz, E.; Alvarez, S., *J. Chem. Soc., Chem. Commun.* **1998**, 2767.
11. Ruiz, E.; Alvarez, S.; Rodriguez-Fortea, A.; Alemany, P.; Pouillon, Y.; Massobrio, C., In *Magnetism: Molecules to Materials II*, Miller, J. S.; Drillon, M., Eds.; Wiley-VCH: Weinheim, Germany, 2001; p 227.
12. Gillon, B.; Mathoniere, C.; Ruiz, E.; Alvarez, S.; Cousson, A.; Rajendiran, T. M.; Kahn, O., *J. Am. Chem. Soc.* **2002**, *124*, 14433.
13. Desplanches, C.; Ruiz, E.; Alvarez, S., *Eur. J. Inorg. Chem.* **2003**, 1756.
14. Paulovic, J.; Cimpoesu, F.; Ferbinteanu, M.; Hirao, K., *J. Am. Chem. Soc.* **2004**, *126*, 3321.

15. Whangbo, M. H.; Koo, H. J., *Inorg. Chem.* **2002**, *41*, 3570.

16. Dai, D.; Whangbo, M.-H., *J. Chem. Phys.* **2003**, *118*, 29.

17. Mallah, T.; Ferlay, S.; Scuiller, A.; Verdaguer, M., In *NATO ASI Ser., Ser. C*, Willett, R. D.; Gatteschi, D.; Kahn, O., Eds.; Reidel, Dordrecht, The Netherlands, 1996; Vol. 484, p 597.

18. Verdaguer, M.; Bleuzen, A.; Marvaud, V.; Vaissermann, J.; Seuleiman, M.; Desplanches, C.; Scuiller, A.; Train, C.; Garde, R.; Gelly, G.; Lomenech, C.; Rosenman, I.; Veillet, P.; Cartier, C.; Villain, F., *Coord. Chem. Rev.* **1999**, *190-192*, 1023.

19. Bennett, M. V.; Beauvais, L. G.; Shores, M. P.; Long, J. R., *J. Am. Chem. Soc.* **2001**, *123*, 8022.

20. Shores, M. P., Ph.D. Dissertation, University of California, Berkeley, 2002.

21. Beauvais, L. G.; Long, J. R., *J. Am. Chem. Soc.* **2002**, *124*, 12096.

22. Tulsky, E. G.; Crawford, N. R. M.; Baudron, S. A.; Batail, P.; Long, J. R., *J. Am. Chem. Soc.* **2003**, *125*, 15543.

23. Yan, B.; Zhou, H.; Lachgar, A., *Inorg. Chem.* **2003**, *42*, 8818.

24. Goodenough, J. B., *Struct. Bonding (Berlin)* **2001**, *98*, 1.

25. Daul, C. A.; Ciofini, I.; Bencini, A., In *Reviews of Modern Quantum Chemistry*, Sen, K. D., Ed.; World Scientific, Singapore, 2002; Vol. 2, p 1247.

26. Veciana, J.; Iwamura, H., *MRS Bulletin* **2000**, *25*, 41.

27. Rovira, C., *Struct. Bonding (Berlin)* **2001**, *100*, 163.

28. Iwamura, H.; Inoue, K., In *Magnetism: Molecules to Materials II*, Miller, J. S.; Drillon, M., Eds.; Wiley-VCH: Weinheim, Germany, 2001; p 61.

29. Rajca, A., *Mol. Cryst. Liq. Cryst. Sci. Technol., Sect. A*, **1997**, *305*, 567.

30. Rajca, S.; Rajca, A., *J. Solid State Chem.* **2001**, *159*, 460.

31. Heisenberg, W., *Z. Physik* **1928**, *49*, 619.

32. The HDVV equation is described in further detail in Chapter II.

33. Kramers, H. A., *Physica (The Hague)* **1934**, *1*, 182.

34. Anderson, P. W.; Seitz, F. S.; Turnbull, D., *Solid State Physics* **1963**, *14*, 99.

35. Noodleman, L., *J. Chem. Phys.* **1981**, *74*, 5737.

36. Noodleman, L.; Case, D. A., *Adv. Inorg. Chem.* **1992**, *38*, 423.

37. Caballol, R.; Castell, O.; Illas, F.; de Moreira, I.; Malrieu, J. P., *J. Phys. Chem. A* **1997**, *101*, 7860.

38. Adamo, C.; Barone, V.; Bencini, A.; Totti, F.; Ciofini, I., *Inorg. Chem.* **1999**, *38*, 1996.

39. Carlin, R. L., *Magnetochemistry*; Springer-Verlag: Berlin, Germany, 1989.

40. Kremer, R. K., Simon, A., *J. Less-Common Metals* **1987**, *127*, 262.

41. Simon, A.; Mattausch, H. J.; Miller, G. J.; Bauhofer, W.; Kremer, R. K., In *Handbook on the Physics and Chemistry of Rare Earths*, Gschneidner, K. A.; Eyring, L., Eds.; Elsevier Science: Amsterdam, The Netherlands, 1991; Vol. 15, p 191.

42. Simon, A., *J. Alloys Compd.* **1995**, *229*, 158.

43. Kasten, A.; Muller, P. H.; Schienle, M., *Solid State Commun.* **1984**, *51*, 919.

44. Felser, C.; Ahn, K.; Kremer, R. K.; Seshadri, R.; Simon, A., *J. Solid State Chem.* **1999**, *147*, 19.

45. Hughbanks, T.; Corbett, J. D., *Inorg. Chem.* **1988**, *27*, 2022.

46. Kittel, C., *Introduction to Solid State Physics,* Sixth Edition; John Wiley and Sons: New York, NY, 1986; p 640.

47. Jensen, J.; Mackintosh, A. R., *Rare Earth Magnetism: Structures and Excitations*; Oxford University Press: Oxford, England, 1991.

48. Ruderman, M. A.; Kittel, C., *Phys. Rev. B: Condens. Matter* **1954**, *96*, 99.

49. Kasuya, T., *Prog. Theor. Phys. (Japan)* **1956**, *16*, 45.

50. Yosida, K., *Phys. Rev. B: Condens. Matter* **1957**, *106*, 893.

51. Wallace, W. E., *Prog. Solid State Chem.* **1985**, *16*, 127.

52. Fidler, J., In *Inst. Phys. Conf. Ser.* **1998**, *152*, 805.

53. Radwanski, R. J.; Michalski, R.; Ropka, Z.; Blaut, A., *Physica B: Condens. Matter* **2002**, *319*, 78.

54. NIST Exchange Splitting Energies for Gd. http://physics.nist.gov/cgi-bin/AtData/main-asd

55. Koch, W.; Holthausen, M. C., *A Chemist's Guide to Density Functional Theory, Second Edition*; Wiley-VCH: Weinheim, Germany, 2000.

56. Cramer, C. J., *Essentials of Computational Chemistry: Theories and Models, Second Edition*; John Wiley & Sons: New York, NY, 2004.

57. Jensen, F., *Introduction to Computational Chemistry*; John Wiley & Sons: Chichester, England, 1999.

58. Young, D., *Computational Chemistry: A Practical Guide for Applying Techniques to Real World Problems*; Wiley-Interscience: New York, NY, 2001.

59. Lowe, J. P., *Quantum Chemistry, Second Edition*; Academic Press: New York, NY, 1993.

60. Szabo, A.; Ostlund, N. S., *Modern Quantum Chemistry: Introduction to Advanced Electronic Structure Theory*; Dover Publications: Mineola, NY, 1996.

61. Parametric dependence means that for different arrangements of nuclei, Ψ_{elec} is a different function of the electronic coordinates. The nuclear coordinates to not explicitly appear in the wave function.

62. Landrum, G. A. *YAeHMOP: Yet Another extended Huckel Molecular Orbital Package*, 3.0.3; 2004. Available on the web at: http://yaehmop.sourceforge.net/

63. Ren, J.; Liang, W.; Whangbo, M. H. *Crystal and Electronic Structure AnalyzeR Using CAESAR*, 2.0; 2002. Available on the web at: http://www.primec.com/

64. Fermi, E., *Atti Accad. Naz. Lincei Cl. Sci. Fis. Mat. Nat.* **1927**, *6*, 602.

65. Thomas, L. H., *Proc. Cambridge Phil. Soc.* **1927**, *23*, 542.

66. Hohenberg, P.; Kohn, W., *Phys. Rev.* **1964**, *136*, B864.

67. Kohn, W.; Sham, L. J., *Phys. Rev.* **1965**, *137*, 1697.

68. Leach, A. R., *Molecular Modelling: Principles and Applications, Second Edition*; Prentice Hall: Harlow, England, 2001.

69. Becke, A. D., *Phys. Rev. A: At. Mol. Opt. Phys.* **1988**, *38*, 3098.

70. Lee, C.; Yang, W.; Parr, R. G., *Phys. Rev. B: Condens. Matter* **1988**, *37*, 785.

71. Miehlich, B.; Savin, A.; Stoll, H.; Preuss, H., *Chem. Phys. Lett.* **1989**, *157*, 200.

72. Vosko, S. H.; Wilk, L.; Nusair, M., *Can. J. Phys.* **1980**, *58*, 1200.

73. Jellium is a hypothetical "substance" in which electron-electron interactions are included for a homogeneous electron "gas" and a uniform background of positive charge. In this theory at zero temperature, the system properties are dependent only on the density of electrons. This allows for the simplistic calculation of the electron-electron correlation energy being a ratio between the free-electron kinetic energy and the Coulomb potential energy.

74. Colle, R.; Salvetti, O., *Theor. Chim. Acta* **1975**, *37*, 329.

75. Delley, B., *J. Chem. Phys.* **1990**, *92*, 508.

76. Delley, B., *J. Chem. Phys.* **2000**, *113*, 7756.

77. Delley, B., *Comput. Mater. Sci.* **2000**, *17*, 122.

78. Becke, A. D., *J. Chem. Phys.* **1993**, *98*, 1372.

79. Zhang, Y.; Yang, W., *J. Chem. Phys.* **1998**, *109*, 2604.

80. Gruening, M.; Gritsenko, O. V.; van Gisbergen, S. J. A.; Baerends, E. J., *J. Phys. Chem. A* **2001**, *105*, 9211.

81. Cremer, D.; Filatov, M.; Polo, V.; Kraka, E.; Shaik, S., *Int. J. Mol. Sci.* **2002**, *3*, 604.

82. Ruiz, E.; Alemany, P.; Alvarez, S.; Cano, J., *Inorg. Chem.* **1997**, *36*, 3683.

83. Moreira, I. d. P. R.; Illas, F., *Phys. Rev. B: Condens. Matter* **1997**, *55*, 4129.

84. Ruiz, E.; Cano, J.; Alvarez, S.; Alemany, P., *J. Am. Chem. Soc.* **1998**, *120*, 11122.

85. Cano, J.; Alemany, P.; Alvarez, S.; Verdaguer, M.; Ruiz, E., *Chem. Eur. J.* **1998**, *4*, 476.

86. Ruiz, E.; Cano, J.; Alvarez, S.; Alemany, P., *J. Comput. Chem.* **1999**, *20*, 1391.

87. Fabrizi de Biani, F.; Ruiz, E.; Cano, J.; Novoa, J. J.; Alvarez, S., *Inorg. Chem.* **2000**, *39*, 3221.

88. Cano, J.; Rodriguez-Fortea, A.; Alemany, P.; Alvarez, S.; Ruiz, E., *Chem. Eur. J.* **2000**, *6*, 327.

89. Ruiz, E.; Cano, J.; Alvarez, S.; Alemany, P.; Verdaguer, M., *Phys. Rev. B: Condens. Matter* **2000**, *61*, 54.

90. Rodriguez-Fortea, A.; Alemany, P.; Alvarez, S.; Ruiz, E.; Scuiller, A.; Decroix, C.; Marvaud, V.; Vaissermann, J.; Verdaguer, M.; Rosenman, I.; Julve, M., *Inorg. Chem.* **2001**, *40*, 5868.

91. Rodriguez-Fortea, A.; Alemany, P.; Alvarez, S.; Ruiz, E., *Chem. Eur. J.* **2001**, *7*, 627.

92. Ciofini, I.; Daul, C. A.; Bencini, A., In *Recent Advances in Computational Chemistry*, Chong, D. P., Ed.; World Scientific: Singapore, 2002; Vol. 1, p 106.

93. Rodriguez-Fortea, A.; Alemany, P.; Alvarez, S.; Ruiz, E., *Inorg. Chem.* **2002**, *41*, 3769.

94. Ruiz, E.; de Graaf, C.; Alemany, P.; Alvarez, S., *J. Phys. Chem. A* **2002**, *106*, 4938.

95. Desplanches, C.; Ruiz, E.; Rodriguez-Fortea, A.; Alvarez, S., *J. Am. Chem. Soc.* **2002**, *124*, 5197.

96. Atanasov, M.; Daul, C. A., *Chem. Phys. Lett.* **2003**, *381*, 584.

97. Ruiz, E.; Llunell, M.; Alemany, P., *J. Solid State Chem.* **2003**, *176*, 400.

98. Ruiz, E.; Rodriguez-Fortea, A.; Alvarez, S., *Inorg. Chem.* **2003**, *42*, 4881.

99. Ruiz, E.; Cano, J.; Alvarez, S.; Caneschi, A.; Gatteschi, D., *J. Am. Chem. Soc.* **2003**, *125*, 6791.

100. Perez-Jimenez, A. J.; Perez-Jorda, J. M.; Illas, F., *J. Chem. Phys.* **2004**, *120*, 18.

101. Ruiz, E.; Rodriguez-Fortea, A.; Cano, J.; Alvarez, S., *J. Phys. Chem. Solids* **2004**, *65*, 799.

102. Rodriguez-Fortea, A.; Alemany, P.; Alvarez, S.; Ruiz, E., *Eur. J. Inorg. Chem.* **2004**, 143.

103. Carrasco, R.; Cano, J.; Mallah, T.; Jones, L. F.; Collison, D.; Brechin, E. K., *Inorg. Chem.* **2004**, *43*, 5410.

104. Ruiz, E.; Cano, J.; Alvarez, S., *Chem. Eur. J.* **2005**, *11*, 4767.

105. Ruiz, E.; Alvarez, S., *ChemPhysChem* **2005**, *6*, 1094.

106. Davidson, E. R.; Clark, A. E., *J. Phys. Chem. A* **2002**, *106*, 7456.

107. Delley, B. Private communication, Professor, Paul Scherrer Institut, Switzerland.

108. Illas, F.; Moreira, I. d. P. R.; De Graaf, C.; Barone, V., *Theor. Chem. Acc.* **2000**, *104*, 265.

109. Perdew, J. P.; Chevary, J. A.; Vosko, S. H.; Jackson, K. A.; Pederson, M. R.; Singh, D. J.; Fiolhais, C., *Phys. Rev. B: Condens. Matter* **1992**, *46*, 6671.

110. Hess, B. A., *Berichte der Bunsen-Gesellschaft* **1997**, *101*, 1.

111. Pyykko, P., *Chem. Rev.* **1988**, *88*, 563.

112. Fedorov, D. G.; Koseki, S.; Schmidt, M. W.; Gordon, M. S., *Int. Rev. Phys. Chem.* **2003**, *22*, 551.

113. Balasubramanian, K., *Relativistic Effects in Chemistry Part A: Theory and Techniques*; Wiley-Interscience: New York, NY, 1997.

114. Balasubramanian, K., *Relativistic Effects in Chemistry Part B: Applications to Molecules and Clusters*; Wiley-Interscience: New York, NY, 1997.

115. Christiansen, P. A.; Ermler, W. C.; Pitzer, K. S., *Annu. Rev. Phys. Chem.* **1985**, *36*, 407.

116. Moss, R. E., *Advanced Molecular Quantum Mechanics; An Introduction to Relativistic Quantum Mechanics and the Quantum Theory of Radiation*; Chapman and Hall: London, England, 1973.

117. Foldy, L. L.; Wouthuysen, S. A., *Phys. Rev.* **1950**, *78*, 29.

118. van Lenthe, E.; Baerends, E. J.; Snijders, J. G., *J. Chem. Phys.* **1993**, *99*, 4597.

119. Ermler, W. C.; Ross, R. B.; Christiansen, P. A., *Adv. Quantum Chem.* **1988**, *19*, 139.

120. Te Velde, G.; Bickelhaupt, F. M.; Baerends, E. J.; Fonseca Guerra, C.; Van Gisbergen, S. J. A.; Snijders, J. G.; Ziegler, T., *J. Comput. Chem.* **2001**, *22*, 931.

121. Baerends, E. J.; Autschbach, J. A.; Bérces, A.; Bo, C.; Boerrigter, P. M.; Cavallo, L.; Chong, D. P.; Deng, L.; Dickson, R. M.; Ellis, D. E.; Fan, L.; Fischer, T. H.; Fonseca Guerra, C.; van Gisbergen, S. J. A.; Groeneveld, J. A.; Gritsenko, O. V.; Grüning, M.; Harris, F. E.; van den Hoek, P.; Jacobsen, H.; van Kessel, G.; Kootstra, F.; van Lenthe, E.; Osinga, V. P.; Patchkovskii, S.; Philipsen, P. H. T.;

Post, D.; Pye, C. C.; Ravenek, W.; Ros, P.; Schipper, P. R. T.; Schreckenbach, G.; Snijders, J. G.; Sola, M.; Swart, M.; Swerhone, D.; te Velde, G.; Vernooijs, P.; Versluis, L.; Visser, O.; van Wezenbeek, E.; Wiesenekker, G.; Wolff, S. K.; Woo, T. K.; Ziegler, T. *ADF2004.01*, 2004.01; SCM, Theoretical Chemistry, Vrije Universiteit: Amsterdam, The Netherlands, 2004.

122. Ruiz, E.; Rodriguez-Fortea, A.; Tercero, J.; Cauchy, T.; Massobrio, C., *J. Chem. Phys.* **2005**, *123*, 074102/1.

123. Delley, B., *Int. J. Quantum Chem.* **1998**, *69*, 423.

124. van Lenthe, E.; Baerends, E. J.; Snijders, J. G., *J. Chem. Phys.* **1994**, *101*, 9783.

125. Users of the ADF program using Symmetry option should be certain that the parameter A1FIT is set high enough (for example, 10 Å) to avoid errors that this method can otherwise introduce.

126. Dirac, P. A. M., *Proc. Roy. Soc. (London)* **1929**, *A123*, 714.

127. Van Vleck, J. H., *The Theory of Electric and Magnetic Susceptibilities*; The Clarendon: Oxford, England, 1932.

128. Alternative definitions for the exchange coupling constants are also common in the literature. In some cases, the Heisenberg Hamiltonian is expressed as $\hat{H} = +J_{ij}\hat{S}_i\hat{S}_j$ where the positive and negative values of *J* indicate antiferromagnetic and ferromagnetic coupling, respectively. Also, the Hamiltonian $\hat{H} = -2J_{ij}\hat{S}_i\hat{S}_j$ is also used and the reported coupling constants must be multiplied by 2 to make them comparable with those obtained using Eq. 2.39.

129. Cano, J.; Ruiz, E.; Alemany, P.; Lloret, F.; Alvarez, S., *J. Chem. Soc., Dalton Trans.* **1999**, 1669.

130. Li, J.; Noodleman, L.; Case, D. A., In *Inorganic Electronic Structure and Spectroscopy*, Solomon, E. I.; Lever, A. B. P., Eds.; Wiley-Interscience: New York, NY, 1999; Vol. 1, p 661.

131. Blanchet-Boiteux, C.; Mouesca, J.-M., *J. Am. Chem. Soc.* **2000**, *122*, 861.

132. Triki, S.; Gomez-Garcia, C. J.; Ruiz, E.; Sala-Pala, J., *Inorg. Chem.* **2005**, *44*, 5501.

133. Ruiz, E.; Alvarez, S.; Cano, J.; Polo, V., *J. Chem. Phys.* **2005**, *123*, 164110/1.

134. Barone, V.; Bencini, A.; Gatteschi, D.; Totti, F., *Chem. Eur. J.* **2002**, *8*, 5019.

135. Dixon, J. M.; Tuszynski, J. A., *Phys. Lett. A* **2001**, *283*, 300.

136. Dai, D.; Whangbo, M.-H., *J. Chem. Phys.* **2001**, *114*, 2887.

137. Freeman, A. J., In *Magnetic Properties of Rare Earth Metals*, Elliot, R. J., Ed. Plenum: London, England, 1972; p 245.

138. Harmon, B. N.; Freeman, A. J., *Phys. Rev. B: Condens. Matter* **1974**, *10*, 1979.

139. Tinkham, M., *Group Theory and Quantum Mechanics*; McGraw-Hill: Berkeley, CA, 1964.

140. Simon, A., *Inst. Phys. Conf. Ser.* **1978**, *39*, 353.

141. Mee, J. E.; Corbett, J. D., *Inorg. Chem.* **1965**, *4*, 88.

142. Stowe, K.; Tratzky, S.; Beck, H. P.; Jungmann, A.; Claessen, R.; Zimmermann, R.; Meng, G.; Steiner, P.; Huefner, S., *J. Alloys Compd.* **1997**, *246*, 101.

143. Ahn, K.; Felser, C.; Seshadri, R.; Kremer, R. K.; Simon, A., *J. Alloys Compd.* **2000**, *303-304*, 252.

144. Eremin, I.; Thalmeier, P.; Fulde, P.; Kremer, R. K.; Ahn, K.; Simon, A., *Phys. Rev. B: Condens. Matter* **2001**, *64*, 064425/1.

145. Deisenhofer, J.; Krug von Nidda, H. A.; Loidl, A.; Ahn, K.; Kremer, R. K.; Simon, A., *Phys. Rev. B: Condens. Matter* **2004**, *69*, 104407/1.

146. Simon, A.; Holzer, N.; Mattausch, H., *Z. Anorg. Allg. Chem.* **1979**, *456*, 207.

147. Mattausch, H.; Hendricks, J. B.; Eger, R.; Corbett, J. D.; Simon, A., *Inorg. Chem.* **1980**, *19*, 2128.

148. Bullett, D. W., *Inorg. Chem.* **1980**, *19*, 1780.

149. Masse, R.; Simon, A., *Mater. Res. Bull.* **1981**, *16*, 1007.

150. Ebbinghaus, G.; Simon, A.; Griffith, A., *Z. Naturforsch., A: Phys. Sci.* **1982**, *37A*, 564.

151. Bauhofer, W.; Simon, A., *Z. Naturforsch., A: Phys. Sci.* **1982**, *37A*, 568.

152. Bullett, D. W., *Inorg. Chem.* **1985**, *24*, 3319.

153. Simon, A., *J. Solid State Chem.* **1985**, *57*, 2.

154. Morss, L. R.; Mattausch, H.; Kremer, R.; Simon, A.; Corbett, J. D., *Inorg. Chim. Acta* **1987**, *140*, 107.

155. Simon, A.; Mattausch, H.; Mikheev, N. B.; Keller, C., *Z.Naturforsch. B: Chem. Sci.* **1987**, *42*, 666.

156. Mikheev, N. B.; Simon, A.; Mattausch, A. H., *Radiokhimiya* **1988**, *30*, 314.

157. Mikheev, N. B.; Kamenskaya, A. N.; Rumer, I. A.; Novichenko, V. L.; Simon, A.; Mattausch, H., *Z.Naturforsch. B: Chem. Sci.* **1992**, *47*, 992.

158. Yee, K. A.; Hughbanks, T., *Inorg. Chem.* **1992**, *31*, 1620.

159. Koo, H. J.; Whangbo, M. H., *J. Solid State Chem.* **2000**, *151*, 96.

160. Both calculations employed a restricted open-shell configuration.

161. We were only able to obtain an energy gap for the difference between d_{z^2} orbitals using ADF, calculated to be 4806 cm^{-1}.

162. Calculation employed 662 and 762 ***k***-points for the single layer and the crystal structure, respectively.

163. The broken symmetry solution would not converge.

164. Bondi, A., *J. Phys. Chem.* **1964**, *68*, 441.

165. Hedinger, R.; Ghisletta, M.; Hegetschweiler, K.; Toth, E.; Merbach, A. E.; Sessoli, R.; Gatteschi, D.; Gramlich, V., *Inorg. Chem.* **1998**, *37*, 6698.

166. Lokken, D. A.; Corbett, J. D., *Inorg. Chem.* **1973**, *12*, 556.

167. Bauhofer, W.; Cockcroft, J. K.; Kremer, R. K.; Mattausch, H.; Schwarz, C.; Simon, A., *J. Phys., Colloq.* **1988**, *8*, C8.

168. Band calculations and quantities derived therefrom (energies, spin densities) were carried out using a mesh of 10 *k*-points for all the states, except the ferromagnetic and antiferromagnetic ground spin-state patterns where 25 *k*-points were used to obtain density-of-states (DOS) plots of higher resolution. Since all band calculations were carried out on a system with a doubled cell, $Gd_8Cl_{12}(OPH_3)_4$, the 10 k-point mesh is equivalent to a 20 k-point set for the

conventional unit cell. Typical differences between spin-state pattern energies using a mesh of 10 *k*-points and 25 *k*-points was about 0.17%.

169. Calculations were performed using 256 ***k***-points.

170. The 1D model is arranged such that the basal metal-metal bond is along the *z*-axis.

171. Two EHTB calculations are performed with parameters appropriate for up-spin 5*d*/6*s*-electrons and one for down-spin 5*d*/6*s* electrons and the Fermi levels for both calculation were set equal.

172. Ganguly, P., *J. Am. Chem. Soc.* **1993**, *115*, 9287.

173. Hatscher, S. T.; Urland, W., *Angew. Chem., Int. Ed.* **2003**, *42*, 2862.

174. It is worth emphasizing, here and subsequently, that this corresponds to an energy difference between $|\uparrow_7,\uparrow_7\rangle$ and $|\uparrow_7,\downarrow_7\rangle$ of ~0.75 cm^{-1} (see Eqn. 2.44).

175. Liu, S.; Gelmini, L.; Rettig, S. J.; Thompson, R. C.; Orvig, C., *J. Am. Chem. Soc.* **1992**, *114*, 6081.

176. Urland and authors published the single-crystal structures and magnetic behavior of $Gd(HF_2CCOO)_3(H_2O)_2{\cdot}2H_2O$ and $Gd(H_3CCOO)_3(H_2O)_2{\cdot}2H_2O$ showing antiferromagnetic coupling for the former and ferromagnetic coupling for the latter. This structure type is different than the one in this study. Rohde, A., *et al.*, *J. Alloys Compd.* **2004**, *374*, 137.

177. Hernandez-Molina, M.; Ruiz-Perez, C.; Lopez, T.; Lloret, F.; Julve, M., *Inorg. Chem.* **2003**, *42*, 5456.

178. Costes, J.-P.; Clemente Juan, J.-M.; Dahan, F.; Nicodeme, F., *J. Chem. Soc., Dalton Trans.* **2003**, 1272.

179. Hou, H.; Li, G.; Li, L.; Zhu, Y.; Meng, X.; Fan, Y., *Inorg. Chem.* **2003**, *42*, 428.

180. Plass, W.; Fries, G., *Z. Anorg. Allg. Chem.* **1997**, *623*, 1205.

181. Calculated Mulliken charges and spin populations for $[\{Gd(O_2CR)_3(H_2O)_2\}_2]$ and $[Gd(AmPh)]_2$ are supplied in Appendix C.

182. Evans, W. J.; Zucchi, G.; Ziller, J. W., *J. Am. Chem. Soc.* **2003**, *125*, 10.

183. Evans, W. J.; Lee, D. S.; Ziller, J. W., *J. Am. Chem. Soc.* **2004**, *126*, 454.

184. Evans, W. J.; Lee, D. S.; Rego, D. B.; Perotti, J. M.; Kozimor, S. A.; Moore, E. K.; Ziller, J. W., *J. Am. Chem. Soc.* **2004**, *126*, 14574.

185. Maron, L.; Eisenstein, O., *J. Phys. Chem. A* **2000**, *104*, 7140.

186. Maron, L.; Eisenstein, O., *New J. Chem.* **2001**, *25*, 255.

187. Clark, D. L.; Gordon, J. C.; Hay, P. J.; Martin, R. L.; Poli, R., *Organometallics* **2002**, *21*, 5000.

188. Eisenstein, O.; Hitchcock, P. B.; Khvostov, A. V.; Lappert, M. F.; Maron, L.; Perrin, L.; Protchenko, A. V., *J. Am. Chem. Soc.* **2003**, *125*, 10790.

189. Perrin, L.; Maron, L.; Eisenstein, O.; Lappert, M. F., *New J. Chem.* **2003**, *27*, 121.

190. Brady, E. D.; Clark, D. L.; Gordon, J. C.; Hay, P. J.; Keogh, D. W.; Poli, R.; Scott, B. L.; Watkin, J. G., *Inorg. Chem.* **2003**, *42*, 6682.

191. A more complete table is included in Appendix C.

192. A geometry optimization on a model for $[(2,6\text{-}t\text{Bu}_2\text{C}_6\text{H}_3\text{O})_2(\text{thf})_2\text{Y}]_2(\text{N}_2)$ produces similar results: N–N and Y–N computed distances were 1.255 Å and 2.346Å/2.361Å, respectively. The yttrium analog of the aryloxide complex has not been synthesized, therefore, no comparison can be made and our discussion will focus on the disilylamide complex.

193. Arnett, E. M.; Wu, C. Y., *J. Am. Chem. Soc.* **1960**, *82*, 4999.

194. Arnett, E. M.; Wu, C. Y., *J. Am. Chem. Soc.* **1962**, *84*, 1684.

195. Arnett, E. M.; Wu, C. Y., *J. Am. Chem. Soc.* **1962**, *84*, 1680.

196. Okada, M.; Suyama, K.; Yamashita, Y., *Tetrahedron Lett.* **1965**, 2329.

197. L. Sweet and T. Hughbanks, submitted.

198. Mattausch, H.; Warkentin, E.; Oeckler, O.; Simon, A., *Z. Anorg. Allg. Chem.* **2000,** *626*, 2117.

199. Satpathy, S.; Andersen, O. K., *Inorg. Chem.* **1985**, *24*, 2604.

200. Warkentin, E.; Masse, R.; Simon, A., *Z. Anorg. Allg. Chem.* **1982**, *491*, 323.

201. Kritikos, M.; Moustiakimov, M.; Wijk, M.; Westin, G., *J. Chem. Soc., Dalton Trans.* **2001**, 1931.

202. Westin, G.; Kritikos, M.; Wijk, M., *J. Solid State Chem.* **1998**, *141*, 168.

203. Daniele, S.; Hubert-Pfalzgraf, L. G.; Daran, J.-C., *Polyhedron* **1996**, *15*, 1063.

204. Dudis, D. S.; Corbett, J. D.; Hwu, S. J., *Inorg. Chem.* **1986**, *25*, 3434.

205. Payne, M. W.; Corbett, J. D., *Inorg. Chem.* **1990**, *29*, 2246.

206. Jensen, E. A.; Corbett, J. D., *Inorg. Chem.* **2002**, *41*, 6199.

207. Jensen, E. A.; Corbett, J. D., *J. Solid State Chem.* **2003**, *172*, 132.

208. Gao, S.; Xu, G.; Li, L., *Inorg. Chem.* **1992**, *31*, 4829.

209. Sweet, L.; Roy, L.; Meng, F.; and Hughbanks, T., *J. Am. Chem. Soc.*, accepted. Magnetic susceptibility results supplied by Luke Sweet.

210. Calculations on a 17 cluster bonding electron (CBE) system with a t_{1u}^{5} configuration, resulted in different orbitals being occupied for the high-spin and broken symmetry state.

211. Bradley, D. C.; Ghotra, J. S.; Hart, F. A.; Hursthouse, M. B.; Raithby, P. R., *J. Chem. Soc., Dalton Trans.* **1977**, 1166.

212. A table depicting energies for all competing spin patterns is in Appendix D. Spin patterns with two up-spin and one down-spin CBEs (M_S = 1/2), which are primarily (though not entirely) derived from the doublet excited states of the cluster t_{1u}^{3} CBE configuration (^2E_u, $^2T_{2u}$, and $^2T_{1u}$) that, when coupled to the $4f^7$ moments, yield energies that are interspersed with and bracketed by those listed in Figure 5.5 (the lowest at 3975 cm^{-1}; see Appendix D).

213. Roy, L. E.; Hughbanks, T., *Mater. Res. Soc. Symp. Proc.* **2002**, *755*, 25.

214. Roy, L.; Hughbanks, T., *J. Solid State Chem.* **2003**, *176*, 294.

215. Roy, L. E.; Hughbanks, T., *J. Am. Chem. Soc.* **2006**, *128*, 568.

216. Artelt, H. M.; Meyer, G., *J. Chem. Soc., Chem. Commun.* **1992**, 1320.

217. Calculations performed using 120 ***k***-points.

218. Meng, F., Ph.D. Dissertation, Texas A&M University, 2002.

219. The lowest energy M_S = 1/2 spin pattern is at 4539 cm^{-1}.

220. Calculations were performed using 8 ***k***-points for each compound.

221. The C 2*p* character on $S = 0$ is ambiguous because spin densities on the C_2^{6-} units cancel each other.

222. Westin, G.; Moustiakimov, M.; Kritikos, M., *J. Sol-Gel Sci. Tech.* **2003**, *26*, 115.

223. Prokopuk, N.; Shriver, D. F., *Adv. Inorg. Chem.* **1998**, *46*, 1.

224. Hughbanks, T.; Hoffmann, R., *J. Am. Chem. Soc.* **1983**, *105*, 3528 and references therein.

225. Hughbanks, T.; Hoffmann, R., *J. Am. Chem. Soc.* **1983**, *105*, 1150.

226. Cotton, F. A.; Stanley, G. G., *Chem. Phys. Lett.* **1978**, *58*, 450.

227. Maverick, A. W.; Najdzionek, J. S.; MacKenzie, D.; Nocera, D. G.; Gray, H. B., *J. Am. Chem. Soc.* **1983**, *105*, 1878.

228. Arratia-Perez, R.; Hernandez-Acevedo, L., *J. Chem. Phys.* **1999**, *110*, 2529.

229. Honda, H.; Noro, T.; Tanaka, K.; Miyoshi, E., *J. Chem. Phys.* **2001**, *114*, 10791.

230. Deluzet, A.; Duclusaud, H.; Sautet, P.; Borshch, S. A., *Inorg. Chem.* **2002**, *41*, 2537.

231. Gray, T. G.; Rudzinski, C. M.; Meyer, E. E.; Holm, R. H.; Nocera, D. G., *J. Am. Chem. Soc.* **2003**, *125*, 4755.

232. Hughbanks, T., *Prog. Solid State Chem.* **1989**, *19*, 329 and references therein.

233. Lin, M.; Zhang, Q., *J. Mol. Struct.* **1991**, *228*, 139.

234. Whangbo, M.-H.; Koo, H.-J.; Dai, D., *J. Solid State Chem.* **2003**, *176*, 417.

235. Koo, H.-J.; Whangbo, M.-H., *Inorg. Chem.* **2001**, *40*, 2161.

236. Koo, H.-J.; Whangbo, M.-H.; VerNooy, P. D.; Torardi, C. C.; Marshall, W. J., *Inorg. Chem.* **2002**, *41*, 4664.

237. Whangbo, M. H.; Koo, H. J.; Dai, D.; Jung, D., *Inorg. Chem.* **2003**, *42*, 3898.

238. Koo, H. J.; Whangbo, M. H.; Lee, K. S., *Inorg. Chem.* **2003**, *42*, 5932.

239. Koo, H. J.; Dai, D.; Whangbo, M. H., *Inorg. Chem.* **2005**, *44*, 4359.

240. Rauch, H.; Zawisky, M.; Stellmach, C.; Geltenbort, P., *Phys. Rev. Lett.* **1999**, *83*, 4955.

241. Child, H. R.; Cable, J. W., *J. Appl. Phys.* **1969**, *40*, 1003.

242. Guillaume, M.; Fischer, P.; Roessli, B.; Allenspach, P.; Trounov, V., *Physica C (Amsterdam)* **1994**, *235-240*, 1637.

243. Champion, J. D. M.; Wills, A. S.; Fennell, T.; Bramwell, S. T.; Gardner, J. S.; Green, M. A., *Phys. Rev. B: Condens. Matter* **2001**, *64*, 140407/1.

244. Matsuda, M.; Kikkawa, A.; Katsumata, K.; Ebisu, S.; Nagata, S., *J. Phys. Soc. Jpn.* **2005**, *74*, 1412.

245. Barandiaran, J. M.; Gignoux, D.; Schmitt, D.; Gomez-Sal, J. C.; Rodriguez Fernandez, J.; Chieux, P.; Schweizer, J., *J. Magn. Magn. Mater.* **1988**, *73*, 233.

246. Bruckel, T.; Hupfeld, D.; Strempfer, J.; Caliebe, W.; Mattenberger, K.; Stunault, A.; Bernhoeft, N.; McIntyre, G. J., *Eur. Phys. J. B* **2001**, *19*, 475.

247. Rotter, M.; Doerr, M.; Loewenhaupt, M.; Lindbaum, A.; Ziebeck, K.; Beuneu, B., *Physica B: Condens. Matter (Amsterdam)* **2004**, *350*, e63.

248. Luca, S. E.; Amara, M.; Galera, R. M.; Givord, F.; Granovsky, S.; Isnard, O.; Beneu, B., *Physica B: Condens. Matter (Amsterdam)* **2004**, *350*, e39.

249. Rotter, M.; Loewenhaupt, M.; Doerr, M.; Lindbaum, A.; Sassik, H.; Ziebeck, K.; Beuneu, B., *Phys. Rev. B: Condens. Matter* **2003**, *68*, 144418/1.

250. Tomala, K.; Sanchez, J. P.; Vulliet, P.; Canfield, P. C.; Drzazga, Z.; Winiarska, A., *Phys. Rev. B: Condens. Matter* **1998**, *58*, 8534.

251. Kmiec, R.; Swiatkowska, Z.; Kruk, R.; Tomala, K., *J. Magn. Magn. Mater.* **2004**, *271*, 326.

252. Yamaguchi, Y.; Ohoyama, K.; Yamauchi, H.; Indoh, K.; Onodera, H., *Appl. Phys. A* **2002**, *74*, S877.

253. Kuwahara, K.; Sugiyama, S.; Iwasa, K.; Kohgi, M.; Nakamura, M.; Inamura, Y.; Arai, M.; Kunii, S., *Appl. Phys. A* **2002**, *74*, S302.

254. Ohoyama, K.; Kaneko, K.; Indoh, K.; Yamauchi, H.; Tobo, A.; Onodera, H.; Yamaguchi, Y., *J. Phys. Soc. Jpn.* **2001**, *70*, 3291.

255. Smith, P. K.; Gilles, P. W., *J. Inorg. Nucl. Chem.* **1967**, *29*, 375.

256. Smith, P. K., Ph. D. Dissertation, University of Kansas, 1965.

257. Bauer, J.; Bars, O., *Acta Cryst. B* **1980**, *B36*, 1540.

258. Van Duijn, J.; Suzuki, K.; Attfield, J. P., *Angew. Chem., Int. Ed.* **2000**, *39*, 365.

259. The space group for this proposed structure was incorrectly reported in the original paper ($P\bar{4}2c$); the appropriate space group is $P4_2/mcm$.

260. Burdett, J. K.; Canadell, E.; Hughbanks, T., *J. Am. Chem. Soc.* **1986**, *108*, 3971.

261. Rocquefelte, X.; Boulfelfel, S. E.; Ben Yahia, M.; Bauer, J.; Saillard, J.-Y.; Halet, J.-F., *Angew. Chem., Int. Ed.* **2005**, *44*, 7542.

262. Sakai, T.; Adachi, G.; Shiokawa, J., *Solid State Commun.* **1981**, *40*, 445.

263. Yamauchi, H.; Onodera, H.; Ohoyama, K.; Onimaru, T.; Kosaka, M.; Ohashi, M.; Yamaguchi, Y., *J. Phys. Soc. Jpn.* **1999**, *68*, 2057.

264. van Duijn, J.; Attfield, J. P.; Suzuki, K., *Phys. Rev. B: Condens. Matter* **2000**, *62*, 6410.

265. Hirota, K.; Oumi, N.; Matsumura, T.; Nakao, H.; Wakabayashi, Y.; Murakami, Y.; Endoh, Y., *Phys. Rev. Lett.* **2000**, *84*, 2706.

266. Kaneko, K.; Onodera, H.; Yamauchi, H.; Sakon, T.; Motokawa, M.; Yamaguchi, Y., *Phys. Rev. B: Condens. Matter* **2003**, *68*, 012401/1.

267. Yanagisawa, T.; Goto, T.; Nemoto, Y.; Watanuki, R.; Suzuki, K.; Suzuki, O.; Kido, G., *Phys. Rev. B: Condens. Matter* **2005**, *71*, 104416/1.

268. Sakai, T.; Adachi, G.-Y.; Shiokawa, J., *J. Less-Common Metals* **1982**, *84*, 107.

269. Matsumura, T.; Oumi, N.; Hirota, K.; Nakao, H.; Murakami, Y.; Wakabayashi, Y.; Arima, T.; Ishihara, S.; Endoh, Y., *Phys. Rev. B: Condens. Matter* **2002**, *65*, 094420/1.

270. 4*f*-electron systems, with orbital as well as spin degrees of freedom, frequently show electric quadrupole ordering (cooperative orbital alignment in *f*-electron systems) in addition to magnetic dipole ordering at low temperatures. Electric quadrupole interactions can give rise to ferroquadrupolar (FQ) or antiferroquadrupolar (AFQ) ordering – terms which respectively describe a uniform Ln quadrupole moment alignment or as having staggered components. The magnitudes of the quadrupolar interactions and the dipolar interactions compete in determining the type of ordering that prevails at a given temperature.

271. Tejada-Rosales, E. M.; Rodriguez-Carvajal, J.; Casan-Pastor, N.; Alemany, P.; Ruiz, E.; El-Fallah, M. S.; Alvarez, S.; Gomez-Romero, P., *Inorg. Chem.* **2002**, *41*, 6604.

272. The program $DMol^3$ does not include the option to project orbitals/atoms.

273. Mulliken charges for YB_2C_2 using DFT and EHTB can be found in Appendix E.

274. The surfaces were obtained by numerical fitting of the two bands separately; they bands mix to a small extent where the bands overlap and a more accurate Fermi surface for the EHTB calculation can be obtained using the program CAESAR – see Appendix E.

275. Sleight, A. W.; Prewitt, C. T., *Inorg. Chem.* **1968**, *7*, 2282.

276. Prewitt, C. T.; Sleight, A. W., *Inorg. Chem.* **1968**, *7*, 1090.

277. Ebisu, S.; Iijima, Y.; Iwasa, T.; Nagata, S., *J. Phys. Chem. Solids* **2004**, *65*, 1113.

278. Flahaut, J.; Guittard, M. M.; Patrie, M., *Bull. Soc. Chim. Fr.* **1959**, 1917.

279. Picon, M.; Domange, L.; Flahaut, J.; Guittard, M.; Patrie, M., *Bull. Soc. Chim. Fr.* **1960**, *2*, 221.

280. Zachariasen, W. H., *Acta Cryst.* **1949**, *2*, 57.

281. Becker, G.; Feldhaus, J.; Westerholt, K.; Methfessel, S., *J. Magn. Magn. Mater.* **1977**, *6*, 14.

282. Andrianov, D. G.; Drozdov, S. A.; Lazareva, G. V.; Ponomarev, N. M.; Fistul, V. I., *Fiz. Nizk. Temp. (Kiev)* **1977**, *3*, 497.

283. Andrianov, D. G.; Drozdov, S. A.; Lazareva, G. V.; Ponomarev, N. M., *Zh. Eksp. Teor. Fiz.* **1978**, *75*, 2228.

284. Kikkawa, A.; Katsumata, K.; Ebisu, S.; Nagata, S., *J. Phys. Soc. Jpn.* **2004**, *73*, 2955.

285. Katsumata, K.; Kikkawa, A.; Tanaka, Y.; Shimomura, S.; Ebisu, S.; Nagata, S., *J. Phys. Soc. Jpn.* **2005**, *74*, 1598.

286. DFT and EHTB calculations were performed using the Gd_2S_3 unit cell with 12 and 1000 ***k***-points, respectively.

287. Holtzberg, F.; Gambino, R. J.; McGuire, T. R., *J. Phys. Chem. Solids* **1967**, *28*, 2283.

288. Smith, G. S.; Johnson, Q.; Tharp, A. G., *Acta Cryst.* **1967**, *22*, 269.

289. This polyhedron can be best thought of as a cuboctahedron with two vertices added to the opposite ends of a square face, fulfilling the CN=14.

290. Iglesias, J. E.; Steinfink, H., *J. Less-Common Metals* **1972**, *26*, 45.

291. Pecharsky, V. K.; Gschneidner, K. A., *J. Alloys Compd.* **1997**, *260*, 98.

292. Szade, J.; Skorek, G., *J. Magn. Magn. Mater.* **1999**, *196-197*, 699.

293. Szade, J.; Neumann, M., *J. Phys.: Condens. Matter* **1999**, *11*, 3887.

294. Szade, J.; Neumann, M., *J. Phys.: Condens. Matter* **2001**, *13*, 2717.

295. Skorek, G.; Deniszczyk, J.; Szade, J., *J. Phys.: Condens. Matter* **2002**, *14*, 7273.

296. Szade, J.; Skorek, G.; Neumann, M.; Schneider, B.; Fangmeyer, F.; Matteucci, M.; Paolucci, G.; Goldoni, A., *Surf. Sci.* **2002**, *497*, 29.

297. Nirmala, R.; Sankaranarayanan, V.; Sethupathi, K.; Morozkin, A. V., *J. Alloys Compd.* **2001**, *326*, 174.

298. Pecharsky, A. O.; Gschneidner, K. A.; Pecharsky, V. K., *J. Appl. Phys.* **2003**, *93*, 4722.

299. Tang, H.; Pecharsky, V. K.; Samolyuk, G. D.; Zou, M.; Gschneidner, K. A., Jr.; Antropov, V. P.; Schlagel, D. L.; Lograsso, T. A., *Phys. Rev. Lett.* **2004**, *93*, 237203/1.

300. Vecchini, C.; Moze, O.; Pecharsky, A. O.; Pecharsky, V. K.; Gschneidner, K. A., Jr.; Bruck, E.; Bewley, R.; Kolesnikov, A., *J. Appl. Phys.* **2004**, *95*, 7207.

301. Tyszka, B.; Szade, J.; Skorek, G.; Neumann, M., *J. Alloys Compd.* **2005**, *400*, 51.

302. Magen, C.; Morellon, L.; Algarabel, P. A.; Ibarra, M. R.; Arnold, Z.; Kamarad, J.; Lograsso, T. A.; Schlagel, D. L.; Pecharsky, V. K.; Tsokol, A. O.; Gschneidner, K. A., Jr., *Phys. Rev. B: Condens. Matter* **2005**, *72*, 024416/1.

303. Mozharivskyj, Y.; Pecharsky, A. O.; Pecharsky, V. K.; Miller, G. J., *J. Am. Chem. Soc.* **2005**, *127*, 317.

304. Barclay, J. A., *Adv. Cryog. Eng.* **1988**, *33*, 719.

305. Gschneidner, K. A., Jr.; Pecharsky, V. K.; Pecharsky, A. O.; Zimm, C. B., *Mater. Sci. Forum* **1999**, *315-317*, 69.

306. Spichkin, Y. I.; Zvezdin, A. K.; Gubin, S. P.; Mischenko, A. S.; Tishin, A. M., *J. Phys. D: Appl. Phys.* **2001**, *34*, 1162.

307. Gschneidner, K. A., *J. Alloys Compd.* **2002**, *344*, 356.

308. Long, J. R., In *Chemistry of Nanostructured Materials*, Yang, P,. Ed.; World Scientific: Singapore, 2003; p 291.

309. Brueck, E., *J. Phys. D: Appl. Phys.* **2005**, *38*, R381.

310. Gschneidner, K. A., Jr.; Pecharsky, V. K.; Tsokol, A. O., *Rep. Prog. Phys.* **2005**, *68*, 1479.

311. Zhang, X. X.; Wang, F. W.; Wen, G. H., *J. Phys.: Condens. Matter* **2001**, *13*, L747.

312. Wang, D.; Han, Z.; Cao, Q.; Huang, S.; Zhang, J.; Du, Y., *J. Alloys Compd.* **2005**, *396*, 22.

313. Methfessel, S.; Kneller, E., *Appl. Phys. Lett.* **1963**, *2*, 115.

314. Pecharsky, V. K.; Gschneidner, K. A., Jr., *Phys. Rev. Lett.* **1997**, *78*, 4494.

315. Levin, E. M.; Pecharsky, V. K.; Gschneidner, K. A., Jr.; Miller, G. J., *Phys. Rev. B: Condens. Matter* **2001**, *64*, 235103/1.

316. DFT and EHTB calculations were performed using the Gd_5Si_4 and Gd_5Ge_4 unit cell with 12 and 1000 ***k***-points, respectively.

317. Stoner, E. C., *Proc. Roy. Soc. (London)* **1939**, *A169*, 339.

318. Ishikawa, N.; Sugita, M.; Okubo, T.; Tanaka, N.; Iino, T.; Kaizu, Y., *Inorg. Chem.* **2003**, *42*, 2440.

319. Ishikawa, N.; Iino, T.; Kaizu, Y., *J. Phys. Chem. A* **2002**, *106*, 9543.

320. Ishikawa, N.; Sugita, M.; Ishikawa, T.; Koshihara, S.-Y.; Kaizu, Y., *J. Am. Chem. Soc.* **2003**, *125*, 8694.

321. Ishikawa, N.; Otsuka, S.; Kaizu, Y., *Angew. Chem., Int. Ed.* **2005**, *44*, 731.

322. Ishikawa, N.; Sugita, M.; Wernsdorfer, W., *Angew. Chem., Int. Ed.* **2005**, *44*, 2931.

323. For the collinear approximation, the spin polarization for each point in space has the same direction (default is the in the direction of the *z*-axis). For a noncollinear approximation, the spin polarization can have a different direction for each point in space. See the ADF Manual for more information: http://www.scm.com/

APPENDIX A

COMPUTATIONAL IMPLEMENTATION

DMol^3. Setting up the high-spin and broken-symmetry calculation for a Gd-containing molecule or solid is fairly simple. To facilitate SCF convergence, one *must* include the keyword Start_Spin_Populations, which allows one to input starting spin densities for selected atoms in the model. This can either be specified directly in the input file, or found under the Electronic State section in the Run subheading of the DMol^3 card in Quantum 1 menu of the Cerius2® graphical user interface. Other important keywords are Spin, Charge, and Spin_Polarization. Using the example of $[\{[(H_3Si)_2N]_2(thf)Gd\}_2(N_2)]^+$, a section of the broken symmetry calculation input file would resemble:

Charge	1.000
Spin_Polarizaton	unrestricted
Spin	1
Start_Spin_Populations	on 1 -7.000 2 7.000

where Charge refers to the charge on the molecule, Spin_Polarization refers to a restricted to unrestricted calculation, Spin refers to the net number of unpaired electrons, and Start_Spin_Populations refers to the initial spin density on Gd1 and Gd2. These numbers are based on where the atoms appear in the Cartesian (car) file. In this example, one of the Gd atoms has positive (up) spin density, and the other has the

opposite (down) spin density. The calculation will then converge with one Gd atom having 7 electrons with alpha (up) spin, 7 electrons of beta (down) spin, and one electron residing on the diazenido bridge. Mulliken population analysis can easily verify this orbital occupation. If Start_Spin_Population keyword was not included, the program would try to converge the model that has alpha and beta electrons spread equally, so there is no localization of the spin density on either atom.

There are several "tricks" used to obtain SCF convergence for difficult systems, which includes, in particular, the solid-state Gd systems. It is often possible to achieve SCF convergence with a coarse integration grid, then using that converged potential, one restarts the calculation with a medium-sized grid, then repeating that procedure until finally reaching a SCF converged energy using a fine integration grid. Another method involves smearing the electrons among all orbitals within a given range of the Fermi level. Generally, one would start in the range of ~0.01 a.u. and after achieving SCF convergence, restart the calculation using that potential but employing a smaller smear range until achieving integer occupation numbers. This improves convergence of the SCF procedure by allowing orbitals to relax more rapidly.

ADF. Using ADF, SCF convergence for the high-spin solution is relatively easy, but broken-symmetry solutions require much more time and patience. To set up the input file for the high-spin case, one needs to include the symmetry of the system and the total number of unpaired electrons in addition to all the other pertinent information (i.e., basis sets, functionals, atomic positions, etc.). For the broken-symmetry input file, one needs to specify the lower symmetry of the system and include the keyword

Modifystartpotential. For example, an excerpt from a broken symmetry input file using a molecule such as $[Gd_3I_6(OPH_3)_{12}]^{2+}$ (which has formal D_{3h} symmetry) will then be:

```
Symmetry C(2v) Tol=1.000E-03

Modifystartpotential
Gd/1  7  0
Gd/2  7  0
Gd/3  0  7

Unrestricted
Charge  2  8
```

where Tol refers to the tolerance for atomic positions being symmetry equivalent and Gd/1 refers to gadolinium, atom 1 and so on. The 4*f* potential will break the symmetry of the system from D_{3h} to C_{2v}. As with the use of the Start_Spin_Populations keyword for DMol^3 , the user-defined start potential usually improves SCF convergence. However, ADF has a bothersome tendency to place an unpaired electron either in the *d*-shell or to pair the electron with the $4f^7$ shell to produce an f^8 configuration. In some cases, the program will pair all *f*-electrons for the broken symmetry solution to produce an equal number of α and β electrons in the 4*f* shell. Sometimes this problem can be alleviated using the Occupations keyword, where one specifies the number of alpha and beta electrons in an irreducible representation. One can obtain the correct Aufbau filling of the molecule from the *converged* yttrium (or lanthanum) analog and then determine which irreducible representations span the *f*-orbitals using group theory. Continuing with our trinuclear example, a sample file using the Occupations keyword may look like;

```
Occupations &
A1  46 // 43
A2  25 // 23
B1  33 // 31
```

B2 37 // 36
END

where A1, A2, B1, and B2 refer to the irreducible representations in C_{2v} symmetry.

YAeHMOP. Despite its semi-empirical nature, the extended Hückel tight binding (EHTB) approach has been successful in providing a semi-quantitative description of the magnetic coupling found in transition metal magnetic molecules and solids.[234, 271] In our EHTB calculations, the 4*f* orbitals on a lanthanide atoms are not explicitly included and it is generally understood that they play a minor role in bonding. Nevertheless, an adaptation of the method provides a means for interpreting the magnetic properties of Gd-containing solids. In outline, our procedure is as follows: We use density functional (DFT) band calculations, which take into account the two-electron interactions, to provide a semiquantitative description of a nonmagnetic member of the solid state compounds. Parameters for EHTB calculations (H_{ii}'s) were adjusted to simulate as closely as possible the DFT band structure and density of states (DOS) for Gd_2Cl_3. These values were then used in the calculation of Gd-containing metallic solids, discussed in more detail in Chapter VI. Then the exchange effects exerted by the 4*f* moments are included as a spin-dependent perturbation to the Gd atom 5*d*- and 6*s*-orbital's energies (H_{dd} and H_{ss}) in the EHTB calculations. In effect, a Gd atom with *up-spin* (down-spin) 4*f* electrons, labeled "Y^+"("Y^-") in are assigned more(less) negative 5*d*/6*s* orbital energies for *up-spin* 5*d*/6*s* electrons in the tight-binding approach. Of course, the situation is reversed for *down-spin* 5*d*/6*s* electrons, which are assigned less(more) negative 5*d*/6*s* orbital energies in the vicinity of an *up-spin* (down-spin) 4*f* center.

APPENDIX B

EXTENDED HÜCKEL/TIGHT BINDING PARAMETERS

Table B1. Extended Hückel exponents (ζ), valence shell ionization potential (H_{ii}'s in eV), and coefficients.

Atom	Orbital	H_{ii} (eV)	ζ_1	ζ_2	c_1	c_2
B	2*s*	-15.2	1.30			
	2*p*	-8.5	1.30			
C	2*s*	-21.4	1.625			
	2*p*	-11.4	1.625			
Si	3*s*	-17.300	1.3830			
	3*p*	-9.200	1.3830			
S	3*s*	-20.000	2.1220			
	3*p*	-10.700	1.6370			
Cl	3*s*	-26.300	2.1830			
	3*p*	-14.200	1.7330			
Ge	4*s*	-16.000	2.1600			
	4*p*	-8.600	1.4900			
Y	5*s*	-7.02	1.74			
	5*p*	-4.40	1.70			
	4*d*	-6.80	1.40	3.60	0.8316	0.3041
"Gd^+" [a]	5*s*	-7.12	1.74			
	5*p*	-4.40	1.70			
	4*d*	-7.02	1.40	3.60	0.8316	0.3041
"Gd^-"[a]	5*s*	-6.91	1.74			
	5*p*	-4.40	1.70			
	4*d*	-6.58	1.40	3.60	0.8316	0.3041

[a] Gd^+ and Gd^- are used to model the spin-dependent energies of valence *s* and *d* electrons for Gd centers with spins that are respectively aligned parallel and antiparallel with the local spin direction of the 4*f* electrons.

APPENDIX C

SUPPLEMENTARY MATERIAL FOR CALCULATIONS OF $[Gd(AmPh)]_2$, $[\{Gd(O_2CR)_3(H_2O)_2\}_2]$, AND $\{[(Me_3Si)_2N]_2(thf)Y\}_2(N_2)$

Table C1. Calculated charges and net spin densities for models of $[Gd(AmPh)]_2$.

Mulliken Charges			
Atom	Ph = 3	Ph = 1	Ph = 0
Gd	1.845	1.864	1.875
O	-0.824	–0.819	–0.777
C	0.321	0.325	0.324

Gd Spin Populations						
Gd	S = 7	S = 0	S = 7	S = 0	S = 7	S = 0
6s	0.022	0.022	0.023	0.022	0.022	0.022
5d	0.048	0.051	0.047	0.049	0.051	0.053

Table C2. Calculated charges and net spin densities for models of $[\{Gd(O_2CR)_3(H_2O)_2\}_2]$.

Mulliken Charges			
Atom	H	CH_3	CF_3
Gd	1.806	1.795	1.804
O	–0.624	–0.687	–0.675
C	0.352	0.521	0.554

Gd Spin Populations						
Gd	S = 7	S = 0	S = 7	S = 0	S = 7	S = 0
6s	0.021	0.021	0.022	0.022	0.022	0.022
5d	0.062	0.063	0.062	0.062	0.062	0.063

Table C3. Selected experimental, DFT optimized, and 1-e$^-$ oxidized bond distances (Å) and angles (deg) for $\{[(Me_3Si)_2N]_2(thf)Y\}_2(N_2)$. (Partial geometry optimization was performed for the 1-e oxidized model and all other distances and angles were kept constant using the experimental geometry.)

	Experimental	Geometry Optimization	1-e$^-$ Oxidation
		Bond Distances (Å)	
Y—N3 (diazenido)	2.296(2)	2.340	2.560
Y—N4	2.317(2)	2.369	2.602
N4—N3	1.268(3)	1.256	1.181
Y—N1 (disilylamide)	2.244(2)	2.283	2.207
N1—Si1	1.715(2)	1.748	1.741
N1—Si2	1.710(2)	1.747	1.729
Y···Si1	3.402(2)	3.478	3.159
Y···Si2	3.411(2)	3.474	3.530
Y···C3	3.349(2)	3.489	
Y···C6	3.472(2)	3.562	
Y···H′	3.044	3.256	2.723
Y···H″	3.129	3.243	3.530
Si1—$CH_3$3(···Y)	1.879(2)	1.911	
Si1—$CH_3$3(other)	1.876(2)	1.909	
	1.880(2)	1.910	
Si2—$CH_3$6(···Y)	1.868(2)	1.911	
Si2—$CH_3$6(other)	1.864(2)	1.909	
	1.867(2)	1.910	
C3—H′ (···Y)	0.981	1.102	
C3—H′ (other)	0.980	1.099	
	0.980	1.101	
C6—H″ (···Y)	0.979	1.097	
C6—H″ (other)	0.980	1.096	
	0.980	1.101	
Y—N2 (disilylamide)	2.264(2)	2.295	2.207
N2—Si3	1.711(2)	1.747	1.731
N2—Si4	1.720(2)	1.754	1.745
Y···Si3	3.359(2)	3.451	3.114
Y···Si4	3.523(2)	3.565	3.606
Y···C8	3.275(2)	3.444	
Y···C9	3.942(2)	3.993	
Y···H‴	3.047	3.340	2.636
Y···H⁗	3.543	3.594	3.814

Table C3. Continued.

Si3—$CH_3$8 (···Y)	1.884(2)	1.917	
Si3—$CH_3$8 (other)	1.877(2)	1.912	
	1.886(2)	1.923	
C8—H‴ (···Y)	0.980	1.104	
C8—H‴ (other)	0.980	1.099	
	0.979	1.103	
		Bond Angles (deg)	
N3—Y—N4 (diazenido)	31.90(8)	30.94	26.4
N1—Y—N2(disilylamide)	117.44(6)	117.13	114.9
Y—N1—Si2	118.61(8)	118.45	106.2
Y—N1—Si1	117.83(8)	118.65	126.4
N1—Si1—$CH_3$3	107.92(10)	109.35	
N1—Si2—$CH_3$6	110.76(9)	111.09	
Si2—N—Si1	123.54(9)	133.81	127.4
Si2—C6—H′ (···Y)	109.42	113.03	
Si1—C3—H″ (···Y)	109.51	113.58	
Si2—C6—H′ (other)	109.43	112.59	
	109.55	108.59	
Si1—C3—H″ (other)	109.43	113.47	
	109.55	108.38	
Y—N2—Si3	114.61(8)	116.57	103.9
Si3—N2—Si4	123.79(8)	122.83	124.8
N2—Si3—$CH_3$8	108.72(9)	109.90	
N2—Si4—$CH_3$9	112.05(9)	110.675	
Si3—C8—H‴(···Y)	109.48	113.58	
Si3—C8—H‴(other)	109.46	112.87	
	109.44	108.84	
		Dihedral Angles(deg)	
Y—N1—Si1—$CH_3$3	4.00	6.56	
Y—N1—Si2—$CH_3$6	11.05	14.54	
Y—N2—Si3—$CH_3$8	5.10	7.29	

APPENDIX D

SUPPLEMENTARY MATERIAL FOR

CALCULATIONS OF $[Gd_6MI_{12}](OPH_3)_6$ (M = Co, N)

Table D1. Spin pattern energies (cm^{-1}) and symmetry imposed by the 4*f* moments for 20 competing spin patterns on the single cluster model of $[Gd_6CoI_{12}](OPH_3)_6$.

Spin Pattern	Symmetry	Energy (cm^{-1})
S=45/2	O_h	0
S=31/2	C_{4v}	1380.546471
S=17/2	D_{4h}	2787.133537
S=17/2	C_{2v}	2797.071524
S=43/2	O_h	3975.128778
S=15/2	D_{4h}	3989.103385
S=3/2	C_{2v}	4246.372188
S=3/2	C_{3v}	4252.66844
S=29/2	C_{4v}	4466.433871
S=15/2	C_{2v}	4598.040892
S=13/2	D_{4h}	5107.137833
S=1/2	C_{3v}	5266.013988
S=13/2	C_{2v}	5571.371237
S=11/2	D_{4h}	5746.96427
S=11/2	C_{2v}	5747.600477
S=27/2	C_{4v}	6126.428623
S=41/2	O_h	6954.506411
S=25/2	C_{4v}	7291.147476
S=39/2	O_h	8892.018887
S=1/2	C_{2v}	---*

* No convergence for this spin pattern.

Table D2. Spin pattern energies (cm^{-1}) and symmetry imposed by the 4*f* moments for 20 competing spin patterns on the single cluster model of $[Gd_6NI_{12}](OPH_3)_6$.

Spin Pattern	Symmetry	Energy (cm^{-1})
S=45/2	O_h	0
S=31/2	C_{4v}	1944.03997
S=17/2	C_{2v}	3911.04693
S=17/2	D_{4h}	4101.19488
S=15/2	C_{2v}	4539.35510
S=1/2	C_{2v}	4748.00177
S=29/2	C_{4v}	4811.58549
S=13/2	D_{4h}	4956.31331
S=43/2	O_h	5142.12702
S=15/2	D_{4h}	5670.63601
S=3/2	C_{3v}	5922.04418
S=3/2	C_{2v}	6117.53173
S=1/2	C_{3v}	6497.76061
S=27/2	C_{4v}	7060.85414
S=13/2	C_{2v}	7555.00200
S=11/2	C_{2v}	8159.71762
S=11/2	D_{4h}	8404.46804
S=41/2	O_h	9478.62190
S=25/2	C_{4v}	10496.43070
S=39/2	O_h	12914.44420

APPENDIX E

SUPPLEMENTARY MATERIAL FOR CALCULATIONS OF YB_2C_2

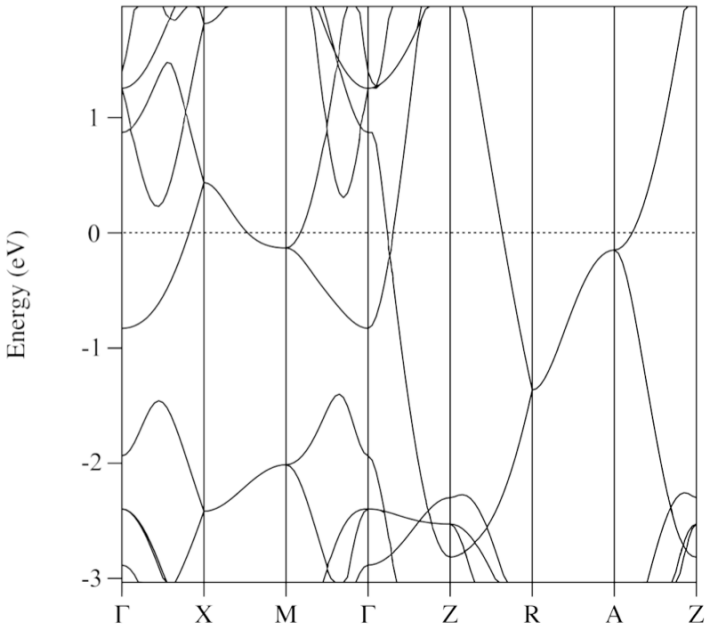

Figure E1. Full band structure of YB_2C_2 using DFT.

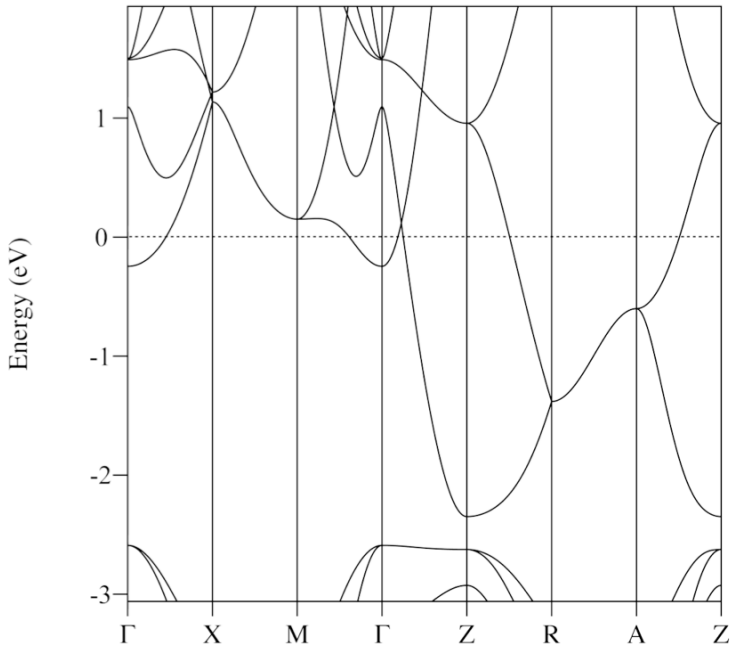

Figure E2. Full band structure of YB_2C_2 using EHTB.

Table E1. Mulliken charges for YB_2C_2 from DFT and EHTB.

Atom	DFT	EHTB
Y	1.352	1.848
C	-0.863	-1.305
B	0.187	0.382

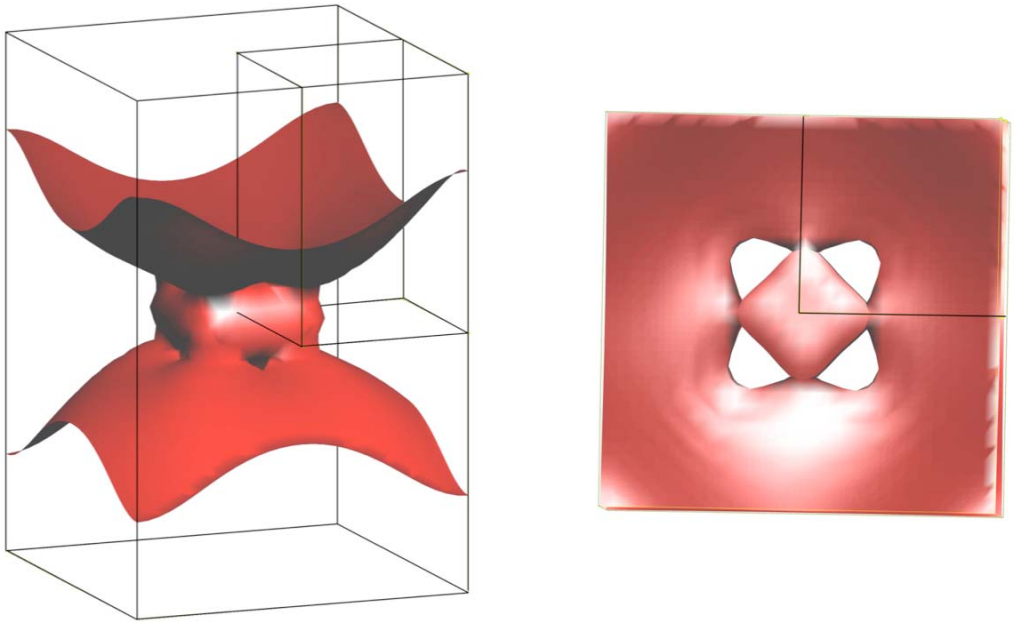

Figure E3. Fermi Surface for YB_2C_2 using CAESAR.[63]

APPENDIX F

SUPPLEMENTARY MATERIAL FOR

CALCULATIONS OF $[Tb(pc)_2]^-$

Table F1. Clebsch-Gordan coefficients for $J = 6$ state where $|J, M_J\rangle = |S, M_S\rangle|L, M_L\rangle$.

$$|6,\pm6\rangle = |3,\pm3\rangle|3,\pm3\rangle$$

$$|6,\pm5\rangle = \frac{1}{\sqrt{2}}|3,\pm2\rangle|3,\pm3\rangle + \frac{1}{\sqrt{2}}|3,\pm3\rangle|3,\pm2\rangle$$

$$|6,\pm4\rangle = \frac{\sqrt{10}}{2\sqrt{11}}|3,\pm1\rangle|3,\pm3\rangle + \frac{\sqrt{6}}{\sqrt{11}}|3,\pm2\rangle|3,\pm2\rangle + \frac{\sqrt{10}}{2\sqrt{11}}|3,\pm3\rangle|3,\pm1\rangle$$

$$|6,\pm3\rangle = \frac{1}{\sqrt{11}}|3,0\rangle|3,\pm3\rangle + \frac{3}{\sqrt{22}}|3,\pm1\rangle|3,\pm2\rangle + \frac{3}{\sqrt{22}}|3,\pm2\rangle|3,\pm1\rangle + \frac{1}{\sqrt{11}}|3,\pm3\rangle|3,0\rangle$$

$$|6,\pm2\rangle = \frac{\sqrt{3}}{3\sqrt{11}}|3,\mp1\rangle|3,\pm3\rangle + \frac{2\sqrt{6}}{3\sqrt{11}}|3,0\rangle|3,\pm2\rangle + \frac{\sqrt{5}}{\sqrt{11}}|3,\pm1\rangle|3,\pm1\rangle + \frac{2\sqrt{6}}{3\sqrt{11}}|3,\pm2\rangle|3,0\rangle + \frac{\sqrt{3}}{3\sqrt{11}}|3,\pm3\rangle|3,\mp1\rangle$$

$$|6,\pm1\rangle = \frac{\sqrt{3}}{6\sqrt{11}}|3,\mp2\rangle|3,\pm3\rangle + \frac{\sqrt{5}}{2\sqrt{11}}|3,\mp1\rangle|3,\pm2\rangle + \frac{5\sqrt{6}}{6\sqrt{11}}|3,0\rangle|3,\pm1\rangle + \frac{5\sqrt{6}}{6\sqrt{11}}|3,\pm1\rangle|3,0\rangle + \frac{\sqrt{5}}{2\sqrt{11}}|3,\pm2\rangle|3,\mp1\rangle + \frac{\sqrt{3}}{6\sqrt{11}}|3,\pm3\rangle|3,\mp2\rangle$$

$$|6,0\rangle = \frac{\sqrt{3}}{6\sqrt{77}}|3,\mp3\rangle|3,\pm3\rangle + \frac{\sqrt{3}}{\sqrt{77}}|3,\mp2\rangle|3,\pm2\rangle + \frac{5\sqrt{3}}{2\sqrt{77}}|3,\mp1\rangle|3,\pm1\rangle + \frac{10\sqrt{3}}{3\sqrt{77}}|3,0\rangle|3,0\rangle + \frac{5\sqrt{3}}{2\sqrt{77}}|3,\pm1\rangle|3,\mp1\rangle + \frac{\sqrt{3}}{\sqrt{77}}|3,\pm2\rangle|3,\mp2\rangle + \frac{\sqrt{3}}{6\sqrt{77}}|3,\pm3\rangle|3,\mp3\rangle$$

$$|5,\pm5\rangle = \frac{1}{\sqrt{2}}|3,\pm3\rangle|3,\pm2\rangle - \frac{1}{\sqrt{2}}|3,\pm2\rangle|3,\pm3\rangle$$

Table F1. Continued.

$$|5,\pm4\rangle = \frac{1}{\sqrt{2}}|3,\pm3\rangle|3,\pm1\rangle - \frac{1}{\sqrt{2}}|3,\pm1\rangle|3,\pm3\rangle$$

$$|5,\pm3\rangle = \frac{1}{\sqrt{3}}|3,\pm3\rangle|3,0\rangle + \frac{1}{\sqrt{6}}|3,\pm2\rangle|3,\pm1\rangle - \frac{1}{\sqrt{6}}|3,\pm1\rangle|3,\pm2\rangle - \frac{1}{\sqrt{3}}|3,0\rangle|3,\pm3\rangle$$

$$|5,\pm2\rangle = \frac{1}{\sqrt{6}}|3,\pm3\rangle|3,\mp1\rangle + \frac{1}{\sqrt{3}}|3,\pm2\rangle|3,0\rangle - \frac{1}{\sqrt{3}}|3,0\rangle|3,\pm2\rangle - \frac{1}{\sqrt{6}}|3,\mp1\rangle|3,\pm3\rangle$$

$$|5,\pm1\rangle = \frac{\sqrt{15}}{6\sqrt{7}}|3,\pm3\rangle|3,\mp2\rangle + \frac{3}{2\sqrt{7}}|3,\pm2\rangle|3,\mp1\rangle + \frac{\sqrt{30}}{6\sqrt{7}}|3,\pm1\rangle|3,0\rangle$$
$$- \frac{\sqrt{30}}{6\sqrt{7}}|3,0\rangle|3,\pm1\rangle - \frac{3}{2\sqrt{7}}|3,\mp1\rangle|3,\pm2\rangle - \frac{\sqrt{15}}{6\sqrt{7}}|3,\mp2\rangle|3,\pm3\rangle$$

$$|5,0\rangle = \frac{\sqrt{3}}{6\sqrt{7}}|3,\pm3\rangle|3,\mp3\rangle + \frac{2\sqrt{3}}{3\sqrt{7}}|3,\pm2\rangle|3,\mp2\rangle + \frac{5\sqrt{3}}{6\sqrt{7}}|3,\pm1\rangle|3,\mp1\rangle$$
$$- \frac{5\sqrt{3}}{6\sqrt{7}}|3,\mp1\rangle|3,\pm1\rangle - \frac{2\sqrt{3}}{3\sqrt{7}}|3,\mp2\rangle|3,\pm2\rangle - \frac{\sqrt{3}}{6\sqrt{7}}|3,\mp3\rangle|3,\pm3\rangle$$

$$|4,\pm4\rangle = \frac{\sqrt{3}}{\sqrt{11}}|3,\pm3\rangle|3,\pm1\rangle - \frac{\sqrt{5}}{\sqrt{11}}|3,\pm2\rangle|3,\pm2\rangle + \frac{\sqrt{3}}{\sqrt{11}}|3,\pm1\rangle|3,\pm3\rangle$$

$$|4,\pm3\rangle = \frac{3\sqrt{2}}{2\sqrt{11}}|3,\pm3\rangle|3,0\rangle - \frac{1}{\sqrt{11}}|3,\pm2\rangle|3,\pm1\rangle - \frac{1}{\sqrt{11}}|3,\pm1\rangle|3,\pm2\rangle + \frac{3\sqrt{2}}{2\sqrt{11}}|3,0\rangle|3,\pm3\rangle$$

$$|4,\pm2\rangle = \frac{3\sqrt{3}}{\sqrt{77}}|3,\pm3\rangle|3,\mp1\rangle + \frac{\sqrt{6}}{2\sqrt{77}}|3,\pm2\rangle|3,0\rangle - \frac{10}{\sqrt{385}}|3,\pm1\rangle|3,\pm1\rangle$$
$$+ \frac{\sqrt{6}}{2\sqrt{77}}|3,0\rangle|3,\pm2\rangle + \frac{3\sqrt{3}}{\sqrt{77}}|3,\mp1\rangle|3,\pm3\rangle$$

$$|4,\pm1\rangle = \frac{\sqrt{15}}{\sqrt{77}}|3,\pm3\rangle|3,\mp2\rangle + \frac{4}{\sqrt{77}}|3,\pm2\rangle|3,\mp1\rangle - \frac{5\sqrt{6}}{2\sqrt{385}}|3,\pm1\rangle|3,0\rangle$$
$$- \frac{5\sqrt{6}}{2\sqrt{385}}|3,0\rangle|3,\pm1\rangle + \frac{4}{\sqrt{77}}|3,\mp1\rangle|3,\pm2\rangle + \frac{\sqrt{15}}{\sqrt{77}}|3,\mp2\rangle|3,\pm3\rangle$$

$$|4,0\rangle = \frac{3\sqrt{2}}{2\sqrt{77}}|3,\pm3\rangle|3,\mp3\rangle + \frac{7\sqrt{2}}{2\sqrt{77}}|3,\pm2\rangle|3,\mp2\rangle + \frac{\sqrt{2}}{2\sqrt{77}}|3,\pm1\rangle|3,\mp1\rangle$$
$$- \frac{3\sqrt{2}}{\sqrt{77}}|3,0\rangle|3,0\rangle + \frac{\sqrt{2}}{2\sqrt{77}}|3,\mp1\rangle|3,\pm1\rangle + \frac{7\sqrt{2}}{2\sqrt{77}}|3,\mp2\rangle|3,\pm2\rangle + \frac{3\sqrt{2}}{2\sqrt{77}}|3,\mp3\rangle|3,\pm3\rangle$$

$$|3,\pm3\rangle = \frac{1}{\sqrt{6}}|3,\pm3\rangle|3,0\rangle - \frac{1}{\sqrt{3}}|3,\pm2\rangle|3,\pm1\rangle + \frac{1}{\sqrt{3}}|3,\pm1\rangle|3,\pm2\rangle - \frac{1}{\sqrt{6}}|3,0\rangle|3,\pm3\rangle$$

Table F1. Continued.

$$|3,\pm2\rangle = \frac{1}{\sqrt{3}}|3,\pm3\rangle|3,\mp1\rangle - \frac{1}{\sqrt{6}}|3,\pm2\rangle|3,0\rangle + \frac{1}{\sqrt{6}}|3,0\rangle|3,\pm2\rangle - \frac{1}{\sqrt{3}}|3,\mp1\rangle|3,\pm3\rangle$$

$$|3,\pm1\rangle = \frac{1}{\sqrt{3}}|3,\pm3\rangle|3,\mp2\rangle - \frac{1}{\sqrt{6}}|3,\pm1\rangle|3,0\rangle + \frac{1}{\sqrt{6}}|3,0\rangle|3,\pm1\rangle - \frac{1}{\sqrt{3}}|3,\mp2\rangle|3,\pm3\rangle$$

$$|3,0\rangle = \frac{1}{\sqrt{6}}|3,\pm3\rangle|3,\mp3\rangle + \frac{1}{\sqrt{6}}|3,\pm2\rangle|3,\mp2\rangle - \frac{1}{\sqrt{6}}|3,\pm1\rangle|3,\mp1\rangle$$
$$+\frac{1}{\sqrt{6}}|3,\mp1\rangle|3,\pm1\rangle - \frac{1}{\sqrt{6}}|3,\mp2\rangle|3,\pm2\rangle - \frac{1}{\sqrt{6}}|3,\mp3\rangle|3,\pm3\rangle$$

$$|2,\pm2\rangle = \frac{\sqrt{30}}{6\sqrt{7}}|3,\pm3\rangle|3,\mp1\rangle - \frac{\sqrt{15}}{3\sqrt{7}}|3,\pm2\rangle|3,0\rangle + \frac{\sqrt{2}}{\sqrt{7}}|3,\pm1\rangle|3,\pm1\rangle$$
$$-\frac{\sqrt{15}}{3\sqrt{7}}|3,0\rangle|3,\pm2\rangle + \frac{\sqrt{30}}{6\sqrt{7}}|3,\mp1\rangle|3,\pm3\rangle$$

$$|2,\pm1\rangle = \frac{5\sqrt{3}}{6\sqrt{7}}|3,\pm3\rangle|3,\mp2\rangle - \frac{\sqrt{5}}{2\sqrt{7}}|3,\pm2\rangle|3,\mp1\rangle + \frac{1}{\sqrt{42}}|3,\pm1\rangle|3,0\rangle + \frac{1}{\sqrt{42}}|3,0\rangle|3,\pm1\rangle$$
$$-\frac{\sqrt{5}}{2\sqrt{7}}|3,\mp1\rangle|3,\pm2\rangle + \frac{5\sqrt{3}}{6\sqrt{7}}|3,\mp2\rangle|3,\pm3\rangle$$

$$|2,0\rangle = \frac{5\sqrt{3}}{6\sqrt{7}}|3,\pm3\rangle|3,\mp3\rangle - \frac{3}{2\sqrt{21}}|3,\pm1\rangle|3,\mp1\rangle + \frac{2\sqrt{3}}{3\sqrt{7}}|3,0\rangle|3,0\rangle$$
$$-\frac{3}{2\sqrt{21}}|3,\mp1\rangle|3,\pm1\rangle + \frac{5\sqrt{3}}{6\sqrt{7}}|3,\mp3\rangle|3,\pm3\rangle$$

$$|1,\pm1\rangle = \frac{\sqrt{3}}{2\sqrt{7}}|3,\pm3\rangle|3,\mp2\rangle - \frac{\sqrt{5}}{2\sqrt{7}}|3,\pm2\rangle|3,\mp1\rangle + \frac{\sqrt{6}}{2\sqrt{7}}|3,\pm1\rangle|3,0\rangle - \frac{\sqrt{6}}{2\sqrt{7}}|3,0\rangle|3,\pm1\rangle$$
$$+\frac{\sqrt{5}}{2\sqrt{7}}|3,\mp1\rangle|3,\pm2\rangle - \frac{\sqrt{3}}{2\sqrt{7}}|3,\mp2\rangle|3,\pm3\rangle$$

$$|1,0\rangle = \frac{3}{2\sqrt{7}}|3,\pm3\rangle|3,\mp3\rangle - \frac{1}{\sqrt{7}}|3,\pm2\rangle|3,\mp2\rangle + \frac{1}{2\sqrt{7}}|3,\pm1\rangle|3,\mp1\rangle$$
$$-\frac{1}{2\sqrt{7}}|3,\mp1\rangle|3,\pm1\rangle + \frac{1}{\sqrt{7}}|3,\mp2\rangle|3,\pm2\rangle - \frac{3}{2\sqrt{7}}|3,\mp3\rangle|3,\pm3\rangle$$

$$|0,0\rangle = \frac{1}{\sqrt{7}}|3,\pm3\rangle|3,\mp3\rangle - \frac{1}{\sqrt{7}}|3,\pm2\rangle|3,\mp2\rangle + \frac{1}{\sqrt{7}}|3,\pm1\rangle|3,\mp1\rangle - \frac{1}{\sqrt{7}}|3,0\rangle|3,0\rangle$$
$$+\frac{1}{\sqrt{7}}|3,\mp1\rangle|3,\pm1\rangle - \frac{1}{\sqrt{7}}|3,\mp2\rangle|3,\pm2\rangle + \frac{1}{\sqrt{7}}|3,\mp3\rangle|3,\pm3\rangle$$

VITA

NAME AND ADDRESS: Lindsay Elizabeth Roy

502 Southwest Pkwy #904, College Station, TX 77840

EDUCATION: B.S., Chemistry, University of North Texas, 1999

SELECT PUBLICATIONS:

"Rules for Understanding and Designing Novel Molecule-Based Rare-Earth Magnetic Compounds," Lindsay E. Roy, and Timothy Hughbanks, *Materials Research Society Symposium Proceedings*, Vol. 755, DD1.6.1-DD1.6.6 (2003).

"*d*-Electron Mediated $4f^7$-$4f^7$ Exchange in Gd-rich Compounds; Spin Density Functional Study of Gd_2Cl_3," Lindsay E. Roy and Timothy Hughbanks, *Journal of Solid State Chemistry*, 76, 294-305 (2003).

"Magnetic Coupling in Dinuclear Gd Complexes," Lindsay E. Roy and Timothy Hughbanks, *Journal of the American Chemical Society*, 128, 568-575 (2006).

"Ferromagnetic Coupling in Hexanuclear Gd Cluster," Lucas Sweet, Lindsay E. Roy, Fanqin Meng, and Timothy Hughbanks, *Journal of the American Chemical Society*, accepted for publication.

"Electronic Transitions in $[Re_6S_8X_6]^{4-}$ (X=Cl, Br, I): Results from Time-Dependent Density Functional and Solid State Calculations," Lindsay E. Roy and Timothy Hughbanks, *Inorganic Chemistry*, submitted for publication.

"GdB_2C_2: From Structural to Magnetic Ordering," Lindsay E. Roy and Timothy Hughbanks, *Journal of the American Chemical Society*, to be submitted for publication.